

# Li, Na, K, Mg, Zn, Al, and Ca Anode Interface Chemistries Developed by Solid-State Electrolytes

Sambhaji S. Shinde, Nayantara K. Wagh, Sung-Hae Kim, and Jung-Ho Lee\*

Solid-state batteries (SSBs) have received significant attention due to their high energy density, reversible cycle life, and safe operations relative to commercial Li-ion batteries using flammable liquid electrolytes. This review presents the fundamentals, structures, thermodynamics, chemistries, and electrochemical kinetics of desirable solid electrolyte interphase (SEI) required to meet the practical requirements of reversible anodes. Theoretical and experimental insights for metal nucleation, deposition, and stripping for the reversible cycling of metal anodes are provided. Ion transport mechanisms and state-of-the-art solid-state electrolytes (SEs) are discussed for realizing high-performance cells. The interface challenges and strategies are also concerned with the integration of SEs, anodes, and cathodes for large-scale SSBs in terms of physical/chemical contacts, space-charge layer, interdiffusion, lattice-mismatch, dendritic growth, chemical reactivity of SEI, current collectors, and thermal instability. The recent innovations for anode interface chemistries developed by SEs are highlighted with monovalent (lithium ( $\text{Li}^+$ ), sodium ( $\text{Na}^+$ ), potassium ( $\text{K}^+$ )) and multivalent (magnesium ( $\text{Mg}^{2+}$ ), zinc ( $\text{Zn}^{2+}$ ), aluminum ( $\text{Al}^{3+}$ ), calcium ( $\text{Ca}^{2+}$ )) cation carriers (i.e., lithium-metal, lithium-sulfur, sodium-metal, potassium-ion, magnesium-ion, zinc-metal, aluminum-ion, and calcium-ion batteries) compared to those of liquid counterparts.

operational life, and safety standards with reasonable prices are critical requirements of the industry.<sup>[3,4]</sup> Advanced Li-ion batteries (LIBs) suffer from their energy limits and are challenged by energy-storage market demands of  $\geq 500 \text{ Wh kg}^{-1}$  at the cell level.<sup>[5]</sup> However, serious safety issues, limited energies, and electrochemical/thermal instabilities due to flammable organic liquid electrolytes are the main problems of existing LIBs. Solid-state batteries (SSBs) comprising solid-state electrolytes (SEs) have received remarkable scientific and industrial attention for electrical energy storage with promising new battery chemistries. SSBs yield inspiring benefits such as 1) improving safety anxieties by the removal of flammable organic liquids, 2) inhibiting short-circuit failures by delaying metal dendrites, 3) bending, punching, or piercing deprived of risky annoying safety hazards, 4) larger electrochemical windows (EWs) utilizing high voltage cathode materials.<sup>[6]</sup> SSBs consist of bulk- and thin-film types. Bulk-type SSBs exhibit the compressing active materials in pellets and stacks or preparing slurries with tape


casting owing to their high-energy, low cost, and safe, which illustrates suitability for future energy-storage systems. Thin-film SSBs exhibit thin layered active materials loading and applicability for micro-batteries.<sup>[7]</sup> Researchers anticipated SSBs would reveal multiple advantages, including high reversibility and acceptable cycle life with broad temperature operations. Also, SEs should possess the major standard parameters of  $\text{M}^+$ -ion conductance ( $> 10^{-4} \text{ S cm}^{-1}$ ), sufficient mechanical strengths (shear modulus  $G_{\text{separator/electrolyte}} > G_{\text{anode}}$ ), and slightest defects to prevent metal-dendrites infiltration, lower activation energies for metal  $\text{M}^+$ -diffusion (lower the surface diffusion barriers of  $\text{M}^+$ -ions with high surface energies), and scalable fabrication processes with abundant resources.<sup>[8,9]</sup>

SEs research initiates with high modulus solid-ion conductors that can project direct pathways for practical high-energy batteries with metal anodes.<sup>[1]</sup> Recently SEs focused on several developments involving high-performance materials, enlarged safety issues, and different applications. SEs comprise organic (polymers) and inorganic (oxides, sulfides, hydrides) solids. Numerous SEs with different chemistries display superb ion conductivity at room-temperature ( $\approx 1 \text{ mS cm}^{-1}$ ) relative to those of flammable liquid electrolytes. Sulfide-based inorganic SEs

## 1. Introduction

Recent battery systems, including lithium-ion, lead-acid, nickel-metal hydride, and flow batteries, have been utilized for electric vehicles, portable electronics, and grid-scale stationary storage; however, they do not satisfy projected energy, lifetimes, cost, and safety demands.<sup>[1,2]</sup> Batteries with high energy density, long

S. S. Shinde, N. K. Wagh, S.-H. Kim, J.-H. Lee  
Department of Materials Science and Chemical Engineering  
Hanyang University  
Ansan, Gyeonggi-do 15588, Republic of Korea  
E-mail: jungho@hanyang.ac.kr  
S. S. Shinde, N. K. Wagh, S.-H. Kim, J.-H. Lee  
FLEXOLYTE Inc.  
Ansan 15588, Republic of Korea

 The ORCID identification number(s) for the author(s) of this article can be found under <https://doi.org/10.1002/advs.202304235>

© 2023 The Authors. Advanced Science published by Wiley-VCH GmbH. This is an open access article under the terms of the Creative Commons Attribution License, which permits use, distribution and reproduction in any medium, provided the original work is properly cited.

DOI: 10.1002/advs.202304235

display higher ion-conductivities than those of all other SEs (oxides, polymers, or composites) owing to their body-centered-cubic (*bcc*)-like anions structures, which is favorable for Li-ion or other metal-ions (such as Na, K, Zn, Mg, Al, Ca) diffusion.<sup>[6]</sup> Precisely, the inorganic SEs,  $\text{Li}_{10}\text{GeP}_2\text{S}_{12}$  ( $12 \text{ mS cm}^{-1}$ ),  $\text{Li}_7\text{P}_3\text{S}_{11}$  ( $17 \text{ mS cm}^{-1}$ ),  $\text{Li}_{9.54}\text{Si}_{1.74}\text{P}_{1.44}\text{S}_{11.7}\text{Cl}_{0.3}$  ( $25 \text{ mS cm}^{-1}$ ), and  $\text{Li}_2\text{S-P}_2\text{S}_5$  ( $17 \text{ mS cm}^{-1}$ ) as intrinsic single-ion conductors manifest high charge-transfer capability comparable to liquids, illustrating great promise for future high-energy batteries.<sup>[10–12]</sup> However, the solid-solid interfaces are the key scientific concern that limits the practical applications of SSBs. For instance, Li-ions diffuse across anode/SEs and SEs/cathode interfaces for transport. Simultaneously, electrons leave one side of battery cells upon discharge through current collectors (CCs)/anode interfaces and arrive on the opposite side via cathode/CC interfaces and vice-versa upon charge. The oxidation/reduction reactions for electrode/SEs interfaces are the primary source for interfacial reactions in SSBs. A comprehensive understanding of this interface kinetics is critically necessary for stable operations for SSBs.

Using metal anodes (Li, Na, K, Mg, Zn, Al, Ca) has been investigated to find a promising approach for high-energy storage technologies. In principle, replacing graphite ( $372 \text{ mAh g}^{-1}$ ) anode with Li ( $3860 \text{ mAh g}^{-1}$ ) or other metals makes it possible to reach an energy density of  $\geq 500 \text{ Wh kg}^{-1}$  with suitable battery chemistries.<sup>[5,9]</sup> Unlike graphite, however, metal anodes are highly reactive, have poor mechanical yields, are inclined to large volume deviations upon charge-discharge processes, and have numerous metal-ions concentrations for electrochemical reactions. The solid-electrolyte interphase (SEI) plays a significant role in determining metal anodes' reversible cycle life.<sup>[13]</sup> SEI allows the metal-ions diffusion to preserve reaction kinetics and electronic insulation among the electrodes and SEs (i.e., limits parasitic reactions), promoting uniform metal electrodepositions by controlling solid ion flux. Ideal properties required for the SEI layer are superb cations conductivity with larger electronic resistances, uniform thickness (10–20 nm), larger mechanical strengths that facilitates the tolerance for volumetric changes upon charging, insolubility in the electrolytes, and stable operating capabilities for high voltages and wide temperatures. The robust SEI is essential for long-life battery operations for metal or ion-insertion anodes. SEI growth (homogenous or heterogeneous, rapid or gradual) features are the key indicator predicting dendritic growth or anode/SEs interface kinetics.<sup>[14–16]</sup> Considering the different improvements of SSBs for Li, Na, K, Mg, Zn, Al, and Ca relative to those of liquid counterparts, it is essential to critically evaluate the present status and prospects for SEs and SEs/anode interfaces with distinctive battery chemistries.

This review begins with the thermodynamics, chemistries, and electrochemical kinetics for desirable SEI formation required for practical reversible metal anodes. The experimental and theoretical insights have been summarized for the nucleation of metals, electrodepositions, and stripping for reversible metal anodes. We discuss ion-transport mechanisms, state-of-the-art of SEs, and interface challenges for realizing high-performance cells. Then we focus on recent innovations for various anode interface chemistries enabled by SEs, including monovalent ( $\text{Li}^+$ ,  $\text{Na}^+$ ,  $\text{K}^+$ ) and multivalent ( $\text{Mg}^{2+}$ ,  $\text{Zn}^{2+}$ ,  $\text{Al}^{3+}$ ,  $\text{Ca}^{2+}$ ) cation carriers (for example, lithium-metal, lithium-sulfur, sodium-metal, potassium-ion, magnesium-ion, zinc-metal, aluminum-ion, and calcium-

ion systems). Finally, the challenges and future perspectives for SEs, reversible anodes, and electrode/SEs interface chemistries and technologies are summarized.

## 2. Fundamentals of Thermodynamics and Electrochemical Kinetics for Desirable SEI

The rational design of next-generation batteries with various single/multivalent metals (Na, Li, K, Mg, Al, Zn, and Ca) is of significant attention. Since 1970,<sup>[17]</sup> the SEI formation at the anode surface has been regarded as one of the key parameters for liquid/solid batteries. Several strategies have been demonstrated for the development of SEI of different metals. The physicochemical properties of Na and K are comparable with Li; however, they possess more electronegativity resulting in different modulus and solubility of SEI formulations (Figure 1a).<sup>[18]</sup> Given Mohs hardness and bulk/shear modulus, Na and K are softer than Li metal, indicating the suppression of dendrites is considerable. In contrast, the SEI formation for multivalent metals has yet to be explored. The high modulus of Al and Zn implies severe dendrite growth. Besides, a larger charge density of multivalent ions validates the poor mobility of ions in the SEI that limits the robust construction of SEI. Theoretical calculations clarify the lowest diffusion barriers for Mg compared to those of Li, Na, Zn, and Al (Figure 1b), demonstrating smooth structure formation. Hexagonal closest packed (HCP) structures of Mg and  $\text{ZnS/ZnF}_2\text{-Zn(101)}$  favor high-coordination configurations than those of Li and Na (face-centered/body-centered cubic; FCC/BCC) metals.<sup>[9,19]</sup>

Theoretical calculations also show that LiF, NaF, and ZnF have favorable ionic transport by vacancy defects (Figure 1c). Li-ion has a faster transport behavior by LiF due to high diffusion coefficients compared to Na-ion by NaF and Zn-ion by ZnF.<sup>[20–24]</sup> Both  $\text{Li}^+$  and  $\text{Na}^+$  can be migrated by Na-SEI (NaF and  $\text{Na}_2\text{CO}_3$ ) and Li-SEI (LiF and  $\text{Li}_2\text{CO}_3$ ) via direct hopping or knock-off or vacancy mechanisms (Figure 1d).<sup>[20]</sup> The low polarity of  $\text{Na}^+$  provides the most stable Na-SEI compared to those of Li-SEI, implying poorer stripping/plating efficiency for Na compared to Li and larger capacity loss, especially in carbonate electrolytes (Figure 1e).<sup>[25]</sup> The inorganic NaF and  $\text{Na}_2\text{O}$  strongly contribute to the high Coulombic efficiency (CE) of 99.9% for Na plating/stripping in the  $\text{NaPF}_6$  in diglyme electrolytes.<sup>[26]</sup> The construction of stable Li-SEI over the Na-metal (heterostructural design) has been clarified as the alternative approach to shield the Na-metal-anode. Fluoroethylene or vinylene carbonate (FEC/VC), and di-oxolane (DOL) for inorganic/organic SEI show similar chemical properties for both Na and Li, while  $\text{NaNO}_3$  has adverse effects for Na than ideal  $\text{LiNO}_3$  for Li because of the severe decomposition of electrolytes. In Li/Na hybrids, the more negative redox potential of Li/ $\text{Li}^+$  offers the shielding effect for  $\text{Na}^+$  that controls the dynamic interphase for dense electrodeposition.<sup>[27,28]</sup> The softest metal among the anodes is K which has similar properties to Na and Li; however, the high reactivity of K with solvents forms unstable SEI even for a small current density ( $0.2 \text{ mA cm}^{-2}$ ). Highly concentrated electrolytes can stabilize SEI for K effectively.<sup>[29]</sup>

The high polarization occurs due to low ionic radius and large charge number. Ca and Mg sustain reversible plating/stripping with greatly destructive and lower oxidative stable electrolytes. In contrast, carbonate electrolytes tend to have poor conductivity in

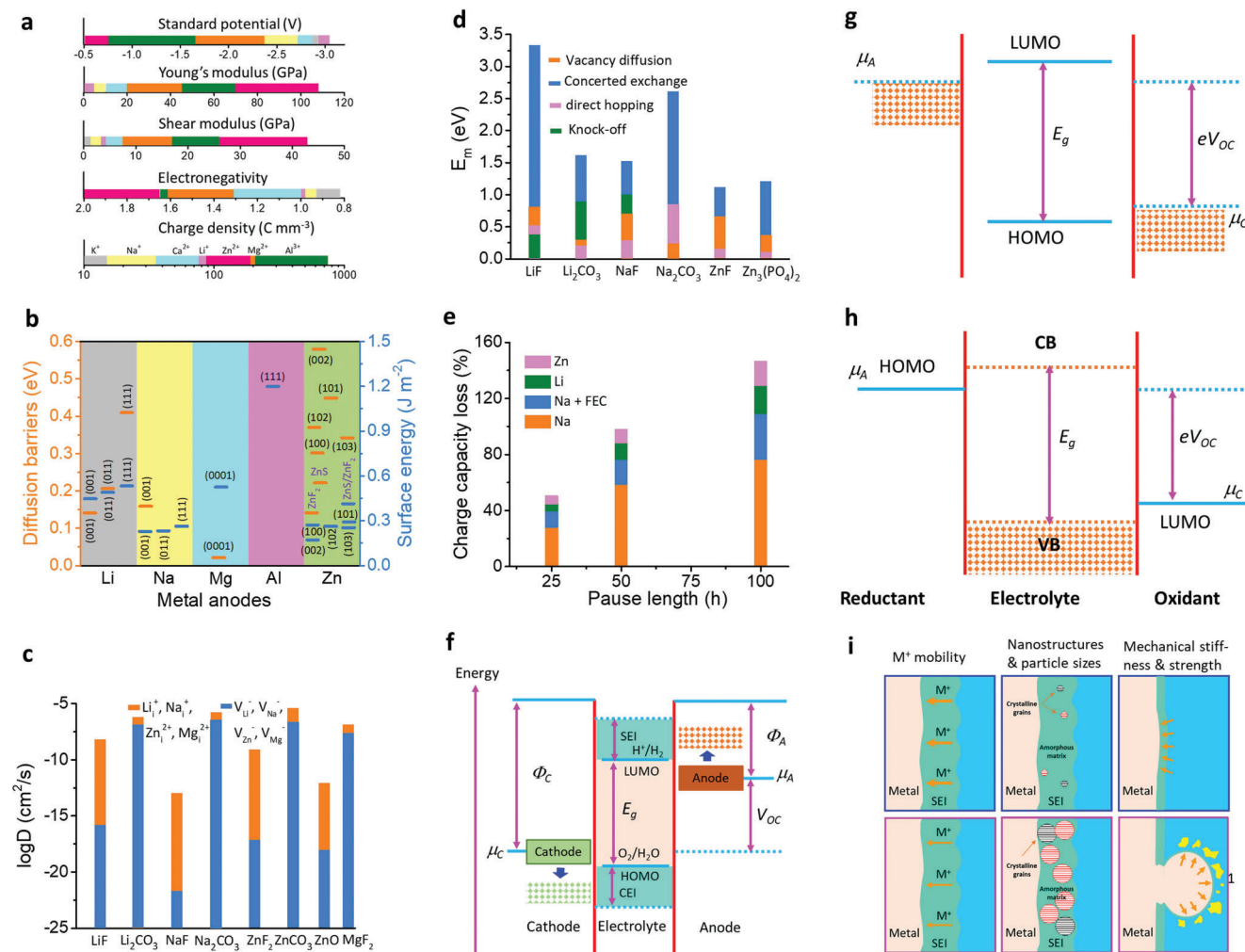


**Figure 1.** a) Intrinsic physicochemical properties of different metals.<sup>[18]</sup> b) The diffusion barriers and surface energies of various metals (Li, Na, Mg, Al, Zn, ZnS, ZnF<sub>2</sub>) for different crystal reflections.<sup>[9,19]</sup> c) Self-diffusion coefficients for Li-, Na-, Zn-, and Mg-SEI.  $\text{Li}_i^+$ ,  $\text{Na}_i^+$ ,  $\text{Zn}_i^{2+}$ , or  $\text{Mg}_i^{2+}$  denotes the excess interstitial Li-, Na-, Zn-, and Mg-ions.  $V_{\text{Li}}^-$ ,  $V_{\text{Na}}^-$ ,  $V_{\text{Zn}}^-$ , and  $V_{\text{Mg}}^-$  denote the negatively charged Li-, Na-, Zn-, and Mg vacancies.<sup>[20–24]</sup> d) Migration energy barriers for various hetero-diffusion kinetics. e) Charge capacity loss of Li, Na, and Zn metals inclined by SEI dissolution.<sup>[25,26]</sup> f) Schematic energy states for electrolytes and electrodes that facilitate the SEI and CEI formation.  $\mu_C$  and  $\mu_A$  refer to the energy levels of cathode and anode electrodes. LUMO and HOMO define the electrolytes' lowest unoccupied molecular orbital and highest occupied molecular orbital. CB and VB imply the conduction and valence bands, respectively. VOC represents the open-circuit voltage of the cells. Reproduced with permission.<sup>[36]</sup> Copyright 2009, American Chemical Society. g) Electrochemical potential window for liquid electrolytes. h) Electrochemical potential window for solid electrolytes. Reproduced with permission.<sup>[4]</sup> Copyright 2013, American Chemical Society. i) Schematics represent the SEI contributions to the flat and dense metal electrodeposition (positively in the top blue boxes and negatively in the bottom purple boxes).<sup>[49]</sup>

SEI with the degradation of plate/strip processes. Al undergoes reversible plate/strip with highly corrosive ionic liquids ( $\text{AlCl}_3$  + 1-ethyl-3-methylimidazolium chloride). Artificial SEI enables the operations of Ca, Mg, and Al under non-aqueous/aqueous electrolytes, which vindicates the impact of SEI on multivalent metals.<sup>[30–32]</sup> Zn compatibility with water enables intrinsic safety, whereas dendrite formation and volume change limit the commercial application for larger Zn utilizations. Zn metal typically practices  $\text{Zn}_5(\text{CO}_3)_2(\text{OH})_6$  layer at ambient conditions that easily oxidized in mild acids and conveyed to movable interphase of  $\text{Zn}_4\text{SO}_4(\text{OH})_6 \cdot x\text{H}_2\text{O}$ , which results in low CEs and severe dendritic-growth.<sup>[33]</sup> For alkaline media, the creation of soluble  $\text{ZnO}_2^{2-}$  and irreversible ZnO on the anode suffers structural dis-

tortions. Cation-selective membranes, polymer-based additives, epitaxial electrodeposition with lower lattice mismatch, and artificial ZnS/ZnF<sub>2</sub>-based SEI have been applied to protect the Zn anode.<sup>[9,34,35]</sup>

Figure 1f–h demonstrates the energy states of electrodes and the chemical stability of electrolytes. Apart from high ion conductivity or transfer number and compatible mechanical properties, the lowest unoccupied molecular orbital (LUMO) or conduction band (CB) should be higher than the chemical potential ( $\mu_A$ , or Fermi energy) of the anode and the highest occupied molecular orbital (HOMO) or valence band (VB) should be lower than the  $\mu_C$  of the cathode which are the most notable standards for designing liquid or solid electrolytes (Figure 1f–h).<sup>[36–39]</sup> The

energy gap ( $E_g$ ) between LUMO (or CB) and HOMO (or VB) of electrolytes determines the thermodynamically stable electrochemical potential window and driving force to practice the SEI layer for solid or liquid electrolytes with high-voltage cathodes and metal anodes, which is significant for high-energy secondary batteries. Further, the difference in chemical potential of the cathode ( $\mu_C$ ) and anode ( $\mu_A$ ) corresponds to the open-circuit potential of the cells (Equation 1).<sup>[39]</sup>

$$eV_{OC} = \mu_A - \mu_C \leq E_g \quad (1)$$

where  $e$  is the electron charge magnitude. If the Fermi energy of the anode is higher than the LUMO of electrolytes, then electrolyte reduction ensues at the anode interface to form an SEI. On the other hand, if the Fermi energy of the cathode is lower than the HOMO of electrolytes, electrolyte oxidation follows for the cathode interface to form a cathode-electrolyte interphase (CEI). The electrochemical window is projected by the onset points of current–voltage curves (i.e., oxidation voltage of electrolyte) using linear sweep voltammetry.

Notably, the SEI allows the metal-ions (Li, Na, Mg, Zn, K, Ca, Al) diffusion through a layer under a uniform electric field with reducing concentration polarization and the overpotential, which prevents the aggregation of electrochemically active species with maintaining uniform chemical compositions of electrodes. Besides, thickening the SEI layer likely increases the internal resistance of the cell by consuming metal ions from cathodes, diminishing the capacity and power. Under the carbonate-based electrolytes, the SEI layer forms at  $\approx 1$  V versus Li/Li<sup>+</sup> or Na/Na<sup>+</sup> for the metals, oxides, or carbons.<sup>[40]</sup> Anode materials with K-storage voltages are  $\approx 0$ –1  $V_K$ . For example, K-metal (0  $V_K$ ), graphite ( $\approx 0.1$   $V_K$ ), alloys ( $\approx 0.8$   $V_K$ ), and red phosphorus ( $\approx 0.7$   $V_K$ ) possess higher Fermi energy than LUMO.<sup>[41–43]</sup> Mixed ionic and electronic conducting behavior of SEI/CEI deteriorates the overall cell performances. Inert materials protection for anode/cathode has shown a promising approach to alleviate chemical reactions. Interphase reactions show vital characteristics to reach the full potentials of batteries; e.g., Li<sup>+</sup> ions diffuse via grain boundaries and Schottky vacancies of bulk electrolytes, in which electronegativity, contact circumstance, and interphase structures strongly influence the overall energy delivery of cells.<sup>[14,44]</sup>

The cation-anion or cation-solvent interactions strongly influence the reduction stabilities of solvents/anions as they control the solvation structures and the solvent coordination numbers nearby the cation centers. When cations coordinate with solvents or anions, their LUMO levels decline due to the donation of electron pairs to the cations. Thus, the formation of ion pairs and solvation promotes the decomposition of electrolytes. DFT calculations display the lower LUMO levels of ion-solvent complexes (i.e., FEC, propylene carbonate (PC), diethyl carbonate (DEC), ethylene carbonate (EC), 1,2-dimethoxyethane (DME), and 1,3-dioxolane (DOL)) compared to pure solvents.<sup>[29,45,46]</sup> Lower LUMO level magnitudes of carbonate solvents are in the order of Li<sup>+</sup> > Na<sup>+</sup> > K<sup>+</sup>, revealing a linear correlation with binding energy. In contrast, ether solvents demonstrate larger LUMO level changes in Na<sup>+</sup> > K<sup>+</sup> > Li<sup>+</sup>.<sup>[45]</sup> SEI formation and reduction stability of electrolytes are influenced by cations with electrolytes, which requires the understanding of the dissimilarities for the SEI layer among Na, Li, K, Zn, Mg, Al, and Ca batteries.

In the perspective of electronic structures for aqueous batteries, water is the oxide having  $E_g$  of 8.7–8.9 eV. If the LUMO–HOMO energy gap reflects the EW, water could be solvent for Na, K, or Zn-ion batteries. The thermodynamic potential of water is 1.23 V, which limits the hydrogen evolution at  $-4.02$  eV and oxygen evolution at  $-5.25$  eV (i.e., 0 V vs SHE at pH 7) corresponding to the energy level of  $-4.44$  eV at absolute scale (electron energy of 0 eV in vacuum). However, there is no correlation between the LUMO–HOMO energy gaps of water and Fermi levels of the electrons for the oxidation and reduction of water in the solutions.<sup>[47,48]</sup> The actual chemical potentials comprise the impact of the surface potentials.

Figure 1i illustrates how SEI properties can contribute the even metal electrodepositions (positively or negatively). The ideal SEI metal deposit over the electrode surface calls for three parameters: 1) high M<sup>+</sup> mobility is desired, 2) small crystalline particles permit the large uniformity, 3) robust SEI (high elastic modulus and yield strength) overpowers the whisker nucleation by suppressing metal protrusions, whereas the small yield strength permits the whisker growth in the electrolytes. The diffusion through SEI for cation desolvation, exchange current density, and charge transfer influences the exchange current density subject to the rate-limiting steps. Tuning the solvation energy of cation at the interface via artificial interphases or ionic polymers having functional groups with large affinity to the cations is the suitable approach for minor exchange current density, which enable the in-plane electrodeposition of metals (Li, Na, Zn).<sup>[49,50]</sup> Insights for ion transports, chemical compositions, nanostructures, and mechanical properties of SEI are fundamental to designing long-life operative metal electrodes. The intrinsic properties of electrode/electrolytes possess three types of interfaces: robust SEI without chemical side reactions of electrolyte decomposition, SEI with electronic insulation but offers M<sup>+</sup> transport pathways, and SEI with mixed ionic and electronic conductivity. Constructing the stable artificial passivation layer between the electrodes can balance the interfacial losses with a compatible M<sup>+</sup>-conducting layer, which can apply to practical applications.<sup>[51]</sup>

### 3. Ion Transport Mechanisms for SEs

The ion transport depends on the distribution and concentrations of defects and ion-binding sites for crystalline solids. Increasing carrier concentration by insertion of aliovalent cations is a practical approach. High-valence cations generate cation vacancy/anion interstitials, whereas low valence forms the cation interstitials/anion vacancies. The potential difference redistributes the mobile carriers due to lattice distortion at boundaries and interfaces. Ion diffusion kinetics enabled by Schottky and Frenkel defects comprise the vacancy and diffusion mechanisms (i.e., divacancy, interstitial, interstitial–substitution, and collective, Figure 3a).<sup>[52,53]</sup> Special structures offer superior conductivity without many defects, which involves crystal structures with immobile ions, two or more sublattices, and sublattices for mobile species. Basically, three major parameters are required to obtain high-ion conductance. 1) Large number of equivalent sites for mobile ions to occupy compared to the number of mobile species; 2) lowest migration energy barriers for nearby accessible sites that can follow hopping; and 3) formation of continuous diffusion pathways.<sup>[54,55]</sup> Nernst-Planck defines the current density



(j) by relating the flux of charged species for dilute electrolytes to electrical and chemical potential gradients ( $\nabla\varphi$  and  $\nabla c_i$ , respectively) and mass conversion.<sup>[56]</sup>

$$j = -F^2 \nabla \varphi \sum_i \mu_i c_i - F \sum_i D_i \nabla c_i + F \bar{u} \sum_i c_i \quad (2)$$

where  $F$  is the Faraday constant,  $\mu_i$  is the charged species  $i$  mobility,  $c_i$  is the dissociated ion pairs concentration,  $D_i$  is the coefficient of diffusion, and  $\bar{u}$  is the convection velocity for the medium through the ion transfer.

For SE,  $\bar{u}$  is very small even for potentials higher than the thermal voltage ( $k_B T/e = RT/F$  where  $k_B$  is the Boltzmann's constant,  $T$  is the temperature,  $R$  is the gas constant, and  $e$  is the electronic charge) and the concentration gradient is smaller for reasonable potential. According to these conditions, Equation 2 can be defined to calculate the conductivity of electrolytes.

$$\sigma = -j/\nabla \varphi = F^2 \sum_i \mu_i c_i \quad (3)$$

where diffusion coefficient and mobility are related by  $\mu_i = D_i/RT$ .

High ion mobility and concentration of mobile ions required for superior conductivity, as per Equation 3, facilitate simultaneous dissociation of ion pairs and minimal resistance for ion motion. A key to enhancing battery operation capability is maximizing the cation transfer number. The diffusion coefficient is defined with a migration-free energy ( $\Delta G_{\text{mig}}$ ):

$$D_i = \gamma a^2 f_0 \exp(-\Delta G_{\text{mig}}/RT) \quad (4)$$

where  $\gamma$  the geometrical effects factor,  $a$  is hopping distance, and  $f_0$  is the ion hopping frequency.<sup>[57]</sup> Based on Equations 3 and 4, electrical conductivity is,

$$\sigma_i = F^2/RT \times \left[ c_i \gamma a^2 f_0 \exp(\Delta S_{\text{mig}}/R) \exp(-\Delta H_{\text{mig}}/RT) \right] \quad (5)$$

where  $\Delta S_{\text{mig}}$  and  $\Delta H_{\text{mig}}$  the entropy and enthalpy of migration, respectively. Further, thermal activation of dissociation of ion pairs relates the  $c_i$  with formation enthalpy ( $\Delta H_f$ ) as,<sup>[58]</sup>

$$c_i = c_0 \exp(-\Delta H_f/RT) \quad (6)$$

where  $c_0$  is the initial concentration of ion pairs before thermal activation. Considering the different activation energies as a single barrier ( $E_a$ ), Equation 5 defines the Arrhenius form as,

$$\sigma = \sigma_0/T \times \exp(-E_a/RT) \quad (7)$$

where  $\sigma_0$  is weak for temperature and  $E_a = \Delta H_f + \Delta H_{\text{mig}}$  is the total activation energy for the formation and migration steps. Inorganic or crystalline ion conductors obey the Arrhenius Equation 7.

For glassy materials, amorphous solids possess short- and medium-range ordered structures with high entropy and free volume for motion. The ion transports initiate with excited local sites ions to the adjacent sites as collective diffusions for macroscopic scale consistent with crystals.<sup>[59]</sup> Ion transfer follows the

Arrhenius equation below the glass transition. In contrast, above the glass transition temperature ( $T_g$ ), the polymeric SEs involve the microscopic ionic transfer correlated to the segmental motion of polymer chains (Figure 2a).<sup>[60]</sup> Segmental motion generates the free volume to hop metal (Li, Na, K, Zn, Mg) ions that are coordinated to polar groups. Continuous hopping determines the long-distance transfer kinetics under the applied electric fields (Figure 2b,c). The dissociation ability of metal salts in the polymeric chains provides the number of mobile ions.<sup>[59,60]</sup> The Vogel–Fulcher–Tammann (VFT) equation defines the correlation for ionic conductivity as a function of a temperature difference as:

$$\sigma = \sigma_0/T \times \exp \left[ (-E_a/R) (T - T_0) \right] \quad (8)$$

where  $T_0$  the below  $T_g$  ( $\approx 50\text{K}$ ).  $RT_0$  the potential barrier for a local motion of chains.<sup>[61]</sup> Most of the polymer electrolytes follow the VFT kinetics.

FCC or HCP packing of anions shows a high-energy landscape than BCC for various anion-host matrices. The recognized fast  $\text{Li}^+$  conductors ( $\text{Li}_{10}\text{GeP}_2\text{S}_{12}$  (LGPS) and  $\text{Li}_3\text{OCl}$ ,  $\text{Na}^+$ ,  $\text{Mg}^{2+}$ , and  $\text{Ag}^+$  ion conductors) consist of BCC anion matrices. MD simulations disclosed that LGPS, LLZO, NASICON, and  $\text{Li}_{1.3}\text{Al}_{0.3}\text{Ti}_{1.7}(\text{PO}_4)_3$  (LATP) have multiple ions hopping to adjacent sites instead of isolated ion hopping over energy barriers.<sup>[62]</sup> Further, cubic LLZO shows 3D ion diffusion pathways with increased ion conductivity due to the redistribution of Li ions for LMBs. High-molecular-weight polymers enable intersegmental hopping, whereas low-molecular-weight polymers have diffusion mechanisms.<sup>[60]</sup> Batteries contain several interfaces, such as homogeneous (grain boundary) and heterogeneous (electrodes/electrolytes) forms, facilitating the vital ion-transport role. LLZO or LISICON shows the grain boundary conductivity for charge transfer. The space-charge layer is formed at the interface for heterogeneous interfaces due to the local transfer of uncompensated charges across the boundaries. This results in the accumulation of mobile carriers on the front side of the interface and depletion to the backside.<sup>[63,64]</sup> For example, inserting  $\text{LiNbO}_3$  buffer into  $\text{LiCoO}_2$  and LGPS electrolytes suppresses the growth of the space-charge layer with excess ion-transfer pathways.<sup>[65]</sup>

## 4. Evaluation of Structural Amendments during Metal Plating/Stripping

Nucleation of metal deposition, high surface-area structures, and morphological disparity in stripping are major checkpoints for durable plating and stripping.

### 4.1. Nucleation Kinetics

Nucleation kinetics critically depends on the current density, potentials, and SEI for solid-state electrolytes. The nucleation barriers are effectively adjusted with varying electrochemical supersaturation by regulating reduction reaction overpotential at the working electrode for stable electrodeposition (Figure 3a). Driving forces for electro-crystallization processes are four types, including the reaction-overpotential,

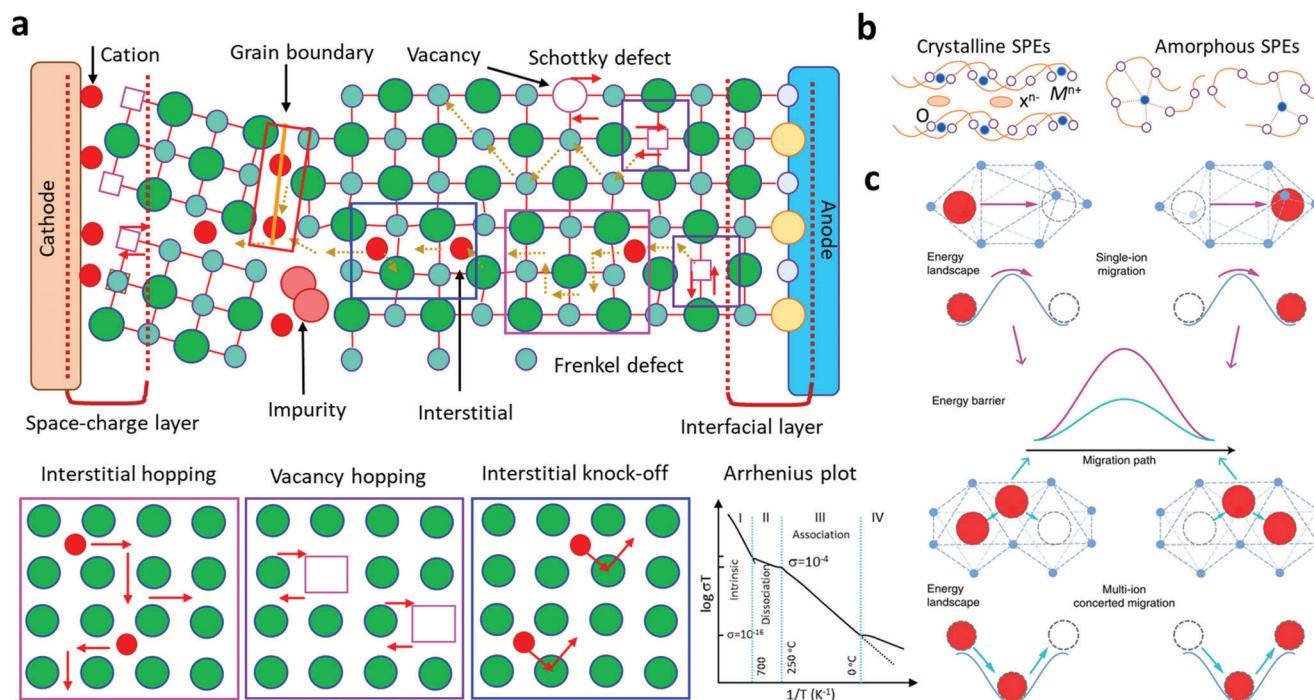


**Figure 2.** a) Ion-migration kinetics for SIEs based on the Frenkel and Schottky defects (i.e., vacancy, interstitial and interstitial knock-off hopping), grain boundaries. Depending on operating conditions, the interface layer formed due to different chemical potentials of electrodes in contact can boost or impede ion-migration kinetics. b) Ion migration for amorphous and crystalline SPEs. For crystalline, conduction follows through ordered domains generated by polymer segments, whereas for amorphous, migration and hopping of  $M^{n+}$ -ions are based on the motion of polymer segments. c) Migration pathways for single (upper)/multiple (lower) ions. Reproduced under the terms of a Creative Commons CC BY 4.0 license.<sup>[62]</sup> Copyright 2017, Nature Publishing Group.

charge-transfer-overpotential, crystallization-overpotential, and diffusion-overpotential. According to the limitation for the distinction of electrodes-polarizations, the two typical overpotentials are considered for metal depositions: 1) nucleation-overpotentials ( $\eta_n$ , the value of voltage spike for the onset of M-depositions;  $M = \text{Li, Na, K, Zn, Mg, Al, Ca}$ ), and 2) plateau-overpotentials ( $\eta_p$ , the value after nucleation happens and M-growth remains). During galvanostatic plating, the working electrode potential drops  $< 0$  V versus  $\text{Li/Li}^+$  to  $-\eta_n$  at electrochemical overpotential, which is appropriate for driving the nucleation of Li embryos (Figure 3b). After initiation, the overpotential increases to  $-\eta_p$  (negative values versus  $\text{Li/Li}^+$ ) and proceeds the growth of Li nuclei, even for lower electrode polarization for Li growth relative to those of nucleation. It ascribes to the favorable insertion of Li adatom with prevailing Li nuclei with lower energy barrier than those of evolving stable Li-atoms cluster.<sup>[66–70]</sup> For heterogeneous nucleation, the nuclei size is inversely proportional to the electrochemical overpotential, and areal nuclei density is proportional to the cube of the nucleation overpotential following the spherical nuclei (Figure 3c–e). The nucleation barrier and stable Li plateau enhance with a cumulative current density, consistent with the Butler-Volmer relationship for current and voltages. Favorable conditions for Li deposit is  $\eta_p < \eta_n$ . Li domains are relatively large and meagerly distributed for low current densities (growth dominated), while small and dense distributions are for high current densities (nucleation dominated, Figure 3c). The excess charge is essential to complete the nucle-

ation step for low current density due to the simultaneous deposition of Li and SEI formation.<sup>[71]</sup> This feature is consistent with other metals such as Mg, Zn, Na, Al, K, and Ca.<sup>[72–77]</sup> Nucleation theory explains the critical radius at which growth is thermodynamically favorable and evaluated by Gibbs free energy of formed nuclei as:

$$\Delta G_{\text{total}} = 4/3 \times \pi r^3 \Delta G_{\text{Li}} + 4\pi r^2 W_{\text{interface}} \quad (9)$$

where  $\Delta G_{\text{Li}}$  is the energy for Li depositions (or free energy change per volume),  $W_{\text{interface}}$  is the work for CC/Li/SEs interface (or surface energy). Upon consideration of boundary conditions and nucleation barriers, the critical radius becomes:

$$r_{\text{crit}} = \frac{2\gamma V_M}{F} |\eta| \quad (10)$$

where  $\gamma$  is surface energy,  $V_M$  is molar volume,  $F$  is the Faraday constant, and  $\eta$  is nucleation overpotential. For fixed plating capacity, the nuclei density  $N$  times the nuclei volume should be constant. Thus, nuclei density is  $N \sim \eta^3/\gamma^3$  (Figure 3c).

Critical radius is the boundary conditions for Li nuclei formation; below  $r_{\text{crit}}$ , no Li metal nuclei can be generated. Figure 3d explains a few mV overpotentials ( $\eta$ ) required as driving forces to generate first Li nuclei for diffusion-bonded CC/Li/SEs interfaces. When nuclei undergo the applied pressure, it will further increase the potential driving forces obligatory for driving the

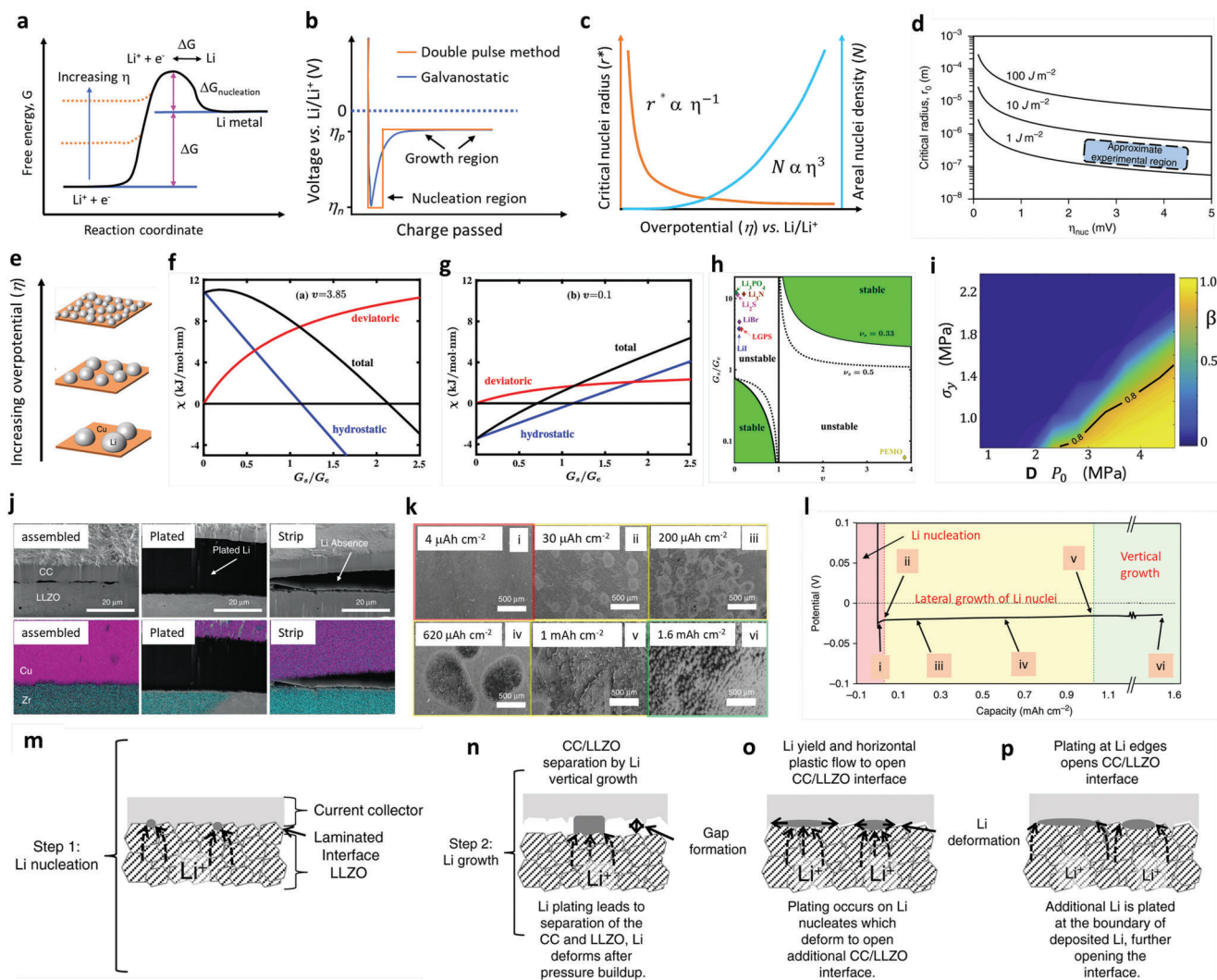


**Figure 3.** a) Free energy schematics for overpotentials versus nucleation energy barriers. b) Voltage profile schemes for galvanostatic (blue) and double phase (potentiostatic, orange) methods. c) The critical nuclei radius and areal nuclei density for the nucleation overpotentials. d) Critical radius versus nucleation overpotential. Reproduced with permission under Creative Commons CC BY 4.0 license.<sup>[66]</sup> Copyright 2020, Nature Publishing Group. e) Metal nucleation schemes. Reproduced with permission.<sup>[70]</sup> Copyright 2017, American Chemical Society. f.g) Stability parameters for  $\nu > 1$  (f) and  $\nu < 1$  (g). h) Stability phase diagram for shear modulus and volume ratios. Reproduced with permission.<sup>[81]</sup> Copyright 2017, American Institute of Physics. i) Degree of plasticity ( $\beta$ ) for Li relative to yield strength  $\sigma_y$ . Reproduced with permission.<sup>[67]</sup> Copyright 2020, Elsevier. j) SEM and EDS images of Li/LLZO interfaces for various conditions. k) LLZO SEs surface after plating for various capacities. l) Voltage profile displaying Li nucleation, lateral growth, and amalgamation of nuclei and their vertical growth. m-p) Nucleation and growth process illustrations: Li nucleation (m), nuclei deposit leads to vertical growth and adjacent CC/LLZO interface separation (n), continuous electrodeposition over nuclei with mechanical forces at the interfaces, and lower Li yield leads the horizontal plastic flow for Li (o), deposition over nuclei edges (p). Reproduced under the terms of a Creative Commons CC BY 4.0 license.<sup>[66]</sup> Copyright 2020, Nature Publishing Group.

nucleation and growth processes. Nucleation overpotential is defined as:

$$h \approx (V_{Li}/F) \times p \quad (11)$$

where  $p$  is the pressure in the nuclei. Reported critical radius for Li, Mg, Zn, Na, and K are in 1–6  $\mu\text{m}$  range. For instance, an applied pressure of 4 MPa further requires  $\eta$  of 0.5 mV.<sup>[66]</sup> Motoyama et al.<sup>[69]</sup> also reported that Li-plating for CC/LiPON SEs interfaces have voltage rises of 30 and 50 mV for 90 and 30 nm CC, respectively, but <10 mV for 1  $\mu\text{m}$  CC with a fixed

strain of 0.2%. This theory confirms that surface and interfacial energies are critical parameters for Li plating. Biswal et al.<sup>[78]</sup> verified the composition of SEI strongly influences the effective surface energy of Li metal. Morphology and distribution of Li electrodeposition concerning plated capacity propose the interfacial forces define the nucleation and flat growth of isolated Li to the uniform coalesced layer.<sup>[66,68,69]</sup> MD simulations reported that Li reduces preferentially with homogeneous growth at the LiF SEI cracks, highlighting the surface tension and mechanical properties strongly influencing Li nucleation.<sup>[79]</sup> Butler-Volmer equation defines the change in the electrochemical potential of



electrons for interfaces based on surface tension and interfacial stresses as:<sup>[80–83]</sup>

$$\Delta\mu_{e-} = -1/2z \times (V_M + V_M^{Z+}) \times [-\gamma\kappa + e_n^2 (\tau_d^e - \tau_d^s)] + 1/2z (V_M - V_M^{Z+}) (\Delta p^e + \Delta p^s) \quad (12)$$

where  $\Delta p^e$  and  $\Delta p^s$  as well as  $\tau_d^e$  and  $\tau_d^s$  are the pressures and deviatoric stresses at electrodes and electrolytes of interfaces,  $e_n$  the unit normal pointing towards SEs from metal,  $\kappa$  the mean curvature at the interface, and  $V_M^{Z+}$  the molar volume of  $M^{Z+}$  in SEs. After boundary conditions (i.e., bulk force = 0) and constitutive laws for linearly elastic isotropic materials with the shear modulus ( $G$ ) and Poisson's ratio ( $\nu$ ), the  $\Delta\mu_{e-}$  for interface becomes:<sup>[80–83]</sup>

$$\Delta\mu_{e-} = \chi \times Re(Ae^{ikx}) \text{ with } \chi (G_e, G_s, \nu_e, \nu_s, \gamma, \kappa, z, V_M, V_M^{Z+}) \quad (13)$$

where  $\chi$  the stability factor includes surface tension, hydrostatic, and deviatoric stresses. If the current density and  $\Delta\mu_{e-}$  are out of phase with perturbation, then stable deposition is possible. Figure 3f,g shows hydrostatic contributions are initially positive and decrease monotonically with  $G_s/G_e$ , which results in stability for  $G_s/G_e \geq 2.2$ , whereas hydrostatic stresses are initially negative and increase stability for  $G_s/G_e \leq 0.7$ . For  $\nu > 1$ , the electrodeposition is stable beyond the critical shear modulus ratio ( $\chi < 0$ ), whereas, for  $\nu < 1$ , stable deposition is possible below critical shear modulus ( $\chi > 0$ ). Figure 3h exhibits the stability phase diagram for a shear modulus and molar volume ratio. For  $\nu > 1$ , stable deposition is possible when SEs with shear modulus  $\gg$  critical shear modulus. The required shear modulus enhances severely with the unity of molar volume ratio, reducing the stability window. For  $\nu < 1$ , stable deposition is possible with soft SEs, provided Li in SEs is more densely-packed than Li in Li-metals (i.e., density-driven stability). For  $\nu = 1$ , stability requires hydrostatic stresses to dominate as stability parameters (i.e., pressure-driven stability). The stress-driven phase transitions at solid-solid interfaces, the interplay among the work and elastic energy terms defines the growth and stability of interfaces.<sup>[80,81]</sup> Small exchange current density via SEI increases the compatibility of deposition. Further, organic fluorine with flexible polymeric elements in SEI strongly prevents the dissolution of dead Li by constructing the condensed SEI, which illustrates the energetic LiF with oligomers and polymers stabilizes the Li anode.

NASICON-type  $\text{Na}_3\text{Zr}_2\text{Si}_2\text{PO}_{12}$  (NZSP) with monoclinic and rhombohedral phases displays the 3D Na-ion transmission channel. The  $\text{Na}^+$  diffusion is faster with large ion transport pathways due to the lower electronegativity and sizeable ionic radius of the S atoms in the sulfide electrolytes, which significantly decreases the grain boundary resistances. Besides, the distribution of  $\text{Na}^+$  nuclei is more homogeneous for lower concentrations. Overpotential from the mass transfer is higher for low  $\text{Na}^+$  concentrations, enabling excess nuclei formation. The excess  $\text{Na}^+$  ions show more pronounced nuclei merging with close-packed nuclei.<sup>[72–74]</sup> SEI formed for Zn has a similar influence on alkali metals for lower current regions. Zn crystal facet displays

the high anisotropy ensuing the hexagonal close-packed lattices for a c/a ratio of 1.85, which enforces major impacts over growth kinetics. The (002) texture accelerates the Zn nucleation rate with abundant nuclei for higher currents, which enables stable deposition and high resistance to dendrite growth and interfacial reactions. During electrolysis, the negative electrodes are surrounded by  $\text{Zn}^{2+}$  and  $\text{H}^+$  ions with weak Van der Waals bond that allows favorable surface diffusion with  $\text{Zn}^0$  deposits over the Cu plate.<sup>[75]</sup> Voltage profiles with  $1.6\text{NH}_3/\text{MgO}$  composites display stable interfaces (low overpotentials) for low currents, while imbalanced kinetics are followed for higher currents. This high overpotential for nucleation compared to the growth indicates that Mg electrodeposition follows the instantaneous nucleation process ascribed to the Gaussian size dispersion.<sup>[76]</sup>

Zhu et al.<sup>[84]</sup> reports the Na nucleation behavior with various group-II metal-foils (Be, Mg, Ba) with definite solubility in Na as substrates for Na plating compared to those of Al and Cu foils. It exhibits low overpotentials of 36.3, 35.5, and 12.1 mV for Be, Mg, and Ba relative to Al (53 mV) and Cu (44.9 mV) foils, implying smaller nucleation barriers for Na-deposits. Flat and compact Na-loadings over group-II metals are shown with homogeneous nucleation in spheres and domes, whereas Al and Cu show non-uniform heterogeneous nucleation with plenty of dendrites. Further, the infinite solubility of group-II metals enables surface metallic atoms dissolution in the Na before producing pure Na-phase causing solid-solution layers. Liu et al.<sup>[85]</sup> states the current density or areal capacity changes the nucleation overpotential for highly-ordered CNTs, which is 1/3 of graphene and Cu electrodes. Homogeneous electric fields and low binding energy of highly-ordered CNTs gather massive K-deposition of graphene current-collector than Cu-electrodes. Liu et al.<sup>[86]</sup> reports the epitaxial electrocrystallization of Mg over 3D magnesiophilic substrates by interactions of lattice mismatch, electrostatic confinements, and magnesiophilic interfaces.  $\text{Ni}(\text{OH})_2$  substrates display strong magnesiophilic characteristics and lower lattice misfit for Mg, implying the condition for heteroepitaxial Mg nucleation. It shows periodic and hillock-like electrostatic fields on the exposed surfaces that precisely confine the reduced  $\text{Mg}^0$  over the localized electron-enriched atomic-level sites.  $\text{Ni}(\text{OH})_2/\text{CC}$  undergoes uniform Mg-deposition and electrocrystallization with locked crystal reflections and improved plate/strip kinetics. Hu et al.<sup>[87]</sup> reports insertion of  $\text{Mg}(\text{BH})_4$  in the magnesium bis(trifluoromethanesulfonyl)imide ( $\text{Mg}(\text{TFSI})_2$ ) increases the Mh-nucleation sites that are closely packed for electrodes at initial stages of depositions and then rapid growth of large clusters. McClary et al.<sup>[88]</sup> reports heterogeneous ultrathin CaO stabilizes the  $\text{Ca}^{2+}$  plate/strip processes efficiently rather than  $\text{CaH}_2$  with 5–10 nm SEI thickness. The structural and compositional heterogeneities enable  $\text{Ca}^{2+}$ -conduction via CaO films similar to  $\text{Li}^+$ -conduction models through SEI. Boundaries among the neighboring CaO crystals and minor phases of CaO control the lower migration barriers with superior transport-pathways.

## 4.2. Growth Morphology

Generally, the electrodeposition shows the horizontal, vertical, and randomly oriented growth structures (such as fractal-like



micron-scaled dendrites, chemotaxis-like, mossy-like whiskers, and wires) for different electrolytes under applied current densities (above/below their critical limits). Dendrites (fractal-like) with tip growth are commonly observed for all metals of Zn, Li, Mg, Al, and K due to the electrolyte transport limits.<sup>[72–77]</sup> The concentration of ions for anodes is depleted for above critical current density at Sand's time.<sup>[89]</sup> Diffusion limitations, chemical instability, and physical orphaning describe the metal's propensity for undergoing side reactions with porous, heterogeneous, and dendrite morphology, leading to the plating/stripping efficiency of 50–90%. This non-compact porous electrodeposition shows volume expansion over the anode surface. Zheng and Archer reported<sup>[75]</sup> the heterogeneous Zn deposition exhibits a high modulus of 108 GPa compared to those of Li (5 GPa) and Na (10 GPa), and it penetrates separators/membranes while making a physical bridge of electrode, defining as cell failure.<sup>[35,90,91]</sup> Reversibility process influences two major parameters of geometry and assembly modes of microstructural building blocks. The geometry describes the dimension and symmetries of microstructural building blocks [1D ( $\Phi = 1 \mu\text{m}$ ), 2D ( $\Phi = 5 \mu\text{m}$ )]; however, the assembly modes describe the orientations/alignments of building blocks relating to electrode surfaces. Plating/stripping reversibility of different morphologies as horizontally aligned ( $\approx 99\%$ ) > non-aligned  $\approx$  randomly oriented wires/moss-like (80–90%) > vertically aligned dendrites (<50%).<sup>[91,92]</sup> In contrast to Li, poor reactivity of Zn validates a substantial amount of Coulombic inefficiency arises due to the loss of active materials via parasitic reactions with SEs, illustrating the failure for Zn is severely relates to the loss of electrochemical accesses for depositions. Figure 3j displays non-uniform growth of the intermediate phase upon plating, whereas it disappears upon stripping with retention of the gap, increasing the impedance. Figure 3k,l exhibits the surface morphology distribution with increased plating capacities in nucleation, lateral growth of Li nuclei, and vertical growth of Li film regions. Nucleation and growth kinetics with subsequent processes, including nuclei initiation, vertical growth of Li columns, the horizontal plastic flow of Li for new LLZO/CC interface, plastic deformation under compression, or direct plating of Li over LLZO/CC interface have been shown in Figure 3m–p.

Mossy growth of metal consists of intertwined nano-sized whiskers without specific direction following the root growth. The intrinsic electrochemical instability of Li (or others) with electrodes leads to SEI generation. Slower ion transfer via SEI facilitates the poor exchange current density with microscopic reacted-limited growth. The buds will grow in all directions for low overpotentials, in contrast to the root-growth-based whiskers for high overpotentials. First, nuclei will grow in the square root of time, then be pushed away from the root with rapid growth in length; after that growth rate reduces (Figure 1i). Typically, SEI plays a vital role in the growth mechanism. SEI will grow slowly with rapid Li-ions transfer from thin SEI for small overpotential. This metal deposition is covered by a thin SEI layer without mechanical resistance. On the other hand, SEI forms quickly for high overpotentials with thick SEI covered on the electrode surface with eventual whiskers. Favorable growth depends on operating conditions, electrolytes, and current collectors.<sup>[93]</sup> Surface inhomogeneity causes the local amplification of von Mises stress ( $\sigma_v$ ) and hydrostatic pressure ( $P$ ) for the interfaces. Ceder

et al.<sup>[67]</sup> reports the distribution of  $P$  and  $\sigma_v$  for Li at the interface for yield strength ( $\sigma_y = 0.8 \text{ MPa}$ ) and various stack pressure ( $P_0$ ). As the  $P$  increases, the  $P_0$  also increases, reaching a maximum of 5.8 MPa value. Interfacial  $\sigma_v$  also enhances; however, it bounds with a yield strength ( $\sigma_y = 0.8 \text{ MPa}$ ), illustrating surface irregularity has maximum  $\sigma_v$  with plasticity. Further, the application of large  $P_0$  exhibits the growth of plastic regions from the peak area (Figure 3i). Conclusively, stress-gradient, self-diffusion, and limited surface diffusion describe the growth mechanism.

Theoretical calculations explained that Mg has a more considerable free energy difference for low and high dimensional phases than Li, illustrating the preferred 2D/3D growth relative to 1D Li growth. However, several reports vindicated the dendrites growth of Mg anode for all electrolytes.<sup>[76,94]</sup> Yu et al.<sup>[72]</sup> reported Na-dendrites with PEO/NaTFSI electrolytes; however, insertion of  $\text{Na}_3\text{SbS}_4$  filler forms the NaF-based SEI for smooth growth. The role of anions for solvation critically impacts the SEI compositions. Na/NASICON/Na shows rapid dendritic growth and diffusion of grain boundaries, consistent with Li/LLZO/Li. Further, an increase in the local electric field during charging tends to plate Na on grain boundaries; however, thinner dendrites are possible due to narrow grain boundary edges that facilitate the realization of more dendrites.<sup>[95,96]</sup>

Kim et al.<sup>[97]</sup> reports in situ NaF-rich protective layers over Na-metal surface as SEI that prevents the depletion of the electrolyte during cycling. Na//Na cells display lower overpotentials of 8, 50, and 70 mV for 1, 5, and 10  $\text{mA cm}^{-2}$  current densities without dendritic growth. Smaller interface resistance is attributed to the ameliorated ion conductance and smaller diffusion barriers for Na-ions across the interfacial layer. Wei et al.<sup>[98]</sup> presents  $\text{Ga}_5\text{Mg}_2$  alloys as  $\text{Mg}^{2+}$ -conductive, corrosive resistant, and magnesiophilic Mg-anodes. The lower chemical reactivity of  $\text{Ga}_5\text{Mg}_2$  than Mg-foils displays a protective layer for interfacial corrosion over reversible Mg plate/strip. Theoretical results confirm the lower diffusion barriers of 1.91 and 2.55 eV for intra- and cross-layers diffusions implying the faster  $\text{Mg}^{2+}$ -diffusion kinetics. Uniform and dendrite-free Mg-plating is obtained for  $\text{Ga}_5\text{Mg}_2$ -Mg over long operations, whereas Mg-foils display dendrites even after 10 cycles, which verifies the inhibition of Mg-dendrites. Ma et al.<sup>[99]</sup> reports the electroplated Zn over carbon nanofibers as anodes with large surface area and enhanced permeation of electrolytes. Liu et al.<sup>[100]</sup> reports the nucleation and growth behaviors of Zn over the stainless-steel hosts. It shows hexagonal-like layered flakes at different applied current densities and areal capacities for various dimensions. Distribution of Zn flake size decreases with increased current densities for all areal capacities, manifesting uniform depositions even for higher current densities. Zn has two overpotentials: 1) Initial sharp voltage downhill spike corresponds to nucleation overpotentials that drive Zn embryos nucleation, 2) Plateau potentials are the growth overpotentials that show Zn-growth energy barriers. Nucleation and growth overpotentials increased from 86 and 42 mV at 0.25  $\text{mA cm}^{-2}$  to 396 and 220 mV at 20  $\text{mA cm}^{-2}$ , illustrating the realization of numerous nuclei over the substrates. Tian et al.<sup>[101]</sup> reports 3D Zn-Cu alloy ( $\text{Zn}_5\text{Cu}$ ) interface materials for dual-cation electrolytes ( $\text{Zn}^{2+}/\text{Mg}^{2+}$  and  $\text{Zn}^{2+}/\text{Na}^+$ ). Thin ZnO surface engineering significantly enhances plate/strip kinetics for low and high current densities.

#### 4.3. Formation of Dead Metals and Approaches for 2D Plating

Generally, using metal anodes for commercialization is limited by porous and mossy metal growth for long-term cycling. Structural deficiencies in the anode show capacity loss due to the inflated surface area and evolution of inactive metal through stripping. SEI formation is a fundamental parameter for displaying severe capacity degradation at high CEs. The inactive metals (Li, Na, Zn, Mg, Al, or Ca), generally denoted as “dead metal,” are the controlling parameter around CEs <95%.<sup>[92]</sup> For all metal anodes, the plating/stripping rates are the determining factors for evolving metal morphologies during cycling.<sup>[72–77]</sup>

For different metal anodes, it is necessary to determine the compatible approaches for the realization of 2D plating with minimal structural disorders and CEs of 99.9% for realistic metal batteries. For instance, the 3D electrode design is one of the alternate approaches to mitigating the shape change and reactivation of dead Li. Pulse charging, high current densities, and lower salt concentrations are suitable for compensating diffusion kinetics. Plating/stripping current densities influence overpotentials and reversibility reaction kinetics. The stable SEI regulates the nucleation and growth kinetics by minimizing the internal stress to realize flat 2D plating.

Fang et al.<sup>[92]</sup> reported total inactive Li is equivalent to capacity fade for plate/strip, illustrating linear relation with CEs. The quantity of SEI Li<sup>+</sup> can be determined as Total inactive Li (known) = metallic Li (unreacted, measured) + SEI Li<sup>+</sup>. Notably, the metallic unreacted Li<sup>0</sup> enhances significantly with reducing CEs, whereas SEI Li<sup>+</sup> retains lower values for all testing conditions. The morphology of inactive Li changes from sheet-like to clusters with increased stripping rates for highly concentrated electrolytes, in contrast to whisker-like Li depositions with thick inactive Li under conventional electrolytes. Note that residues display a loss of electrically conductive pathways. Mohammad et al.<sup>[77]</sup> argued that the electroplating of Al metal composed of Al crystallites with ionic polymer electrolytes fulfills the basic compatibility need. Guo et al.<sup>[102]</sup> reported the Mg<sup>2+</sup> shows stable depositions under solid electrolytes (NASICON, oxides, hydrides, and chalcogenides) by using various strategies such as doping, binary or ternary phased SEs, amorphous or single crystalline phase structures with high thermal stability, and increased anions volume, etc. Na metal and ceramic SE effectively minimize the interfacial resistances and dendrites by improving the wetting of interlayer (i.e., uniform sodium flux across interface).<sup>[95]</sup> The following sections will consider macroscopic reactions restriction directed by the transport of metal ions via SEI, and the interface structures vital for stable operations of various metal anodes chemistries with practical requirements.

Landmann et al.<sup>[74]</sup> reports plate/strip behavior of Na for high-temperatures carbon-coated ceramic Na-β"-alumina electrolyte. It shows a plate/strip for a high current density of 2600 mA cm<sup>-2</sup> with a cumulative capacity of 10 Ah cm<sup>-2</sup> at 250 °C without dendritic-growth. Wang et al.<sup>[103]</sup> reports MoO<sub>2</sub> nanocrystals@N-doped carbon nanofibers self-supporting anode under polyvinylidene fluoride hexafluoropropylene-based Na<sup>+</sup>-electrolyte, in which reduction peaks of 1.38 and 0.9 V relates to SEI formation without nay oxidation peaks, illustrating insertion/desertion of Na<sup>+</sup> over 0.01–1 V potential-range. After 2000 cycles, MoO<sub>2</sub> NCs@N-CNFs possess 1D-ordered networks with

sodiate/desodiate MoO<sub>2</sub> (–121) reflections that manifests rational Na<sup>+</sup>-storage kinetics. MoO<sub>2</sub> subnanoclusters encapsulated in nitrogen-doped carbon nanofibers as anodes are also reported for Na<sup>+</sup>-storage with PMMA SEs.<sup>[104]</sup> Qin et al.<sup>[105]</sup> reports Na-cycling via polydopamine/multilayer graphene-based polypropylene (mPG-12@PP) for stable operations of 2000 h at 4 mV overpotential. Under polypropylene, Na-dendrites with loosely moss-like structures are observed at 1 mAh cm<sup>-2</sup>, whereas mPG-12@PP provides dense and smooth Na-depositions without dendrites even at 2 mAh cm<sup>-2</sup>, which confirms the key role of mPG-12 toward control for Na<sup>+</sup>-plate/strip. Cohn et al.<sup>[106]</sup> reports efficient plating/stripping for Na-metal for 4 mA cm<sup>-2</sup> with Na-loading up to 12 mAh cm<sup>-2</sup>, and long operations for 1000 cycles at 0.5 mA cm<sup>-2</sup>. The carbon layer reduces the overpotential from 19 to 12 mV for plating and improved performance attributed to the large surface area of carbon, reactive sp<sup>3</sup>-carbon sites and oxygen-comprising functional groups, and initial storage of Na<sup>+</sup>-ions in C-framework. Wu et al.<sup>[107]</sup> reports potassium bis(fluorosulfonyl)imide (KFSI)-dimethoxyethane (DME) based electrolytes generate reversible K<sup>+</sup>-plating/stripping with SEI and 99% CEs. It shows ordered surface morphology preventing parasitic reactions and maintaining dendrite-free K<sup>+</sup>-plate/strip upon cycling. XPS verifies the –SO<sub>2</sub><sup>–</sup> species due to FSI<sup>–</sup>-anions depletion, S-F bond breakage, and S=O/C=O species as SEI compositions. Theoretical calculations demonstrate the requirements for Mg-metal anodes regarding mobility, electronic band gaps, and stability by analyzing 27 binary, ternary, and quaternary compounds for wider-chemical space. MgSiN<sub>2</sub>, MgI<sub>2</sub>, MgBr<sub>2</sub>, MgSe, and MgS are identified as potential materials against the highly reductive Mg-anodes, and MgAl<sub>2</sub>O<sub>4</sub> and Mg(PO<sub>3</sub>)<sub>2</sub> are promising for high-voltage cathodes (≈3 V).<sup>[108]</sup> Bae et al.<sup>[109]</sup> reports amorphous MgO-coated Zn-framework as CCs for an anode-free Mg battery to allow reversible Mg<sup>2+</sup> plating/stripping in oxidatively stable electrolytes. The lattice mismatch among the MgO and Zn persuades the disorders, manifesting a defective interface of amorphous MgO + Mg<sub>x</sub>O<sub>y</sub> + Mg with a mixed ionic–electronic conductor. Dueramae et al.<sup>[110]</sup> reports the compatibility of carboxymethyl cellulose electrolytes with the Zn-salt complex (GPE<sub>A</sub> 15). Zn//Zn cells display larger voltage fluctuations from 0.5–10 mA cm<sup>-2</sup> current densities reflecting the high internal resistance of cells that impedes charge accumulation over the boundaries and poor interfaces with electrodes. Larger overpotential implies poor Zn<sup>2+</sup>-nucleation, attributed to thicker SEI and the accumulation of electronically detached/dead Li fibrils over interfaces.<sup>[111]</sup>

#### 5. Solid-State Electrolytes (SEs)

With the limited resources and uneven distribution of Li, there is a revival of interest in other batteries, including Na, K, Mg, Zn, and Al. Notably, ion conductivity is the critical parameter of SEs. However, commercial electrochemical conversion or storage systems require several major properties, such as super-ionic conductivity, high ion-selectivity, excellent chemical and electrochemical compatibility, broad electrochemical window, scalable and facile preparation processes, superior electronic area-specific resistance, smaller ionic area-specific resistance, excellent thermal stability and mechanical properties, cost-effective, superior device adaptation, and environmental friendliness.<sup>[10–12,112–128]</sup>

Extensive efforts have been reported for organic and inorganic SEs. Table 1 provides the state-of-the-art multivalent SEs and their properties.<sup>[10–12,32,39,102,112–232]</sup>

### 5.1. Inorganic SEs

Solid inorganic electrolytes (SIEs) consist of different types according to their crystal structures, such as garnet, sulfide (glasses, LGPS, argyrodite, thio-LISICON), perovskites, NASICONs, halides, oxides, hydrides, borate or phosphates. Perovskites SEs ( $\text{Li}_{3x}\text{La}_{2/3-x}\text{TiO}_3$ ) display exceptional Li-ion conductivity ( $>10^{-3} \text{ S cm}^{-1}$ ); however, severe reduction of  $\text{Ti}^{4+}$  with Li-metal clarifies the incompatibility for Li-batteries. NASICONs SEs have been demonstrated as the first SEs in the 1960s<sup>[112]</sup> with chemical formula  $\text{AM}_2(\text{PO}_4)_3$ , where A is the Li, Na, K, Mg, Zn, and M the Ge, Zr, Ti, or Si. Sn and Hf substitution improved a lower conductivity of  $\text{LiZr}_2(\text{PO}_4)_3$ .<sup>[113]</sup> Further,  $\text{Li}_{1+x}\text{M}_x\text{Ti}_{2-x}(\text{PO}_4)_3$  with M = Fe, Sc, Ga, Cr, Al, Lu, In, La, or Y has been demonstrated in which Al is most efficient due to a wide electrochemical stability window.<sup>[114,115]</sup> Lower covalency of Na–O than Li–O, exchanging  $\text{Na}^+$  by  $\text{Li}^+$  in  $\text{Na}_{1+x}\text{Zr}_x\text{Si}_{3-x}\text{O}_{12}$  NASICON degrades the conductivity. The systems were extended for Na, Mg, Zn, and K (in terms of  $\text{Na}_3\text{Zr}_2\text{Si}_2\text{PO}_{12}$ ,  $\text{MgZr}_4(\text{PO}_4)_6$ ,  $\text{ZnZr}_4(\text{PO}_4)_6$ ) with ion conductivities in the range of  $10^{-7}$ – $10^{-12} \text{ S cm}^{-1}$  at room temperature (RT); however, it significantly enhances to  $10^{-3} \text{ S cm}^{-1}$  for 300–500 (Li, Na) and 800–1000 °C (Mg, Zn).<sup>[116–120]</sup>  $\text{Li}_3\text{N}$ ,  $\text{Li}_3\text{PO}_4$ , and  $\text{LiI}$  have been reported as Li-ion conductors.<sup>[121,122]</sup> Yin et al.<sup>[123]</sup> reported  $\text{Li}_3\text{MCl}_6$  (M = Y, Sc, In, Ho) based electrolytes, in which  $\text{Li}_{0.388}\text{Ta}_{0.238}\text{La}_{0.475}\text{Cl}_3$  SE possesses  $3.02 \text{ mS cm}^{-1}$  Li-ion conductivity at 30 °C with the generation of gradient interfacial passivation layer to stabilize Li-metal.

Sulfide SEs based on the  $\text{Li}_2\text{S}$ – $\text{GeS}_2$ ,  $\text{Li}_2\text{S}$ – $\text{SiS}_2$ , and  $\text{Li}_2\text{S}$ – $\text{P}_2\text{S}_5$ – $\text{LiI}$  further displayed  $10^{-4} \text{ S cm}^{-1}$  conductivity. Kanno and Murayama<sup>[124]</sup> reported the first crystalline sulfide SEs ( $\text{Li}_{3.25}\text{Ge}_{0.25}\text{O}_{0.7}\text{S}_4$ ) of  $2.2 \text{ mS cm}^{-1}$  ionic conductivity. Partial crystalline  $\text{Li}_7\text{P}_3\text{S}_{11}$  with Li conductivity of  $3.2 \text{ mS cm}^{-1}$  was reported for glassy  $\text{Li}_2\text{S}$ – $\text{P}_2\text{S}_5$ .<sup>[12]</sup> Li-argyrodite  $\text{Li}_6\text{PS}_5\text{X}$  (X = Cl, Br, I) was reported by Deiseroth with the highest conductivity of  $4.96 \text{ mS cm}^{-1}$  using solid-state reactions.<sup>[125]</sup> The  $\text{Li}_{10}\text{GeP}_2\text{S}_{12}$  superion SEs with  $12 \text{ mS cm}^{-1}$  at RT comparable to conventional aprotic electrolytes for LIBs were reported by Kamaya.<sup>[10]</sup> Tatsumisago et al.<sup>[126]</sup> ( $\text{Li}_7\text{P}_3\text{S}_{11}$  with  $17 \text{ mS cm}^{-1}$ ), Kato et al.<sup>[11]</sup> ( $\text{Li}_{9.54}\text{Si}_{1.74}\text{P}_{1.44}\text{S}_{11.7}\text{Cl}_{0.3}$  with  $25 \text{ mS cm}^{-1}$ ) and, Iwasaki et al.<sup>[127]</sup> (single crystal  $\text{Li}_{10}\text{GeP}_2\text{S}_{12}$  along with [001] orientation with  $27 \text{ mS cm}^{-1}$ ) reported the superior conductors. Over time, chlorine-rich argyrodite ( $\text{Li}_{5.5}\text{PS}_{4.5}\text{Cl}_{1.5}$ ) exhibited  $12 \text{ mS cm}^{-1}$  ion conductivity.<sup>[128]</sup> Several promising Li-argyrodites, such as  $\text{Li}_{6-x}\text{PS}_{5-x}\text{ClBr}_x$  ( $0 \leq x \leq 0.8$ ) or  $\text{Li}_{6+x}\text{M}_x\text{Sb}_{1-x}\text{S}_5\text{I}$  (M = Si, Ge, Sn) ( $24 \text{ mS cm}^{-1}$ ),  $\text{Li}_{10}\text{Ge}(\text{Sb}_{0.075}\text{P}_{0.925})_2\text{S}_{12}$  ( $17.3 \text{ mS cm}^{-1}$ ),  $\text{Li}_{10.35}\text{Ge}_{1.35}\text{P}_{1.65}\text{S}_{12}$  ( $14.2 \text{ mS cm}^{-1}$ ), and  $\text{Li}_{6.5}\text{Sb}_{0.5}\text{Ge}_{0.5}\text{S}_5\text{I}$  ( $16.1 \text{ mS cm}^{-1}$ ) reported superior conductivity surpassing to liquid counterparts.<sup>[129–137]</sup>  $\text{Li}^+$  smaller radius allows the fast transfer kinetics, whereas the lower Lewis acidity of  $\text{Na}^+$  enables cation desolvation. Under similar structures, Na SE can have a higher ion conductivity relative to Li SE. SE of  $\text{Na}_3\text{P}_{1-x}\text{As}_x\text{S}_4$  ( $0 \leq x \leq 1$ ) exhibits  $1.46 \text{ mS cm}^{-1}$  of Na-ion conductivity. For comparison, Na, Mg, and Zn-based sulfide SEs (cubic  $\text{Na}_3\text{PS}_4$ ,  $\text{Na}_7\text{P}_3\text{S}_{11}$ ,  $\text{Na}_{2.88}\text{Sb}_{0.88}\text{W}_{0.12}\text{S}_4$ ,  $\text{Na}_{5-2x}\text{Al}_{1-x}\text{Ta}_x\text{S}_4$ ,

$\text{Na}_{5-2x}\text{In}_{1-x}\text{Sb}_x\text{S}_4$ , tetragonal  $\text{Na}_{4-x}\text{Sn}_{1-x}\text{Sb}_x\text{S}_4$ ;  $\text{MgS}$ – $\text{P}_2\text{S}_5$ – $\text{MgI}_2$ ,  $\text{MgSc}_2\text{Se}_4$ ,  $\text{MgSc}_{1.9}\text{Ti}_{0.075}\text{Se}_4$ ;  $\text{ZnPS}_3$ ) have been reported with a maximum conductivity of  $10^{-2}$ – $10^{-3} \text{ S cm}^{-1}$ .<sup>[138–146]</sup> Specifically, mesoporous  $\text{Zn}_y\text{S}_{1-x}\text{F}_x$  displays  $\text{Zn}^{2+}$  conductivity of  $0.66 \text{ mS cm}^{-1}$ .<sup>[147]</sup>  $\text{Mg}^{2+}$  phosphate SE with NASICON ( $\text{MgZr}_4(\text{PO}_4)_6$ ) exhibits  $6.1 \text{ mS cm}^{-1}$  ion conductivity for 800 °C, which is much poorer than  $\text{Na}^+$ ,  $\text{Li}^+$ , and other SEs. The stronger electrostatic interactions of  $\text{Mg}^{2+}$  and principal counterions due to the high charge density of  $\text{Mg}^{2+}$  ( $205 \text{ C mm}^{-3}$ ) relative to  $\text{Li}^+$  ( $87 \text{ C mm}^{-3}$ ) illustrate lower mobility of  $\text{Mg}^{2+}$  at low temperatures.<sup>[118,148]</sup>  $\text{Zn}^{2+}$  diffusion is also slower, like  $\text{Mg}^{2+}$  in NASICON structures with  $0.0013 \text{ mS cm}^{-1}$  at 500 °C.  $\text{Zn}^{2+}$  ions are octahedrally coordinated by  $[\text{P}_2\text{S}_6]^{4-}$  polyanions in the distorted honeycomb of  $\text{ZnPS}_3$ . P–P bonds follow the stretching to improve structural distortion.<sup>[146]</sup>

$\text{Mg}(\text{BH}_4)(\text{NH}_2)$  based  $\text{Mg}^{2+}$  SEs show the structural tunnels designed by zigzag chains for Mg ions (distance of Mg–Mg  $\approx 3.59 \text{ \AA}$ ) and anion frameworks. The distance of Mg–Mg ions is smaller than those of  $\text{Mg}(\text{BH}_4)_2$ ; thus, it facilitates the Mg hopping with high ion conductivity of  $10^{-3} \text{ mS cm}^{-1}$  for 150 °C, EW of  $>3 \text{ V}$ , and reversible Mg plating/stripping.<sup>[149]</sup> However, this  $\text{Mg}^{2+}$  conductivity is extremely poorer than those of  $\text{Li}^+$  in  $\text{Li}_2(\text{BH}_4)(\text{NH}_2)$  ( $\approx 0.2 \text{ mS cm}^{-1}$  at RT).<sup>[143]</sup> The high  $\text{Mg}^{2+}$  mobility for spinel selenides ( $\text{MgSr}_2\text{Se}_4$ ) provides large conductivity of  $\approx 0.01$ – $0.1 \text{ mS cm}^{-1}$  at RT.<sup>[150–153]</sup> Nanoconfined  $\text{LiBH}_4/\text{Al}_2\text{O}_3$  (orthorhombic) or  $\text{LiBH}_4\text{–LiI}/\text{Al}_2\text{O}_3$  (hexagonal) reveals rapid local interfacial Li-ion kinetics with small  $E_a$  of 0.1 eV, which facilitates faster long-range 2D ion transport.  $\text{Li}_6\text{PS}_6(\text{BH})_4$  exhibits  $1.8 \text{ mS cm}^{-1}$  ion conductivity with  $E_a$  of 0.015 eV.<sup>[150,154,155]</sup> Mostly reported halide SEs contain  $\text{Li}_3\text{MCl}_6$  (M = Sc, Y, In, Yb, Er) with maximum ion conductivity of  $\approx 1 \text{ mS cm}^{-1}$ .  $\text{Na}^+$  halide SEs ( $\text{Na}_2\text{ZrCl}_6$ ,  $\text{Na}_{3-x}\text{Er}_{1-x}\text{Zr}_x\text{Cl}_6$ , and  $\text{Na}_{3-x}\text{Y}_{1-x}\text{Zr}_x\text{Cl}_6$ ) have limited research due to expensive central metals and poor conductivity.<sup>[156–159]</sup>

Garnet SEs contain the structure of  $\text{A}_3\text{B}_2\text{Si}_3\text{O}_{12}$  with A and B cations having eight- and sixfold coordinations. Since 1969,<sup>[160]</sup> numerous garnets, including ( $\text{Li}_3\text{M}_2\text{Ln}_3\text{O}_{12}$  (M = W or Te),  $\text{Li}_{5.5}\text{La}_3\text{M}_{1.75}\text{B}_{0.25}\text{O}_{12}$  (M = Nb or Ta; B = In or Zr),  $\text{Li}_6\text{Ala}_2\text{M}_2\text{O}_{12}$  (A = Ca, Sr or Ba; M = Nb or Ta),  $\text{Li}_5\text{La}_3\text{M}_2\text{O}_{12}$  (M = Nb or Ta), and the cubic  $\text{Li}_7\text{La}_3\text{Zr}_2\text{O}_{12}$  and  $\text{Li}_{7.06}\text{M}_3\text{Y}_{0.06}\text{Zr}_{1.94}\text{O}_{12}$  (M = La, Nb or Ta) have been reported with highest ion conductivity of  $1.02 \text{ mS cm}^{-1}$  for the  $\text{Li}_{6.5}\text{La}_3\text{Zr}_{1.75}\text{Te}_{0.25}\text{O}_{12}$  at RT.<sup>[161–166,66–68]</sup>  $\beta$ -Alumina SE (BASE) is the  $\text{Na}^+$  ion conductor for Na–S high-temperature batteries. Similarly, K-incorporated BASE shows  $\text{K}^+$  ion conductivity. K-BASE displays 10 and  $56 \text{ mS cm}^{-1}$  conductivity for 150 and 300 °C, respectively. Besides, Eremin et al.<sup>[167]</sup> reported  $\text{K}^+$  ion conductors ( $\text{K}_5\text{As}_3\text{O}_{10}$ ,  $\text{K}_4\text{V}_2\text{O}_7$ ,  $\text{K}_2\text{Zn}_3\text{O}_4$ ,  $\text{K}_2\text{Sb}_4\text{O}_{11}$ ,  $\text{K}_3\text{NbAs}_2\text{O}_9$ , and  $\text{K}_3\text{NbP}_6$ ) based on their diffusion pathways and  $E_a$ .  $\text{K}_4\text{V}_2\text{O}_7$  and  $\text{K}_2\text{Al}_2\text{Sb}_2\text{O}_7$  show promising 2D and 3D conducting pathways. Yuan et al.<sup>[168]</sup> reported the open framework K-ferrite ( $\text{K}_2\text{Fe}_4\text{O}_7$ ) as additional  $\text{K}^+$  SE with *c*- and *b*-axes. It comprises both  $\text{FeO}_4$  tetrahedra and  $\text{FeO}_6$  octahedra units for edges and corners, offering proper  $\text{K}^+$  diffusion pathways. Polycrystalline  $\text{K}_2\text{Fe}_4\text{O}_7$  displays  $50 \text{ mS cm}^{-1}$  at RT ( $E_a$  of 0.16 eV), while a single crystal along the *a*-axis reveals 350 (RT) and  $500 \text{ mS cm}^{-1}$  (500 °C) with  $E_a$  of 0.08 eV.  $\text{MgHf}(\text{WO}_4)_3$  exhibits  $0.25 \text{ mS cm}^{-1}$  conductivity at 600 °C owing to 1D alignments of  $\text{Mg}^{2+}$  and  $\text{Hf}^{4+}$  ions interchanging for quasi-layered  $\text{WO}_4^{2-}$  units at  $\text{Sc}^{3+}$  sites in  $\text{Sc}_2(\text{WO}_4)_3$ .<sup>[169,170]</sup>

**Table 1.** State-of-the-art solid electrolytes.<sup>[10–12,32,39,102,112–232]</sup>

Metal ions	Materials	Ion conductivity [S cm <sup>-1</sup> ]	Activation energy [eV]	Remarks
<b>Sulfides</b>				
Li <sup>+</sup>	Li <sub>2</sub> S-P <sub>2</sub> S <sub>5</sub> , Li <sub>2</sub> S-P <sub>2</sub> S <sub>5</sub> -MS <sub>x</sub> , LGPS, Li <sub>3</sub> PS <sub>4</sub> , Li <sub>7</sub> P <sub>3</sub> S <sub>11</sub> , Li <sub>3</sub> SbS <sub>4</sub> (glass), Li <sub>9.54</sub> Si <sub>1.74</sub> P <sub>1.44</sub> S <sub>11.7</sub> Cl <sub>0.3</sub> , Li <sub>7</sub> P <sub>3</sub> Se <sub>11</sub> , Li <sub>6</sub> PS <sub>5</sub> Br, Li <sub>3.833</sub> Sn <sub>0.833</sub> As <sub>0.166</sub> S <sub>4</sub> , Li <sub>7-x</sub> PS <sub>6-x</sub> Cl <sub>x</sub> , Li <sub>6</sub> PS <sub>5</sub> Cl, Li <sub>4</sub> SnS <sub>4</sub> ,	10 <sup>-7</sup> –10 <sup>-3</sup>	0.1–0.25	Superion conductivity, Great mechanical properties, Lower grain boundaries resistances, Sensitive to moisture, Superior ion selectivity, Low chemical stability
Na <sup>+</sup>	Na <sub>3</sub> PS <sub>4</sub> (cubic), Na <sub>7</sub> P <sub>3</sub> S <sub>11</sub> , Na <sub>7</sub> P <sub>3</sub> Se, Na <sub>3</sub> SbS <sub>4</sub> , Na <sub>2.9375</sub> PS <sub>3.9375</sub> Cl <sub>0.0625</sub> , Na <sub>3</sub> P <sub>0.62</sub> As <sub>0.38</sub> S <sub>4</sub> , Na <sub>2.88</sub> Sb <sub>0.88</sub> W <sub>0.12</sub> S <sub>4</sub> , Na <sub>4-x</sub> Sn <sub>1-x</sub> Sb <sub>x</sub> S <sub>4</sub> , Na <sub>5-2x</sub> Al <sub>1-x</sub> V <sub>x</sub> S <sub>4</sub> , Na <sub>5-2x</sub> Al <sub>1-x</sub> Ta <sub>x</sub> S <sub>4</sub> , Na <sub>5-2x</sub> In <sub>1-x</sub> Sb <sub>x</sub> S <sub>4</sub>	10 <sup>-5</sup> –10 <sup>-2</sup>	0.2–0.3	Poor oxidation stability, High-ion conductivity, Poor chemical, oxidation, and reduction stability
Mg <sup>2+</sup>	MgS-P <sub>2</sub> S <sub>5</sub> -MgI <sub>2</sub> , MgSc <sub>2</sub> Se <sub>4</sub> , MgSc <sub>1.9</sub> Ti <sub>0.075</sub> Se <sub>4</sub> , MgLn <sub>2</sub> X <sub>4</sub> (Ln = Lu, Tm, Er, Ho, Dy, Tb, Sm, Pm, Nd, Pr, La, Y, Ce, Gd, Yb and X = S, Se), MgIn <sub>2</sub> S <sub>4</sub> , MgSc <sub>2</sub> Se <sub>4</sub> , MgY <sub>2</sub> Se <sub>4</sub> , MgY <sub>2</sub> S <sub>4</sub> , MgIn <sub>2</sub> Se <sub>4</sub> , MgSc <sub>2</sub> Te <sub>4</sub> , and MgY <sub>2</sub> Te <sub>4</sub>	10 <sup>-6</sup> –10 <sup>-4</sup>	–	Poor ion-conductivity, High mechanical strength, Poor compatibility with cathodes, Low flexibility and high cost Chemical and structurally unstable, High electronic conductivity
Zn <sup>2+</sup>	ZnPS <sub>3</sub> , Zn <sub>y</sub> S <sub>1-x</sub> F <sub>x</sub> , ZnSc <sub>2</sub> S <sub>4</sub> , ZnY <sub>2</sub> S <sub>4</sub> , ZnIn <sub>2</sub> S <sub>4</sub> , ZnY <sub>2</sub> Se <sub>4</sub> , ZnSc <sub>2</sub> Se <sub>4</sub> , ZnIn <sub>2</sub> Se <sub>4</sub> ,	10 <sup>-9</sup> –10 <sup>-3</sup>	0.3–0.4	Poor conductivity and oxidation stability, Limited thermal stability, Poor interface compatibility, Excess grain boundaries
<b>Halides</b>				
Li <sup>+</sup>	LiI, Li <sub>2</sub> ZnI <sub>4</sub> , Li <sub>3</sub> N, Li <sub>3</sub> OCl, Li <sub>3</sub> MCl <sub>6</sub> (M = Y, In, Sc, Ho), Li <sub>0.388</sub> Ta <sub>0.238</sub> La <sub>0.475</sub> Cl <sub>3</sub> , ZrO <sub>2</sub> -(LiCl)-Li <sub>2</sub> ZrCl <sub>6</sub> , ZrO <sub>2</sub> -2Li <sub>2</sub> ZrCl <sub>5</sub> F, Li <sub>3</sub> MX <sub>6</sub> (X = Cl, Br)	10 <sup>-8</sup> –10 <sup>-3</sup>	–	Stable with Li metal, Good mechanical properties, Poor oxidation voltage and conductivity, Moisture sensitive, Poor chemical and thermal stability, Excellent reduction stability, ion selectivity, High processing cost
Na <sup>+</sup>	NaAlCl <sub>4</sub> , Na <sub>3</sub> MX <sub>6</sub> (X = Cl, Br, I), ZrO <sub>2</sub> -(NaCl)-Na <sub>2</sub> ZrCl <sub>6</sub> , Na <sub>3-x</sub> Er <sub>1-x</sub> Zr <sub>x</sub> Cl <sub>6</sub> , Na <sub>3-x</sub> Y <sub>1-x</sub> Zr <sub>x</sub> Cl <sub>6</sub> , NaAlCl <sub>4</sub>	10 <sup>-6</sup> –10 <sup>-4</sup>	–	High processing cost, Poor ion conductivity and chemical stability, Poor thermal stability
<b>Oxides</b>				
Li <sup>+</sup>	Li <sub>7</sub> P <sub>3</sub> O <sub>11</sub> , Li <sub>7</sub> La <sub>3</sub> Zr <sub>2</sub> O <sub>12</sub> garnet, Perovskites, Li <sub>3.3</sub> La <sub>0.56</sub> TiO <sub>3</sub> , Li <sub>2</sub> Ti(PO <sub>4</sub> ) <sub>3</sub> , Li <sub>14</sub> Zn(GeO <sub>4</sub> ) <sub>4</sub> , Li <sub>6.5</sub> La <sub>3</sub> Zr <sub>1.75</sub> Te <sub>0.25</sub> O <sub>12</sub> , Li <sub>7.06</sub> M <sub>3</sub> Y <sub>0.06</sub> Zr <sub>1.94</sub> O <sub>12</sub> (M = La, Nb or Ta), Li <sub>6</sub> Ala <sub>2</sub> M <sub>2</sub> O <sub>12</sub> (A = Ca, Sr or Ba; M = Nb or Ta), (Li <sub>3</sub> M <sub>2</sub> Ln <sub>3</sub> O <sub>12</sub> (M = W or Te), Li <sub>5.5</sub> La <sub>3</sub> M <sub>1.75</sub> B <sub>0.25</sub> O <sub>12</sub> (M = Nb or Ta; B = In or Zr)	10 <sup>-5</sup> –10 <sup>-3</sup>	0.3–0.5	High chemical and electrochemical stability, High electrochemical oxidation voltage, High oxidation and thermal stability, Low processing cost and mechanical properties
Na <sup>+</sup>	Na <sub>7</sub> P <sub>3</sub> O <sub>11</sub> , NaTi <sub>2</sub> (PO <sub>4</sub> ) <sub>3</sub> , Na <sub>3</sub> Zr <sub>2</sub> Si <sub>2</sub> PO <sub>12</sub> , Na <sub>2.8</sub> Zr <sub>2</sub> Si <sub>1.8</sub> P <sub>1.2</sub> O <sub>12</sub> , Na <sub>3.2</sub> Zr <sub>2</sub> Si <sub>2.2</sub> P <sub>0.8</sub> O <sub>12</sub>	10 <sup>-6</sup> –10 <sup>-4</sup>	0.5–0.8	Good electrochemical stability, Non-flexible, Poor device integration
Mg <sup>2+</sup>	Mg <sub>0.5</sub> Zr <sub>2</sub> (PO <sub>4</sub> ) <sub>3</sub> , Mg <sub>0.5</sub> Ti <sub>2</sub> (PO <sub>4</sub> ) <sub>3</sub> , MgHf(WO <sub>4</sub> ) <sub>3</sub> , Mg <sub>0.5</sub> Zr <sub>2</sub> (AsO <sub>4</sub> ) <sub>3</sub> (PO <sub>4</sub> ) <sub>3</sub> , Mg <sub>0.5</sub> Ce <sub>0.2</sub> Zr <sub>1.8</sub> (PO <sub>4</sub> ) <sub>3</sub> , MgZr <sub>4</sub> P <sub>4</sub> O <sub>24</sub> , Zr <sub>2</sub> O(PO <sub>4</sub> ) <sub>2</sub>	10 <sup>-7</sup> –10 <sup>-4</sup> (500–600 °C)	–	Good electrochemical oxidation voltage, High mechanical strength, Expensive for large-scale, High thermal stability and safety
K <sup>+</sup>	K <sub>5</sub> As <sub>3</sub> O <sub>10</sub> , K <sub>4</sub> V <sub>2</sub> O <sub>7</sub> , K <sub>2</sub> Zn <sub>3</sub> O <sub>4</sub> , K <sub>2</sub> Sb <sub>4</sub> O <sub>11</sub> , K <sub>3</sub> NbAs <sub>2</sub> O <sub>9</sub> , K <sub>3</sub> NbP <sub>6</sub> , K <sub>2</sub> Al <sub>2</sub> Sb <sub>2</sub> O <sub>7</sub> , K <sub>2</sub> Fe <sub>4</sub> O <sub>7</sub> , K-BASE	10 <sup>-5</sup> –10 <sup>2</sup>	0.2–0.6	High ion conductivity, Poor chemical compatibility, Poor device integration
Zn <sup>2+</sup>	Zn silicate, Bi <sub>2</sub> Zn <sub>0.1</sub> V <sub>0.9</sub> O <sub>5.35</sub> , ZIF-8, ZnMOF-808	10 <sup>-6</sup> –10 <sup>-3</sup>	0.15–0.5	Poor chemical and electrochemical stability, High cost, Poor device integration, Poor thermal stability
Ca <sup>2+</sup>	β"-Al <sub>2</sub> O <sub>3</sub>	10 <sup>-4</sup> –10 <sup>-2</sup> (300 °C)	–	Poor device integration, operations only for high temperatures, high interface resistance

(Continued)



Table 1. (Continued)

Metal ions	Materials	Ion conductivity [S cm <sup>-1</sup> ]	Activation energy [eV]	Remarks
<b>Polymers</b>				
Li <sup>+</sup>	PEO, PVDF, LiTFSI-PEO, LiClO <sub>4</sub> -PEO, LiClO <sub>4</sub> -PEO, (10:1, 20:1, 30:1) Mw = 600k-5000k, PVDF-LLZO, PAN-LiClO <sub>4</sub> , PEO-LTO, PEGMEA-LLZO, PAN-LiTFSI, PAM-LiTFSI, PPA-LiTFSI, PSA-LiTFSI	10 <sup>-8</sup> –10 <sup>-4</sup>	0.4–1.0	Flexible and low conductivity Low shear modulus, Scalable for large-area, Stable with Li-metal, High processing cost, Poor thermal, oxidation, reduction, and chemical stability
Na <sup>+</sup>	PEO, NaTFSI-PEO, NaClO <sub>4</sub> -PEO, NaClO <sub>4</sub> -PEO with 5 wt% TiO <sub>2</sub> , (10, 20, 30:1) Mw = 600k-5000k, PEO-NaPF <sub>6</sub> , NaSCN, PEO-NSS, PEO-NASICON, PEO-NPSO	10 <sup>-9</sup> –10 <sup>-4</sup>	–	Limited thermal and chemical stability, Low oxidation voltage, Poor ion conductivity
Mg <sup>2+</sup>	MgCl <sub>2</sub> -PEO <sub>16</sub> , PVA-PEG-Mg(NO <sub>3</sub> ) <sub>2</sub> , Mg(ClO <sub>4</sub> ) <sub>2</sub> -PVDF-HFP-TiO <sub>2</sub> , Mg(AlCl <sub>2</sub> -EtBu) <sub>2</sub> -PEO, Mg(AlCl <sub>2</sub> -EtBu) <sub>2</sub> -PVDF, Mg(TFSI) <sub>2</sub> or Mg(Tf) <sub>2</sub> with PEO, PAN or PVP	10 <sup>-7</sup> –10 <sup>-6</sup>	–	Poor ion conductivity and electrochemical stability, High interfacial resistance, Fine interfacial contact, Limited thermal and mechanical stability, High flexibility, Facile manufacturing process
Zn <sup>2+</sup>	CNF-PAM-Zn(CF <sub>3</sub> SO <sub>3</sub> ) <sub>2</sub> , ZnTFSI-PEO, ZnSO <sub>4</sub> -PEO, Zn-Alginate/PAM, Gelatine, CMC, Gelatin-g-PAM, Xantum, PVA, and PPA with Zn-salts	10 <sup>-9</sup> –10 <sup>-5</sup> (SPEs) 10 <sup>-6</sup> –10 <sup>-3</sup> (GPEs)	0.5–1.8 (SPEs) 0.3–0.8 (GPEs)	Prohibit Zn dendrites growth and corrosion, rapid degradation, Flexible and compressible, Operate for subzero temperatures, Extremely large swelling
K <sup>+</sup>	PPC-KFSA, PMMA-KPF <sub>6</sub> , PMMA-KFSA, PEO-KFSA, PA-KPF <sub>6</sub> , PEO-KFSI, PPC-KFSI,	10 <sup>-8</sup> –10 <sup>-5</sup>	–	Poor ion conductivity, Poor thermal, chemical, and oxidation stability
Al <sup>3+</sup>	1-ethyl-3-methylimidazolium chloride-AlCl <sub>3</sub> , AlCl <sub>3</sub> -PA-Et <sub>3</sub> NHCl, IL-AlCl <sub>3</sub>	10 <sup>-9</sup> –10 <sup>-3</sup>	–	Poor ion conductivity, Poor thermal, chemical, and oxidation stability
Ca <sup>2+</sup>	PEGDA-Ca-salts (nitrate, TFSI, FSI, BF <sub>4</sub> , ClO <sub>4</sub> ), PTHF-Epoxy-Ca(NO <sub>3</sub> ) <sub>2</sub> , PEGDA-Ca(BF <sub>4</sub> ) <sub>2</sub> , EO/Ca,	10 <sup>-9</sup> –10 <sup>-4</sup>	0.22–0.8	Poor chemical and thermal stability, Poor ion conductance, High interface resistance, Poor EWs
<b>Hydrides</b>				
Li <sup>+</sup>	LiBH <sub>4</sub> , LiBH <sub>4</sub> -LiX (X = Cl, Br, or I), LiNH <sub>2</sub> , LiBH <sub>4</sub> -LiNH <sub>2</sub> , Li <sub>3</sub> AlH <sub>6</sub> , Li <sub>2</sub> NH, Li <sub>2</sub> (BH <sub>4</sub> )(NH <sub>2</sub> )	10 <sup>-7</sup> –10 <sup>-4</sup>	0.3–0.7	Lower grain boundary resistance, Good mechanical strength, Stable with Li, Poor thermal, chemical, and oxidation stability, High reduction stability and ion selectivity
Na <sup>+</sup>	Na <sub>2</sub> (BH <sub>4</sub> )(NH <sub>2</sub> )	10 <sup>-4</sup> –10 <sup>-3</sup>	0.5–0.8	Expensive for large scale, Average mechanical properties
Mg <sup>2+</sup>	Mg(BH <sub>4</sub> )(NH <sub>2</sub> ), Mg(BH <sub>4</sub> ) <sub>2</sub> (en), Mg(BH <sub>4</sub> ) <sub>2</sub> (NH <sub>3</sub> ), Mg(BH <sub>4</sub> )(BH <sub>3</sub> NH <sub>3</sub> ) <sub>2</sub> , Mg(BH <sub>4</sub> ) <sub>2</sub> .xNH <sub>3</sub> , Mg(BH <sub>4</sub> ) <sub>2</sub> .xNH <sub>3</sub> -MgO	10 <sup>-7</sup> –10 <sup>-5</sup> , (10 <sup>-3</sup> at 70–100 °C)	1–1.5	Good mechanical strength, Lower grain boundary resistance, Poor compatibility with cathodes Poor cation transfer
Ca <sup>2+</sup>	CaB <sub>12</sub> H <sub>12</sub> , CaBH <sub>4</sub>	10 <sup>-9</sup> –10 <sup>-5</sup> (800–1200 °C)	0.65–1.5	Low migration barriers, Poor ion conductivity, High interface resistance, Poor chemical compatibility
<b>NASICONs</b>				
Li <sup>+</sup>	LiZr <sub>2</sub> (PO <sub>4</sub> ) <sub>3</sub> , LiTi <sub>2</sub> (PO <sub>4</sub> ) <sub>3</sub> , Li <sub>1+x</sub> M <sub>x</sub> Ti <sub>2-x</sub> (PO <sub>4</sub> ) <sub>3</sub> at M = Cr, Al, Fe, Ge, Sc, In, Y, Lu, La; Li <sub>1+x</sub> Al <sub>x</sub> Ge <sub>2-x</sub> (PO <sub>4</sub> ) <sub>3</sub>	10 <sup>-11</sup> –10 <sup>-8</sup> , 10 <sup>-3</sup> (300–500 °C)	0.4–0.6	Poor ionic conductivity, Exceptional electrochemical stability window
Na <sup>+</sup>	Na <sub>3</sub> Zr <sub>2</sub> PSiO <sub>12</sub> , Na <sub>3</sub> Zr <sub>2</sub> Si <sub>2</sub> PO <sub>12</sub> ,	10 <sup>-10</sup> –10 <sup>-7</sup> , 10 <sup>-3</sup> (300–500 °C)	0.3–0.6	Low ion conductivity, Large grain boundary resistance
Mg <sup>2+</sup>	MgZr <sub>4</sub> (PO <sub>4</sub> ) <sub>6</sub>	10 <sup>-12</sup> –10 <sup>-11</sup> , 10 <sup>-4</sup> (800–1000 °C)	0.8–1.0	Poor ion conductivity and chemical compatibility
Zn <sup>2+</sup>	ZnZr <sub>4</sub> (PO <sub>4</sub> ) <sub>6</sub>	10 <sup>-12</sup> –10 <sup>-11</sup> , 10 <sup>-5</sup> –10 <sup>-4</sup> (800–1000 °C)	0.9–1.3	Lowest ion conductivity, Poor chemical and electrochemical stability, Operates for high temperatures
K <sup>+</sup>	KZr <sub>2</sub> (PO <sub>4</sub> ) <sub>3</sub> , KTi <sub>2</sub> (PO <sub>4</sub> ) <sub>3</sub> ,	10 <sup>-12</sup> –10 <sup>-9</sup>	–	Poor ion conductivity and electrochemical (oxidation, reduction) stability, Expensive

(Continued)

**Table 1.** (Continued)

Metal ions	Materials	Ion conductivity [S cm <sup>-1</sup> ]	Activation energy [eV]	Remarks
Al <sup>3+</sup>	(Al <sub>0.2</sub> Zr <sub>0.8</sub> ) <sub>20/19</sub> Nb(PO <sub>4</sub> ) <sub>3</sub>	10 <sup>-6</sup> –10 <sup>-4</sup> (300–600 °C)	>3.1	Poor ion conductivity and electrochemical stability
Ca <sup>2+</sup>	(Ca <sub>x</sub> Hf <sub>1-x</sub> ) <sub>4/(4-2x)</sub> Nb(PO <sub>4</sub> ) <sub>3</sub> , (Ca <sub>0.05</sub> Hf <sub>0.95</sub> ) <sub>4/3.9</sub> Nb(PO <sub>4</sub> ) <sub>3</sub> , Ca <sub>0.5</sub> Zr <sub>2</sub> (PO <sub>4</sub> ) <sub>3</sub> , CaZr <sub>4</sub> (PO <sub>4</sub> ) <sub>6</sub> , Ca <sub>10.5-x</sub> Pb <sub>x</sub> (VO <sub>4</sub> ) <sub>7</sub> for x = 1.9, 3.5, 4.9, Ca <sub>7</sub> MgPbBi(VO <sub>4</sub> ) <sub>7</sub> , Ca <sub>7.5</sub> Zn <sub>0.5</sub> Pb <sub>0.5</sub> Bi(VO <sub>4</sub> ) <sub>7</sub> , Ca <sub>7.5</sub> Cd <sub>0.5</sub> Pb <sub>0.5</sub> Bi(VO <sub>4</sub> ) <sub>7</sub> , Ca <sub>8</sub> PbBi(VO <sub>4</sub> ) <sub>7</sub> , Ca <sub>3</sub> (VO <sub>4</sub> ) <sub>2</sub> , Ca <sub>7.5</sub> Pb <sub>3</sub> (VO <sub>4</sub> ) <sub>7</sub> , Ca <sub>6.5</sub> Pb <sub>4</sub> (VO <sub>4</sub> ) <sub>7</sub> , Ca <sub>6.5</sub> Pb <sub>4.5</sub> (VO <sub>4</sub> ) <sub>7</sub> , ACa <sub>9</sub> (VO <sub>4</sub> ) <sub>7</sub> (A = Gd, Ho, Lu, Er, Eu, Pr, Sm, Bi, La, Nd, Tb, Yb, Y, and Sc),	10 <sup>-8</sup> –10 <sup>-3</sup> (300–900 °C)	1.3–1.5	Extremely poor ion-conductivity for RT, Poor chemical stability and EWs, operates for high temperature only
<b>Borate or Phosphates</b>				
Li <sup>+</sup>	Li <sub>2</sub> B <sub>4</sub> O <sub>7</sub> , Li <sub>3</sub> PO <sub>4</sub> , Li <sub>2</sub> O-B <sub>2</sub> O <sub>3</sub> -P <sub>2</sub> S <sub>5</sub> , Li <sub>3-x</sub> Na <sub>x</sub> PO <sub>4</sub>	10 <sup>-7</sup> –10 <sup>-6</sup>	–	Scalable fabrication process, Good durability, Poor conductivity
<b>Thin films</b>				
Li <sup>+</sup>	LiPON, Li <sub>3.4</sub> V <sub>0.6</sub> Si <sub>0.4</sub> O <sub>4</sub> , LiSiPON, LiSON, LiNbO <sub>3</sub> , Li <sub>3</sub> PO <sub>4</sub> /P <sub>2</sub> S <sub>5</sub> , Li <sub>2</sub> S-SiS <sub>2</sub> -P <sub>2</sub> S <sub>5</sub> , Li <sub>3.25</sub> Ge <sub>0.25</sub> P <sub>0.75</sub> S <sub>4</sub> , PEO/succinonitrile/LiTFSI, Li <sub>1+x</sub> Al <sub>x</sub> Ti <sub>2-x</sub> (PO <sub>4</sub> ) <sub>3</sub> , Li <sub>3</sub> OCl, Li <sub>2</sub> O-B <sub>2</sub> O <sub>3</sub> -Li <sub>2</sub> SO <sub>4</sub> , Li <sub>3</sub> PO <sub>4</sub> -Li <sub>4</sub> SiO <sub>4</sub> , Li <sub>7</sub> La <sub>3</sub> Zr <sub>2</sub> O <sub>12</sub> ,	10 <sup>-9</sup> –10 <sup>-4</sup>	–	Stable with Li and cathode materials, Expensive for large-scale, Excellent reduction, oxidation, and thermal stability, ion selectivity, Extremely poor mechanical properties and device integration High processing cost
Na <sup>+</sup>	NaPON (Na <sub>4</sub> PO <sub>3</sub> N)	10 <sup>-10</sup> –10 <sup>-6</sup> (RT–80 °C)	0.5–1.05	Poor RT ion-conductivity, High interface resistance
Mg <sup>2+</sup>	MgPON, MgPO	10 <sup>-10</sup> –10 <sup>-6</sup> (400–500 °C)	–	Poor ion conductivity at RT, Limited thermal and chemical stability, High cost

Mg<sub>1+x</sub>Zr<sub>4</sub>P<sub>6</sub>O<sub>24+x</sub> + xZr<sub>2</sub>O(PO<sub>4</sub>)<sub>2</sub> and Mg<sub>0.5</sub>Zr<sub>2</sub>(PO<sub>4</sub>)<sub>3</sub> display 10<sup>-7</sup>–10<sup>-9</sup> S cm<sup>-1</sup> at 500 °C.<sup>[169–171]</sup> Aubrey et al.<sup>[172]</sup> reports Mg<sub>2</sub>(2,5-dioxidobenzene-1,4-dicarboxylate) and Mg<sub>2</sub>(4,4'-dioxidobiphenyl-3,3'-dicarboxylate), and MOFs-based SEs with  $\sigma_{Mg^{2+}} \approx 0.25$  mS cm<sup>-1</sup> at RT.

## 5.2. Organic SEs

Polymer electrolytes are classified into three categories: 1) dry solid polymer electrolytes (SPE), gel polymer electrolytes (GPE), and composite polymer electrolytes (CPE) for different types of battery chemistries. SPEs involve the metal salts (Li, Na, Al, Zn, K, Mg, Ca) solid solvents with polymer hosts deprived of any liquids. However, their ion conductivities are extremely poor at RT.<sup>[173]</sup> GPE consists of metal salts and polymeric networks liquefied by water, which feature liquid-like ion conductivity and solid-like compatibility. However, it suffers from large interfacial resistance, poor mechanical properties with high swelling behavior, and rapid degradation with ion conductivity.<sup>[174]</sup> CPEs formed by the combination of polymer hosts with inorganic ceramic fillers to improve conductivity by reducing  $T_g$ . Generally, PEO, PAM, PMMA, PVC, PVDF, or PAN are utilized as polymers along with active (e.g., Li<sub>2</sub>N, LiAlO<sub>2</sub>) and inactive (e.g., MgO, SiO<sub>2</sub>, Al<sub>2</sub>O<sub>3</sub>, TiO<sub>2</sub>) fillers.<sup>[175,176]</sup> CPEs determine the compatibility for Li-metal and the high-voltage cathodes, which is a critical requirement for high-energy SSBs. Theoretical results show thermodynamics for

electrode/electrolyte interface and intrinsic EWs of CPEs with the role of inorganic fillers for leading EWs.<sup>[39,177,178]</sup>

The dual functioning PSA and poly(dimethyl siloxane)-g-[poly(poly(ethylene glycol) methyl ether methacrylate)-r-sodium poly(p-styrene sulfonate) (PPS) as SPE and artificial SEI with 0.056 and 0.45 mS cm<sup>-1</sup> conductivities following VFT mechanism have been reported.<sup>[179,180]</sup> In hybrid electrolytes (SIE-SPE or SIE-liquid) for Li and Na ions, the Na<sup>+</sup> transport occurs via internal interfaces with smaller  $E_a$  due to the lower Lewis acidity of Na<sup>+</sup> and weak interactions for oxygen atoms in polymers or liquids. Theoretical calculations verify the desolvation energy trend as Mg<sup>2+</sup> > Li<sup>+</sup> > Na<sup>+</sup>, enabling cations suitability for new SEs.<sup>[181,182]</sup> Since the 1980s, Mg-based SPEs have been reported; however, GPE composed of PVDF or PEO with Mg(AlCl<sub>2</sub>-EtBu)<sub>2</sub> and tetraglyme plasticizer displayed reversibility of Mg under plating/stripping.<sup>[183]</sup> Further, Mg(BH<sub>4</sub>)<sub>2</sub>-PEO-MgO CPE exhibits the Mg plate/stripping for >98% CE at 100 °C with dissociation of Mg(BH<sub>4</sub>)<sub>2</sub>.<sup>[184]</sup> PEO with Mg(TFSI)<sub>2</sub>, Mg(NO<sub>3</sub>)<sub>2</sub>, and Mg(Tf)<sub>2</sub> displays conductivities of 0.0001, 0.013, 0.000032 mS cm<sup>-1</sup> at RT, respectively.<sup>[102,185–187]</sup> PVDF-HFP with 40 wt% Mg(Tf)<sub>2</sub> shows maximum conductivity of 10<sup>-3</sup> S cm<sup>-1</sup> at RT.<sup>[187]</sup>

Zn<sup>2+</sup> SPEs involve (PEO-ZnCl<sub>2</sub>, Zn(TFSI)<sub>2</sub>, Zn(OTf)<sub>2</sub>) with a thickness of 30–60 μm.<sup>[188,189]</sup> For alkaline Zn-batteries, the transfer of hydroxides is a main source compared to Zn<sup>2+</sup> ions, so such GPEs use basic KOH/NaOH for oxygen solubility and conductivity. Cellulose with quaternary ammonium salts and chitosan biocellulose membrane inhibits the

crossover of cations with 21.2 and 86.7 mS cm<sup>-1</sup> hydroxide conductivity.<sup>[190,191]</sup> Further, the ethylene glycol-based waterborne anionic polyurethane acrylates/PAM (EG-waPUA/PAM) GPE enables freeze-resistance down to -20 °C.<sup>[192]</sup> Al<sup>3+</sup>-based SEs offer a high capacity of 8040 mAh cm<sup>-3</sup> due to the removal of corrosion and moisture effect by liquids.<sup>[32]</sup> For example, SPE of 1-ethyl-3-methylimidazolium chloride (EMIC)-AlCl<sub>3</sub> exhibits 1.46 mS cm<sup>-1</sup> conductivity, Al plate/stripping, and fast charge capability (<10s) for graphite cathodes.<sup>[32,77,193,194]</sup> Potassium bis(fluorosulfonyl)amide (KFSA) with 1,2-dimethoxyethane and 1,3,2-dioxathiolane 2,2-dioxide suppresses interfacial resistance and polarization with 0.02 mS cm<sup>-1</sup> ion conductivity. Degrees of polarization show the tradeoff as Li<sup>+</sup> > Na<sup>+</sup> > K<sup>+</sup>.<sup>[195,196]</sup> Various complexes of PEO with Li, Na, K, Zn, Mg, and Al (i.e., NaSCN, NaTFSi, NaPF<sub>6</sub>, NaYF<sub>6</sub>, KYF<sub>6</sub>, LiSO<sub>3</sub>SF<sub>3</sub>, LiTFSi, LiFSi, ZnTFSi<sub>2</sub>, MgTFSi, AlCl<sub>3</sub>) have been explored for SPEs.<sup>[32,102,179–196]</sup>

Zhou et al.<sup>[197]</sup> presents in situ polymerized poly (ethylene glycol) diacrylate-based electrolytes with  $\sigma_{Na^+} \approx 1.4$  mS cm<sup>-1</sup> at 25 °C. The refined solvation structure of Na<sup>+</sup> restrains the random diffusion of Na<sup>+</sup>-ions due to lower desolvation energy barriers with suppression of dendritic growth over >2000 h Na//Na cells. Yuan et al.<sup>[198]</sup> reports polyvinylidene fluoride hexafluoropropylene (PVDF-HFP)-based solid electrolyte that can operate over -20 to 50 °C with high capacities of 165.6/163.4 mAh g<sup>-1</sup> at 50/25 °C. Hou et al.<sup>[199]</sup> reports 1,3,5-trioxane (TO) and DME-based electrolytes with the construction of mechanically stable SEI enriched with organic components in Li-S batteries. High polymerization of TO displays preferential decomposition with alleviating cracks, regeneration of SEI, and reduction in consumption rate for Li-polysulfides and active Li. Wang et al.<sup>[200]</sup> fabricates the SPEs with 3-(1-vinyl-3-imidazolium) propanesulfonate (VIPS) zwitterionic monomer with  $\sigma_{Zn^{2+}} \approx 2.6$  mS cm<sup>-1</sup> under 20 wt% lean-water content, wider voltage stability window, and Zn plate/strip over 900 h with dense and dendrite-free surfaces. Functionalized biocellulosics (FBN) and chitosan-biocellulosics (CBCs) membrane electrolytes with  $\sigma_{Zn^{2+}} \approx 64$  and 86.7 mS cm<sup>-1</sup> for highly reversible Zn-air batteries are also reported.<sup>[201–208]</sup> Pristine and patterned Zn anodes with FBN and CBCs displayed superior compatibility under plating/stripping over 5000–6000 cycles with capacities of 1–10 mAh cm<sup>-2</sup> per cycle. Further, both electrolytes exhibit chemical and thermodynamic stability for supramolecular polymer intertwined free-standing and powder-based oxygen cathodes with high power and energy efficiencies.

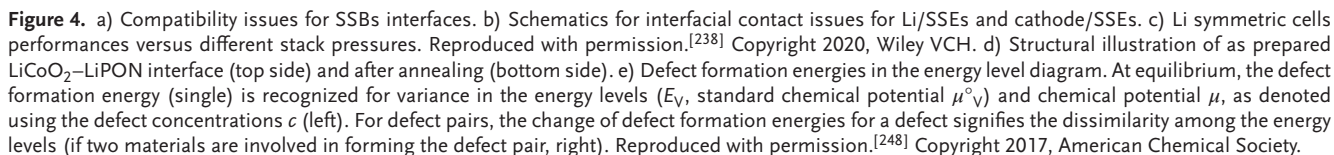
### 5.3. Thin-Film (TF) SEs

Thin film SEs are prepared using various techniques such as chemical vapor or atomic layer or pulsed laser deposition, radio frequency sputtering, thermal/electron-beam evaporation, printing, sol-gel/aerosol, and electrodeposition. Required properties for implementing thin film SEs are RT ion conductivity of 10<sup>-9</sup>–10<sup>-6</sup> S cm<sup>-1</sup>, EW of >5 V versus Li/Li<sup>+</sup>, high electrochemical/thermal stability for anode/cathodes, and facile large-scale manufacturing. Bates et al.<sup>[209–211]</sup> reported amorphous LiPON TFSEs with general formulation as Li<sub>x</sub>PO<sub>y</sub>N<sub>z</sub>. Li<sub>3</sub>PO<sub>4</sub> and N-incorporated Li<sub>3</sub>PO<sub>4</sub> exhibiting 0.00007 and

0.0033 mS cm<sup>-1</sup> ion-conductivity with EW of 5.5 V versus Li/Li<sup>+</sup>. Further, binary/ternary oxides like Li<sub>2</sub>O-Nb<sub>2</sub>O<sub>5</sub>, Li<sub>2</sub>O-SiO<sub>2</sub>-P<sub>2</sub>O<sub>5</sub>, Li<sub>2</sub>O-B<sub>2</sub>O<sub>3</sub>-P<sub>2</sub>O<sub>5</sub>, and Li<sub>2</sub>O-SiO<sub>2</sub>-V<sub>2</sub>O<sub>5</sub> showed 10<sup>-7</sup> to 10<sup>-5</sup> S cm<sup>-1</sup> conductivity range. Amorphous (LLZO, LLTO, sulfides), PEO-composites, and crystalline (Li<sub>3</sub>OCl, NASICON, LISICON, LLZO, LLTO) based TFSEs reported the maximum ion conductivity of 0.14 mS cm<sup>-1</sup>.<sup>[212–215]</sup> Lupo et al.<sup>[216]</sup> reported that Li phosphorous sulfuric oxynitride (LiPSON) SEs display  $\sigma_{Li^+} \approx 9.75$  μS cm<sup>-1</sup> slightly larger than LiPON (3.3 μS cm<sup>-1</sup>).  $E_a$  for LiPSON, LiSiPON, and LiPON are 0.49, 0.41–0.47, and 0.49–0.68 eV, respectively.<sup>[217–222]</sup> Song et al.<sup>[223]</sup> reports Mn-doped LiPON thin film SEs with  $\sigma_{Li^+} \approx 5$  μS cm<sup>-1</sup> and reduces the work function of LiPON that benefits electrochemical interface stability. Mn-doping restricts the blocking effects of SCL for Li<sup>+</sup> due to weakening Li<sup>+</sup>-PO<sub>3</sub>N<sup>4-</sup> tetrahedral bindings. The ionized N-ions binds with phosphate by forming double-ligand N (N<sub>d</sub>, P-N=P) and tri-ligand N (N<sub>t</sub>, P-N < P<sub>p</sub>) during thin film formation, and the multivalent nature of Mn controls an assortment of LiPON binding types.<sup>[224]</sup> Mn-doping serves as a junction for crosslinks for phosphate groups (i.e., Mn<sup>4+</sup> to N<sub>d</sub> and Mn<sup>3+</sup> to N<sub>t</sub>) conducive for isotropic Li<sup>+</sup>-transport. López-Grande et al.<sup>[225]</sup> reports Li<sub>2</sub>PO<sub>2</sub>N oxynitride with nitridation of crystalline Li<sub>4</sub>P<sub>2</sub>O<sub>7</sub> by thermal ammonolysis. Theoretic calculations of Li<sub>2</sub>O-P<sub>2</sub>O<sub>5</sub>-P<sub>3</sub>N<sub>5</sub> equilibria predict no formation of Li<sub>2</sub>PO<sub>2</sub>N lower than 7.3 wt% N. It forms by decomposing γ-Li<sub>3</sub>PO<sub>4</sub> into Li<sub>2</sub>PO<sub>2</sub>N and Li<sub>2</sub>O with increasing N contents. Low N displays two major resonances in NMR for Li<sub>4</sub>P<sub>2</sub>O<sub>7</sub> (-3.9 and -6.1 ppm) and Li<sub>3</sub>PO<sub>4</sub> (9.45 ppm) with minor four Lorentzian profiles (4.74, 10.79, 11.94, and 14.42 ppm), which illustrates the existence of P-atoms for one or more crystals. High N of 7.98 wt% displays similar resonances with 4.34 wt.% N, excluding Li<sub>4</sub>P<sub>2</sub>O<sub>7</sub> phase.

Similar to LiPON, sodium phosphorus oxynitride (NaPON) is also reported with a conformal stoichiometry of Na<sub>4</sub>PO<sub>3</sub>N analogous to sodium polyphosphazene structures and  $\sigma_{Na^+} \approx 0.1$  and 2.5 μS cm<sup>-1</sup> for 25 and 80 °C and  $E_a \approx 0.53$  eV, two times higher magnitude than air-exposed films.<sup>[226]</sup> XPS results clarify the presence of Na<sup>+</sup>-O<sup>-</sup>=P-, O<sup>-</sup>-Na=, doubly-coordinated N (P-N=P), and triply coordinated N (P-N<P<sub>2</sub>). Fontecha et al.<sup>[227]</sup> also reported NaPON using PEALD for 150–350 °C and obtained  $\sigma_{Na^+} \approx 8.2$  nS cm<sup>-1</sup> at 80 °C. N content and coordination states of N (N<sub>d</sub> or N<sub>t</sub>) in NaPON or LiPON are crucial for high-ion mobility. Lacivita et al.<sup>[214]</sup> confirms the higher N<sub>t</sub> coordination states suffer poor ion conductivity, and high N<sub>d</sub> offers large ion conductivity for LiPON and NaPON. Bulk Li<sub>3.6</sub>PO<sub>3.4</sub>N<sub>0.6</sub> (b-LiPON) crystalline polymorph is also prepared by ball-milling with  $\sigma_{Li^+} \approx 5$  μS cm<sup>-1</sup> for 70 °C and 5 V versus Li/Li<sup>+</sup> window.<sup>[228]</sup> b-LiPON consists of distorted hcp arrays of O and N anions. N-anions partially occupy two crystallographic O-sites as O1/N1 and O2/N2, whereas P-cations occupy PO<sub>3.57(13)</sub>N<sub>0.43(13)</sub> coordinated tetrahedra isolated from others and consecutively indicate opposite directions. Li-cations have six distinct places similar to Li<sub>4</sub>SiO<sub>4</sub> in terms of Li6 for octahedral, Li5 for fivefold, and Li4 for tetrahedral coordinations.

Magnesium phosphorus oxynitride (MgPON) SEs are also reported by using ALD with double nitrogen plasma processes at a low deposition temperature of 125 °C.<sup>[229]</sup> MgPON displays amorphous nature without grain boundaries and  $\sigma_{Mg^{2+}} \approx 0.58$  nS cm<sup>-1</sup> at 300 °C, 1.1 times larger than magnesium phosphate (MgPO). For 400 and 500 °C, it shows 6.2 and



Ionic and electrical contacts of SEs and electrodes are highly preferred for achieving high-performance SSBs. The point-to-point contacts are frequently observed for SE/electrode interfaces due to the particle-particle connections or pore existence even under hot pressing, which provides the concerted local electric field and high interface resistance. Surface energy mismatch induces poor wetting for SEs with metals (Li, Na, K, Zn, Al, Ca) and inadequate contacts between them, illustrating poor rate capability, high charge-transfer polarization, and lower energy densities (**Figure 4a,b**). Volume discrepancy of metals during cycling initiates dendritic growth. Dendrites formation strongly depends on the operating current density of cells. For high current densities, the resulting high electric field causes uneven metal plate/strip and grain boundaries of SEs, which induces the voltage penetration of SEs and vital short-circuiting for SSBs. Thus, the rational



design of the interface of SEs and metals is highly challenging. Utilization of polymer buffers, artificial SEI, and preactivation for lower current densities are several approaches reported to develop Li (or other metals)/SEs.<sup>[233–235]</sup> Similarly, physical contacts among the SEs and cathodes are also crucial to recognize lower impedance SSBs. It depends on several factors, including surface morphology of SEs and active cathodes, conductive additives, and stress/volume variations for cathodes during cycle operations. Insertion of buffer layers (i.e., polymers, sulfides, oxides, or hybrids)<sup>[236,237]</sup> can enhance physical/chemical contacts with a considerable decrease in interfacial resistance, rate capacity, cycle life, and energy-power performances.

Another approach is applying high pressure during cell fabrication and operations to enhance the mechanical contacts. However, optimal stack pressure is recommended as per metal-chemistries. For Li-metal, Doux et al.<sup>[238]</sup> reported the optimal stack pressure of  $\leq 25$  MPa for Li/Li<sub>6</sub>PS<sub>5</sub>Cl/Li symmetric cells that enhance Li/SEs contact with decreasing interfacial resistance. Figure 4c displays the influence of stack pressure on the mechanical integrity of SEs versus cycling, in which no obvious shorts are observed up to 1000 h for 5 MPa pressure. This reveals that 5 MPa stack pressure enables the reasonable contact of Li and SE. Cells show failure after 474, 272, 190, and 48 h for 10, 15, 20, and 25 MPa stack pressures during cycling, which ascribes the creeping of Li in the pores of SEs wherein Li dendrites form with eventual short-circuit. Above 75 MPa, cells are mechanically shorted before applying current. Generally, composite cathodes exhibit enhanced kinetics compared to pristine active cathodes with fast ion transport; however, they adversely decrease the electrode mass loading, degrading the operative storage capacity. Zero-strain cathodes diminish the internal stress of SSBs, Koerver et al.<sup>[239]</sup> reported that the blending of LiCoO<sub>2</sub> (LCO) and LiNi<sub>0.8</sub>Co<sub>0.1</sub>Mn<sub>0.1</sub>O<sub>2</sub> (NCM811) in 55:45 wt% displays nearly zero-strain. LCO reveals positive stress during operations, whereas NCM811 has negative stress responses.

To obtain stable performance for SSBs, the chemical contacts related to the electrochemical and chemical stabilities of an interfacial reaction region are also critically important. For example, the sulfides, thiophosphate, titanium, and germanium are unstable in contact with thermodynamically uneven Li metal, and a solid passivation layer gradually forms at Li/SSE interface. There are three types of interphases, as explained in Section 2. The mixed conducting interface (type 3) forms Li dendrites severely. Further, the high electronic conductivity of SEs and overpotential during Li plating also demonstrate the dendrite's growth in bulk SE. Thus, incorporating reactive/nonreactive buffer layers with Li shows the electrochemically and thermodynamically stable SEI construction.<sup>[235,240,241]</sup> Besides, SSE/cathode interface involves the flow of electrons through the cathodes and ions across the cathode/SSE interfaces. Cathode encloses active materials, carbon conductors, and polymer binders, providing a concurrent transfer of Li ions and electrons. Intrinsic resistance of one of these materials can result in poor solid interface contacts (Figure 4b). Different chemical potentials of cathodes/SEs form the larger contact resistances for metal ions from the space charge layer. For example, sulfide SEs have a weak attraction towards Li<sup>+</sup> with low chemical potential relative to the oxide cathode (LiFePO<sub>4</sub>). In sulfide-based SEs, Li-ions transfer in the oxide cathodes with redistribution of Li ions while forming a depletion

layer along the oxide cathode/sulfide SEs interface that offers the additional energy barrier for Li<sup>+</sup> ions transport. Loading of thin layers of Li<sub>4</sub>Ti<sub>5</sub>O<sub>12</sub>, LiNbO<sub>3</sub>, LiAlO<sub>2</sub>, and LiTaO<sub>3</sub> can effectively suppress space charge layers at SSE/cathode interface, as per previous reports. The compositions and structures of buffers significantly control the interface compatibility of SEs/cathode.<sup>[242–244]</sup> According to electronic and Li-ion conductivities, generated interlayers are classified into four groups: 1) interlayer with high ionic and electronic conductivities that unceasingly grow under cycling. 2) Interlayer with high electronic and low ionic conductivities, which causes degradation of SEs and growth of thick interlayer. 3) Interlayer with low electronic and ionic conductivities, which displays substantial interfacial resistance without interphase growth and poor performance of cells. 4) Interlayer with low electronic and high ion conductivities, which has initial growth due to parasitic reactions. The formation has been inhibited after a certain thickness of the interlayer is obtained. These interlayers will enhance the EW of SEs without enlarging interfacial resistance.<sup>[245]</sup> Practical cells display several interlayers over an interface like Li-immobilization, space charge, or interdiffusion. Conclusively, microstructures, operating conditions, and uniformity of materials realize the interface contacts as per battery chemistries (Na, K, Mg, Zn, Al, Ca, etc.).

## 6.2. Space-Charge Layers

Interfacing two electrodes with different electrochemical potentials projects the space-charge layers (SCL), in which simply one charge species can transfer (either electrons or ions) with a building interfacial charged region (noted as space charge layer). The impact of space charge layers on cell performances is highly debatable. Theoretical calculations based on silica or Al<sub>2</sub>O<sub>3</sub> fillers in SEs display increased ion conductivity due to a space charge layer. In contrast, most reports stated that a space charge layer is not applicable. LiMn<sub>2</sub>O<sub>4</sub>/Li<sub>3.25</sub>Ge<sub>0.25</sub>P<sub>0.75</sub>S<sub>4</sub> and LiCoO<sub>2</sub>/Li<sub>3</sub>PS<sub>4</sub> systems vindicate the high interfacial resistance due to space charge layers.<sup>[65,246]</sup> Theoretical results estimated that a possible thickness of the space charge layer is  $\approx 1$  nm; thus, the influence of such resistance will be negligible apart from Li depletion in SEs.<sup>[247]</sup> Fingerle et al.<sup>[248]</sup> reported the in-depth analysis of interface equilibria and reactions required to transfer ion and electronic species through the interface or near-interface regions for LCO and LiPON materials. The electrostatic potential gradient of 0.3 V is observed for the pristine interface, and it remained even after annealing, as verified by band bending in Figure 4d, which is ascribed to the equilibration of the electrochemical potential of Li at the interface.<sup>[249]</sup> The Li-ions losses from LCO state the construction of negatively charged Li-vacancies (V'<sub>Li</sub>) and Li-ions incorporation in the LiPON SEs that recognized generation of positively charged Li-interstitials (Li<sub>i</sub>). Li-interstitials and Li-vacancies accumulate the space charge layers at the interface subject to the charge carrier concentrations (i.e., Debye length).<sup>[250]</sup> Such a prolonged space charge layer (a few nm) in LCO rationalizes a low charge carrier concentration (lower number of Li-vacancies), as denoted by the Fermi level. For LiPON, mobile Li-ion concentration is  $1.5 \times 10^{20}$  cm<sup>-3</sup>, which verifies the compact space charge layer.<sup>[251]</sup> Defect formation energies and energy level structure are displayed in Figure 4e.

Defect formation energy of LCO and LiPON is  $>3$  and  $0.5$  eV depending on the Li-vacancy/Li-interstitial pairs.

Wang et al.<sup>[252]</sup> reported in-situ visualization of space-charge layers for LCO/Li<sub>6</sub>PS<sub>5</sub>Cl or BaTiO<sub>3</sub>-LCO/Li<sub>6</sub>PS<sub>5</sub>Cl interfaces, in which they verified that the built-in electric field and chemical coupling strategies could minimize the SCL to improve Li-transport across the interface. Gu et al.<sup>[253]</sup> reported the SCL in Li<sub>0.33</sub>La<sub>0.56</sub>TiO<sub>3</sub>, the grain boundary cores have excess Li hosted at the 3c interstitial sites, whereas the bulk structure accommodates Li with A-sites. 2D nuclear magnetic resonance results display the intense Li exchange across the Li<sub>x</sub>V<sub>2</sub>O<sub>5</sub>-LAGP interface at  $x = 1$  without SCL; however,  $x = 0.2$  and  $2$  inhibit the Li exchange due to the presence of SCL.<sup>[254]</sup> If grain boundary defects have the mobile charge density, SCL width is independent of space charge potential (i.e., Gouy-Chapman case); if not, SCL width relies upon space charge potential (i.e., Mott-Schottky case).<sup>[255]</sup> Several approaches have been demonstrated to alleviate space charge layers; however, inserting a buffer layer at the electrodes/SEs is the most suitable approach. Other battery chemistries are not researched for SCL's influence, which might be due to poor storage capacity compared to commercial LIBs.

### 6.3. Interdiffusion

The two adjacent materials mutually diffuse to each other with the formation of interlayers, causing interdiffusion issues, including decomposition or dissolution of SEs, electrodes with high interfacial resistance, severe capacity losses, and rate performances. Elemental interdiffusion during thermal processes and electrochemical cycling is the decisive concern. Thermal methods are utilized to fabricate electrode materials, which typically facilitates cross-over among the electrodes and SEs with an elemental exchange or interphase formations along with SEs/electrode interfaces. Miara et al.<sup>[256]</sup> reported the chemical compatibility for spinel cathodes (LiCoMnO<sub>4</sub>, Li<sub>2</sub>FeMn<sub>3</sub>O<sub>8</sub>, Li<sub>2</sub>NiMn<sub>3</sub>O<sub>8</sub>) and SEs (Li<sub>6.6</sub>La<sub>3</sub>Zr<sub>1.6</sub>Ta<sub>0.4</sub>O<sub>12</sub> and Li<sub>1.5</sub>Al<sub>0.5</sub>Ti<sub>1.5</sub>(PO<sub>4</sub>)<sub>3</sub>) during thermal processing, which exhibits spinel cathodes incompatible with Li<sub>6.6</sub>La<sub>3</sub>Zr<sub>1.6</sub>Ta<sub>0.4</sub>O<sub>12</sub> and Li<sub>1.5</sub>Al<sub>0.5</sub>Ti<sub>1.5</sub>(PO<sub>4</sub>)<sub>3</sub> over  $600$  °C due to the formation of ionically insulating interphase with high interfacial resistances. Xu et al.<sup>[257]</sup> reported that the interface of LiMn<sub>2</sub>O<sub>4</sub>-Li<sub>0.33</sub>La<sub>0.57</sub>TiO<sub>3</sub> displays an interdiffusion region of  $300$  μm including Mn, La, and Ti for  $900$  °C. Such interdiffusion is observed for spark plasma and co-sintering processes that verify 40 times higher interfacial impedances. Zhang et al.<sup>[258]</sup> reported interdiffusion of transition metals for LiNi<sub>0.85</sub>Co<sub>0.1</sub>Mn<sub>0.05</sub>O<sub>2</sub>/Li<sub>6</sub>PS<sub>5</sub>Cl configuration. Cryo-TEM results show a  $10$  nm thick amorphous layer containing K, Mn, Co, Ni, and O elements during cycling. Loss in energy from  $12$  to  $8.7$  eV (bulk CE) and  $10.8$  eV for interface region verifies the diffusion of Mn, Co, or Ni in +4 to +3 and +3 to +2 states. Kim et al.<sup>[259]</sup> reported that interparticle diffusion through the graphite electrode interface can enhance the energy density and rate capacity. Besides, anode/SEs also show interdiffusion for LCO/Li<sub>3</sub>PO<sub>4</sub>/Si cells. The initial state did not show interdiffusion elements, whereas the first lithiation of the Si anode displays the transfer of Si in SEs, which deteriorates the capability of active materials.<sup>[260]</sup> The diffusion of P and S from SEs to cathode is observed for LiNi<sub>0.8</sub>Co<sub>0.15</sub>Al<sub>0.05</sub>O<sub>2</sub>//75Li<sub>2</sub>S-22P<sub>2</sub>S<sub>5</sub>-3Li<sub>2</sub>SO<sub>4</sub> inter-

face illustrating higher interface impedance. The buffer coating of LiInO<sub>2</sub> and LiInO<sub>2</sub>-LiI over cathodes prevents interdiffusion by reducing interface resistance.<sup>[261]</sup> Similarly, interdiffusion is observed for Na, Mg, K, and Zn ion battery chemistries.<sup>[262–265]</sup> Various approaches have been reported to prevent interdiffusion; however, artificial buffer layer loading is often promising. **Table 2** demonstrates the summary of buffer layer materials for different battery chemistries.

### 6.4. Lattice Mismatch

Lattice mismatch typically occurs for all interfaces (SEs/anode or SEs/cathode) with deviation in the microstructures and lattice parameters, which initiates the formation of superlattice and strain/stress that illustrates the high interfacial impedance. Generally, there are two types of interfaces with lattice mismatch: 1) identical crystal structures and analogous lattice parameters that enable the fastest metal-ion transport. 2) Strong deviation in the lattice and crystal structures shows complex metal-ions transfer. Thus, the minor lattice differences in interface materials exhibit smaller interface impedances with superior ion conductivity than large deviated lattice structures. However, a large deviation in crystal lattices is the present scenario of SSBs. Metal-ions (Li, Na, Mg, Zn, Al, K, Ca) transport relies on different parameters, including ion conductivity, grain boundaries diffusion characteristics, interface impedance, and lattice structures at interfaces. Poor metal-ion transport is ascribed to lattice-mismatched interfaces and meager bulk ion conductivity.

Interface formation energy is the difference between energy sums for two stress-free pristine phases with the same atomic numbers and totally relaxed interface structures. Interface formation energy ( $E_f$ ) with supercell A and B constituents is stated as<sup>[266]</sup>

$$E_f = E_{AB} - N_A E_A - N_B E_B \quad (14)$$

Where  $E_{AB}$  is the total energy for a totally relaxed interface, including supercell  $N_A$  and  $N_B$  units for A and B, respectively,  $E_A$  and  $E_B$  are the energy for pristine A and B bulk structures (without lattice mismatch). Interface formation energy can be divided into interfacial and strain energy relating to the elastic deformation of A and B in the coherent interface as

$$E_f = 2S\sigma + VE_{\text{elastic}} \quad (15)$$

Where  $S$  is the interfacial area,  $E_{\text{elastic}}$  the elastic strain energy per unit volume,  $V$  the volume totally relaxed cell,  $\sigma$  the interfacial energy, and the value two is related to the two interfaces in one interfacial supercell.

Further, the formed interfaces structures are totally relaxed for the external stress-free states, Pristine A and B structures with similar atomic number and interfacial geometry are relaxed for interface normal direction ( $z$ ) with static strain in-plane lattice vectors ( $x$  and  $y$ ), then interfacial energy is,

$$\sigma = E_{AB(xy,z)} - N_A E_{A(z)} - N_B E_{B(z)} / 2S \quad (16)$$

where  $E_{AB(xy,z)}$  is the total energy for interfacial structures.  $E_{A(z)}$  and  $E_{B(z)}$  are the energy per atomic layer of the pure A and B

**Table 2.** Summary of buffer materials for SSBs under different battery chemistries.

Metal ions	Buffer materials	Thickness range (nm)	Deposition method	Remarks
Li <sup>+</sup>	Al <sub>2</sub> O <sub>3</sub> , carbon/graphite, Li <sub>3</sub> N, Li <sub>3</sub> PO <sub>4</sub> , Li <sub>3</sub> NBO <sub>4</sub> , LiTaO <sub>3</sub> , BaTiO <sub>3</sub> , ZrO <sub>2</sub> , ZnO, Ge, Nb, Sn, Bi, Au, Mg, Al, Li <sub>2</sub> SiO <sub>3</sub> , SFC/CNT, Mg <sub>3</sub> N <sub>2</sub> , Li <sub>x</sub> Zn <sub>y</sub>	2–1000	Sputtering, sol-gel, ALD, CVD, PLD, spray, Thermal/ Electron-beam evaporation,	Good chemical stability, Prevent interdiffusion, Severe wetting and dendrites issues, Contact issue, Space charge layer formation
Na <sup>+</sup>	Mg, Ca, carbon, Al <sub>2</sub> O <sub>3</sub> , ZrO <sub>2</sub> , Au, SFC/CNT, Mg clusters, AlF <sub>3</sub> , Na-K alloy	5–50	ALD, PLD, CVD, sputtering	Contact issue, Chemical and electrochemical stability issues, Wetting and dendrites issue, Interdiffusion issue
Mg <sup>2+</sup>	Carbon, Al <sub>2</sub> O <sub>3</sub> , ZnO, Au, Sn, Phytic acid, CNT,	5–100	Sputtering, sol-gel, ALD, CVD, PLD, spray, Thermal evaporation,	Chemical and electrochemical stability issues, Wetting and dendrites issue, Interdiffusion issue,
Zn <sup>2+</sup>	ZnO, ZnS, ZnF <sub>2</sub> , MXene, CNT, polymers, graphene, carbon, graphite, NC, Ag, MOF, graphdiyne, Polyamide, PAN, PAM, PPA, PAA, Zn-other metal alloys, glue films	5–100	ALD, Immersion, sol-gel, Thermal evaporation	Good chemical and electrochemical stability issues, Prevent dendrites and parasitic reactions, Good surface wetting nature

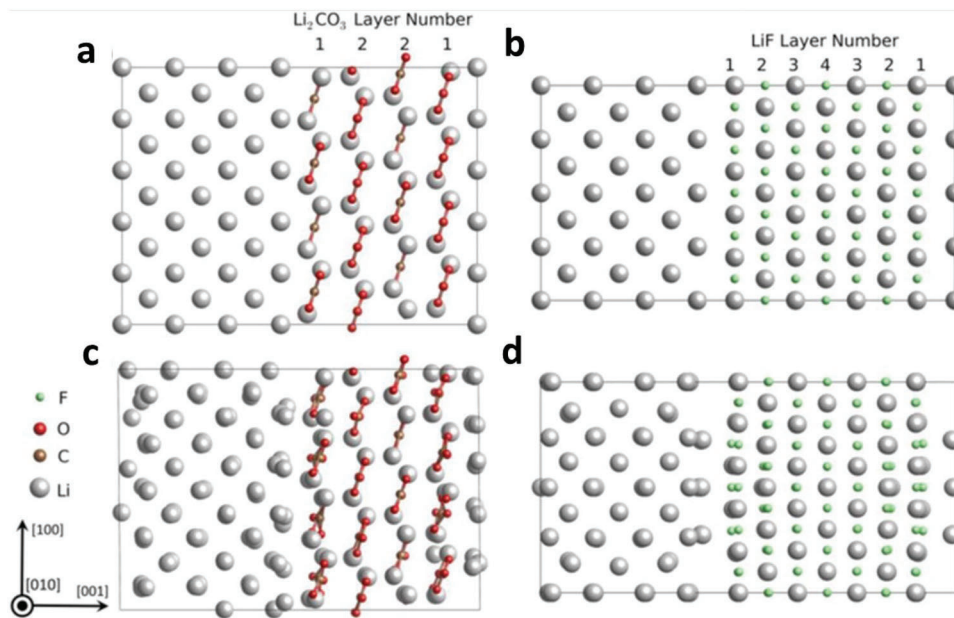


**Figure 5.** Atomic structures. a) as-designed and (b) totally relaxed supercells of Li(001)/Li<sub>2</sub>CO<sub>3</sub>(001) interfaces, (c) as-designed and (d) totally relaxed supercells of Li(001)/LiF(001) interface. Reproduced with permission.<sup>[266]</sup> Copyright 2016, IOP publishing.

bulk structures,  $N_A$  and  $N_B$  are the atomic numbers of A and B interfacial supercells, respectively. The elastic strain energy is

$$E_{\text{Elastic}} = E_f/V - 2S\sigma/V \quad (17)$$

Work adhesion for the interface is

$$W_{\text{Adhesion}} = \gamma_A + \gamma_B - \sigma_{AB} \quad (18)$$

where  $\gamma_A$  and  $\gamma_B$  are the surface energies and  $\sigma_{AB}$  the interfacial energy of the A/B interface.

**Figure 5** displays the interfaces of as-formed (initial) and totally relaxed interfacial super cells (final) for Li(001)/Li<sub>2</sub>CO<sub>3</sub>(001) and

Li(001)/LiF(001).<sup>[266]</sup> Li<sub>2</sub>CO<sub>3</sub>/Li interface shows severe structural changes relative to LiF/Li, which illustrates the larger distortions of CO<sub>3</sub> close to the interface region. The angle for the CO<sub>3</sub> group and interface is denoted as  $A(\text{CO}_3\text{-}010)$  to evaluate the structural relaxation of the Li<sub>2</sub>CO<sub>3</sub>/Li interface.  $A(\text{CO}_3\text{-}010)$  displays a large disparity due to the mismatching of Li<sub>2</sub>CO<sub>3</sub> and Li lattices. For interfacial supercell [Li(001)/Li<sub>2</sub>CO<sub>3</sub>(001)], the  $A(\text{CO}_3\text{-}010)$  varied from 16.8 to 22.7° for interface layer 1. Further, it converges to 20° for layer 2 closer to bulk Li<sub>2</sub>CO<sub>3</sub> (18.6°). For interfacial supercell [Li(110)/Li<sub>2</sub>CO<sub>3</sub>(001)] the deviation of  $A(\text{CO}_3\text{-}010)$  is even higher, (i.e., 17.8 to 27.1° for layer 2). Under vacuum,  $A(\text{CO}_3\text{-}010)$  is closer to bulk values for layer 2, and the work function is united for >4 layers of Li<sub>2</sub>CO<sub>3</sub>. Large distortions for the relaxed

Li(001)/Li<sub>2</sub>CO<sub>3</sub>(001) structures ascribed to prominently different lattice structures [Li metal (bcc) and Li<sub>2</sub>CO<sub>3</sub> (monoclinic)]. For the cubic Li interface, CO<sub>3</sub> tends to decrease the angle with minimizing the total energy. Notably, limited Li ions transport from SEs to anode during charging cycles, the nucleation of undesirable Li dendrites, and growth in SEI have been observed for Li<sub>2</sub>CO<sub>3</sub>/Li relative to those of LiF/Li interfaces. Yan et al.<sup>[267]</sup> stated that the grain boundary resistance is formed for crystalline LLTO matrices interfaces with limiting Li-migration due to structural and chemical deviations for random orientations of adjacent LLTO grains. Lattice mismatch in Li<sub>0.33</sub>La<sub>0.56</sub>TiO<sub>3</sub> with NdGaO<sub>3</sub> substrate for a- and b-axes directions provides the anisotropy in the ionic conductivity.<sup>[268]</sup> Lithiation-induced volume changes will also illustrate lattice mismatch for electrode/SEs during cycling; ion mass transfer disrupts mechanical integrity for both interfaces. Interface lattice mismatch severely causes local structural distribution at the interface, decreasing the cells overall performance. The most promising approach to minimize the lattice mismatch is utilizing the high structural similarity materials in SEs and electrodes and constructing epitaxial interfaces.

## 6.5. Dendrites Growth

Metals (Li, Na, K, Zn, Mg, Al, Ca) are the ideal anode materials for battery chemistries due to their higher intrinsic capacities; however, dendrites formation severely influences the operation capability of their cells. The dominant cell failure mechanism is the penetration of dendrites along the grain boundaries. The probable mechanisms for dendrites nucleation for SPEs and SIEs are as follows. 1) Dendrites grow at the tip and penetrate through a soft part of SPEs, 2) lateral growth of dendrites and prolongs as of the electrode sites and SPEs, 3) subsurface structures triggered the formation of dendrites, 4) Redistribution of charges for metal/SPEs interface induces the dendrite formation. 5) Discontinuous interfaces contacts persuaded dendritic growth (i.e., surface microstructure, defects, voids, and density of SIEs), 6) grain boundary persuaded dendritic growth (i.e., grain boundaries create the metal propagation in the SIEs), 7) Electrons as of residual conductivities, pore surface, and oxygen framework encourages the metal clusters formation in the SIEs, and 8) Enriched electric field along the tips because of highly stable chemical interface among the SIEs and metals causes the dendritic growth (i.e., Interphase effect).

Brissot et al.<sup>[269]</sup> reported the needle-like dendrites at the tip during eventually increased electrodeposition time for symmetric Li|polymer|Li cells, which can penetrate the PEO-based SPEs due to the high ionic concentration of electrolytes. Monroe and Newman<sup>[270]</sup> explained the dendrite growth model based on the surface energy and tip-curvature control for parallel Li|polymer|Li cells. Li deposition probably occurs for dendrite tips because of the faster accumulation of electric charges relative to smoother regions. Once activated, grown dendrites penetrate through SPEs even for low current density and enlarged distance among the electrodes. Considering the elastic deformation, all the factors, including the surface tension, deformable force across the interface, and compressive forces, contribute to the interfacial stability. The shear modulus of the separator (SPEs) is equal to the modulus of Li, which can form a stable interface. In con-

trast, if the shear modulus of SPE is two times higher relative to the Li, then dendritic growth will be mechanically suppressed. Dolle et al.<sup>[271]</sup> reported lateral growth of dendrites for the Cu/polymer/Cu system, leading to delamination among the electrodes and SPEs. Harry et al.<sup>[272]</sup> reported that the dendrite growth process for Li/SPEs reveals the reconstruction of volumes with dendrites buried under electrodes without residing in the electrolytes initially. Zhou et al.<sup>[273]</sup> reported the redistribution of charges, in which lower Li transfer numbers and rapid depletion of anions in SPEs create the double-layer electric field across the Li/SPEs interface, illustrating the decomposition of electrolytes, nucleation of dendrites, and interface instability. Cheng et al.<sup>[274]</sup> reported the inter-granular Li metal propagation via structure-distributed grain boundaries for Li<sub>6.25</sub>Al<sub>0.25</sub>La<sub>3</sub>Zr<sub>2</sub>O<sub>12</sub> SIEs owing to the larger grain boundary resistance, lower shear modulus, and stoichiometric variation than bulk grains. Yu and Siegel reported the transport properties, energetics, and composition for Li<sub>7</sub>La<sub>3</sub>Zr<sub>2</sub>O<sub>12</sub> symmetric tilted grain boundaries. Li transfer in grain boundaries is highly challenging compared to bulk grains and highly sensitive to temperatures and boundary structures.<sup>[275]</sup> Sastre et al.<sup>[276]</sup> reported that the amorphous phase of Li<sub>7</sub>La<sub>3</sub>Zr<sub>2</sub>O<sub>12</sub> creates the Li dendrite shield due to grain boundaries free microstructures. Li stoichiometry variation increases four times higher ion conductivity with minimal electronic transfer. Notably, the Li-plating/stripping should be considered lower than those of critical current density (CCD), which is 0.5–1 mA cm<sup>-2</sup>. Beyond CCD exhibits dendritic growth and penetration via SEs. Insertion of buffer layers significantly improves the interfacial properties. Various types of buffer layers such as Al<sub>2</sub>O<sub>3</sub>, carbon/graphite, LiF, Li<sub>3</sub>N, Li<sub>3</sub>PO<sub>4</sub>, Li<sub>3</sub>NBO<sub>4</sub>, LiTaO<sub>3</sub>, BaTiO<sub>3</sub>, ZrO<sub>2</sub>, ZnO, Ge, Nb, Sn, Bi, Au, Mg, Al, SFC/CNT, Mg<sub>3</sub>N<sub>2</sub>, and Li<sub>2</sub>SiO<sub>3</sub> have been reported as compatible materials for superior interfacial reactions that prevent the Li-dendritic growth.<sup>[277–288]</sup>

Hundekar et al.<sup>[289]</sup> reported that the K-metal undergoes hemispherical depositions for low current density (0.01 mA cm<sup>-2</sup>), a charge-transfer controlled reaction. WI increase in current, the nuclei for dendritic growth initiates with diffusion-controlled reactions. These dendrites are more densely packed, showing decreased diameter with current density. For 2 mA cm<sup>-2</sup>, the K morphology is smoother and non-dendritic in nature. For 1.5 mA cm<sup>-2</sup>, partial dendritic structures are observed. Davidson et al.<sup>[30]</sup> reported the formation of Mg dendrites with enriched Mg and a trace of Cl. Nano-indentation exhibits that the Mg dendrites have an elastic modulus of 27.1 ± 2.8 GPa, which is extremely higher than Newman and Monroe criterion for shear modulus, showing penetration for polymers. Kwak et al.<sup>[290]</sup> reported the operando visualization for Mg morphology evolution. Mg depositions microsized spherical particles from 50–83 μm diameter for 2 and 5 mA cm<sup>-2</sup> current density. However, fatal Mg dendrites are observed for 10 mA cm<sup>-2</sup>. Mg dendrites are sparsely formed in micrometer-scale branches, increasing with high current densities of 20 and 50 mA cm<sup>-2</sup> with fast growth rates.

Al dendrites are typically formed due to inhomogeneous Al electrodeposition resulting from numerous nucleation sites that originated from disruptions in Al<sub>2</sub>O<sub>3</sub> passivation under different electrolytes.<sup>[291,292]</sup> Unlike Li-cells SEI, the Al<sub>2</sub>O<sub>3</sub> is an inorganic phase, which inclines anisotropic cracks with lower Al redox potentials. AlCl<sub>4</sub><sup>-</sup> anions dominate the charge transport instead of



$\text{Al}^{3+}$ , which unsurprisingly drops the ion transport efficiency in the electrolytes and cathodes.<sup>[293]</sup> Al dendrites are topologically branched for 2D structures. The sluggish ion diffusion mechanism of anion-type charge carriers with lower ion supply is challenging to address the moss-like dendrites.<sup>[294,295]</sup> For Zn depositions, Zn ions closer to the Zn electrode surface transfer to nucleation sites with the action of the electric field. Obtained electrons from the Zn anode are deposited on the nucleation sites by overpowering the Zn nucleation energy barrier (i.e., overpotential > nucleation energy barrier). Zn ions will diffuse to energy-favorable sites with forming Zn cores at lower current densities. For high currents, Zn ions display more considerable concentration gradients with uneven nucleation of Zn. In addition, the concentration of zinc ions near the zinc anode is related to the current density. When the current is high, the concentration gradient of zinc ions between the reaction zone and the bulk solution will occur, which is more conducive to the uneven nucleation of zinc. After nucleation, Zn ions are continuously reduced and plated for nucleation sites; Zn will accumulate on the electrode surface during cycling, which has random deposition due to concentration gradient and electric field. Such polarization shows the deviation in the potential for electrodes from equilibrium potential with reduction and accumulation of Zn for the tips of electrodes with higher electric field strength. Due to the abundance of charges over the tips, the uneven Zn depositions will be formed with boundaries, impurities, and dislocations defined as dendrites. Yufit et al.<sup>[296]</sup> reported formation and dissolution kinetics for Zn dendrites, in which dendrites are initiated due to high local current density. Dendrites morphology strongly depends on the electrolyte kinetics (liquid: acid, alkaline, neutral, organic, solid, gel, etc.). Introducing artificial buffer layers among the electrode/electrolytes is a versatile strategy to diminish the interfacial issues for different metal chemistries from Mg, Na, Al, Zn, K, Ca, and Li, as understood from the above discussion (Table 2).<sup>[297–306]</sup>

## 6.6. Li-Immobilization Interlayers

Interlayer construction immobilizes transferable Li-ions from the electrodes, which illustrates a loss in storage capacity. Chen et al.<sup>[260]</sup> reported the formation of a Li-immobilization interlayer for the Si/ $\text{Li}_3\text{PO}_4$  interface by operando neutron depth profiling, in which Si transfers in the  $\text{Li}_3\text{PO}_4$  to generate Li-Si-P-O SEI. However, such an interlayer includes immobilized mobile Li-ions unavailable for cycle operations. These interlayers typically occur under the lithiation process only. In principle, the Li-immobilization interlayer will not influence transport kinetics if enough Li ions are available in SEs and the conduction of  $\text{Li}_3\text{PO}_4$  by hopping kinetics. The Si/LiPON/LiCO batteries show the disordered interlayer at the interface between the LiCO and LiPON. LiPON deposits influence the disordered interlayer under  $\text{N}_2$ -supported Ar unfavorably compared to the  $\text{Li}_3\text{PO}_4$  deposition on the LCO surface under Ar. Disordered interlayers containing  $\text{Li}_2\text{O}$  and  $\text{Li}_2\text{O}_2$  are poor conductive relative to LiPON, which degrades the SSBs' performances.<sup>[307,308]</sup> In summary Li-immobilization interlayer is formulated due to electrochemical reactions at the interfaces that strongly influences by synthesis parameters and materials chemistry.

## 6.7. Current Collectors/Electrode Interfaces

Current collectors (CC)/electrodes interface (external circuit's electrical conductance) strongly influences the metal-ion transport kinetics, including Li, Na, Zn, Al, K, Mg, Ca, etc. Primary requirements of current collectors: 1) Electrochemical stability- CC should be stable for reduction and oxidation electrochemical reactions during discharge/charge processes. High voltage is typically favorable for high-energy cells that need high/low electrochemical potential for cathodes/anodes. 2) Electrical conductivity- All batteries proceed by the sizeable electronic conductivity of CC. During operations, generated electrons transfer via CC to external circuits. It reveals the electrical conductivity of CC and CC/electrode interface illustrates the lower transfer of chemical/electrical energy in thermal runaway during cell charge/discharge steps, which displays high energy and capacity efficiencies. 3) Mechanical strength- typically, electrodes are prepared using a slurry coating, which means CC are mechanical supports. Under cell operations, the volume change of electrodes causes delamination or pulverization; thus, CC with high mechanical strength can retain the integrity of active materials. 4) Density- Generally, CC are electrochemically inactive materials, and utilized cell weight by CC is 20%. Thus low-density CC is highly favorable to enhancing energy density. 5) Sustainability and cost.

There are different types of CCs, including Al (foil, mesh, foam, etched, carbon/graphene oxide-coated, Mn and Al oxide composite coated, chromate-coated, graphene-coated for various cathodes (LCO, LFP, LNMO, NMC111, LMO,  $\text{TiO}_2$ , NMC811, NMC622, NCA), **Figure 6**). Kanamura et al.<sup>[309]</sup> showed a comparison of LNMO for Al mesh and foil CC; however, both displayed  $130 \text{ mAh g}^{-1}$  capacity. Al foam allows excess mass loading of  $42 \text{ mg cm}^{-2}$  with an areal capacity of  $7 \text{ mAh cm}^{-2}$ , three times higher relative to Al foil  $12 \text{ mg cm}^{-2}$  ( $2 \text{ mAh cm}^{-2}$ ).<sup>[310]</sup> Al CC thickness is also varied from 25 to  $10 \mu\text{m}$  to obtain high energy, in which Sony LIBs reported  $12 \mu\text{m}$  Al thickness shows gravimetric and volumetric energy of  $246 \text{ Wh kg}^{-1}$  and  $665 \text{ Wh L}^{-1}$ , whereas  $15 \mu\text{m}$  thick Al results in  $196 \text{ Wh kg}^{-1}$  and  $552 \text{ Wh L}^{-1}$ . Low Al thickness severely affects the power density due to decreased heat transfer property and electrical conductivity.<sup>[311,312]</sup>

Yoon et al.<sup>[313]</sup> reported Al surface etching for mixture of NaOH,  $\text{Na}_2\text{CO}_3$ ,  $\text{C}_6\text{H}_{11}\text{NaO}_7$  and NaOH,  $\text{NaNO}_3$ , and  $\text{C}_6\text{H}_{11}\text{NaO}_7$  for 10 and 70s. It shows four times higher discharge capacity for high C-rates than those of pristine Al, ascribed to increased adhesion among the CC and electrodes, decreasing the charge transfer resistance due to the high rough surface. Such strong adhesion avoids the peeling of cathodes and increases surface hydrophilicity. Crystal orientations and surface properties of CC will significantly modify the cell cycle operations. Wu et al.<sup>[314]</sup> reported three types of Al current collectors, such as unetched Al, etched Al with carbon coating, and etched Al without carbon, in which they observed that etched Al with carbon layer has lower resistance and superior cycle capacity relative to those of other current collectors. Further, Cu and Cu with carbon coating reveal interfacial resistance and capacity of  $\text{Li}_4\text{Ti}_5\text{O}_{12}$  cathodes among the CC, and  $\text{Li}_4\text{Ti}_5\text{O}_{12}$  has the tradeoff as  $\text{Cu-C} < \text{etched-Al-C} < \text{etched-Al}$ . Besides, Cu with conformal graphene facilitates better adhesion with electrodes.<sup>[315]</sup> Nara et al.<sup>[316]</sup> reported interface between the LCO and Al CC with/without carbon coating,

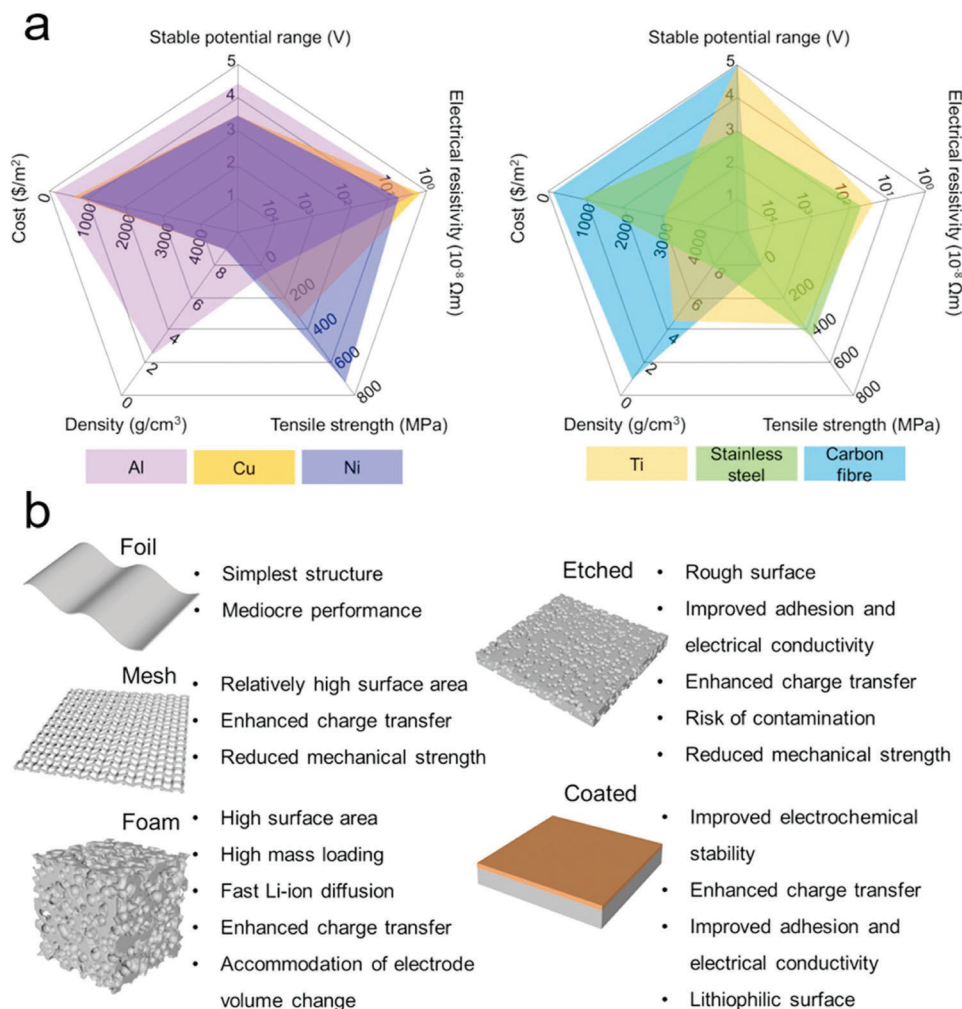


**Figure 6.** a) State-of-the-art for various current collectors. b) Pros and cons for current collectors. Reproduced with permission.<sup>[311]</sup> Copyright 2021, Elsevier.

in which pristine Al CC with LCO showed high resistance with poor contacts, and carbon coating with pressure had a superior interface with lower resistance. Shinde et al.<sup>[191]</sup> reported carbon-coated stainless steel (SS) mesh has superior interfacial performances and adhesion with cathode materials showing high cell capacity for Zn-batteries (1–5 Ah scale).

Samsung and Sony show 10 and 14  $\mu m$  Cu CC thickness that can display gravimetric and volumetric energy of 245, 196  $Wh\ kg^{-1}$  and 657, 552  $Wh\ L^{-1}$ , respectively. Cu CCs are utilized in various forms such as foil, mesh, foam, etched, carbon-, graphene-,  $CuO$ -, Ag-, Ni-,  $ZnO$ -, and PVDF-coated, in which mesh displays high performance due to fast charge transfer kinetics, reduced electrolyte/electrode interface impedance, accommodation of volume change, high surface area lowers the areal current density, and thickness of anode remains unchanged verifying mechanical stability.<sup>[312,317]</sup>

Ni, Ti, SS, and carbonaceous materials are also reported as CC. Regarding electrochemical stability, Ti and carbon fibers have the largest voltage window (0–5 V versus  $Li/Li^+$ ), which can be utilized for both anode/cathode CCs. Al ranges from 0.5–5 V versus  $Li/Li^+$ ; however, alloying reaction with Li gets 0 V versus  $Li/Li^+$ .

Cu and Ni have stable windows for 3.5 V versus  $Li/Li$ , and SS has the smallest 0–3 V versus  $Li/Li^+$  window.<sup>[311]</sup> Therefore, Al or carbon fibers and Cu, Ni, or SS are used for cathodes and anodes CCs, respectively, and can be utilized for different battery chemistries (Li, Na, Mg, K, Zn, Al, and Ca).

## 6.8. Thermal Instability

Thermal runaway induces exothermic thermochemical and electrochemical reactions due to increased battery temperature. The major parameters for thermal runaway are; 1) Electrical exploitation (over-charge or discharge), 2) Thermal explosion, 3) Mechanical exploitation, and 4) Internal short circuit. Spotnitz and Franklin reported a 1-D model to evaluate the thermal runaway exothermic reactions as; SEI layer decomposition occurs for 90–120  $^{\circ}C$ , intercalation reactions with electrolytes  $>120\ ^{\circ}C$  or fluorinated binders, decomposition of electrolytes ( $>200\ ^{\circ}C$ ), decomposition of cathode active materials, overcharge provides the reaction of Li metal to electrolyte, binder reactions with Li, and discharge of cells releases heat owing to ohmic

hesitance, overpotential, and entropy change.<sup>[318]</sup> Utilizing thermally responsive materials such as separators, electrolytes, and temperature-sensitive electrodes for retaining safety issues is the most promising approach. PM-PP, PSS, PBI/PE/PBI, PE-coated PET, EVA-coated PP, PS-co-PBA@SiO<sub>2</sub> coated PP, PE coated anode, paraffin coated electrodes, SEPs/SEs, carbon-black-polymer, or Ni-PVDF composites, P3OT coated CC with ion-blocking, phase transition, and PTC effect kinetics are reported materials to resolve thermal-responses up to 100–140 °C.<sup>[319–322]</sup>

## 6.9. Chemical Reactivity of SEI

SEI is mainly derived by metal and electrolytes electrochemical reactions, which composition depends on the utilized types of electrolytes. Typically, SEI is a mixture of inorganic metal salts (Li, Mg, Na, K, Zn, or others) and organic species; however, their precise distribution and stoichiometries remain a mystery. For example, Li<sub>2</sub>O, LiF, Li<sub>2</sub>CO<sub>3</sub>, Li<sub>2</sub>S, and Li<sub>3</sub>N are the Li-salts, in which LiF is magical salt to realize stable anodes.<sup>[323]</sup> Analysis of SEI is highly challenging due to the thickness (10–100 nm) and sensitivity of SEI for high-energy radiations.<sup>[324]</sup> Li<sub>2</sub>O crystal of SEI acts as nucleophilic agents for the initiation of decomposition of ester electrolytes solvents that explains the mosaic structure of SEI. In contrast, alkyl carbonate Li salts decompose to Li<sub>2</sub>CO<sub>3</sub>, influencing SEI chemical stability. Ideal SEI criteria in terms of kinetics and thermodynamics are as follows. SEI should retain superior metal-ion conductivity for kinetics prospects to enable fast metal-ions transfer kinetics and redox reactions (dissolution or deposition). Homogeneous large ion conductivity is required for uniform chemical distribution and thickness. It can result in spherical or columnar structures commanding minimal stress for SEI with breakage of SEI and formation of dead metals. SEI should possess thermal and chemical stability during cycle operations for thermodynamics prospects. It should have considerable corrosion resistance against electrolytes and high temperatures and be thermodynamically stable against decomposition to maintain cell capability for extended operations.

The interface between the SEs and metals was predicted to be more stable than those of liquid electrolytes. For example, beta-alumina is utilized SEs for high-temperature Na-S and ZEBRA cells, which has stable SEI.<sup>[325]</sup> Thus, using beta-alumina SEs against molten Na for low temperatures is interesting. The chemical stability windows of SEs are quite limited, so they can also decompose in contact with Li. In general, Li and SEs include the generation of Li<sub>2</sub>S, Li<sub>3</sub>P, or Li<sub>2</sub>O binary compounds with the reduction of metal cations. For example, Ti or Ge in NASICON, Li<sub>2</sub>S, Li<sub>3</sub>P, Ge/Ge<sub>4</sub>Li<sub>15</sub> in LGPS, Li<sub>2</sub>S in Li<sub>3</sub>PS<sub>4</sub> or Li<sub>6</sub>PS<sub>5</sub>Cl, and In, Y, LiCl in Li<sub>3</sub>InCl<sub>6</sub> or Li<sub>3</sub>YCl<sub>6</sub>.<sup>[10,326–331]</sup> Comparatively, oxide SEs have larger EW.<sup>[332]</sup> Theoretically, three types of interfaces for Li and SEs are prominent: 1) thermodynamically stable interface (satisfied with binary compounds Li<sub>2</sub>S, Li<sub>3</sub>P, and Li<sub>3</sub>N only; complex electrodes readily reacts with Li owing to high reducing power). 2) Unstable interfaces (continuous degradation due to mixed ion and electron transfer kinetics). 3) Unstable interfaces that are kinetically stabilized but Li ions conductive. For type 3, the interface requires mechanical and chemical compatibility among the Li and SEs. Favorable types form direct SEI in an ideal scenario (e.g., cubic-Li<sub>7–3x</sub>Al<sub>x</sub>La<sub>3</sub>Zr<sub>2</sub>O<sub>12</sub>). The c-LLZO dis-

plays limited reactions with Li regarding developing a tetragonal-LLZO interface, which prolongs merely over 5 unit cells.<sup>[38,333]</sup> Interface engineering with ex-situ or in-situ coatings is a significant approach to enhancing the compatibility of SEs to cathode materials.

## 7. Anode Interface Chemistry

In contrast to commercial LIBs, the battery chemistries with promising high power, energy, and sustainability with low cost are significantly challenging. The alternate working ions are Na, K, Mg, Al, Zn, and Ca. A fundamental understanding of interface chemistries with suitable electrolytes is critical to delve into various anode reactions.

### 7.1. Monovalent-Ions Battery Technologies

#### 7.1.1. Li-Metal Batteries (LMBs)

All-solid-state LMBs are considered one of the most prominent next-generation energy storage technology owing to high energy densities relative to LIBs. LMBs with SEs have two types, inorganic and organic (polymer), in which inorganic SEs are fire-proof, stable, and have relatively high EW compared to polymer or liquids. Electrode's volume change, a low mass ratio of active materials, poor cycle life, and large interface impedance are the fundamental obstacles for SSBs. For higher ion-conductivity of electrode/SEs interface, the diffusion behavior, and ion transport across the interface, mechanical and structural parameters of SEI and SEs with atomic-level understanding are essential. Typically, the elasticity for SEs and electrodes has a prominent influence over physical/chemical contacts for their interfaces. In practice, the complex SEI at the metal surface influences the ion-conduction characteristics of the SEs/anode interface; thus, proper strategies for the protection of anodes are critically necessary to enhance cell performance. After the Li-TiS<sub>2</sub> system, Li-metal has been considered one of the ultimate anodes due to its theoretical capacity (3860 mAh g<sup>-1</sup>) and minimal redox potential.<sup>[334–336]</sup> However, the severe dendritic growth causes poor interface stability and safety concerns. In the 2000s,<sup>[337]</sup> it was concluded that Li metal is not suitable anode material for rechargeable batteries; however, recently, the research community has revival interest in high-energy Li-metal batteries. Typically, preventing dendritic growth is extremely problematic since it initiates from the nanoscale roughness of surfaces, in which the entered Li ions deposit preferentially over sensible piercing tips and protrude the morphology for intrinsic Li-metal surfaces. Several reports stated that the formation of elastic SEI has a great extent for blocking the open spaces and exerting pressures to suppress interfacial parasitic reactions.

LMBs with SPEs have benefits for ease of fabrication with flexibility and safety, in which instability for electrodes/SEs interface and poor electrochemical working conditions are major restrictions. Polymers displayed in Table 1 are the several options; however, their poor electrochemical stability with high voltage cathodes such as LCO, LMNO, and NMC cannot show the proper pairing. Mixed SPEs and SIEs (polymer/inorganic/polymer or

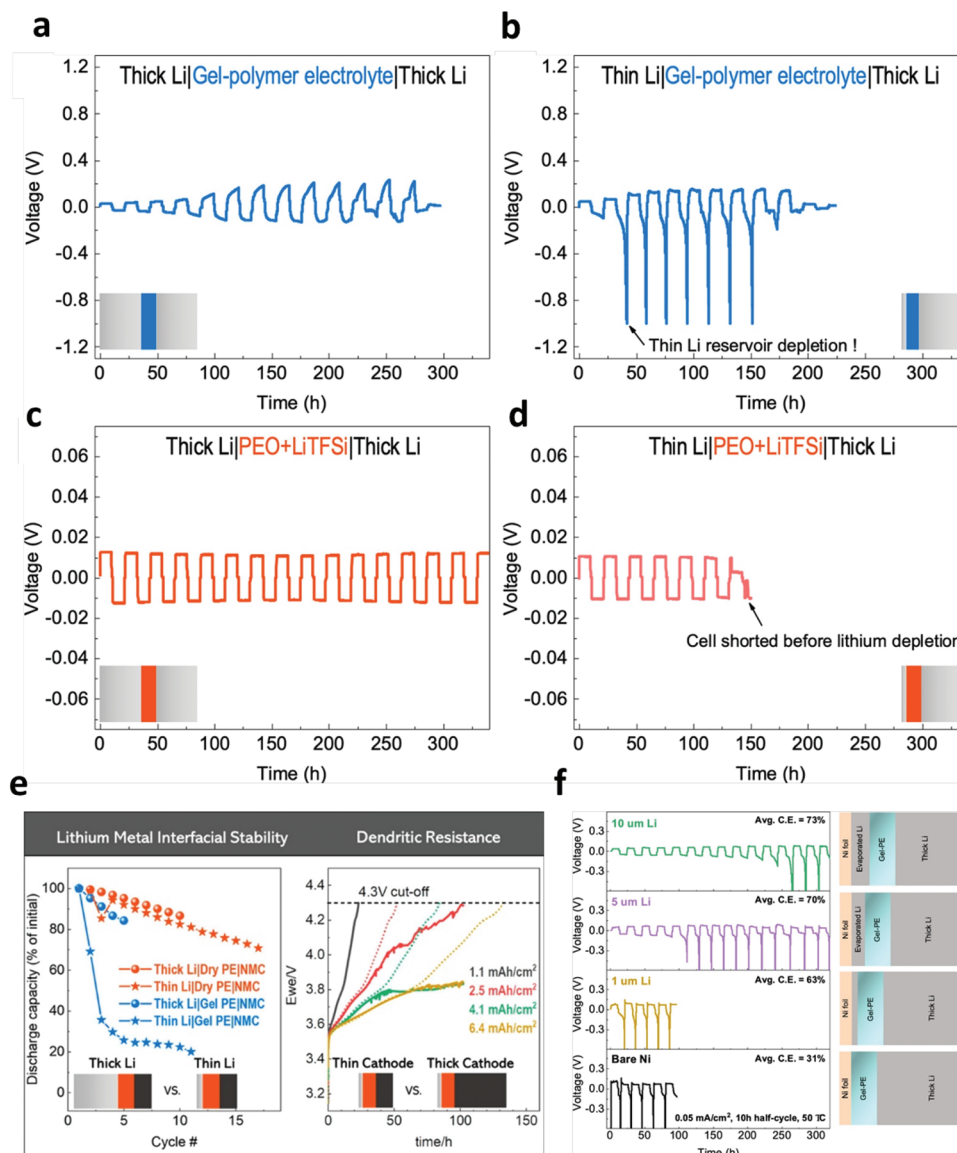


**Figure 7.** a, c) Voltage profile for Li plate/strip under GPE and SPEs (PEO+LiTFSI) electrolytes for thick  $\approx 600 \mu\text{m}$  Li. (b, d) Voltage profile for Li plate/strip under GPE and SPEs (PEO+LiTFSI) electrolytes for thin  $\approx 13 \mu\text{m}$  Li. Current density  $0.05 \text{ mA cm}^{-2}$ . e) Discharge capacity with cycle numbers (left) and charge voltage profiles of Li/PEO+LiTFSI/NMC811 (right). f) Quantification of Li losses. Reproduced with permission.<sup>[338]</sup> Copyright 2021, American Chemical Society.

polymer/inorganic) offer improvement for ASS LMBs due to adjusting the double-layer electric field at the interface with blocking anions transport. Sahore et al.<sup>[338]</sup> evaluated Li metal stability under PEO+LiTFSI SPEs and PEO-PEGDME-LiTFSI-LiAlTiPO<sub>4</sub> GPEs (Figure 7a–d). Thick Li//Li (600  $\mu\text{m}$ ) cells display an increased overpotential of 0.03–0.2 V without exceeding the cutoff limit of  $\pm 1$  V. Upon replacing thin Li (10  $\mu\text{m}$ ), the 2<sup>nd</sup> strip cycle itself reaches the cutoff limit of  $\sim 1$  V with depletion of entire thin Li for SEI formation owing to reductive reactions of GPE with creating dead Li, which illustrates the incompatibility of GPE for realistic LMBs. For SPEs, thick and thin Li displays minimal impedance growth without increasing overpotentials. Li//PEO-LiTFSI//NMC811 cells display an increase in areal capacity from 1.1–6.4  $\text{mAh cm}^{-2}$  among the 3–4.3 V versus Li/Li<sup>+</sup> illustrating

low capacity (1.1  $\text{mAh cm}^{-2}$ ) reaches cutoff of 4.3 V for 1<sup>st</sup> charge without soft/hard shorts. For  $> 4 \text{ mAh cm}^{-2}$  capacity shows severe shorts without a higher state of charge due to poor rate of de-/intercalation of Li (Figure 7e). For pristine Ni, overpotential reached for cutoff at 1<sup>st</sup> cycle, 1, 5, and 10  $\mu\text{m}$  thick Li reservoir hits 1<sup>st</sup>, 5<sup>th</sup>, and 12<sup>th</sup> strip cycles with CEs of 63, 70 and 73%, which is extremely poor for practical cells (Figure 7f).

Wang et al.<sup>[339]</sup> proposed high-strength and ultrathin (10  $\mu\text{m}$ ) poly(methyl methacrylate)–polystyrene based m-PPL SPEs with ion-conductance of  $34.84 \text{ mS cm}^{-1}$  and 103 MPa shear modulus. Li//Li cells demonstrate stable operations for 1500 h for 60 °C verifying better interface compatibility with Li metal. Theoretical calculations clarify the coordination numbers of Li<sup>+</sup>-ions nearby (trifluoromethanesulfonyl)imide (TFSI<sup>−</sup>) pairs and ethylene-oxide



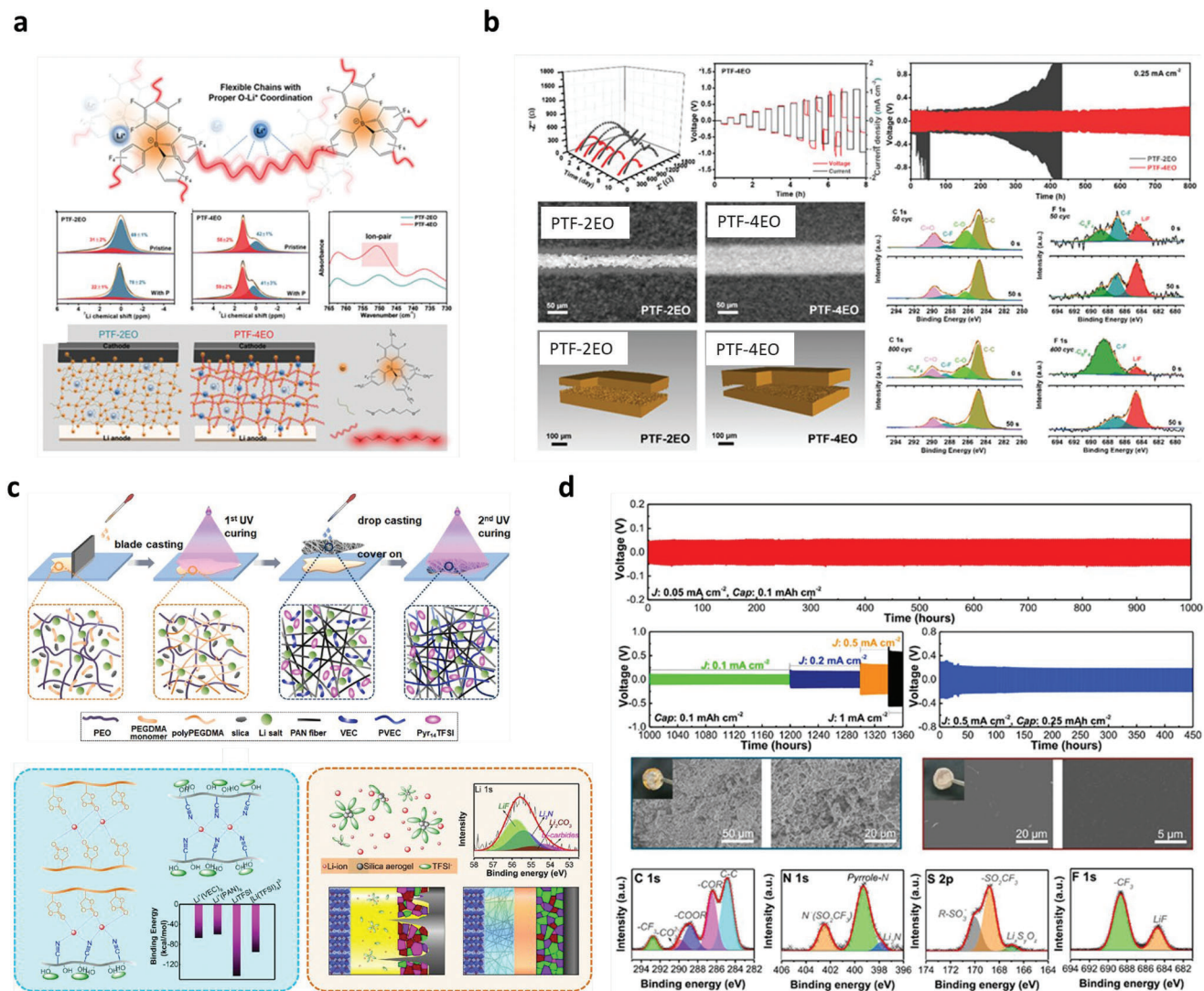


**Figure 8.** a) Structures characterizations for PTF-4EO and PTF-2EO. The blue or light blue balls show mobile Li<sup>+</sup> ions in SPEs. b) Electrochemical and structural performances under PTF-4EO and PTF-2EO SPEs and XPS spectra of Li-metal under PTF-4EO with/without 50 s Ar etching. Reproduced with permission.<sup>[341]</sup> Copyright 2022, Wiley VCH. c) Synthesis processes and schematic illustration for three possible polymers. Li<sup>+</sup> interaction modes, solvation structures in PSPE, and SEI compositions DLPE and PEO/LiTFSI. The mosaic segments specify SEI constituents for various cells. Green block – LiF; purple block – Li<sub>3</sub>N; wine block – Li<sub>2</sub>CO<sub>3</sub>; pink – Li carbides. d) Electrochemical performances Li/Li cells under DLPE or PEO/LiTFSI and XPS results of Li metal surface with DLPEs. Reproduced with permission.<sup>[342]</sup> Copyright 2020, Elsevier.

chains declines the Li/polymer interface facilitating the Li<sup>+</sup> transfer via polymeric host for PEO-black-phosphorus (BP) CPEs. Adsorption of LiTFSI molecules at BP surface indicates the fading of Li and N atomic bindings with increasing dissociation of Li<sup>+</sup> ions.<sup>[340]</sup>

Figure 8a reports the fabrication of single-ion SPEs by crosslinking lithium tetrakis(4-(chloromethyl)-2,3,5,6-tetrafluorophenyl)borate salt with tetraethylene glycol (PTF-4EO). It has  $\sigma_{Li^+}$  0.35 mS cm<sup>-1</sup>, EW >4.8 V, and Li-ion transfer number ( $t_{Li^+}$  ≈ 0.92).<sup>[341]</sup> The ssMAS NMR demonstrates the 4EO enables diamondoid networks with stable coordination of Li<sup>+</sup>-O for Li<sup>+</sup>-transfer kinetics. Li//PTF-4EO//Li cells show stable interface resistance (760 Ω) relative to those of Li//PTF-2EO//Li (Figure 8b). Mechanical strength and dimension stability verify

the inhibition of Li dendrites from 0.1–1.5 mA cm<sup>-2</sup>. Non-destructive synchrotron X-ray tomographs display a uniform interface without dendrites for PTF-4EO, whereas rough with granular dead Li (dendrites) for PTF-2EO verifies no effective media for Li deposition in PTF-2EO. XPS spectra of C 1s and F 1s display the C-O (286.3 eV), C-F (286.3 and 687.1 eV), and LiF (684.6 eV) due to chemical reactions among the [B(C<sub>6</sub>F<sub>4</sub>)<sub>4</sub>]<sup>-</sup> and Li. The -C<sub>6</sub>F<sub>4</sub> (688.9 eV) specifies the direct incorporation of [B(C<sub>6</sub>F<sub>4</sub>)<sub>4</sub>]<sup>-</sup> anions for the SEI layer, illustrating faster Li<sup>+</sup> transfer for Li/PTF-4EO interfaces. Enhanced intensity of LiF and decreased intensity of C=O and -C<sub>6</sub>F<sub>6</sub> after Ar etching implies the inhibition decomposition of PTF-4EO with LiF formation. Such robust LiF-rich Janus SEI renders long-operations for Li-metal anodes.

Figure 8c explains the fabrication of double-layer polymer electrolyte (DLPE), including poly (ethylene oxide)–silica aerogel polymer electrolyte (PSPE) and poly(vinylethylene carbonate)–ionic liquid polymer electrolyte (PIPE).<sup>[342]</sup> The weaker interactions among the PAN/PVEC and Li-ions promote faster Li-ion transfer due to the release of high free Li-ions from  $[\text{Li}(\text{TFSI})_4]^{3-}$  complex. Such coupling/decoupling balances for  $\text{Li}^+ \dots \text{TFSI}^-$  and  $\text{Li}^+ \dots \text{PAN/PVEC}$  facilitating the superior Li-ion-conductance for DLPE. PSPE with Li realizes regular distributions for immobilized anions for the uniform flux of Li-ions. Li 1s XPS displays enriched cubic-LiF and layered- $\text{Li}_3\text{N}$  SEI phases, which vindicates reversible and stable Li-metal anode compared to those of crack states of PEO or other SPEs. Li//DLPEs//Li cells demonstrate stable polarizations from 0.1 to 1 mA cm<sup>-2</sup> owing to regulation of SEI species with SCL and Li nucleation/deposition (Figure 8d). DLPE displays high mechanical properties such as stress/strain of 5.70 MPa/34.3% relative to those of PEO/LiTFSI (1.28 MPa, 379%) and pristine PAN fibers (4.25 MPa, 30%). SEM images of Li anodes exhibit dense and smoother metal deposits (450  $\mu\text{m}$ ) in which silica aerogel and pyrrolidinium contribute synergistically. Li//PEO/LiTFSI//Li displays severe needles/tree-like dendrites and bulky voids influencing parasitic chemical reactions. XPS for Li//DLPE interface demonstrates  $\text{Li}_3\text{N}$ , LiF, Li<sub>2</sub>SiO<sub>3</sub>, and Li-alkylidene peaks for 397.8, 684.8, 166.8, and 288.9 eV. The dominance of  $\text{Li}_3\text{N}$  and LiF obtains more stable SEI from DLPE-based LMBs than those of  $\text{Li}_2\text{CO}_3$  and Li-carbides-based PEO-based SPEs. Overall, SPEs have several limitations in terms of Li-transport kinetics, poor conductivity, EW, rate capacity, physical-chemical properties for stable Li-electrodepositions, and poor interface for high current density; therefore, the SEs with superior properties are critically required beyond SPEs. He et al.<sup>[343]</sup> presented ultrathin 4.2  $\mu\text{m}$  bilayer SPE (UFF/PEO/PAN/LiTFSI SSE) with porous ceramic frameworks and double-layer  $\text{Li}^+$ -conducting polymer with 0.068 mS cm<sup>-1</sup> ion-conductance and  $t_{\text{Li}^+} \approx 0.5$ . UFF defines the ultrathin, fire-proof framework of ceramics. UFF improves mechanical properties (shear modulus of 175 GPa) and inhibits Li dendrites penetration during operations. Li//Li cells display 4 mAh cm<sup>-2</sup> capacity with 99.3% CE at 1 mA cm<sup>-2</sup>. Li anode SEM shows a rough surface with shorter grains composed of  $\text{Li}_2\text{CO}_3$  and lithium oxides and dead Li with a 32  $\mu\text{m}$  thickness under organic liquid electrolytes (OLE). But, Li anodes with PI and PIL-1 (PVDF+IL+LAGP ( $\text{Li}_{1.5}\text{Al}_{0.5}\text{Ge}_{1.5}(\text{PO}_4)_3$ )): 100:100:22.5) electrolytes exhibit relatively compact surfaces, whereas cracks and bumps are seen for PI electrolytes (Figure 9a–f).<sup>[344]</sup> PIL-1 displayed 10  $\mu\text{m}$  Li deposits implying a significant role of PIL-1 in restraining Li dendrites. PIL-1 demonstrates higher LIF content (61.4% and 67.3%) relative to those of OLE (32.1% and 35%) and PI (50.1% and 55.2%) in accordance with F 1s signal to LiF (Figure 9g). It is well-known that LiF phase is more favorable for SEI and inhibition of Li dendritic growth. LiF shows superiority for regulation of  $\text{Li}^+$  transport due to lower diffusion energy barriers and high surface energies of  $\text{Li}^+$ . Besides, the insulating character of LiF effectively obstructs the tunneling of electrons through SEI. Thus, LiF-enriched SEI anticipates the optimal Li electrodepositions and prolonged operational life.

**Figure 10** demonstrates interface compatibility for Li/PISE,<sup>[345]</sup> which is prepared using poly(methyl vinyl ether-alt-maleic anhydride) (PME) and single-ion lithiated polyvinyl

formal (LiPVFM)/lithium bis(trifluoromethylsulfonyl)imide (LiTFSI) composite salts (defined as polymer-in-salt solid electrolyte, PISE). PISE exhibits  $\sigma_{\text{Li}^+} \approx 0.357$  mS cm<sup>-1</sup> and  $t_{\text{Li}^+} \approx 0.62$ . PISE demonstrates the uniform Li plating/stripping over 1100 h with stable polarization voltage. In contrast, dual-ion displays voltage fluctuations after 400 h and drops for 460 h that illustrate penetration of Li dendrites (Figure 10a). Excellent mechanical strength (3.3 GPa) and  $t_{\text{Li}^+}$  of PISE sufficiently diminish the Li dendrites growth, which suggests good interfacial stability. EIS shows no obvious change for interface resistances even after 10 days (Figure 10b). Flexible SEI for Li/PISE interfaces with stronger LiF (684.9 eV) phase, high ion-conductance, and flat and shiny surface confirms the uniform Li plate/stripping (Figure 10c–h). PISE SPEs are hard to peel off from cycled Li even after several washings, which implies ultra-tight physical/chemical contacts.

**Figure 11** proposed the structural evolution of Li/SPEs interface under the polycaprolactone diol (PCL)/LiTFSI/IL/ $\text{Al}_2\text{O}_3$  (10:4:4:1; PIA-SPE; 0.089 mS cm<sup>-1</sup>;  $T_g = -57.7$  °C), PCL/LiTFSI/IL (10:4:4; PI-SPE; 0.038 mS cm<sup>-1</sup>;  $T_g = -58.2$  °C), and PCL/LiTFSI (10:4; PL-SPE; 0.001 mS cm<sup>-1</sup>,  $T_g = -51.7$  °C) electrolytes.<sup>[346]</sup> Li with PIA-SPE displays stable polarization voltage for 800 h, whereas PA-SPE and PL-SPE degrades for 50 h, illustrating the effect of IL for interface stability. SEM and TOF-SIMS images display the localization of F<sup>-</sup>, LiF<sup>-</sup>, S<sup>-</sup>, and  $\text{Li}_3\text{N}^-$  phases over a dense and smooth interface (Figure 11a–c). Li metal surface with PIA-SPE shows no noticeable difference in color and flat and smooth morphology even after 100 cycles (Figure 11a). In contrast, PL-SPE show dimmed coloration and mossy Li with sharp particles ascribed to dead Li or dendrites that responses the inferior Li plate/strip processes (Figure 11b). TOF-SIMS (Figure 11c) maps display localization of F<sup>-</sup>, LiF<sup>-</sup>, S<sup>-</sup>, and  $\text{Li}_3\text{N}^-$  over the interface. The IL reaction with Li metal forms an artificial SEI layer. The chemical states of F 1s, S 2p, and N 1s exhibit significant distribution. F 1s spectra show the 684.9 and 688.4 eV peaks of LiF and  $-\text{CF}_3$  of TFSI<sup>-</sup>. LiF promotes the ionic carrier concentration and limits electrical transport, contributing to a stable interface (Figure 11d). S 2p exhibits peaks for 167.3 and 163.5 for S=O after lithiation with in situ formed  $\text{Li}_2\text{S}_x$  and 168.7 and 170.1 eV for S=O of pristine TFSI. The 399.1 and 402.2 eV peaks in N 1s XPS are ascribed to the N<sup>-</sup> in TFSI<sup>-</sup> and N<sup>+</sup> in IL, respectively. IL surface has the formation of  $\text{Li}_3\text{N}$  phase at 397.2 eV. Asymmetric Li/Cu cells with PIA-SPE display uniform deposits without dendrites in contrast to liquid electrolytes (Figure 11e,f). Li with EMIM+PMMA (PIL) based SPEs explains the charge-discharge voltage gap of 0.12 V, with plate/stripping over 1600 h with micro-short circuits. PIL shows close contact with Li with a uniform thickness of  $\approx 27$   $\mu\text{m}$  deposits.<sup>[347]</sup> Yuan et al.<sup>[348]</sup> reported flexible thin 16  $\mu\text{m}$  high-strength CPEs with  $\sigma_{\text{Li}^+} \approx 0.1$  mS cm<sup>-1</sup>,  $t_{\text{Li}^+} \approx 0.71$ ) obtaining stable Li/CPEs interface for 1000 h. LCO/Li SSBs display 76.1% capacity retention from 145.3 to 110.6 mAh g<sup>-1</sup>.  $\text{LiNO}_3$  was mixed in CPE as Li metal is incompatible with aliphatic succinonitrile to improve interface stability.

**Figure 12** displays the SEI analysis using cryo-TEM under PEO-LiTFSI SPE (C-SPE) and phosphazene-modified PEO-LiTFSI SPE (P-SPE) with Li anodes. SEI for Li/P-SPE interface demonstrates mosaic structure with  $\text{Li}_2\text{O}$ , LiOH,  $\text{Li}_2\text{CO}_3$ , LiF,  $\text{Li}_3\text{N}$ ,  $\text{Li}_3\text{P}$ , and  $\text{Li}_3\text{PO}_4$  phases, which are known for high Li con-



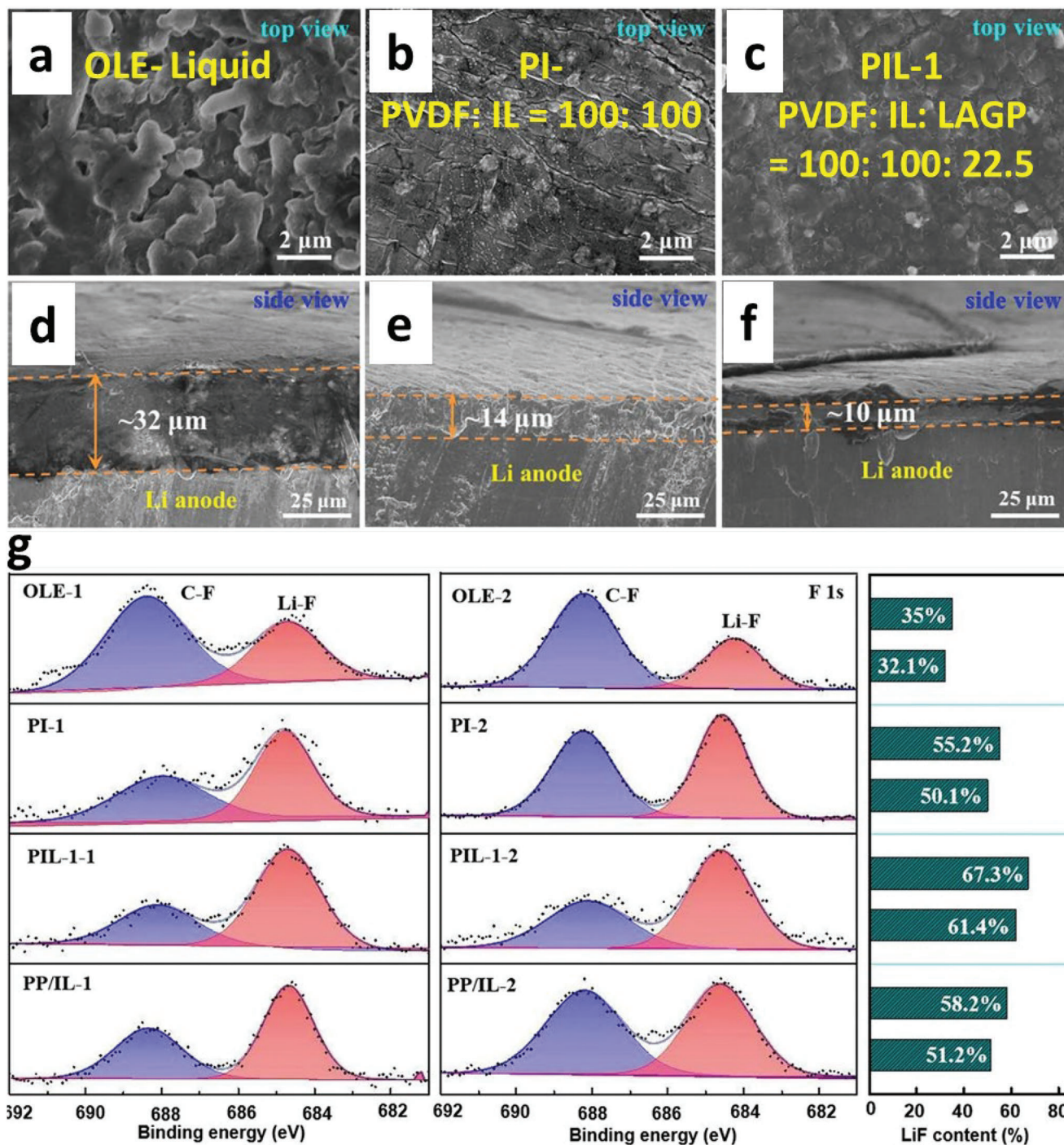


**Figure 9.** SEM images of cycled Li anodes (a, d) OLE (liquid electrolyte), (b, e) PI (PVDF+IL), and (c, f) PIL-1 (PVDF+IL+LAGP) electrolytes, respectively. g) F 1s XPS spectra for Li-metal for diverse electrolytes. Reproduced with permission.<sup>[344]</sup> Copyright 2021, Elsevier.

ductance and superior interface compatibility. FFT patterns display that  $\text{Li}_3\text{N}$ ,  $\text{Li}_3\text{P}$ , and  $\text{Li}_3\text{PO}_4$  have an interplanar spacing of 3.8 Å, 3.3 Å, 3.6 Å, and 5.2 Å with crystal reflections of (001), (101), (010) and (011), respectively (Figure 12a–i).<sup>[349]</sup> P-SPE consists of abundant crystalline phases relative to those of C-SPE. The superior stability of Li with modified SEI components can boost the operational life of LMBs. SEI with C-SPE displays mosaic nanos-

tructures where inorganic Li crystals are implanted inside amorphous organic/polymeric phases. HRTEM and FFT comprise the presence of  $\text{Li}_2\text{O}$ ,  $\text{LiF}$ , and  $\text{Li}_2\text{CO}_3$  by matching the corresponding lattice spacings of 2.3 Å, 3.8 Å, and 2.66 Å, consistent well with (111), (111), and (200) planes, respectively (Figure 12j–r). XPS displays more enriched  $\text{LiF}$  and  $\text{Li}_3\text{N}$  for P-SPE than C-SPE, like TEM, illustrating fast interfacial kinetics (Figure 12s–w).

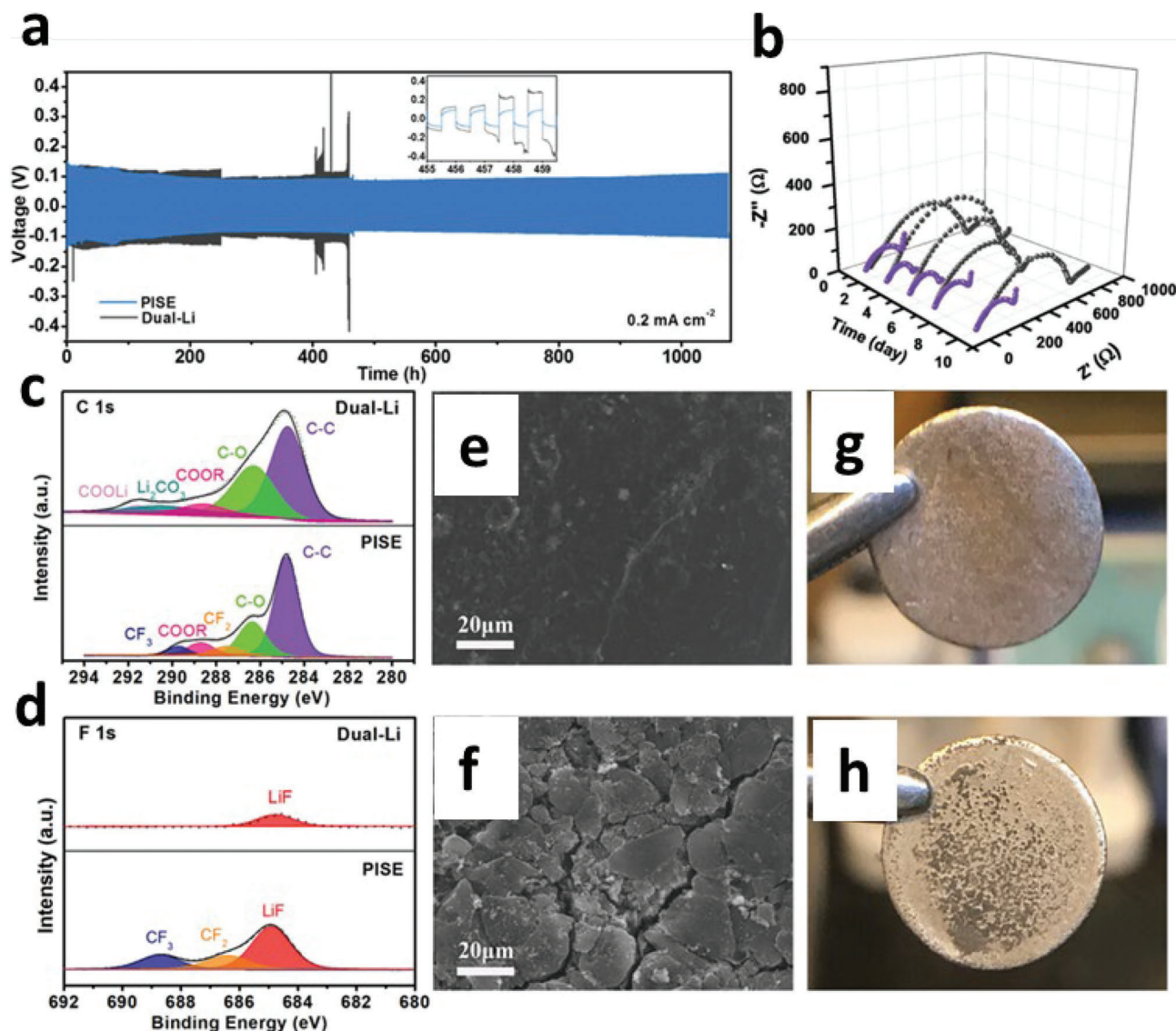


**Figure 10.** a) Voltage profiles for Li//PISE//Li and Li//Dual-Li//Li symmetric cells. b) EIS spectra for Li//PISE//Li and Li//Dual-Li//Li. XPS spectra of c) C 1s and d) F 1s for cycled Li metal for Li//PISE//Li and Li//Dual-Li//Li. SEM image for Li after plate/strip e) 1100 h for Li//PISE//Li and f) 460 h in Li//Dual-Li//Li cells. Photograph of Li metal for g) Li//PISE//Li and h) Li//Dual-Li//Li cells. Reproduced with permission.<sup>[345]</sup> Copyright 2021, Wiley VCH.

LiF-rich and  $\text{Li}_3\text{N}$ -rich interfaces have slow energy barriers for diffusion with promoting homogenous Li-ion flux and transports (Figure 12x). Further, the bidirectional functional polymer electrolytes (BDFPE) with  $\sigma_{\text{Li}^+} \approx 0.58 \text{ mS cm}^{-1}$ ,  $t_{\text{Li}^+} \approx 0.69$ , and 1800 h dendrite-free stable depositions for  $1 \text{ mAh cm}^{-2}$  and  $1 \text{ mA cm}^{-2}$  have also reported by UV solidification processes. Li//BDFPE//NMC622 demonstrates the formation of stable CEI and F-enriched SEI with favorable features for interfacial protection.<sup>[350]</sup>

Li metal deposits under PVDF-PEO/LiTFSI (FPEO) with/without dual-salt of Al/Li have been reported (Figure 13).<sup>[351]</sup> Li metal for single Li-salt displays dendrites with rough (voids/cracks) topography, whereas dual-salts have smooth dendrites-free Li deposits. FPEO firmly adheres to Li

after cycling, providing a favorable adhesive interface that alleviates Li dendritic growth. The residual Li-salt peak (688.9 eV) disappears after sputtering, whereas 685.1 eV peak of LiF increases with sputtering time up to 200 s and then decreases for 500 s, which indicates a LiF-rich SEI layer.  $\text{Al}^{3+}$  and  $\text{Al}_2\text{O}_3$  peaks also disappear upon sputtering. The 75.8, 72.9, and 70.0 eV peaks of  $\text{Li}_x\text{AlO}_y$ ,  $\text{Li}_{1-x}\text{Al}$ , and  $\text{Li}_{1+x}\text{Al}$  species initiate after Al reduction during lithiation reactions. Increased intensity of Li-Al alloy signals after sputtering indicates an alloy-rich layer at the bottom of SEI. TOF-SIMS profiles show a transition of LiF-rich layer to Li-Al-rich layer, verifying the 3D renderings with lithiophilic–lithiophobic gradient SEI that can drastically enhance the Li/SPE interface. Overall, the capacities, rate performances, operating temperature, and cycle life for CPEs are



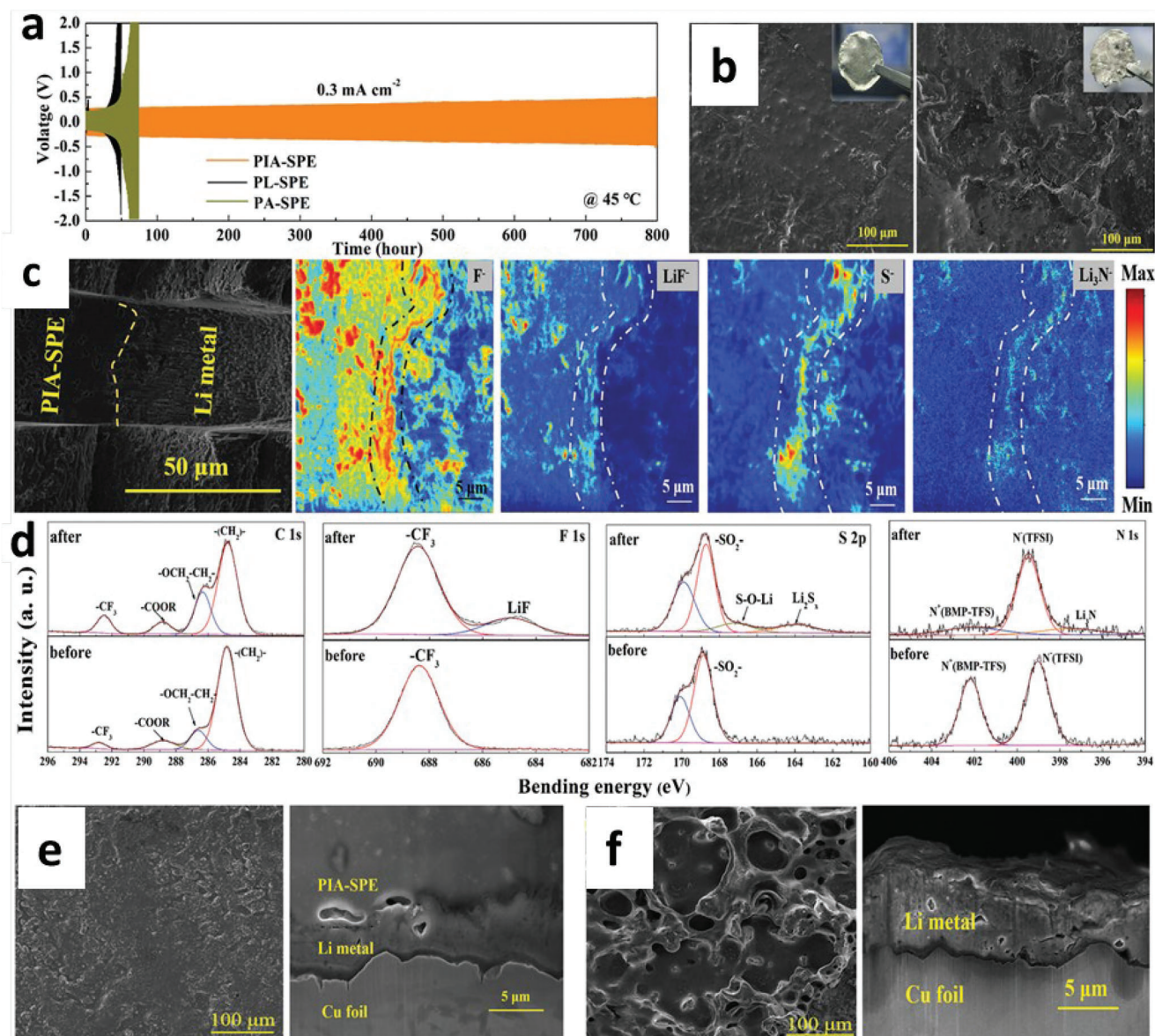


**Figure 11.** a) Symmetric Li cells performance with PIA-SPE, PL-SPE, and PA-SPE. b) SEM images of cycled Li for PIA-SPE (left) and PL-SPE (right). Photographs are in the inset. c) SEM image and TOF-SIMS maps of the Li/PIA-SPE for Li/Li cell after cycling. d) XPS spectra of C 1s, F 1s, S 2p, and N 1s of PIA-SPE interface with/without cycling. e) Surface and cross-section SEM images of lithium deposition morphology on Cu foil of the asymmetric Li/Cu cell with PIA-SPE after 1 h and f) commercial liquid electrolytes. Reproduced under the terms of a Creative Commons CC BY 4.0 license.<sup>[346]</sup> Copyright 2022, Wiley VCH.

inferior, ranging from 0.01 to 0.2 C, which cannot meet the requirements of high-energy applications.

Obtaining high-energy/power and long cycle life compared to commercial LIBs with lower cost and high safety is the future target of LMBs; however, it is a highly formidable undertaking. Fundamental requirements to achieve these conditions are good solid/solid interfaces with exceptional ion transport across interfaces, solid/solid interface stability, and wetting properties. Liu et al.<sup>[352]</sup> proposed Janus interface stability for NASICON-type Li<sub>1.5</sub>Al<sub>0.5</sub>Ge<sub>1.5</sub>P<sub>3</sub>O<sub>12</sub>-based SEs with the application of IL to anode sites and adiponitrile to cathode sides (Li/LAGP/Li and Li/ASHE/LAGP/ASHE/Li). Janus interface re-

builds the cracks obtained by volume changes with retaining combined interfacial contacts and eliminating side reactions for Li and LAGP during operations. XPS reveals the LAGP consists of inorganic components (i.e., Li<sub>2</sub>O, Li<sub>2</sub>O<sub>2</sub>, and Li<sub>2</sub>CO<sub>3</sub>) as SEI elements; however, AGPE or ASHE with LAGP has LiF and LiCOOR phase arises in SEI with 1363–2549 MPa modulus, which illustrates robust SEI. Stabilizing Cl-enriched SEs (Li<sub>5.5</sub>PS<sub>4.5</sub>Cl<sub>1.5</sub>, Li<sub>6</sub>PS<sub>5</sub>Cl, Li<sub>6.5</sub>PS<sub>5.5</sub>Cl<sub>0.5</sub>, and Li<sub>7</sub>P<sub>3</sub>S<sub>11</sub>) due to higher reaction strains is the severe limitation explained by theoretical calculations. Li<sub>5.5</sub>PS<sub>4.5</sub>Cl<sub>1.5</sub> confirms the Li-S-P bonds of Li-argyrodites (161.3 eV) and polysulfide doublet (163 eV) phases with bridging (-S-) and terminal sulfur bonds (P-S<sub>x</sub>-P). Besides, the presence of

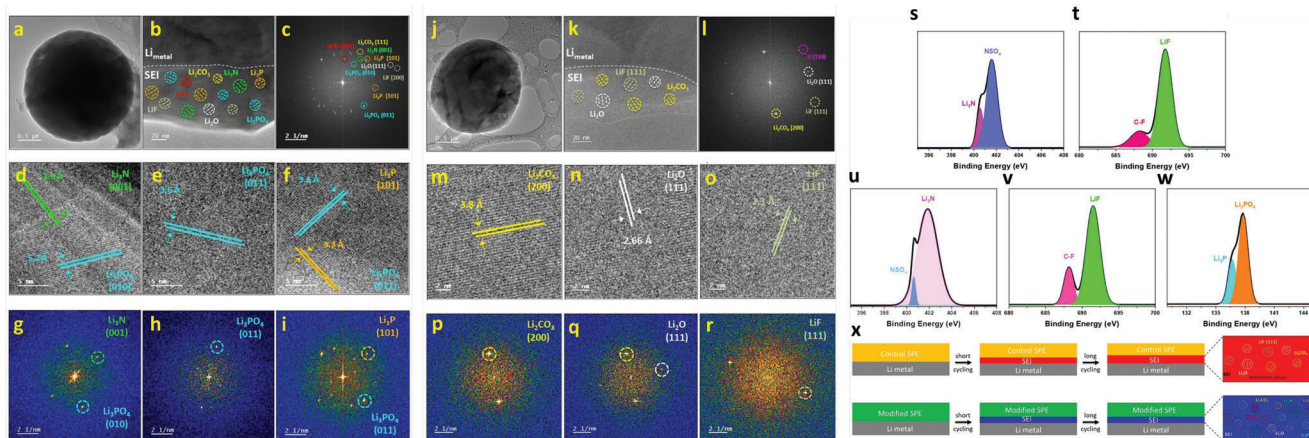


**Figure 12.** Li interface with P-SPE. a) Cryo-TEM image. b) HRTEM of the SEI and c) their FFT pattern. HRTEM images and FFT patterns of  $\text{Li}_3\text{N}$  (d, g),  $\text{Li}_3\text{PO}_4$  (e, h), and  $\text{Li}_3\text{P}$  (f, i) for the SEI layer. Li interface with C-SPE. j) Cryo-TEM image. k) HRTEM of the SEI and l) the FFT pattern. HRTEM and FFT pattern of  $\text{Li}_2\text{CO}_3$  (m, p),  $\text{Li}_2\text{O}$  (n, q), and  $\text{LiF}$  (o, r) for SEI layer. XPS analysis of Li/LFP with C-SPE and P-SPE after C-D 100 cycles. (s,t) C-SPE shows  $\text{Li}_3\text{N}$  and  $\text{LiF}$  phases in the SEI, and (u,v,w) P-SPE shows  $\text{Li}_3\text{N}$ ,  $\text{LiF}$ ,  $\text{Li}_3\text{P}$ , and  $\text{Li}_3\text{PO}_4$  phases in the SEI layer. (x) Illustrations for Li plating with SEI formation under C-SPE and P-SPE. Reproduced with permission.<sup>[349]</sup> Copyright 2023, Elsevier.

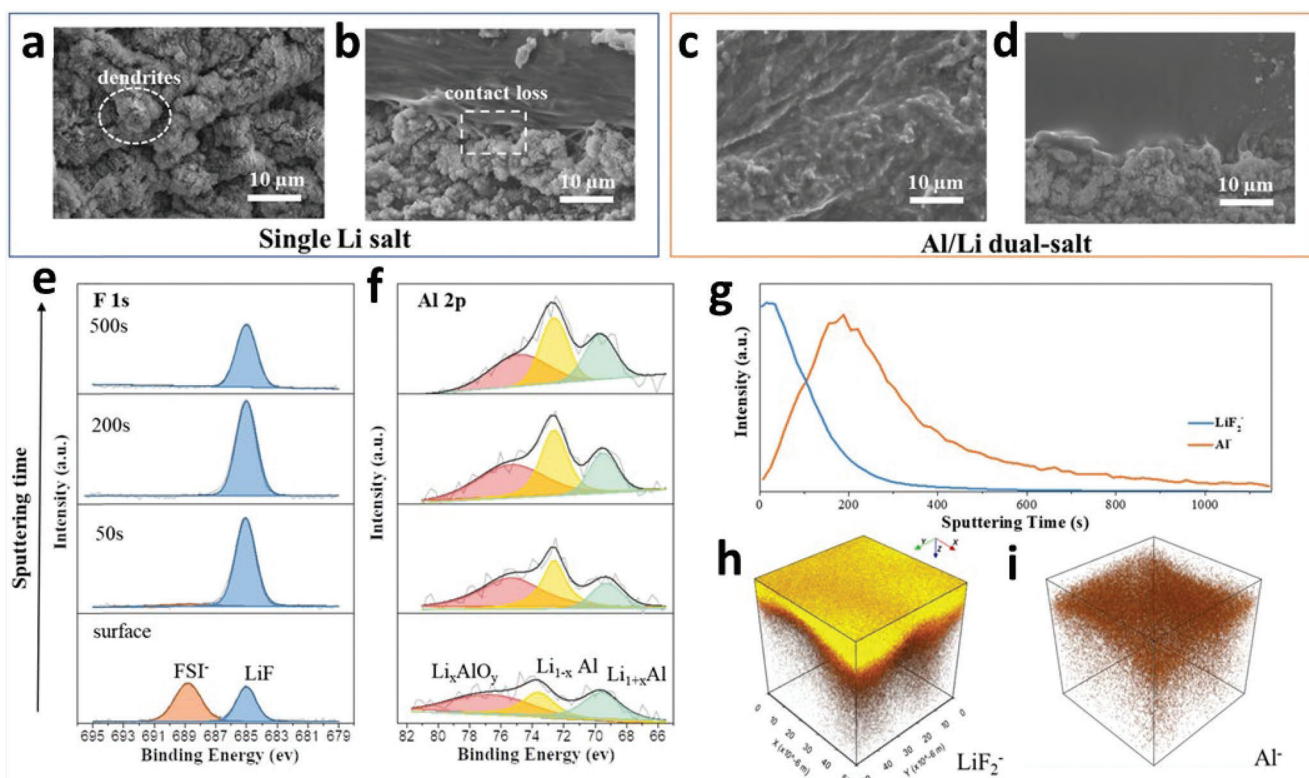


**Figure 13.** Li metal surface SEM images for (a) single Li salt and (c) Al/Li dual-salt. Cross-view SEM images for the Li/electrolyte interface for (b) single Li salt and (d) Al/Li dual-salt. XPS spectra for the sputtering time of (e) F 1s and (f) Al 2p of Li metal surface for dual-salt. (g) TOF-SIMS depth profiles for SEI layer. (h, i) 3D TOF-SIMS depth profiles. Reproduced with permission.<sup>[351]</sup> Copyright 2022, Elsevier.

$\text{SO}_3^{2-}$  relates to the oxidation of  $\text{Li}_2\text{S}$  phase. Low voltage shows  $\text{Li}_2\text{S}$ ,  $\text{Li}_x\text{P}_y$ , and  $\text{LiCl}$  phases after decomposition.<sup>[353]</sup>

Yin et al.<sup>[123]</sup> displays  $\text{Li/Li}_{0.388}\text{Ta}_{0.238}\text{La}_{0.475}\text{Cl}_3$  prolonged interface compatibility with dense surface and homogeneous  $\text{Li}^+$  flux, in which the top surface of SEs has two states of Ta ( $\text{Ta}^{5+}$

and  $\text{Ta}^0$ ). The partial reduction of Ta causes different charging states that imply the electrochemical reduction of  $\text{Ta}^0$  from 13.4 to 2.3% for 3 nm depth of the SE interphase layer. Such gradient reduction ascribes the passivation by electrically insulating the  $\text{LiCl}$  phase due to cation reduction in halide SEs, efficiently



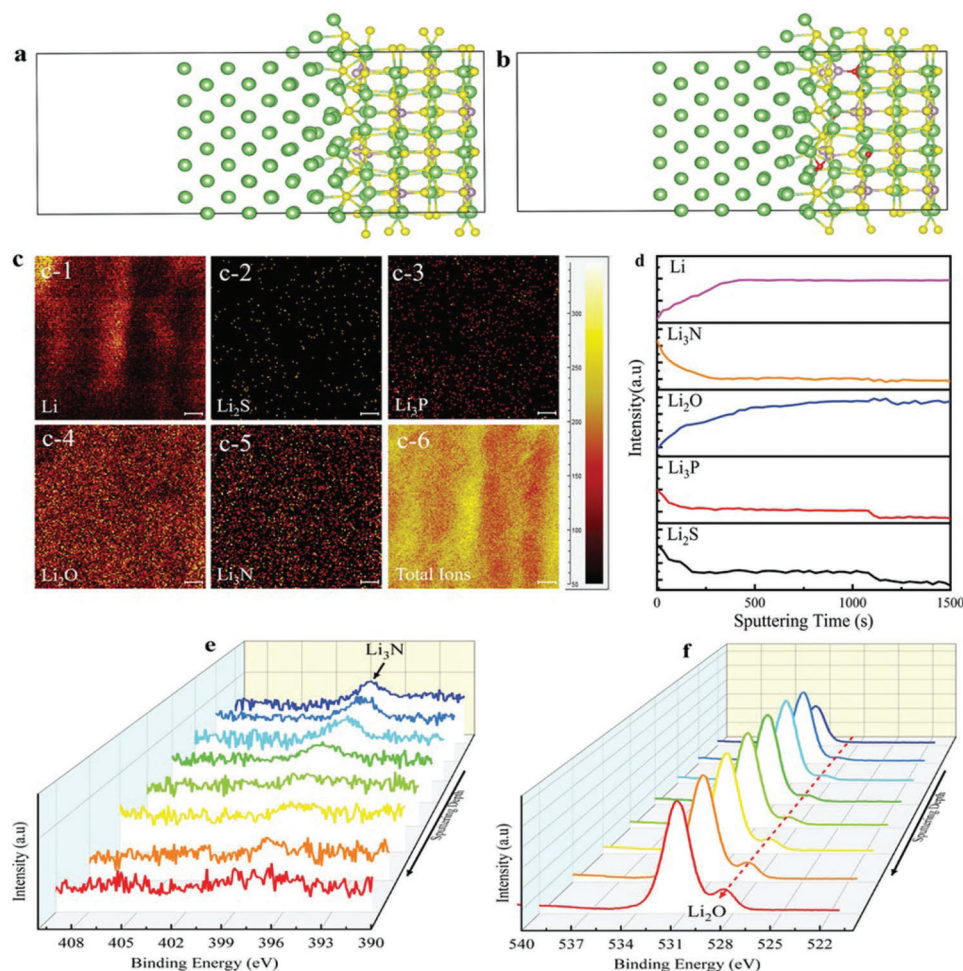


**Figure 14.** DFT interface structures for a) Li/LiPS<sub>4</sub> and b) Li/Li<sub>2.96</sub>P<sub>0.98</sub>S<sub>3.92</sub>O<sub>0.06</sub>-Li<sub>3</sub>N. c) Li-anode surface analysis under Li/Li<sub>2.96</sub>P<sub>0.98</sub>S<sub>3.92</sub>O<sub>0.06</sub>-Li<sub>3</sub>N/Li cells. d) ToF-SIMS depth profiles. XPS depth profiles of Li/Li<sub>2.96</sub>P<sub>0.98</sub>S<sub>3.92</sub>O<sub>0.06</sub>-Li<sub>3</sub>N interface e) N 1s and f) O 1s spectra with sputtering depth. Reproduced with permission.<sup>[358]</sup> Copyright 2022, Wiley VCH.

relieving interface strain and shielding SE at Li metal. Oxide SEs restrain the capacity and cycling life due to Li dendrite's growth along grain boundaries. In contrast, intimate interface contact of sulfide SEs promotes a better cycle life with low areal capacity. Most of chloride and halide SEs suffer for poor interface stability for Li with high overpotential and short cycle life [Li<sub>2</sub>ZrCl<sub>6</sub> (LZC), Li<sub>3</sub>ScCl<sub>6</sub> (LSC), G-LPSC-LGPS, graphite-Li<sub>5.5</sub>PS<sub>4.5</sub>Cl<sub>1.5</sub>-LGPS; Li<sub>7</sub>P<sub>2</sub>S<sub>8</sub>I (LPSI), Li<sub>7</sub>P<sub>2.88</sub>Nb<sub>0.12</sub>S<sub>10.7</sub>O<sub>0.3</sub> (LPNSO), Li<sub>5.5</sub>PS<sub>4.5</sub>Cl<sub>1.5</sub> (LPSC), Al<sub>2</sub>O<sub>3</sub>-coated Li<sub>7</sub>La<sub>2.75</sub>Ca<sub>0.25</sub>Zr<sub>1.75</sub>Nb<sub>0.25</sub>O<sub>12</sub> (A-LLCZNO), Si-coated Li<sub>6.85</sub>La<sub>2.9</sub>Ca<sub>0.1</sub>Zr<sub>1.75</sub>Nb<sub>0.25</sub>O<sub>12</sub> (S-LLCZNO), Ge-coated Li<sub>6.85</sub>La<sub>2.9</sub>Ca<sub>0.1</sub>Zr<sub>1.75</sub>Nb<sub>0.25</sub>O<sub>12</sub> (G-LLCZNO)].<sup>[123,283,354–357]</sup>

Ahmad et al.<sup>[358]</sup> proposed Li<sub>2.96</sub>P<sub>0.98</sub>S<sub>3.92</sub>O<sub>0.06</sub>-Li<sub>3</sub>N SIEs, in which N and O replacement produce functional units of Li<sub>3</sub>N and POS<sub>3</sub><sup>3-</sup> that enable superior  $\sigma_{Li}^{+} \approx 1.58 \text{ mS cm}^{-1}$  and POS<sub>3</sub><sup>3-</sup> units in Li<sub>2.96</sub>P<sub>0.98</sub>S<sub>3.92</sub>O<sub>0.06</sub>-Li<sub>3</sub>N prevents structural degradation under the moisture of 45–50% (Figure 14a–c). Theoretical and experimental results state the Li<sub>3</sub>PS<sub>4</sub> SEs follow the reaction of Li<sub>3</sub>PS<sub>4</sub> + 8Li → 4Li<sub>2</sub>S + Li<sub>3</sub>P + Li<sub>x</sub>P to formulate in situ SEI among the Li and Li<sub>3</sub>PS<sub>4</sub>. The reduced phases of Li<sub>2</sub>S, Li<sub>3</sub>P, and other intermediates Li<sub>x</sub>P are incompetent for active SEI owing to the higher electronic conductivity of Li<sub>3</sub>P/Li<sub>x</sub>P, which im-

plies uneven Li electrodeposits with higher Li-dendrites.<sup>[359,360]</sup> Li//LiPS(100) interface displays S-atoms for 1<sup>st</sup> layer of LiPS shifts to Li-metal with forming Li<sub>2</sub>S at the interface, which illustrates the reformation of the top 3 layers of Li. Besides, three Li and LiPS interface layers did not observe lattice distortion. In contrast, O-LiPS/Li interface implies Li-O with a bond length of 2.1 Å (i.e., 0.3 Å smaller for Li-S), which reveals strong interactions for Li-O than those of Li-S (similar to pristine Li<sub>3</sub>PS<sub>4</sub>). ToF-SIMS and XPS profiles (Figure 14d–f) reveal the formation of pre-SEI enriched with thermodynamically stable Li<sub>2</sub>O and Li<sub>3</sub>N species (minor phases Li, Li<sub>2</sub>S, Li<sub>3</sub>P) at Li/Li<sub>2.96</sub>P<sub>0.98</sub>S<sub>3.92</sub>O<sub>0.06</sub>-Li<sub>3</sub>N interface, which suppresses the interface reactions and dendritic growth of Li inside Li<sub>2.96</sub>P<sub>0.98</sub>S<sub>3.92</sub>O<sub>0.06</sub>-Li<sub>3</sub>N. The peripheral Li<sub>2.96</sub>P<sub>0.98</sub>S<sub>3.92</sub>O<sub>0.06</sub>-Li<sub>3</sub>N SIEs are stable for Li-anode, revealed by no shifts in the binding energy. Li et al.<sup>[361]</sup> reported the influence of 0.5 wt% Li<sub>2</sub>S loading for LPS SEs. During cycling, the Li<sub>3</sub>P, P<sub>2</sub>S<sub>7</sub><sup>4-</sup> and PS<sub>4</sub><sup>3-</sup> phases have been observed that indicate a reaction with Li in LPS. Li<sub>2</sub>S loading reduces the diffusion energy barrier of LPS by promoting stable depositions.

Incorporation of piezo-/ferroelectric BaTiO<sub>3</sub> in CSEs (Li<sub>6.7</sub>La<sub>3</sub>Zr<sub>2</sub>Al<sub>0.1</sub>O<sub>12</sub> (LLZAO) + PEO + LiTFSI) is alternates

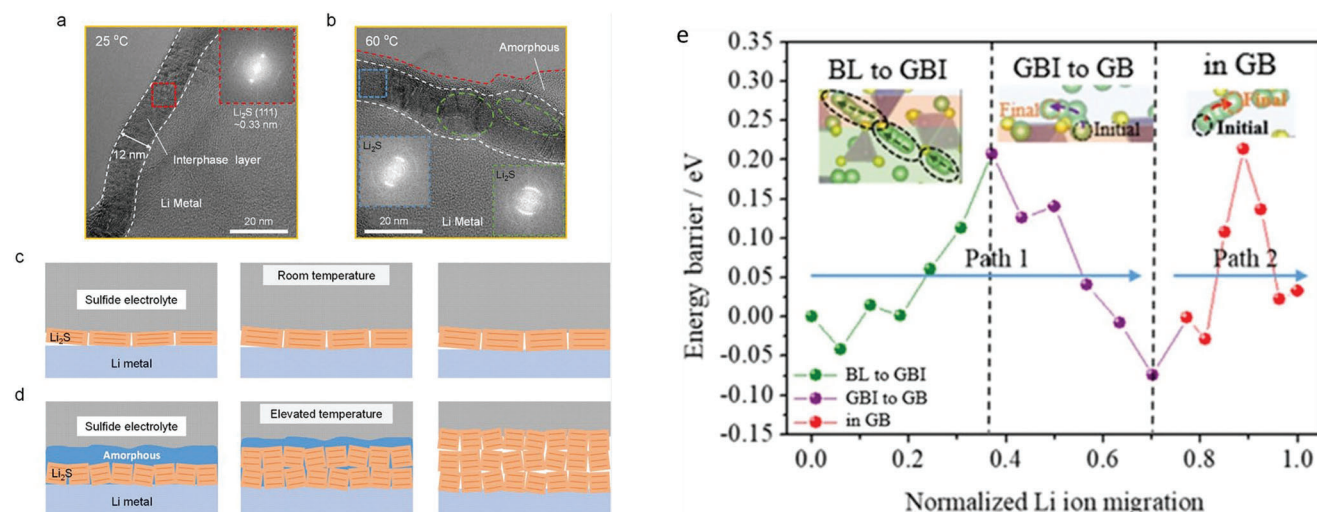


**Figure 15.** TEM images and FFT patterns (a) 25 °C and (b) 60 °C for Li/sulfide SEs. Bright diffraction spots are from the (111) plane of  $\text{Li}_2\text{S}$ . Schematic illustration for interphase evolutions at (c) RT and (d) 60 °C. Reproduced with permission.<sup>[364]</sup> Copyright 2022, American Chemical Society. e) Energy barriers for Li migration as variations with different regions. Reproduced with permission.<sup>[374]</sup> Copyright 2023, American Chemical Society.

strategy to improve CESs ion-transport-kinetics.  $\text{BaTiO}_3$  effectively reduces the driving forces for Li dendrites for high curvatures, whereas ferroelectricity decreases overpotential, illustrating good  $\text{Li}^+$  flux and deposits. Theoretical calculations show that the driving force manifests a bulging area rather than a planar interface. Activation overpotential significantly influences the magnitude and evolution of the driving force, illustrating lower the activation overpotentials – the smaller the driving forces. Piezo-/ferroelectric fields regularize the activation overpotentials for guiding planar Li depositions.<sup>[362,363]</sup>

TEM images of Li/LPSCI verify the highly crystalline  $\text{Li}_2\text{S}$ (111) phase with an interplanar spacing of 0.33 nm with 12 nm SEI thickness at RT, whereas SEI possesses a 3 nm amorphous layer as core-shell of  $\text{Li}_2\text{S}$  at 60 °C (Figure 15a,b).<sup>[364]</sup> For RT, the rate-controlling step is Li diffusion with highly-crystalline  $\text{Li}_2\text{S}$ . The reaction rate gradually decreases with time, ultimately constructing a stable passivation layer. But, at 60 °C, with accelerated diffusion of Li and reaction kinetics, SEs undergo severe decomposition in the disordered Li-P-S-Cl structure with reduction Li and numerous nuclei, which reveals the polycrystalline phases. Such order-disordered  $\text{Li}_2\text{S}$  phase transitions show parasitic reactions for high temperatures (reaction-controlled kinetics). Further, the amorphous layer enlarges with time, increasing interphase thickness with diffusion-controlled kinetics and high interface resistance (Figure 15c,d). PDADMATFSI:LiTFSI (1:1.5) has high conductivity compared to PDADMATFSI and without LiTFSI, illustrating that polyIL facilitates Li-ion conduction. LATP and LAGP NASICON type SEs combined with various artificial SEI such as  $\text{Li}_3\text{PO}_4$ ,  $\text{LiF}$ ,  $\text{MgF}_2$ ,  $\text{B}_2\text{O}_3$ , PEO,  $\text{Al}_2\text{O}_3$ , AZO, ZnO, LiPON, IL-LAGP, and  $\text{SiO}_2$  resolves the reduction of SEs by Li. Promisingly ZnO exhibits prolonged cycle life for Li/Li cells of 2000 h.<sup>[365–367]</sup> Shi et al.<sup>[368]</sup> presented PVDF- $\text{BaTiO}_3$ - $\text{Li}_{0.33}\text{La}_{0.56}\text{TiO}_{3-x}$  CSEs (PVBL), in which polarized dielectric  $\text{BaTiO}_3$  improves the Li-salt dissociation with forming numerous mobile  $\text{Li}^+$  that transfer across the interface with  $\text{Li}_{0.33}\text{La}_{0.56}\text{TiO}_{3-x}$ . Besides,  $\text{BaTiO}_3$ - $\text{Li}_{0.33}\text{La}_{0.56}\text{TiO}_{3-x}$  confines the SCL formation with PVDF, and these CSEs homogenize the in-

terface electric field. The Li/PVL (without  $\text{BaTiO}_3$ ) has a lower overpotential relative to PVBL that ascribes the partial reduction of LLTO from  $\text{Ti}^{4+}$  to  $\text{Ti}^{3+}$  for PVL by Li with the formation of a mixed conductor interface.<sup>[369,370]</sup>

The Li/poly(lithium 4-styrenesulfonate)(PLSS)- $\text{Li}_{6.5}\text{La}_3\text{Zr}_{1.5}\text{Ta}_{0.5}\text{O}_{12}$  (LLZTO) CSEs cells show stronger coordination that built the bridge for  $\text{Li}^+$  transfer, lower energy barrier, and higher diffusion coefficient. It introduces two different interfaces such as LLZTO/PLSS and PLSS/Li; the former is constructed by coordination chemistry of  $\text{Li}^+$  migration due to the coordination of  $-\text{SO}_3\text{Li}$  with LLZTO surface atoms. The latter interface stems from the superior lithiophilicity of PLSS, and it prevents electrons from attacking electrolytes due to the feature of electron blocking.<sup>[371]</sup> Li with triphenyl antimony (p-TPA)@LLZTO enables the mixed ionic/electronic interface with  $\text{Li}_3\text{Sb}$ ,  $\text{Li}_2\text{C}_2$ , and  $\text{LiSbO}_3$  domains, improving the mass and charge transport for Li and LLZTO. The phenyl groups in the a-TPA interlayer imply an even distribution and restrained growth of lithiophilic  $\text{Sb}^0$  sites that favor the homogenization of electric-field distribution, Li alloying, and nucleation processes.<sup>[372,373]</sup>  $\text{Li}_{5.4+x}\text{P}_{1-x}\text{Si}_x\text{S}_{4.4}\text{Cl}_{1.6}$  ( $x = 0, 0.05, 0.1, 0.2, 0.3, 0.4$ ) argyrodite explains the Si doping, in which the LiCl-dominated interphase layer as buffer formed with a homogeneous distribution of Si, P, S, and Cl in the grains. Si doping undergoes P sites with forming metastable argyrodite phases. A large ionic radius of  $\text{Si}^{4+}$  than  $\text{P}^{5+}$  exhibits tetrahedral coordination, whereas  $\text{Cl}^-$  has a smaller ionic radius than  $\text{S}^{2-}$ .<sup>[135]</sup> The Si enlarges the volume of  $(\text{Si},\text{P})\text{S}_4$  polyhedrons; therefore, the 4a/4d sites (Wyckoff positions) for argyrodites occupy the preferential S that results extrusion of Cl atoms from the lattice. Si-doped Cl-rich argyrodites suppress Li dendritic depositions even for high current densities.

Typically, LGPS have a 1D major transport pathway along the c-axis in bulk LGPS. Evaluation of the total Li-ion diffusion pathway from bulk to grain boundaries (GB) is shown in Figure 15e. Two energy barriers are involved for Li-ion conduction for LGPS. Path 1 shows Li-ion transfer from bulk-like (BL) to GB through the grain-boundaries interface (GBI), whereas path 2 involves



Li-ion diffusion across GB.<sup>[374]</sup> For Li-ion migration, path 1 and 2 has energy barriers of 0.248 and 0.286 eV, respectively, which is higher than calculated energy barriers for bulk and comparable to experimental values. The improved energy barrier for Li-ion near GB is relative to complex inhomogeneous atomic structures at the GB, which results in Li-ion exits from BL to the c-axis for 1D pathways to cross the intersection facing numerous further Li ions exits from the BL. The diffusion for GB is the key factor in determining the overall diffusion properties for LGPS during operations. Significant reduction in diffusion rates for Li-ions at GB influences severe parasitic reactions owing to sluggish kinetics; thus, structural contact interfaces are critical for improving the electrochemical performances of SEs. Interface resistances are severely influenced by volume change with stress/strain that declines the physical and chemical contact. A comprehensive understanding of SEs/electrode interfaces is necessary to alleviate the interface stress/strain. Previous reports propose that the rate capability of cathodes is strongly subjective to lattice strain due to Li-ion conductance and minimal blocking defects.

These findings suggest interfacial impedance strongly influences the interface compatibility of Li and rate capabilities. Besides, it provides information for the fabrication of superior interface characteristics for prolonged operational life with Li-metal for the rising attention of all-solid-state Li-metal batteries (ASSLMBs). The inorganic LiF and Li<sub>3</sub>N phases based SEI is more favorable for stable interfacial reactions than other inorganic/organic phases, which can withstand high stress/strain and strong electric field. Poor chemical compatibility, volume change, and low ion conductivity of SPEs exhibit a passive layer with high resistance during cycling, even for extremely poor current densities with accelerating chemical diffusion kinetics. SIEs with sulfides, oxides, and composites display more compatible interface properties with wide electrochemical windows. The commercial realization for Li-metal anodes will not be assured because no present results meet the manufacturing criteria relative to electrochemistry and scalable processing.

### 7.1.2. Li-Sulfur (Li-S) Batteries

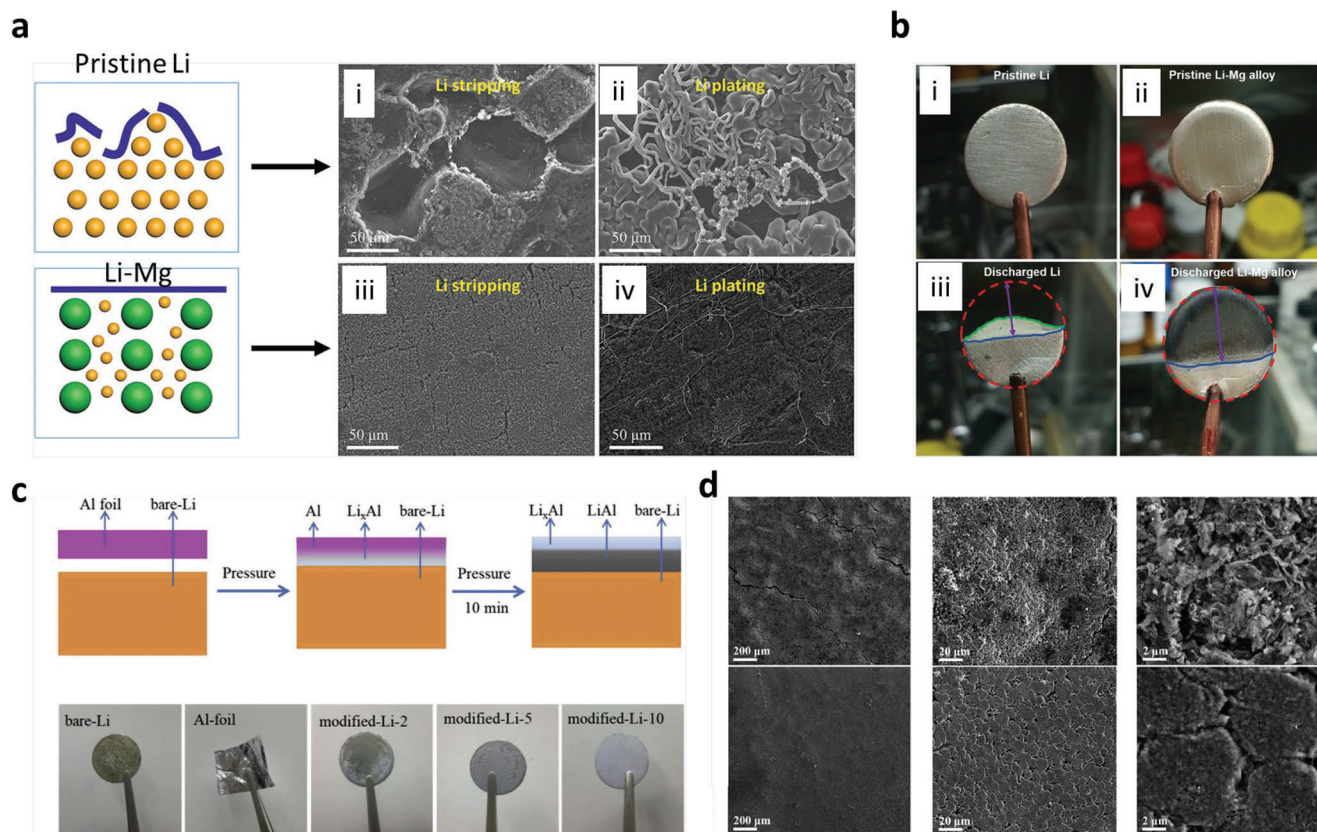
Li-S chemistry has been acknowledged overwhelming consideration due to the high cathode and anode capacities of  $\approx 1675$  and  $\approx 3800$  mAh g<sup>-1</sup>, respectively, which yields a maximum energy density of 2600 Wh kg<sup>-1</sup> with active sulfur and Li for 2–2.5 V operating voltage.<sup>[375–377]</sup> However, the polysulfide shuttle and cell failure by Li-dendritic growth are critical challenges for Li-S batteries that rigorously decreases the feasibility for active S-electrodes, lowers cycle life, and capacity fading. Li-S batteries with SEs can resolve polysulfide diffusion and block dendrite growth. Two main phases for SEs in Li-S have been considered for research. Integration of SEs for Li-S obtained cell performance which is disappointing with cycle life, S-cathode utilization, and rate-capability due to poor kinetics for S-cathodes and electrode/electrolyte interfaces. Liquid electrolytes for cathodes provide ion media for sulfur–polysulfide–sulfide redox reactions and sustain simple Li-ion pathways for cathode or SEI. Several approaches, such as artificial buffer layers at Li/SEI, mechanical pressing of Li in SEs, liquid-soaked polymer addition among the

Li and SEs, and hybrid electrolytes, have been reported; however, they could not provide satisfactory solutions.<sup>[375–378]</sup> NASICON-type Li<sub>1+x</sub>Al<sub>x</sub>Ti<sub>2-x</sub>(PO<sub>4</sub>)<sub>3</sub>-based Li-S batteries demonstrate both the chemical and electrochemical compatibilities influencing the Li-S chemistries by reduction of Ti<sup>4+</sup> to Ti<sup>3+</sup> for 2.4 V versus Li/Li<sup>+</sup> by polysulfide species.<sup>[379,380]</sup> Further, replacing different SEs such as Li<sub>1+x</sub>Al<sub>x</sub>Ge<sub>2-x</sub>(PO<sub>4</sub>)<sub>3</sub>, garnet, LGPS, Li<sub>2</sub>S-P<sub>2</sub>S<sub>5</sub>-P<sub>2</sub>O<sub>5</sub>, Li<sub>x</sub>La<sub>2/3-x/3</sub>TiO<sub>3</sub>, Li<sub>1+x</sub>Y<sub>x</sub>Zr<sub>2-x</sub>(PO<sub>4</sub>)<sub>3</sub>, LiPON, Li<sub>7</sub>La<sub>3</sub>Zr<sub>2</sub>O<sub>12</sub>-PEO-LiClO<sub>4</sub>, Li<sub>6</sub>PS<sub>5</sub>Cl, PEO-LiTFSI, PEO-LiCF<sub>3</sub>SO<sub>3</sub>, and PEO-LiClO<sub>4</sub>, and LLZO SEs could improve the compatibility concerns. In contrast, operational cycle life and capacity fading are not reasonable.<sup>[379–389]</sup> To improve Li interface structures with SEs, different Li-alloys (Figure 16) have been reported, such as Li-In, Li-Sn, Li-Al, Li-Mg, etc.<sup>[390–393]</sup>

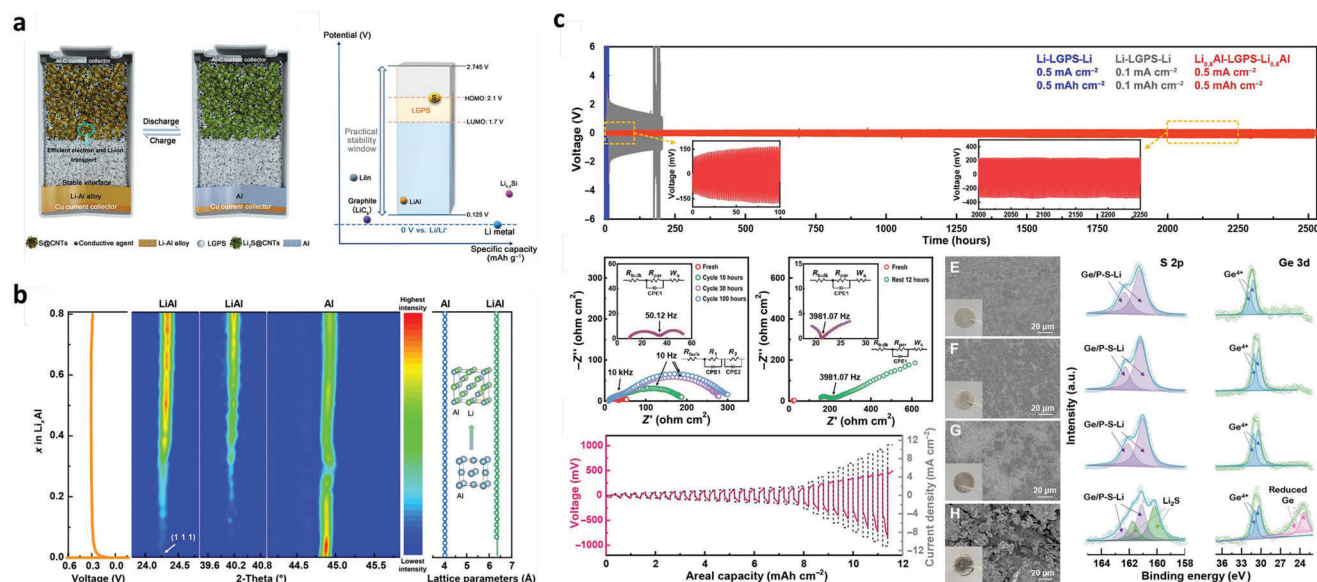
Li/LGPS with LiI displays prolonged cycle life for 800 h; however, pristine Li/LGPS exhibits an increased overpotential of 2 V with cell failure.<sup>[394]</sup> EIS displays a severe increase in interface resistance from 72 to 6000  $\Omega$ , illustrating the electrochemical decomposition of LGPS and physical deterioration with cracks and large Li volume change. XPS shows reduced P, Li<sub>3</sub>P, and PS<sub>4</sub> for LGPS; however, with LiI, Li/LGPS did not show a reduction of Ge<sup>4+</sup> or P<sup>5+</sup>, which indicates an excellent interface with dendrites. Incorporating LiI enhances the mechanical strength, chemical stability, and excellent toughness that offers suitable chemistry with sulfide electrolytes.

Figure 17 proposes the carbon- and binder-free Li-Al alloy anode and their compatibility with LGPS. LGPS has an EW of 1.7–2.1 V versus Li/Li<sup>+</sup>, Li-In alloy, or Li<sub>4</sub>Ti<sub>5</sub>O<sub>12</sub> of 1.55 V versus Li/Li<sup>+</sup> with an operable potential of <1.7 V (Figure 17a).<sup>[395,396]</sup> Oxidative limit of LGPS is 2.8 V versus Li/Li<sup>+</sup>. During lithiation, the LiAl peaks increase gradually with the Al peak. It indicates Li<sub>0.8</sub>Al is a mixture of Al and LiAl with Al:LiAl = 1:4 with biphasic reactions at constant potential. Lattice parameters of Al (Fm3m) and LiAl (Fd3m) verify the volume change of Li<sub>0.8</sub>Al (74.95%), which is lower than those of other Li<sub>4.4</sub>Si and Li<sub>4.4</sub>Ge alloy anodes (Figure 17b).<sup>[397]</sup> The (111) crystal plane of LiAl initiates to appear with the lithiation step. Li<sub>0.8</sub>Al/LGPS/Li<sub>0.8</sub>Al cells exhibit a low overpotential of 100–150 mV over 2500 h, whereas Li/LGPS/Li exceeds the detecting limits with overpotential >3–6 V. Alloy concentrations for Al, Si, Sn, In, and Mg significantly affect the cycle stability. Li<sub>0.8</sub>Al has mixed ionic-electronic conduction kinetics and displays Li-ion conducting SEI. Li<sub>0.8</sub>Al/LGPS has smooth morphology without dendrites; however, Li/LGPS has rough and uneven growth. XPS suggests LGPS strongly reduced by Li forming Li<sub>2</sub>S and reduction of Ge<sup>4+</sup> (Figure 17c).

PST was reported by copolymerization of sulfur and vinyllic monomer triallylamine with forming inorganic/organic hybrid SEI by organosulfides/organopolysulfides for Li-metal surface (Figure 18).<sup>[398]</sup> Organosulfide/organopolysulfide acts as a plasticizer that creates more flexible and stable Li depositions without Li dendrites. SEM images display porous and loose structure for C-SEI, smooth with few cracks for S-SEI, and uniform and planar morphology without cracks for PST-90-SEI, which illustrates C-SEI has continuous breaks, S-SEI cannot withstand volume change, and PST-90-SEI suppress dendrites with enhanced CEs. XPS spectra verify the presence of Li<sub>2</sub>S<sub>x</sub> and Li<sub>2</sub>S<sub>2</sub> in S-SEI corresponds to the Li polysulfide phases. PST-90-SEI confirms the organosulfides (RS<sub>x</sub>Li<sub>6</sub>) and Li<sub>2</sub>S<sub>x</sub> phases, and C-SEI shows –CF<sub>3</sub> functional groups. F 1s spectra display the presence of more



**Figure 16.** a) SEM images of Li and Li-Mg alloy after i, iii) Li stripping and ii, iv) following Li plating. b) Photographs of i, iii) Li foil, and ii, iv) Li-Mg alloy foil before and after Li stripping. Reproduced with permission.<sup>[393]</sup> Copyright 2019, Wiley VCH. c) Illustration of Li-B anode modified by in situ reaction with aluminum foil (top), and typical photograph of bare-Li, aluminum foil, modified-Li-anodes (bottom). Reproduced with permission.<sup>[392]</sup> Copyright 2018, Elsevier. d) SEM images for pristine Li (top row) and Li/C/Sn (bottom row) electrodes after 250 cycles. Reproduced with permission.<sup>[391]</sup> Copyright 2019, Elsevier.



**Figure 17.** a) Schematic of a rechargeable all-solid-state LSB with Li-Al alloy anode and its reaction mechanism. b) In situ XRD patterns for lithiation processes for Al and their lattice parameters of Al and LiAl. c) Compatibility tests for Li<sub>0.8</sub>Al anodes under LGPS SSEs. Reproduced with permission.<sup>[395]</sup> Copyright 2022, American Association for the Advancement of Science.



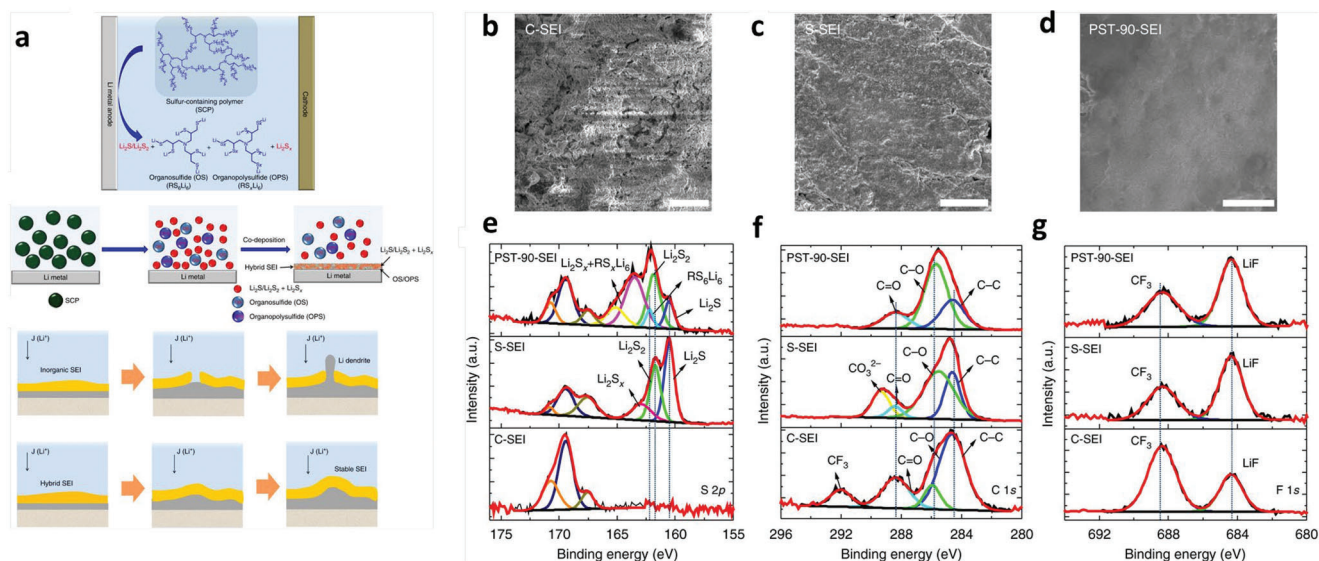


**Figure 18.** a) Schematics illustration. b-d) SEM image of C-SEI layer (b), S-SEI layer (c), and PST-90-SEI layer (d). e-g) XPS spectra of S 2p (e), C 1s (f), and F 1s (g) for the SEI layer. Reproduced under the terms of a Creative Commons CC BY 4.0 license.<sup>[398]</sup> Copyright 2017, Nature Publishing Group.

**Table 3.** State-of-the-art for Li-alloys-based anodes.

Metal alloys	Methods	Remarks
Li-Sn	Fusion reaction, Electrochemical lithiation	Small interface impedance, a strong affinity for Li, poor reversibility
Li-Si		Large volume expansion, poor reversibility, high overpotentials
Li-Ge	Electrochemical lithiation	Faster Li diffusion, poor reversibility
Li-B	Fusion reaction	Porous structures accommodate Li, and structure collapse
Li-Al	Sputtering, Fusion reaction, Electrochemical lithiation	Small volume change, phase transfer,
Li-Bi	Electrochemical lithiation	High volumetric capacity, working temperature >380 °C
Li-In		High electro-positivity of Li, high cost
Li-Sb		Working temperature >350 °C, large volume expansion
Li-Mg		High Li diffusion, poor Li kinetics
Li-Na		Large volume expansion, high reactivity
Li-Au		Less structure change, high cost, eliminating the nucleation barriers
Li-Ag	Fusion reaction, Electrochemical lithiation	
Li <sub>x</sub> CuP	Fusion reaction	Good cycling stability
Li <sub>4.4</sub> Ge <sub>x</sub> Si <sub>1-x</sub>	Ball milling	Increase Li ion accommodation, good reversibility
Li-Cu-Sb	Ball milling, Electrochemical lithiation	Good cycling stability and electronic conductivity
Li <sub>2</sub> MgSi	Ball milling + annealing	Prevent dissociation of Li-Mg, complex synthesis
Li <sub>x</sub> Cu <sub>6</sub> Sn <sub>5</sub>	Electrochemical lithiation	Small irreversible capacity
Li-B-Mg	Fusion reaction	Complex synthesis, porous structure, good strength
Li-In-Sb	Ball milling + Electrochemical lithiation	Good reversibility, small volume change

substantial LiF peaks for PST-90-SEI than those of C-SEI and S-SEI, enabling a stable SEI. Several Li-alloy anodes have been reported because they effectively reduce the Li nucleation overpotential and interfacial resistance by controlling Li electrodepositions (Table 3).<sup>[390–404]</sup> Binary Li-alloys have several critical issues, such as great volume change (i.e., Li-Si, Li-Sn), high cost (i.e., Li-Ag, Li-Cu), high reaction activity (i.e., Li-Na), and low energy density (i.e., Li-Bi, Li-Zn), thus ternary/multiple Li-alloys have typical advantages, but specific energy is reduced because addi-

tional metals did not involve for electrochemistry. Substantial alteration for specific volume during charge/discharge leads to a loss in electrical contacts with capacity fading. Further, complex fabrication processes and prices are also critical to be considered. Li-alloy with graphene, CNTs, polymers, and anodic aluminum oxide (AAO) membrane effectively limits the volume change during electrochemistry.<sup>[405,406]</sup> Sun et al.<sup>[407]</sup> reported LAGP/PVDF composite layer over the Li metal prevents the polysulfides by Li reactions. Li-S battery shows great cycle stability for LiNO<sub>3</sub>-free

electrolytes with a discharge capacity of 832.1 mAh g<sup>-1</sup> after 100 cycles at 0.5C.

The comprehensive analysis confirms that Li-S chemistry has several technical limitations to reaching commercial standards like LIBs or other batteries. Furthermore, Li or Li-alloys anodes have higher reduction potentials to polysulfide shuttle effect and dendrites growth; thus, Li metal protection with Li-S chemistry is more complex than commercial LIBs. Modifying the chemical properties of in situ or ex-situ SEI with regulating current distributions for Li depositions is the future scope for research. Artificial buffer layers for anodes make uniform Li-ion flux and balanced mechanical yield; hybrid layers offer advantages of organic and inorganic components that can form a stable interface.

### 7.1.3. Sodium (Na)–Metal Batteries (SMBs)

Na metal has many interests due to its natural abundance, low cost, high theoretical capacity of 1166 mAh g<sup>-1</sup>, low redox potential of -2.71 V versus SHE, and equivalent physicochemical properties with Li.<sup>[408,409]</sup> However, the high reactivity of Na endorses the inevitable side reactions and dendritic growth, which illustrates the severe deterioration of electrochemical performances with unstable SEI, consumption of electrolytes, and serious safety or thermal concerns limiting their practical applications. Much effort has been considered to overcome these intrinsic shortcomings with four major approaches 1) optimization for electrolytes in terms of solvents, additives, and salts for liquid or gel electrolytes as well as finding electrolytes that are compatible for high voltage cathodes using ionic liquids or high-concentration electrolytes; 2) constructing artificial SEI layer with a superior interface by Na anode; 3) develop SEs with high ion conductivity and exceptional interface compatibility that functions physical barriers to block parasitic reactions and mechanical barriers to suppress Na-dendrites; 4) constructing 3D confined frameworks with high sodiophilicity.<sup>[408–412]</sup> Such a 3D framework modifies the nucleation and growth kinetics by providing a porous host that can accommodate Na-anode volume change and controls the Na<sup>+</sup> nucleation process for stable electrodeposition. The high surface of 3D frameworks regulates local current density and Na<sup>+</sup> flux distribution with inhibition of mossy Na-dendrites. Na-infused carbon felt, wood, oxygenated CNTs, Fe<sub>2</sub>O<sub>3</sub>-coated carbon textiles, and Sn<sup>2+</sup> pillared Ti<sub>3</sub>C<sub>2</sub> MXene are the most effective frameworks reported.<sup>[408,413–416]</sup> Thus, it is critically necessary to develop solid-state Na-batteries. Similar to Li-batteries SEs, the SEs for Na-batteries are also devolved in terms of SPEs, oxide, halides, NASICON,  $\beta$ -Al<sub>2</sub>O<sub>3</sub>, sulfides, complex hydrides, etc.<sup>[413]</sup> A widespread understanding of nucleation behavior and initial stages of Na-growth to obtain stable metallic electrodepositions is essential. Electrodeposition and thermal infusion are basic approaches for storing Na-metal; however, electrodeposition is highly vulnerable to uneven nucleation and growth, having high localized current and overpotentials. In the case of thermal infusion, poor wettability among the molten Na and host causes intermittent Na distributions.

The grain-boundaries engineering approach for stabilization of the Na//Na<sub>3</sub>Zr<sub>2</sub>Si<sub>2</sub>PO<sub>12</sub> (NASICON) interface and Na-ion transport across the interface has been reported (Figure 19).<sup>[417]</sup> XPS analysis verifies the stronger intensity for Na 1s ascribes

to enhanced coverage of interface products. Zn 3d and Si 2p for NASICON electrolytes suggest a reduction to sub-oxides (Figure 19a). Theoretical calculations also justify the reduction in Zn<sup>4+</sup> and Si<sup>4+</sup> for NASICON by Na-metal.<sup>[418]</sup> Zhang et al. verified the Zr 3d, Na 1s, Si 2p, P 2p, and O 1s spectra for the pristine NASICON and after Na-depositions, in which they found an increase of Na-metal fractions after two-deposition steps without interphase. Zr and Si undergo reductions to ZrO<sub>x</sub> or Si<sub>x</sub>O<sub>y</sub> from varying +4 to +3 and +2 to +1 oxidation states, respectively. P 2p did not show any noticeable reduction in NASICON. Figure 19b shows the desired low resistance stable SEI interphase for Na//NZSP-10NBO//Na cells. NASICON-NBO shows the formation of Na<sup>+</sup>-rich SEI with a reaction of Na-blocking electron transport that guarantees stable Na-migration. Cycled Na-anode did not show obvious dendrites with stable and uniform Na-electrodepositions (Figure 19c,d). High ion conductivity (1.72 mS cm<sup>-1</sup>) and better compatibility with Na-metal exhibits homogeneous Na-plating/stripping cycles of 2500 h for Na//Na<sub>3</sub>Zr<sub>2</sub>Si<sub>2</sub>PO<sub>12</sub>-10wt% Na<sub>2</sub>B<sub>4</sub>O<sub>7</sub>//Na cells for RT and elevated temperatures (Figure 19e,f). Wang et al.<sup>[419]</sup> reported the discrete Na metal islands for NASICON at 1250 °C with Na dendrites of 10 mm, whereas NASICON (at 1300 °C-15 min/1200 °C) shows the uniform distribution, suggesting Na-enriched SEI by using TOF-SIMS/depth-profile maps. Insertion of plasticizer in SEs accelerates the Na<sup>+</sup> transfer kinetics in the cathodes.<sup>[419]</sup>

Figure 20 shows the pseudo-quaternary phase diagram of Na<sub>3</sub>Zr<sub>2</sub>Si<sub>2</sub>PO<sub>12</sub> using open quantum materials database (OQMD). The ground-state structure of Na<sub>3</sub>Zr<sub>2</sub>Si<sub>2</sub>PO<sub>12</sub> drops on the energy convex hull, illustrating the stable phase formation. Na<sub>3</sub>Zr<sub>2</sub>Si<sub>2</sub>PO<sub>12</sub> has EW of 1.11–3.41 V versus Na/Na<sup>+</sup>. Phase equilibria and decomposition reaction energies of Na<sub>3</sub>Zr<sub>2</sub>Si<sub>2</sub>PO<sub>12</sub> reveal reduction initiates from 1.11 V, demonstrating instability against Na. Reduction for Na<sub>3</sub>Zr<sub>2</sub>Si<sub>2</sub>PO<sub>12</sub> at 0 V forms Na<sub>3</sub>P, Na<sub>2</sub>ZrO<sub>3</sub>, Na<sub>4</sub>SiO<sub>4</sub>, and ZrSi with small reaction energy of -0.27 eV/atom. The LGPS, Li<sub>7</sub>P<sub>3</sub>S<sub>11</sub>, and LiPON decomposition energies at thermodynamic equilibria with Li are -1.25, -1.67, and -0.66 eV/atom, respectively.<sup>[420]</sup> This feature confirms the small thermodynamic driving force and slower kinetics for reduction reaction than those of thiophosphates and LiPON owing to the lowest decomposition energy (-0.27 eV/atom) of Na<sub>3</sub>Zr<sub>2</sub>Si<sub>2</sub>PO<sub>12</sub> in equilibria. This reaction energy involves the parabolic rate constants for diffusion-controlled SEI growth.<sup>[421]</sup>

Brissot et al. propose the classical model for the progression of ions transfer and concentrations through the Li plating process and their impact on dendritic nucleation and growth. When ion depletion occurs for inhomogeneous SCL among the metal electrodes and SIEs, the dendrites initiate nucleation and aggressively grow upright to metal surfaces (Li, Na, K, Figure 21a).<sup>[269,422]</sup> Unbalanced ions and electron transports with an inhomogeneous electric field for Na//SIEs interface are two major kinetics features. Removal of these features plays a significant role in realizing thermodynamically favored Na-electrodepositions. The ferroelectric phase stems from spontaneous polarizations to create the internal electric field and macroscopic charges for ferroelectric surfaces. External polar species are absorbed for the ferroelectric surface to screen surface charges.<sup>[423]</sup> Producing different electric fields to realize homogeneous distributions of space charge locally conflicting with the original field among the metal and SIEs, defined as the ferroelec-



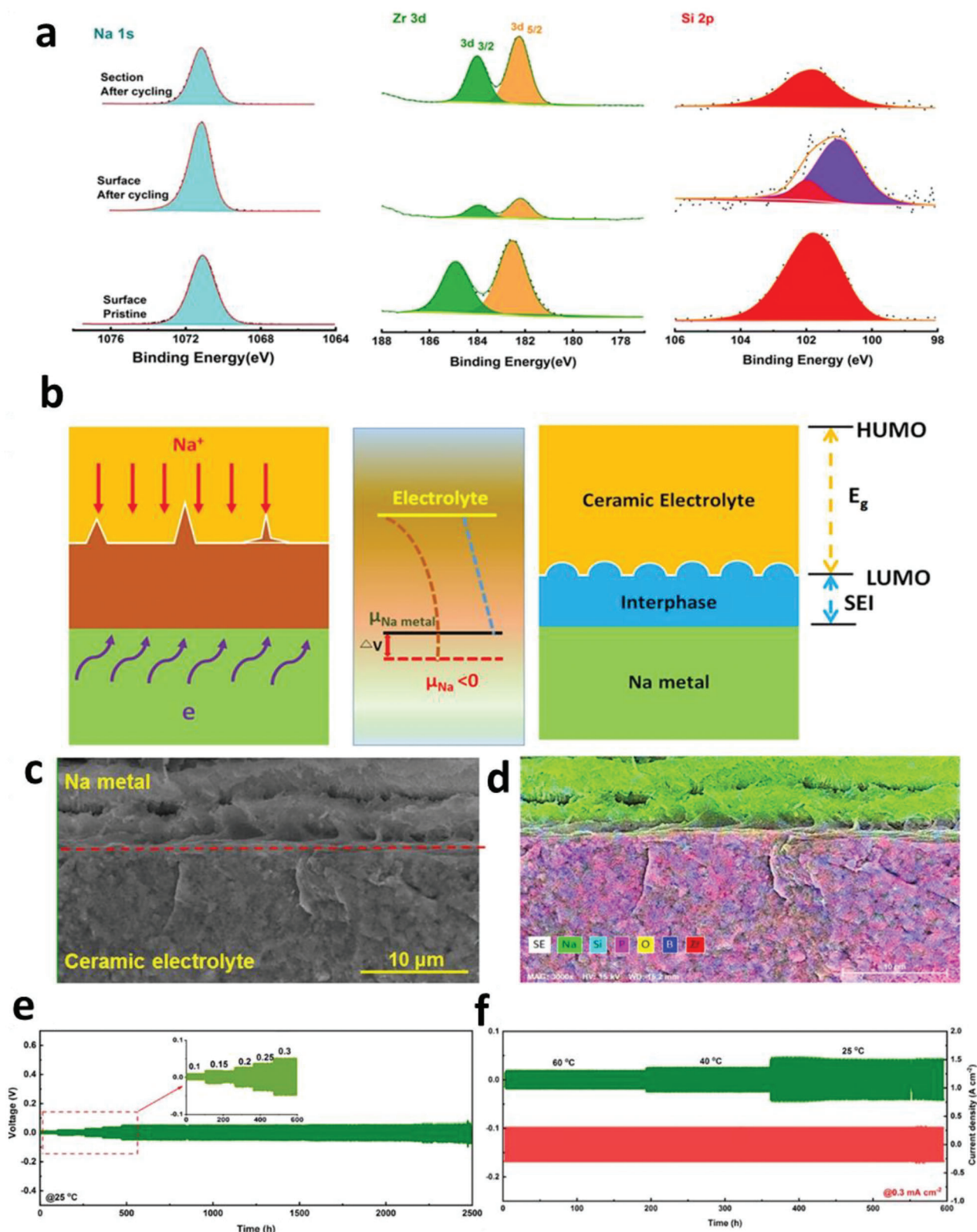


**Figure 19.** a) Na 1s, Zr 3d, and Si 2p XPS spectra for pristine, surface, and section after cycling with NZSP-10NBO. b) Illustrations for potential distribution among the Na metal and SSEs for various interphases, Na/NZSP (left) and Na/NZSP-10NBO (right). c,d) Cross-SEM and EDS map for NZSP-10NBO//Na interface after 2500 h. e,f) Na plating/stripping for NZSP-10NBO at RT (e) and different temperatures (f). Reproduced with permission.<sup>[417]</sup> Copyright 2021, Elsevier.

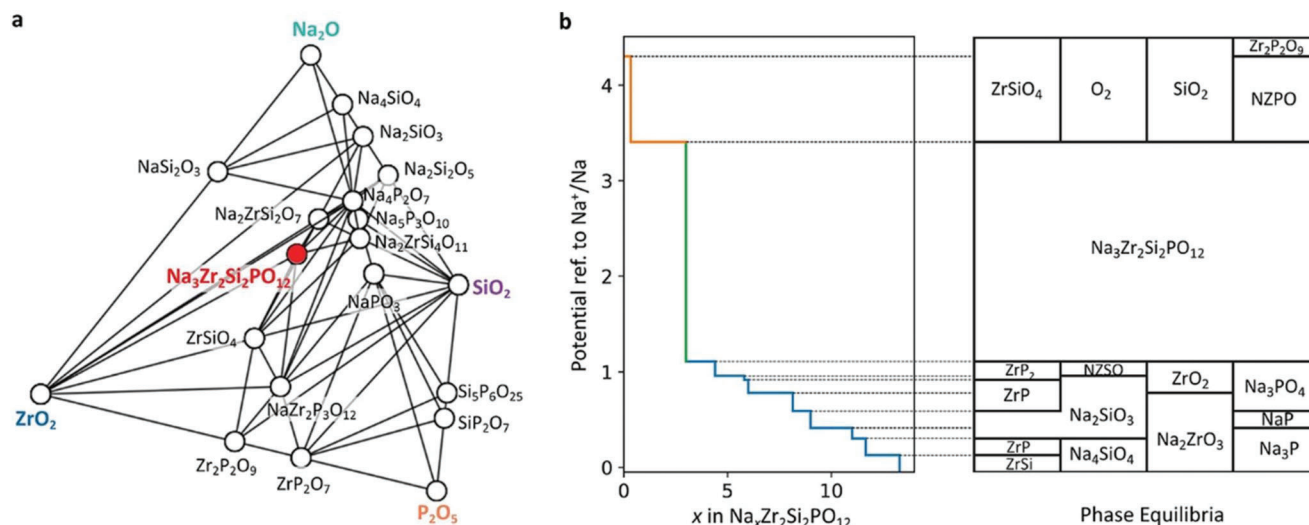


**Figure 20.** a) Pseudoquaternary phase diagram for Na<sub>2</sub>O–ZrO<sub>2</sub>–SiO<sub>2</sub>–P<sub>2</sub>O<sub>5</sub> system. b) Voltage profile of Na<sub>3</sub>Zr<sub>2</sub>Si<sub>2</sub>PO<sub>12</sub> and the phase equilibria of all the reaction stages. The calculated EW for Na<sub>3</sub>Zr<sub>2</sub>Si<sub>2</sub>PO<sub>12</sub> is from 1.11–3.41 V versus Na<sup>+</sup>/Na. [NaZr<sub>2</sub>(PO<sub>4</sub>)<sub>3</sub> – NZPO, Na<sub>2</sub>ZrSi<sub>2</sub>O<sub>7</sub> – NZSO]. Reproduced with permission.<sup>[418]</sup> Copyright 2020, American Chemical Society.

tric effect, would be a feasible approach. The ferroelectric phase in ceramics lattice shows the bridging or deflection for the cracks and devours the driving force of cracks propagation Figure 21b. This mechanical energy transferred to electrical energy by piezoelectric effect or concurrently disbursed by the stress-persuaded ferroelectric phase transformations results in the improvement in the fracture toughness for ceramic electrolytes. Incorporation of ferroelectric phases such as (BaTiO<sub>3</sub>, K<sub>0.5</sub>Na<sub>0.5</sub>NbO<sub>3</sub>, and others) to NASICON SIEs and A<sub>3–2x</sub>Ba<sub>x</sub>ClO (A = Li, Na, K, x = 0.005–0.01) accelerates the Na<sup>+</sup> (others)-migrations and uniform distributions of charges for the Na//NASICON or Na//A<sub>3–2x</sub>Ba<sub>x</sub>ClO interfaces during cycling illustrating the dense Na-/other-metals electrodepositions with high CCD.<sup>[422,424,425]</sup>

Na//NASICON-3BTO shows flat and dense morphology, whereas wattle-like Na-metal for NASICON only (Figure 21c–h), verifying the superior interface that ascribes to the even Na-depositions persuaded by dynamically self-adaptive interfaces. Ferroelectric phase BTO provides the conformal and switchable electric polarization for ordered distributions of charge carriers. Meanwhile, an additional out-of-plane piezoelectric field initiated from plating/stripping-persuaded stress lifts the Na<sup>+</sup>-transports. Local hysteresis loop displays the typical polarization switching even after cycle operations corresponding to a high PFM value and a 150° shift for phase signals (Figure 21i). XPS shows notable changes for Ti<sup>4+</sup> and Si<sup>4+</sup> states, which indicates the existence of Ti and Si in lower valence for Na/NASICON-3BTO interface (Figure 21j). Figure 21k displays theoretical results for Na-ion distributions for electrode/electrolyte interfaces with/without ferroelectrics.<sup>[424]</sup> For the cathode/electrolyte interface, Na<sup>+</sup>-accumulated and Na<sup>+</sup>-deficient layers are separately formed for interfacial cathodes and electrolytes. To keep equilibria, Na<sup>+</sup>-moderately appears closer to Na<sup>+</sup>-accumulated layers inside the provisional electrolytes. Similar types of ion distributions are obtained for the anode/electrolyte interface. Preferred ferroelectric polarizations efficiently diminish the SCLs for electrolyte/ferroelectric/electrode interfaces. The substitution

of Sc<sup>3+</sup>, Yb<sup>3+</sup>, Zn<sup>2+</sup>, Mg<sup>2+</sup>, Al<sup>3+</sup>, Nd<sup>3+</sup>, Y<sup>3+</sup>, Ge<sup>4+</sup>, Ga<sup>3+</sup>, and Nb<sup>5+</sup> in the NASICON has also been researched to enhance the ion conductivity (maximum  $\sigma_{Na^+} \approx 2.44 \text{ mS cm}^{-1}$ ) and compatibility with Na-anodes.<sup>[426]</sup> Chi et al.<sup>[427]</sup> reported the stable Na//Sn/beta-alumina SEs/Sn//Na interface with 54  $\Omega \text{ cm}^{-2}$  area-surface-resistance (ASR) for 1000 h. Insertion of Sn interlayer for Na//beta-alumina interface shows the vivid lowest values of interfacial and charge-transfer resistances are 9.6 and 26.7  $\Omega \text{ cm}^{-2}$ , respectively, which indicates the modified interfaces are comparable to those of garnet-type SEs interfaces.<sup>[428]</sup>

Ceramic ( $\beta$ -Al<sub>2</sub>O<sub>3</sub> and NASICON-type oxides) SIEs display superior chemical stability for Na-metals; however, high ion-conductivity can be obtained when they are treated to nearby theoretical densities, which requires >1500 °C annealing temperature for long-time-interval and possess poor wettability with Na-metal owing to rough and rigid surfaces.<sup>[429]</sup> Previous reports confirm the Na-metal prefers the propagation with distinct grain boundaries for SEs generating dendritic growth with eventual cell failures (Figure 22a).<sup>[430]</sup> This is a source of controversy for SEs because ceramic/oxide SEs have an excess modulus of 200 GPa and offer beyond adequate elastic and shear modulus to repel Na-dendrites. Glass-ceramic SEs (Na<sub>3</sub>PS<sub>4</sub> or others) possess submissively soft surfaces with fewer precise grain boundaries owing to substantial amounts of glassy phases (5–50 vol%) that can fade the dendritic growth. However, interfacing with Na exhibits the unstable SEI (Figure 22b),<sup>[431]</sup> thus alloy type anodes (Na-Sn, Na-Au, or other) are preferred that can increase the voltage of anodes but degrades the energy density. Until now, no SEs can show all the requirements for high-energy SSBs regarding chemical, electrochemical, mechanical, and process parameters. Thus, researchers have reported mixed oxysulfide (Na<sub>3</sub>PS<sub>3</sub>O, Na<sub>3</sub>PS<sub>4–x</sub>O<sub>x</sub>; NSPO) based SEs//Na metal interfaces relative to pristine sulfide SEs.<sup>[432,433]</sup> This consists of fine grains, agglomerated powders, and oxygen-content-dependent structures illustrating dense and homogeneous smooth glasses even for nominal 300 MPa. Formation of homogenous bulk glassy phase is a

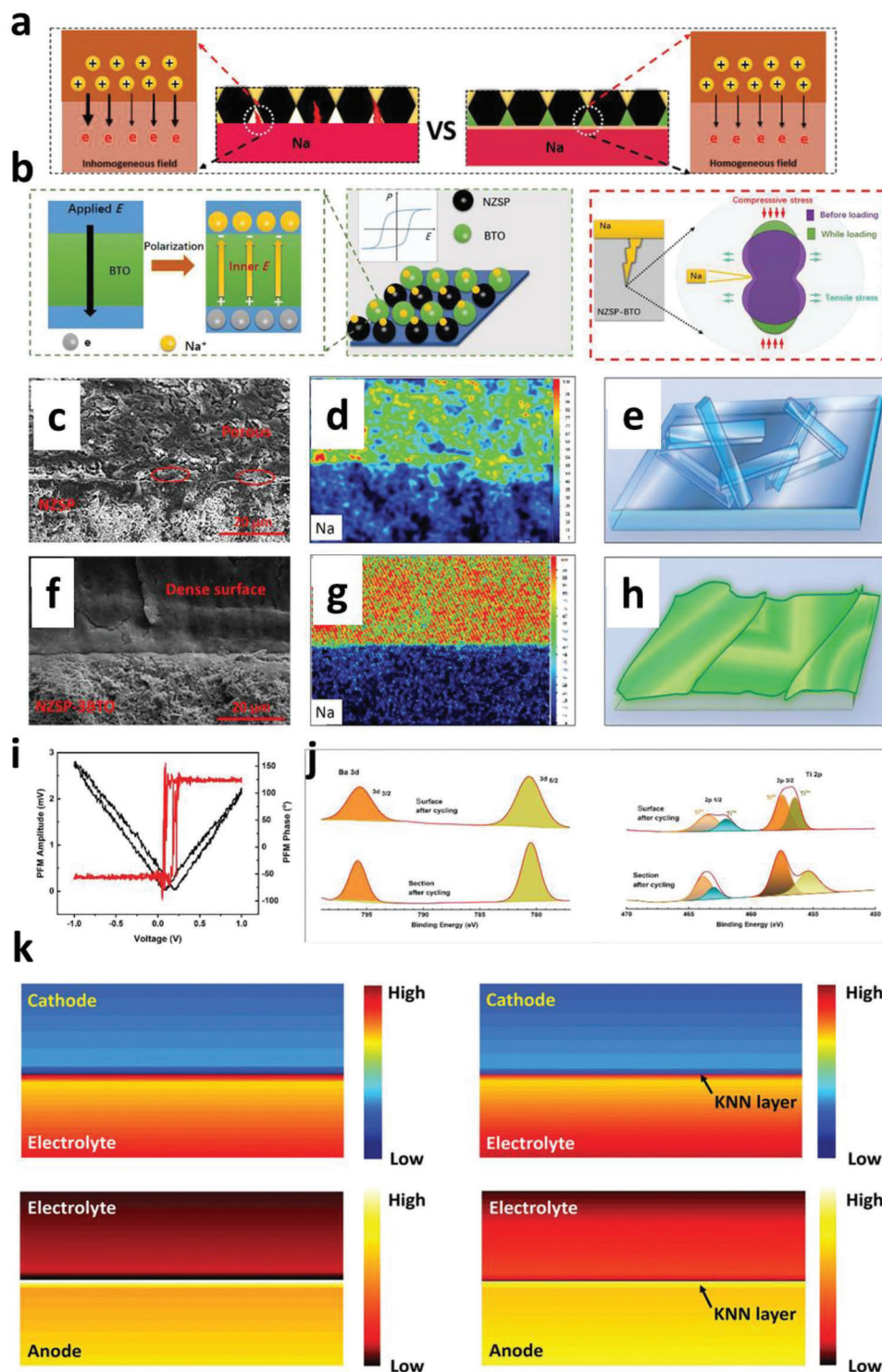


**Figure 21.** a) Na metal dendrite suppression kinetics for different SIEs. b) Ferroelectricity influence for  $\text{Na}^+$  distribution. c, f) SEM images and d, g) EDS maps for Na anode after cycling with Na/NZSP/Na and Na/NZSP-3BTO/Na cells. e, h) Schematic illustrations for surface analysis. i) Local PFM hysteresis loops of NZSP-3BTO after cycling. j) After cycling, Ba 3d and Ti 2p XPS spectra of the surface and section of NZSP-3BTO/Li cells. Reproduced with permission.<sup>[422]</sup> Copyright 2022, Wiley VCH. k) Simulated Na-ion concentration at cathode/SEs and anode/SEs interfaces with/without the  $\text{K}_{0.5}\text{Na}_{0.5}\text{NbO}_3$  layer. Reproduced under the terms of a Creative Commons CC BY 4.0 license.<sup>[424]</sup> Copyright 2022, Wiley VCH.



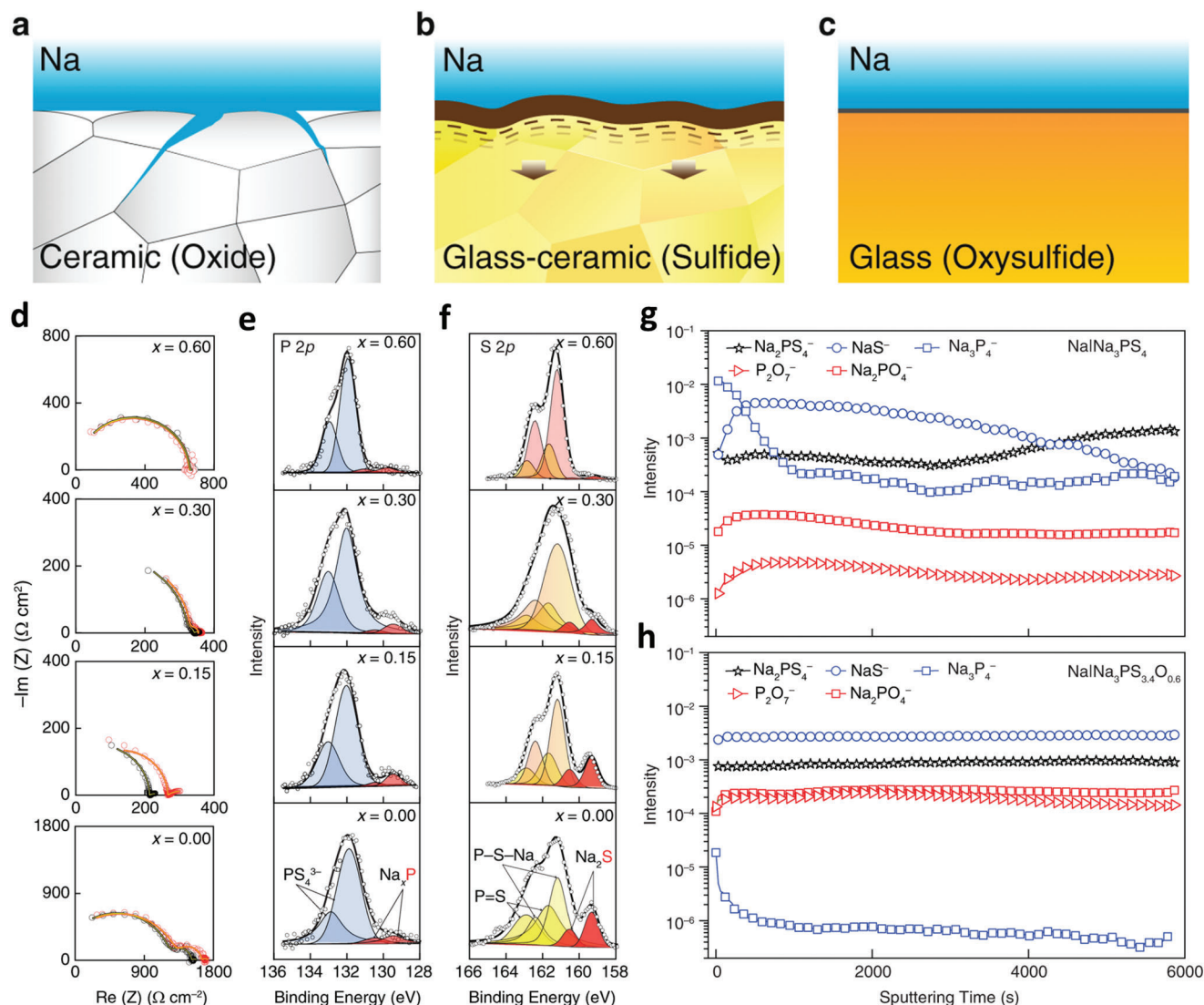


**Figure 22.** a) Na dendrites propagate along grain boundaries of oxide electrolytes, b) decomposition of sulfide-based glass-ceramic electrolyte contacting Na metal, c) homogeneous oxysulfide glassy electrolytes form a stable interface with Na metal. d) EIS spectra for Na//SEs//Na as prepared (black) and after 5 h (red). e, f) XPS spectra for P 2p (e) and S 2p (f) for Na//SEs interface. g, h) TOF-SIMS depth profiles for Na//Na<sub>3</sub>PS<sub>4</sub> and Na//Na<sub>3</sub>PS<sub>3.4</sub>O<sub>0.6</sub> interfaces. Reproduced under the terms of a Creative Commons CC BY 4.0 license.<sup>[432]</sup> Copyright 2022, Nature Publishing Group.

critical character to stabilize Na-metal in terms of mechanical, chemical, or electrochemical features (Figure 22c).

EIS (Na//NPSO//Na) displays mixed bulk and grain-boundaries resistance with capacitance (high-frequency); characteristic capacitance obtained from capacitance and interface resistance for SEI of Na/SEs (mid-frequency, Figure 22d). Figure 22e,f displays two doublet pairs of P 2p and S 2p spectra for Na//Na<sub>3</sub>PS<sub>4-x</sub>O<sub>x</sub>,  $x = 0, 0.15$ , and  $0.30$  SEs interfaces, which ascribes to the reduced sulfide and phosphide species. Theoretical and experimental results manifest that the reduced species of Na<sub>2</sub>S and Na<sub>3</sub>P have mixed ionic and electronic conducting behavior that cause decomposition of SEs with unstable SEI, well consistent to pristine Na<sub>3</sub>PS<sub>4</sub>, Na<sub>3</sub>SbS<sub>4</sub>, Na<sub>3</sub>PSe<sub>4</sub> SEs.<sup>[434,435]</sup> ToF-SIMS (Figure 22g,h) displays two strong signals of NaS<sup>-</sup> and Na<sub>3</sub>P<sup>-</sup> fragments for Na//Na<sub>3</sub>PS<sub>4</sub> interface. It is reduction of Na<sub>3</sub>PS<sub>4</sub> to Na<sub>2</sub>S and Na<sub>3</sub>P as:  $8\text{Na} + \text{Na}_3\text{PS}_4 \rightarrow 4\text{Na}_2\text{S} + \text{Na}_3\text{P}$ .

SEI thickness is  $\approx 1000\text{s}$  of Cs<sup>+</sup> etching. Whereas, Na<sub>3</sub>P<sup>-</sup> fragments intensity is three orders ( $10^{-5}$ ) lower in magnitude for Na//Na<sub>3</sub>PS<sub>3.4</sub>O<sub>0.6</sub> interface, which verifies the initial reduction of SEI suppresses for a factor of 1000 and SEI thickness reduced by a factor of 10 and later interface stabilizes with Na-metal plating. Self-passivating nature ascribes to the formation of insulating Na<sub>2</sub>O. Other fragments P<sub>2</sub>O<sub>7</sub><sup>-</sup>, Na<sub>2</sub>PO<sub>4</sub><sup>-</sup>, and Na<sub>2</sub>PS<sub>4</sub><sup>-</sup> are from the bulk Na<sub>3</sub>PS<sub>3.4</sub>O<sub>0.6</sub>.

Weng et al.<sup>[436]</sup> reported interface stabilities for Na//Na<sub>3</sub>SbS<sub>4</sub>//Na, Na//Na<sub>2.95</sub>Sb<sub>0.95</sub>W<sub>0.05</sub>S<sub>4</sub>//Na, and Na//Na<sub>2.95</sub>Sb<sub>0.95</sub>W<sub>0.05</sub>S<sub>3.9</sub>O<sub>0.1</sub>//Na cells, in which Na//Na<sub>2.95</sub>Sb<sub>0.95</sub>W<sub>0.05</sub>S<sub>3.9</sub>O<sub>0.1</sub>//Na interface suppresses the resistance due to the W and O co-doping. Oxygen doping for Na<sub>3</sub>SbS<sub>4</sub> via W and O co-doping alleviates the degradation of Na/SEI induced by W substitution. Interface formation kinetics among the Na<sub>3</sub>BS<sub>4</sub>//Na and Na<sub>3</sub>PS<sub>4</sub>//Na systems display a stationary Na plating/stripping with few nanometers



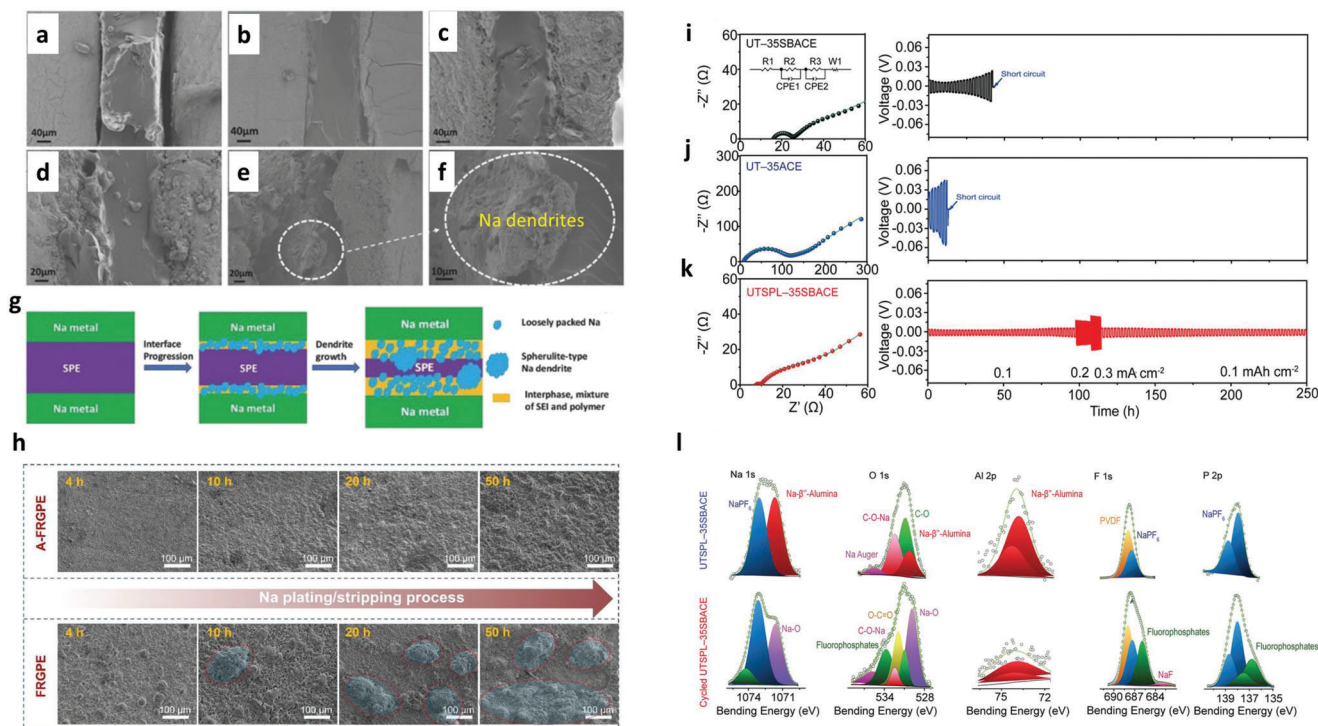


**Figure 23.** Cross SEM images for Na//SPEs//Na cells for interface kinetics: a) as-fabricated, b) after heating at 80 °C for 12 h, c) after 10 h cycle operations and d) after 100 h cycle operations, and e) cycled to short circuit and f) enlarged dendrite SEM. g) Schematics of the development and migration for Na//SPEs interfaces. Reproduced with permission.<sup>[446]</sup> Copyright 2018, Wiley VCH. h) Ex-situ SEM images for Na anodes with Na/A-FRGE/Na and Na/FRGE/Na cells. Reproduced with permission.<sup>[443]</sup> Copyright 2023, Elsevier. Impedance and symmetric cycles of i) Na/UT-35SBACE/Na, j) Na/UT-35ACE/Na, and k) Na/UTSP-35SBACE/Na cells. l) XPS data of the UTSP-35SBACE membrane before and after cycling in a symmetric Na/Na cell. Reproduced with permission.<sup>[444]</sup> Copyright 2023, Wiley VCH.

interphase passivation.<sup>[437]</sup> The orthorhombic  $\text{NaAlCl}_4$  SEs ( $\sigma_{\text{Na}^+} \approx 0.0039 \text{ mS cm}^{-1}$ ) demonstrates the 1D-preferred 2D  $\text{Na}^+$ -conduction pathways and voltage stability  $\approx 4 \text{ V}$  versus  $\text{Na}/\text{Na}^+$ .  $\text{NaCrO}_2\text{-Na}_3\text{Sn}/\text{NaAlCl}_4/\text{Na}$  displays 82.9% capacity retention after 500 cycles at 1C.<sup>[156]</sup> The  $\text{Na}_3\text{Sb}/\text{Na}_3\text{PS}_4/\text{Na}_3\text{Sb}$  alloy-based anode cells display stable and lowest overpotentials of 150 mV over 500 h relative to those of  $\text{Na}_{15}\text{Sn}_4/\text{Na}_3\text{PS}_4/\text{Na}_{15}\text{Sn}_4$  (1.8 V), which ascribes to the high electrochemical potential of  $\text{Na}_3\text{Sb}/\text{Na}_3\text{PS}_4$  SEs ( $\approx 0.4 \text{ V}$  versus  $\text{Na}/\text{Na}^+$ ) and lower interface resistance.<sup>[438]</sup> The composite of  $\text{Na}_3\text{SbS}_4$  (NSS, 30 wt%) with oxysulfide glass (NaPSO) demonstrates significantly strengthened interface stability with a polarization potential of 0.42 V after 200 h compared to those of NaPSO and NSS ( $>4 \text{ V}$  versus  $\text{Na}/\text{Na}^+$ ), which verifies the effective isolation of NSS from Na-metal enhancing the interface reactions.

Wang et al.<sup>[439]</sup> reports the interfacial kinetics for perfluoropolyether-terminated polyethylene oxide (PEO)-based block copolymer (EO10-PFPE,  $t_{\text{Na}^+}$  of 0.46 and  $\sigma_{\text{Na}^+}$  of  $0.047 \text{ mS cm}^{-1}$ ) SPEs/Na for safe and stable SMBs. Block copolymer tolerates self-assembled *bcc* nanostructures having high storage modulus for 100 °C, and PEO domains provide transport channels for high-salt concentrations (ethylene oxide/sodium = 8/2). Insertion of PFPE-species in PEO significantly impedes voids and dendrites formation implying stable SEI for Na-metal surface. This structure is highly advantageous for diminishing side reactions and restricting SEI growth,

suggesting a stable plate/strip.<sup>[440,441]</sup> Cell resistance for Na/Na cells with EO10-CTRL/Solupor exhibits continuous shifts to lower values with abrupt drops implying cell failures. Whereas with EO10-PFPE/Solupor displays ultra-stable cell resistance upon cycle operations for 1000 h, which verifies the formation of stable SEI among the EO10-PFPE and Na-metals.

The SMBs failure kinetics compared to LMBs are still not well investigated. Wei et al. explain that Na-metal's electrolyte depletion during operations is critical for SMBs failure besides Na-dendrites growth based short-circuit.<sup>[442]</sup> This feature was confirmed by observing voltage diversion rather than abrupt drops related to SMBs failure, and it ascribes to the relative softness of Na-metal (RT hardness  $\approx 0.5 \text{ MPa}$  and shear modulus  $\approx 3.3 \text{ GPa}$ ) compared to Li-metal. SEM images for as-fabricated, thermally treated, and failed cells and after 10 or 100 h cycling without abrupt voltage drops (Figure 23a–g) were analyzed to demonstrate failure kinetics. Larger gaps are obtained among the SPEs (thickness  $\approx 160 \mu\text{m}$ ) and Na-electrodes, which ascribes to the communal influence of fewer superlattice conformal loading for SPE on Na and the experimental splitting processes. Thermal treatment (80 °C for 12 h) successfully removes these gaps. After 10 h operations, the Na//SPEs interface exhibits an irregular surface with small voids nearby the interface. Notably, after 100 h operations, SPEs thickness was severely reduced from 160 to 60  $\mu\text{m}$ . Further, it decreases to  $\approx 30 \mu\text{m}$  after short-circuits with larger Na-dendrites on the SPEs surface. Specifically, there is no sign

of Na dendrites for the early stages of cycle operations (<100 h cycling). Such substantial reduction for SPEs is well relative to the reported SMBs.<sup>[442]</sup> Na metal//asymmetric flame-retardant GPE (A-FRGPE) have homogeneous dense topography relative to those of FRGPE (rough and dendrites with uncontrolled Na<sup>+</sup> flux, Figure 23h). Insertion of g-C<sub>3</sub>N<sub>4</sub> (pyridinic-N) in FRGPE delivers numerous lone-pairs to seize metal-ions,

promotes Na-salt dissociation, and decreases Na<sup>+</sup> nucleation overpotential, and molecular structure with porous channels suggest the enhanced Na<sup>+</sup>-transport.<sup>[443]</sup> EIS of Na//Na cells for UT-35SBACE, UT-35SBACE, and UTSP-35SBACE ultrathin CSEs displays total interface resistances of 66.8, 200.2, and 43.1 Ω, respectively (Figure 23i–k).<sup>[444–446]</sup> UTSP-35SBACE//Na interface exhibits lower polarization potential with stable cycling relative to others. Na 1s, O 1s, and Al 2p show peaks for 1071.8, 530.2, and 74 eV, corresponding to sodium-beta-alumina, which illustrates the stability of SBA particles with PVDF (Figure 23l).<sup>[446]</sup> Extensive efforts have been performed to develop different types of polymer SPEs and hybrids with ceramics or sulfides such as biopolymers or celluloses or PEO- or PVDF-NaTFSI or NaClO<sub>4</sub>, PEO-NaClO<sub>4</sub>-TiO<sub>2</sub>, PEO-NSS, PEO-NPSO, or PEO-NASICON and Na-alloys anodes such as (Na-Mg, Na-Sn, Na-Sb, Na-Au, Na-Ag, etc.) to stabilize the Na-metal/SPEs or CSEs interfaces to obtain overall high performances for SMBs or SIBs.<sup>[439–449]</sup> However, poor ion conductivity, oxidation/reduction potential, and limited thermal/electrochemical stabilities inhibit their practical applications.

The comprehensive analysis clarifies that the primary goal for next-generation SMBs or SIBs is obtaining long-time operations with retaining high capacity or energy density and safety performances at affordable cost. Poor ion conductivity of SEs and deprived wettability for Na-metals demonstrate unsatisfactory performances relative to those of liquid counterparts. Considerable interfacial resistance for Na//SEs interfaces limits the homogeneous Na-electrodepositions and deteriorates chemical instability with high voltage hysteresis. Solid/solid interface or inside SEs have several physical/chemical contacts among the Na//SEs with multiple grain boundaries or defects, which results in uncontrolled dendritic growth. Thus, the controlled Na-nucleation with uniform depositions for multiple solid interphases is crucial for all solid-state SMBs future.

#### 7.1.4. Potassium-Ion Batteries (KIBs)

Potassium batteries offer prospective alternatives for LIBs or SIBs for grid-scale energy storages owing to the low cost, earth abundance, and low K/K<sup>+</sup> electrode potential (−2.93 V versus SHE, comparable to LIBs −3.04 V versus SHE) relative to those of Na, which implies K-batteries has a higher voltage, power or energy densities.<sup>[450,451]</sup> However, two fundamental challenges, such as poor K//SEs interfacial contacts and limited areal capacity caused by the intrinsic low melting point or poor mechanical strength of K, dendrites growth, and small K self-diffusion coefficient impedes their practical applications.<sup>[283]</sup> The low affinity of K with SEs provides the random distribution of micropores for interfaces. Thus charge flux localizes anomalously upon application of current at the interface with significant voltage polarization, dendritic growth, and lower areal capacity. Previous

efforts have been carried out to improve K metal wettability by inserting sodiophilic or lithiophilic interlayers or composites with reduced surface energy for low interface resistance and conformal interface.<sup>[301,452]</sup> However, the delamination of the K//SEs interface occurs for repetitive deposition/dissolution to the initial conformal interface with unsatisfactory CCD and areal capacities, which ascribes to sluggish self-diffusion kinetics of K.<sup>[452]</sup> Metal atoms at the interface convert to metal ions under applied current and transfer in the SEs with the formation of interface vacancies. This illustrates the growth of larger micropores due to poor self-diffusion coefficients of metals that cannot fill the vacancies from transferred metal ions. Several approaches have been reported for limiting interface delamination, such as increased pressure or temperature, composite SEs, 3D-interconnected interfaces, etc. Carbonaceous materials such as carbon allotropes, graphene, polymers, or CNTs show the feasibility of improving K-diffusion kinetics and sustainability of de-/intercalation chemistries.<sup>[452–454]</sup>

Wu et al.<sup>[450]</sup> reports the 3D interconnected and conductive network for K-10% reduced graphene oxide (RGO) composite ultrathin metal anodes (50 μm) with favorable K<sup>+</sup>-diffusion coefficient ( $2.38 \times 10^{-8} \text{ cm}^2 \text{ s}^{-1}$ ) toward high-temperature stability (200 °C), which illustrates the fast/versatile K-migration pathways, alleviates the leakage of fused K, and suppress structure deformations enabling homogeneous distribution and thermo-stability of K. K-10% RGO symmetric cells with β/β'-Al<sub>2</sub>O<sub>3</sub> SEs confirms the stable K-plate/stripping with lower interface resistance of 1.3 Ω cm<sup>2</sup>, high areal capacity (11.86 mAh cm<sup>−2</sup>), and CCD (2.8 mA cm<sup>−2</sup>). **Figure 24a–c** exhibits conformal K-10% RGO//SE interface for the initial state without micropores; even for 3 mAh cm<sup>−2</sup> K-stripping interface is well intact, and for 6 mAh cm<sup>−2</sup> interface is still well retained with the formation of several micropores. Interface inhomogeneity manifests uneven current distribution due to voids at the interface upon cycling and self-diffusion kinetics that are unable to replenish transported K-ions from interphase to SEs.<sup>[455]</sup> Like Li//SEs,<sup>[456]</sup>  $J_D$  defines the K<sup>+</sup>-flux based on K self-diffusion in metal foil and  $J_C$  the K<sup>+</sup>-flux in SEs due to applied current density. For  $J_D < J_C$ , metal ions from nearby surfaces distribute faster relative to the bulk with the formation of voids and strong delamination of metal anodes from SEs after continuous cycling, which illustrates cell failure for lower current densities (Figure 24d–f). For  $J_D > J_C$ , the metal ions firmly migrate from the bulk by replenishing the adjacent ions that can disperse in SEs. This results in the simultaneous preservation of intact interfaces and voids creation for the bulk of anodes (Figure 24g–i). K-metal provides high energy relative to other reported anodes (carbon, Sn-Sb, metal-carbon, oxides, MoSSe). Monoclinic-KFeHCF displays flat potential plateaus for galvanostatic K<sup>+</sup> extraction/insertion through two-phase reactions. In contrast, cubic-KFeHCF has tangential curves via a single-phase regime verifying superior potential stabilities for K.<sup>[457]</sup>

Theoretical calculations verify crystal structures, cation-anion interactions, and defects influence the interface transport for borohydride SEs//K.<sup>[458]</sup> Neutral NH<sub>3</sub>B<sub>3</sub>H<sub>7</sub> includes the H<sup>+</sup> (in NH<sub>3</sub>) and B<sub>3</sub>H<sub>8</sub><sup>−</sup> anions with hydritic H that can combine across dihydrogen bonding. The B<sub>3</sub>H<sub>8</sub><sup>−</sup>·NH<sub>3</sub>B<sub>3</sub>H<sub>7</sub> complex has more positive electrostatic potentials (−4.48 to −1.55 eV) relative to the B<sub>3</sub>H<sub>8</sub><sup>−</sup> anions (−5.37 to −4.05 eV), which illustrates weak interactions for K<sup>+</sup> than B<sub>3</sub>H<sub>8</sub><sup>−</sup>.<sup>[459]</sup> Thus coordination

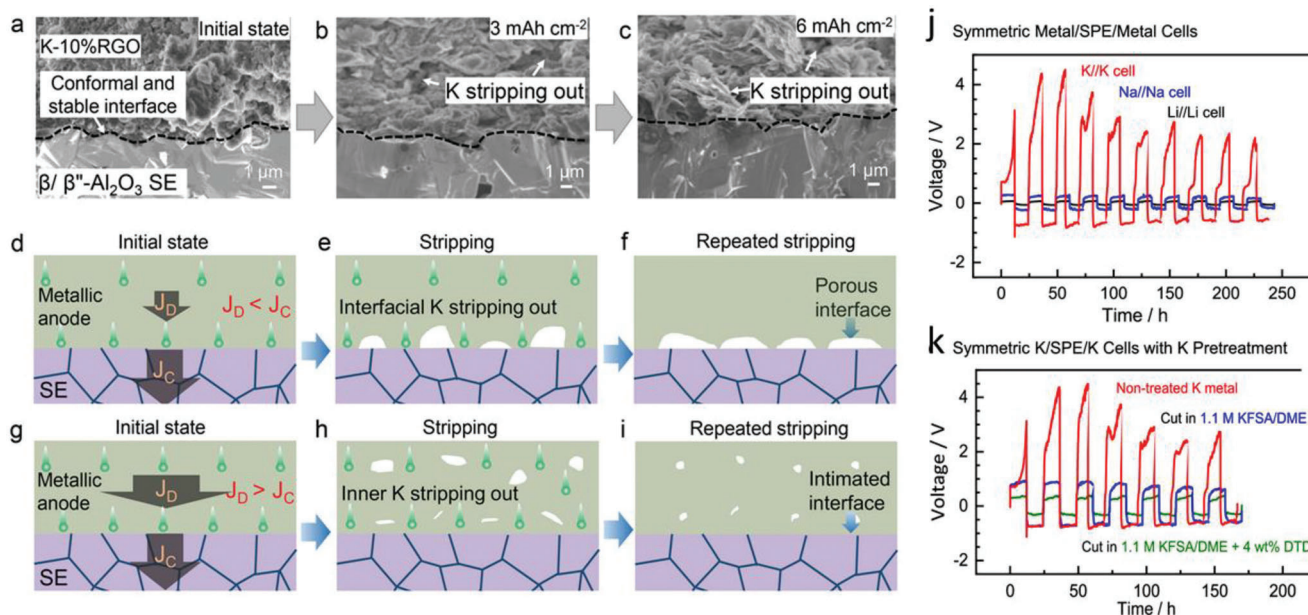


**Figure 24.** SEM images of K–10% RGO/SEs interface for a) initial states, b) K strips for 30 h, and c) for 60 h. Schematics of interfacial structure evolution after strips under two different conditions, d–f)  $J_D < J_C$  and g–i)  $J_D > J_C$ . Reproduced with permission.<sup>[450]</sup> Copyright 2023, Wiley VCH. Voltage profiles of symmetric (j) Li/SPE/Li, Na/SPE/Na, and K/SPE/K cells (non-treated) and (k) K/SPE/K cells with pretreated K metal. Reproduced under the terms of a Creative Commons CC BY 4.0 license.<sup>[195]</sup> Copyright 2022, American Chemical Society.

of  $\text{NH}_3\text{B}_3\text{H}_7$  exhibits reduced binding interactions among the  $\text{K}^+$  and  $\text{B}_3\text{H}_8^-$  facilitating superior mobility for  $\text{K}^+$  ions ( $t_{\text{K}^+} \approx 0.93$ ). EWs for  $\text{KB}_3\text{H}_8 \cdot \text{NH}_3\text{B}_3\text{H}_7$ ,  $\text{KB}_3\text{H}_8 \cdot 0.5\text{NH}_3\text{B}_3\text{H}_7$ , and  $\text{KB}_3\text{H}_8 \cdot 1.5\text{NH}_3\text{B}_3\text{H}_7$  are of 1.2–3.5, 1.4–3.3, and 0.9–3.2 V, respectively. For increasing EWs, incorporating oxides such as  $\text{SiO}_2$  or  $\text{Al}_2\text{O}_3$  is the promising approach owing to strong interfacial reactions among the  $\text{KB}_3\text{H}_8 \cdot \text{NH}_3\text{B}_3\text{H}_7$  and oxides. Notably, long operations for K-ion SEs are very scarce due to the high reactivity of K-metals. Zheng et al.<sup>[460]</sup> presented antiperovskite  $\text{K}_3\text{OI}$  and  $\text{K}_{2.9}\text{Ba}_{0.05}\text{OI}$  ( $\sigma_{\text{K}^+} \approx 3.5 \text{ mS cm}^{-1}$ ) SEs for interface compatibility analysis. For  $\text{K}_3\text{OI}$ , K-ions migrate through K-vacancies and larger vacancies nearby the disordered I–O sites, whereas  $\text{K}_{2.9}\text{Ba}_{0.05}\text{OI}$  greatly reduces  $E_a$  of 0.36 eV with K-ion migration from K vacancies and the possible anion disorder activated for higher temperatures. Compared to LGPS, LPS, NPS, and LLZO for Li or Na, for  $\text{K}_3\text{OI}$ , O, and I have oxidation states of –2 and –1 that cannot reduce further by K-metal or K-alloy anodes.<sup>[461]</sup> K// $\text{K}_{2.9}\text{Ba}_{0.05}\text{OI}$ //K symmetric cell shows 50 mV overpotential for  $0.5 \text{ mA cm}^{-2}$ . Further,  $\text{K}_3\text{Sb}_4\text{O}_{10}(\text{BO}_3)$  SEs show displacement of  $\text{K}^+$  via 1D interconnected channels with good interface stability (low  $E_a$  and interface resistance).<sup>[462]</sup> The  $\text{K}_2\text{Fe}_4\text{O}_7$  SEs with 3D open frameworks for  $\text{K}^+$ -ion transfer containing  $\text{FeO}_6$  octahedral (oct) and  $\text{FeO}_4$  tetrahedral (tet) sites along vertices and edges enables rapid transport for K-ions with the stable interface over EW of 5 V versus K/K<sup>+</sup>.<sup>[463]</sup> Besides,  $\text{K}_2\text{M}_2\text{TeO}_6$  (M = Ni, Mg) and  $\text{KC}_8$ // $\text{KNH}_2$ -based SIEs were also reported for  $\text{K}^+$ -ion transport stabilities.<sup>[464,465]</sup>

Li//SPE and Na//SPE cells exhibit 50 and 280 mV polarization for respective depositions/dissolutions, whereas K//SPE cells display unstable voltage polarizations with larger polarization >1 V, which illustrates larger polarizations are from higher K//SPEs interfacial resistance (Figure 24j).<sup>[195]</sup> Interface resis-

tances for Li, Na, and K are  $10^3$ ,  $10^4$ , and  $10^5 \Omega \text{ cm}^2$ , respectively, which verifies the degree of polarization.<sup>[466]</sup> Further, reduced plate/strip polarizations ascribe the  $\text{FSA}^-$  decomposition and K//K cells high polarization even after 200 h decreases reliability.<sup>[467,468]</sup> The optimal molar ratio for  $[\text{EO}]/[\text{K}^+]$  is 10 for PEO-KFSI SPEs with  $\sigma_{\text{K}^+} \approx 0.27 \text{ mS cm}^{-1}$  for 60 °C.<sup>[467]</sup> Pretreatment for K-metal exhibits reduced interfacial resistance with efficient passivation of the surface by reductive decomposition of  $\text{FSA}^-$  ions, which obtains polarization of 300 mV with stable K-metals (Figure 24k). PPC-KFSI-cellulose SPEs confirm reduction and oxidation peaks of –0.3 and 0.21 V versus K/K<sup>+</sup> with  $\approx 100\%$  CE suggests SPEs interface stability with K-metal.<sup>[469]</sup> The  $(\text{PEO})_{30}/\text{KBPh}_4$  SPEs with Prussian blue electrodes show reversible  $\text{K}^+$ -ion de-/intercalation with a reversible 20 mAh g<sup>–1</sup> capacity and lower-voltage hysteresis.<sup>[470]</sup> Rayung et al.<sup>[471]</sup> reported polyurethane acrylate-based SPE due to inspiration of coordination of characteristic of N–H, C=O, and C–O–C groups for  $\text{K}^+$  stabilization; however, it limits EW  $\approx 2$  V. PEO-based SPEs with K-salts (such as KCl, KFSI, KBr,  $\text{CH}_3\text{COOK}$ ), polyester-based ([–O–(C=O)–O–]) and polyurethane ([–NH–(C=O)–O–]) SPEs and others (PVP, PVA) have been reported for  $\text{K}^+$  interface kinetics; however, their poor ion-conductivity ( $10^{-5}$ – $10^{-8} \text{ S cm}^{-1}$ ) and operating temperatures, and EWs inhibits the chemical and electrochemical stabilities against K-metals.

Zhang et al.<sup>[472]</sup> reported poly(vinylidene fluoride-hexafluoropropylene) potassium bis(fluorosulfonyl)imide polyacrylonitrile (PVDF-HFP-KFSI@PAN) GPEs ( $\sigma_{\text{K}^+} \approx 0.36 \text{ mS cm}^{-1}$ ) for K//GPEs interface with stable SEI and  $\text{K}^+$ -plating/stripping over 1200 h. It displays a maximum plating capacity of  $300 \text{ mAh cm}^{-2}$  for K/K<sup>+</sup> cells relative to those of previous reports (K-rGO@3D-Cu, K-ACM, and Sn@3D-K of 125, 116.5,  $50 \text{ mAh cm}^{-2}$  in liquid electrolytes). Further, the



cardanol-based GPEs with 0.67–0.78 MPa modulus show  $\sigma_K^+ \approx 0.36 \text{ mS cm}^{-1}$  and EW of  $-0.2\text{--}5 \text{ V}$  versus  $\text{K/K}^+$ .<sup>[473]</sup> Overall, solid-state KIBs are in the initial stages due to several limitations from SEs and K-metal anodes regarding ion-conductivity, EWs, and K-metal compatibilities. Comprehensive understanding vindicates the rational design of advanced SEs with stable SEI, stable for high voltage cathodes, and a wide operating temperature range for KIBs will be the future research approach. Further stabilization of electrode/electrolyte interface for continuous  $\text{K}^+$ -plate/strip using artificial SEI or carbon-based, metal-alloys, or oxides-based anodes is also necessary to consider as a major focus.

## 7.2. Multivalent-Ions Battery Technologies

### 7.2.1. Magnesium-Ion Batteries (MIBs)

Multivalent ion batteries (Mg, Zn, Al, Ca) offer great interest due to high energy densities by multi-electron reactions relative to those of monovalent Li-, Na-, and K-ion batteries.<sup>[474–477]</sup> Among these, magnesium (Mg) batteries offer promising candidates for large-scale energy storage owing to their intrinsic merits: 1) high volumetric capacity of  $3830 \text{ mAh cm}^{-3}$  (versus  $2060 \text{ mAh cm}^{-3}$  for Li), 2) insensitive dendrites formation behavior and low air-sensitivity compared to those of Li, Na or K metals, 3) lower electrode potential ( $-2.37 \text{ V}$  versus SHE) relative to those of Zn and Al, 4) high mechanical yields and low chemical reactivity, 5) light metal (density  $\approx 1.74 \text{ g cm}^{-3}$ ), abundant resources, and low cost.<sup>[478,479]</sup> However, MIBs are far from their commercial prospects due to several fundamental issues, such as sluggish solid-state diffusion kinetics of  $\text{Mg}^{2+}$  ions, poor working voltage, and poor cycle life.<sup>[480,481]</sup> Formation of a non-conductive passivation layer over Mg anode with polar aprotic solvents and magnesium salts (magnesium perchlorate, magnesium tetrafluoroborate, TFSI, imide, carbonate, and nitrile), poor EWs, CCs instability, and polysulfides formation prevents migration of  $\text{Mg}^{2+}$  ions during plate/strip processes.<sup>[480,481]</sup> Thus, obtaining reversible  $\text{Mg}^{2+}$ -depositions/strips with compatible electrolyte/electrode interfaces is critically essential. SEs or artificial protection layer with fast  $\text{Mg}^{2+}$  mobility is favorable for alleviating these challenges.<sup>[482]</sup>

Extensive efforts have been explored for Mg-ion mobility in solids owing to their poor transport kinetics  $\sigma_{\text{Mg}}^{2+}$ , and sluggish diffusion kinetics.<sup>[482]</sup> Canepa et al.<sup>[143]</sup> reported the magnesium scandium selenide spinel ( $\text{MgSc}_2\text{Se}_4$ ) SIEs with  $\sigma_{\text{Mg}}^{2+}$  of  $0.01\text{--}0.1 \text{ mS cm}^{-1}$ . Spinel structures show Mg atoms undergo tet-sites instead of favorable oct-sites with reducing  $E_a$  for  $\text{Mg}^{2+}$ -ions diffusion. Theoretical calculations explain migration barriers trend for different anions as  $\text{O}^{2-} > \text{S}^{2-} > \text{Se}^{2-} > \text{Te}^{2-}$ .<sup>[483]</sup> Lower the migration barriers – higher the volume per anion; a higher volume of anions retain large electric polarizability with limiting cation mobility. In spinel structures of  $\text{MgX}_2\text{Z}_4$  ( $\text{Z} = \text{S, Se and X} = \text{In, Y, Sc}$ ), ion transport among two tet-sites ensues by vacant oct-sites shared with tet-sites illustrates the migration topology tet–oct–tet. Migration barriers are evaluated by migration-ion energy shared to triangular (tri) surfaces of oct- and tet-sites subjective to dimensions and anions of tri-surfaces.<sup>[484]</sup> Several chalcogenides such as  $\text{MgSc}_2\text{S}_4$ ,

$\text{MgIn}_2\text{S}_4$ ,  $\text{MgSc}_2\text{Se}_4$ ,  $\text{MgY}_2\text{Se}_4$ ,  $\text{ZnSc}_2\text{S}_4$ ,  $\text{ZnY}_2\text{S}_4$ ,  $\text{ZnIn}_2\text{S}_4$ ,  $\text{ZnY}_2\text{Se}_4$ ,  $\text{MgY}_2\text{S}_4$ ,  $\text{MgIn}_2\text{Se}_4$ ,  $\text{ZnSc}_2\text{Se}_4$ ,  $\text{ZnIn}_2\text{Se}_4$ ,  $\text{MgSc}_2\text{Te}_4$ , and  $\text{MgY}_2\text{Te}_4$  have been considered for investigation, in which  $\text{MgY}_2\text{S}_4$  ( $\approx 360 \text{ meV}$ ),  $\text{MgY}_2\text{Se}_4$  ( $\approx 361 \text{ meV}$ ), and  $\text{MgSc}_2\text{Se}_4$  ( $\approx 375 \text{ meV}$ ) has superior conduction kinetics. Migration barriers of  $361\text{--}375 \text{ meV}$  ( $\text{MgY}_2\text{Se}_4$  and  $\text{MgSc}_2\text{Se}_4$ ) suggest greater Mg mobility equivalent to Li-conductors such as LISICON-like ( $\approx 200\text{--}500 \text{ meV}$ ) and Garnets ( $\approx 400\text{--}500 \text{ meV}$ ).<sup>[483–486]</sup> Zn migration barriers are larger for S/Se spinels ( $>700 \text{ meV}$ ) than those of Mg analogs, clarifying the less favorable coordination (Figure 25a). EIS (Figure 25b) displays high mobility of  $\text{Mg}^{2+}$  for Ta// $\text{MgSc}_2\text{Se}_4$ //Ta cells with mixed ion-conduction behavior. EIS explains coupling of Jamnik–Maier circuit elements in series possesses the bulk and grain boundary contributions. Wang et al. reported 5 and 10 wt% Se-rich  $\text{MgSc}_2\text{Se}_4$  SEs to possess similar  $\sigma_{\text{Mg}}^{2+}$  with  $\text{MgSc}_2\text{Se}_4$  SEs, whereas electronic conductivity is severely increased.<sup>[141]</sup> Further, substituting  $\text{Sc}^{3+}$  with  $\text{Ti}^{4+}$  or  $\text{Ce}^{4+}$  confirms the decrease in electronic conductivity and increase in  $\sigma_{\text{Mg}}^{2+}$  that is favorable for reversible  $\text{Mg}^{2+}$ -plate/stripping.<sup>[143]</sup> Koettgen et al.<sup>[487]</sup> reported  $\text{Mg}^{2+}$  mobility and stability kinetics with  $\text{MgLn}_2\text{X}_4$  ( $\text{Ln} = \text{Lu, Tm, Er, Ho, Dy, Tb, Sm, Pm, Nd, Pr, La, and X} = \text{S, Se}$ ). The  $\text{Mg}^{2+}$  migration barriers were reduced with linear behavior for lanthanides except for  $\text{MgLa}_2\text{S}_4$ , which ascribes the Mg destabilization for oct-states.

Energy profiles display localized, stable sites for the spinel structure of Mg is tet-sites in all materials. The tri has the smallest Mg–X distance and highest energy (transitions) states concerning oct and tet local minima. It suggests preferable excess tet- or small oct-environments for these  $\text{Mg}^{2+}$ -chalcogenides. Typically, stable materials have  $E_{\text{hull}} = 0$ , and fabricated sulfides and selenides are metastable due to  $E_{\text{hull}} = 50 \text{ meV}$  per atom, which ascribes low surface energy and preferential nucleation.<sup>[488]</sup>  $\text{MgLu}_2\text{S}_4$ ,  $\text{MgLu}_2\text{Se}_4$ ,  $\text{MgTm}_2\text{Se}_4$ ,  $\text{MgEr}_2\text{Se}_4$  and  $\text{MgTm}_2\text{S}_4$ ,  $\text{MgEr}_2\text{S}_4$ ,  $\text{MgHo}_2\text{Se}_4$  shows  $E_{\text{hull}} < 25$  and  $< 50 \text{ meV}$  per atom with lowest energy structures, respectively. Spinel structures confirm the vacant oct-sites among the two tet-sites is the  $\text{Mg}^{2+}$ -migration pathway. Imanaka et al.<sup>[489]</sup> reported  $\text{Mg}^{2+}$ -conduction behavior for  $\text{MgZr}_4\text{P}_6\text{O}_{24}$ ,  $\text{Zr}_2\text{O}(\text{PO}_4)_2$ , and  $\text{Mg}_{1+x}\text{Zr}_4\text{P}_6\text{O}_{24+x} + x\text{Zr}_2\text{O}(\text{PO}_4)_2$  composites ( $x = 0.4$ ) for  $800^\circ\text{C}$ , in which composite achieves 2.3 times higher  $\sigma_{\text{Mg}}^{2+}$  than  $\text{Mg}_{1.15}\text{Zr}_4\text{P}_{5.7}\text{Si}_{0.3}\text{O}_{24}$ .

Since Mohtadi et al.<sup>[153]</sup> displayed full inorganic and halide-free SIEs enabling Mg reversible plating/stripping,  $\text{Mg}(\text{BH}_4)_2$ -based several electrolytes such as  $\text{Mg}(\text{BH}_4)(\text{NH}_2)$ ,  $\text{Mg}(\text{BH}_4)_2(\text{en})$ ,  $\text{Mg}(\text{BH}_4)_2(\text{NH}_3)$ ,  $\text{Mg}(\text{BH}_4)(\text{BH}_3\text{NH}_2)_2$ ,  $\text{Mg}(\text{BH}_4)_2 \cdot x\text{NH}_3$ , and  $\text{Mg}(\text{BH}_4)_2 \cdot x\text{NH}_3\text{-MgO}$  have been investigated. The monoclinic composite [ $\text{Mg}(\text{BH}_4)_2 \cdot 1.5\text{THF-MgO}(75\text{wt}\%)$ ] SEs with  $\sigma_{\text{Mg}}^{2+}$  of  $10^{-4} \text{ S cm}^{-1}$  for  $70^\circ\text{C}$ ,  $t_{\text{Mg}}^{2+}$  of 0.99, and EWs of  $\approx 1.2$  versus  $\text{Mg/Mg}^{2+}$  have been demonstrated.<sup>[490]</sup> The analogs of amine magnesium borohydride composites are also reported for improving the  $\sigma_{\text{Mg}}^{2+}$  as  $\text{Mg}(\text{BH}_4)_2 \cdot x\text{NH}_3$  with MgO nanoparticles. The larger surface area of MgO confines the molten state and prevents crystallization with retaining  $\sigma_{\text{Mg}}^{2+}$ .<sup>[76,491]</sup> CV (Figure 25c) shows the initiation of anodic current movement at  $\approx 1.2 \text{ V}$  versus  $\text{Mg/Mg}^{2+}$ , which illustrates oxidation SEs. It is less apparent for increased cycles signifying the stable interface formation for reversible  $\text{Mg}^{2+}$  plating/stripping. Figure 25d displays the electrochemical compatibility of  $\text{Mg}(\text{BH}_4)_2 \cdot 1.5\text{THF-MgO}$  (75 wt%) SEs with Mg with steady polarizations.  $\text{Mg}(\text{BH}_4)_2$ -based SIEs

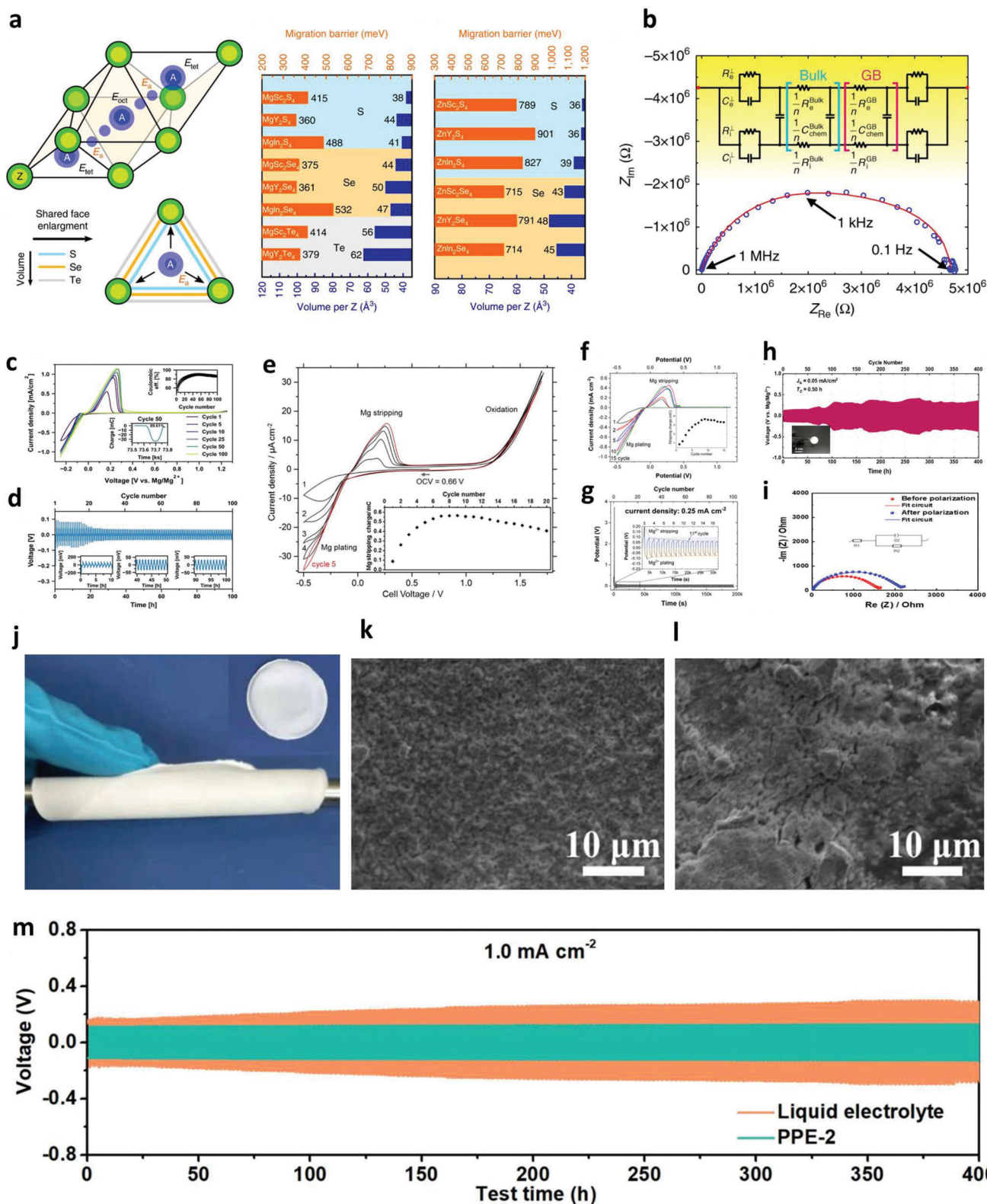


**Figure 25.** a) Theoretical calculations for Mg and Zn migration barriers in sulfides, selenides, and telluride's  $AX_2Z_4$  spinel's (with  $A = \text{Mg}$  or  $\text{Zn}$ ). b) EIS for the  $\text{Ta}/\text{MgSc}_2\text{Se}_4/\text{Ta}$  cell. Reproduced under the terms of a Creative Commons CC BY 4.0 license.<sup>[143]</sup> Copyright 2017, Nature Publishing Group. c) CV and d) Plate/stripping cycles for  $\text{Mg}/\text{Mg}(\text{BH}_4)_2 \cdot 1.5\text{THF} \cdot \text{MgO}(75\text{wt}\%)/\text{Mg}$  cells at  $55^\circ\text{C}$ . Reproduced with permission.<sup>[490]</sup> Copyright 2022, Wiley VCH. e) CVs for  $\text{t}/\text{Mg}(\text{en})_1(\text{BH}_4)_2/\text{Mg}$  cell at  $60^\circ\text{C}$ . Reproduced under the terms of a Creative Commons CC BY license.<sup>[493]</sup> Copyright 2017, Nature

consist of Mg-ions at tet cages surrounded by four  $\text{BH}_4^-$  anions ascribes the lower conductivity, whereas, for high temperatures, tet  $\text{Mg}^{2+}$  coordinates two  $\text{BH}_4^-$  and two  $\text{NH}_2^-$  anions increase the  $\sigma_{\text{Mg}}^{2+}$  and Mg//SIEs compatibility.<sup>[492]</sup> Magnesium ethylenediamine borohydride ( $\text{Mg}(\text{en})_1(\text{BH}_4)_2$ ) SIEs with coordination of  $\text{Mg}^{2+}$ -ions and neutral bidentate ethylenediamine ligands in the ratio of one bidentate ligand per metal atoms show  $\sigma_{\text{Mg}}^{2+} \approx 0.05 \mu\text{S cm}^{-1}$  at 30 °C that stems transport of  $\text{Mg}^{2+}$  ions. CV displays  $-0.2 \text{ V}$  versus  $\text{Mg}/\text{Mg}^{2+}$  for Mg plating and  $0.5 \text{ V}$  versus  $\text{Mg}/\text{Mg}^{2+}$  for reverse stripping, inducing Mg-interface capability (Figure 25e).<sup>[493]</sup> Higashi et al.<sup>[149]</sup> also verified the oxidative potential of  $\text{Mg}(\text{BH}_4)(\text{NH}_2)$  SEs is  $3 \text{ V}$  versus  $\text{Mg}/\text{Mg}^{2+}$ . Further,  $\text{Mg-S}$ ,  $\text{Mg-FeS}$ , and  $\text{Mg-Ag}_2\text{S}$ -based cells with  $\text{Mg}(\text{BH}_4)(\text{NH}_2)$  SEs show OCV of 1.4, 1.2, and 1.3 V at 150 °C, respectively. Theoretical calculations confirm the 2D Mg-diffusion channels are perpendicular to the c-axis. The Mg-atoms transfer to the interstitial sites by forming Frenkel pairs for relatively smaller energies is the Mg-migration precursor states.

CVs of  $\text{Au}/1.6\text{NH}_3@\text{MgO}/\text{Mg}$  asymmetric cell display an increase in plate/strip current for the initial 10 cycles implying interface contact for electrode/SEs enhances upon initial cycles without electrolyte decompositions from 0.5–1.2 V. Upon 20 cycles, potential range increases for  $-0.5$  to  $2.5 \text{ V}$  with irreversible oxidation for  $>1.2 \text{ V}$ , which indicates stable interface layer that conducts  $\text{Mg}^{2+}$  ions with enhancing electrochemical stability (Figure 25f,g). Golub et al.<sup>[494]</sup> stated diffraction of  $\text{Mg}(\text{en})_2(\text{BH}_4)_2$  is achievable for the ratio of  $\text{Mg}(\text{en})_3(\text{BH}_4)_2$  and  $\text{Mg}(\text{BH}_4)_2$  (2:3) by using cryomilling. The formed  $\text{Mg}(\text{en})_2(\text{BH}_4)_2$  phase is thermodynamically favorable, while  $\text{Mg}(\text{en})1.2(\text{BH}_4)_2$  is a meta-stable intermediate. NASICON ( $\text{Mg}_{0.5}\text{Zr}_2(\text{PO}_4)_3$ ) is also fabricated by sol-gel method with  $\sigma_{\text{Mg}}^{2+} \approx 1$  and  $71 \mu\text{S cm}^{-1}$  for RT and 500 °C.  $\text{Mg}_{0.5}\text{Zr}_2(\text{PO}_4)_3$  SEs have EWs of 2.50 V versus  $\text{Mg}/\text{Mg}^{2+}$  and a transfer number of 0.69.<sup>[495]</sup> Magnesium bis(oxalate) borate-based SEs also reported.<sup>[496]</sup> Zheng et al.<sup>[497]</sup> reported  $\text{MG3}@ \text{MOF-199}$  and  $\text{MG3}@ \text{MOF-5}$  based SEs as Mg-ion conductors with  $\sigma_{\text{Mg}}^{2+}$  of 1.93 and  $0.056 \mu\text{S cm}^{-1}$  with  $E_a$  of 0.234 and 0.568 eV, respectively. Ion conduction is strongly influenced by the mole fraction of Mg-salts and the pore size of frameworks.

Deivanayagam et al.<sup>[498]</sup> reported CPEs with mixture of PVDF-HFP,  $\text{Mg}(\text{ClO}_4)_2$ , 1-butyl-1-methylpyrrolidinium bis(trifluoromethyl)sulfonyl imide, and  $\text{TiO}_2$  nanoparticles. It offers  $0.16 \text{ mS cm}^{-1}$  ion-conductivity and stable Mg//Mg cycle operations for 400 h with lower overpotentials of 0.1–0.3 V comparable to liquid counterparts with stable electrolyte/electrode interfacial resistance (Figure 25h,i). Significant coordination for  $\text{Mg}^{2+}$  and  $\text{TFSI}^-$  with amorphization using  $\text{TiO}_2$  fillers describes the superior performance. Further, to enhance the  $\sigma_{\text{Mg}}^{2+}$  and mechanical properties of Mg-SPEs, inserting inorganic fillers such as  $\text{MgO}$ ,  $\text{TiO}$ ,  $\text{SiO}_2$ ,  $\text{Al}_2\text{O}_3$ , and  $\text{ZnO}$  is a highly successful strategy.<sup>[499,500]</sup> Wang et al.<sup>[501]</sup> reported PPE-based SEs with  $\sigma_{\text{Mg}}^{2+}$  of  $0.47 \text{ mS cm}^{-1}$  and EW of 3.1 V (Figure 25j-m). Further, Mg//Mg plate/strip displays 0.13 V

overpotential for 1700 cycles with uniform  $\text{Mg}^{2+}$  loading over the anode. Reversible Mg plating/stripping is observed for various SPEs or GPEs such as  $\text{PEO}/\text{Mg}(\text{BH}_4)_2$ ,  $\text{PMMA-MgTr}$ , oligo(ethylene oxide)-grafted polymethacrylate-Mg-salt,  $\text{P(VdF-co-HFP)}$ ,  $\text{Mg}(\text{ClO}_4)_2\text{-SiO}_2$ , and  $\text{Mg}(\text{AlCl}_2\text{EtBu})_2\text{-PVdF}$ , however, poor ion transfer kinetics and interfacial instabilities constrains the MIBs performances.<sup>[102,298,502–507]</sup>

Mg metal undergoes massive volume expansions of 300–500% with strong stress-strain upon solid-solid phase transformations; the Mg-alloy type anode can be the alternate solution. Several Mg-alloy-based anodes, such as  $\beta\text{-Mg}_3\text{-Bi}_2$ ,  $\text{Mg}_2\text{-Ga}_5$ ,  $\text{Mg}_2\text{Sn}$ ,  $\text{Mg}_2\text{-Sb}$ , and  $\text{MgF}_2\text{-Mg}$ , are also reported to increase the compatibility of Mg-alloys anodes.<sup>[508–511]</sup> Su et al.<sup>[229]</sup> proposes the uniform and conformal magnesium phosphorus oxynitride ( $\text{Mg-PON}$ ) thin films over Si substrates (thickness  $\approx 62 \text{ nm}$ ) by using ALD.  $\text{MgPON}$  SEs  $\sigma_{\text{Mg}}^{2+}$  is of  $62 \text{ nS cm}^{-1}$ ,  $0.36 \mu\text{S cm}^{-1}$ , and  $1.2 \mu\text{S cm}^{-1}$  at 400, 450, and 500 °C, respectively. Despite extensive research stating the feasibility of MIBs, no anode and electrolyte materials are compatible and resolve the significant primary challenges of the passivation effect over Mg anodes, EWs, and ion-conductors for SEs. The MIBs future pathways are a proper cathode-electrolyte configuration with Mg anodes offering high capacity and voltage cells. Stronger electrostatic forces among the Mg and surrounding anions causes diffusion kinetics severely. For electrolytes, primary materials should be compatible with Mg anodes and cathodes by electrochemically, non-corrosive liquids with reasonable safety and low cost. Artificial buffer layers such as carbon-based, heavy metals (Au, Ag, Ta, La, Ce, W), or oxides over Mg anode can be suitable approaches to minimize the Mg passivation.

### 7.2.2. Zinc-Based Batteries (ZBs)

Zinc metal has been considered a promising anode due to its high gravimetric and volumetric capacities ( $820 \text{ mAh g}^{-1}$  and  $5855 \text{ mAh cm}^{-3}$ ), small standard potential ( $-0.762$  versus SHE), low cost and toxicity, abundant resources, environmental benignity, and intrinsic safety.<sup>[512,513]</sup> Zn chemistries insistently undergo irreversible, poor CE, dendritic growth, chemical instabilities for low/high current densities, low Zn utilization, and insufficient areal capacity.<sup>[514,515]</sup> Higher charge-discharge rates are typically utilized to minimize the influence of irreversibility for cycle operation; however, it undergoes severe decomposition of electrolytes. Further, significant excess Zn is required to retain the supply due to consumption by parasitic reactions; however, it displays considerable underutilization of its theoretic capacities.<sup>[516,517]</sup>

The construction of all-solid-state ZBs is a promising approach for these offensive concerns because of their high chemical stability. Thus far, inorganic  $\text{Zn}^{2+}$ -conducting SEs have been rarely reported owing to the stronger electrostatic binding among the  $\text{Zn}^{2+}$  ions and solid lattice that outcomes poor  $\sigma_{\text{Zn}}^{2+}$  ( $<10^{-5}$

Publishing Group. f) CV for  $\text{Au}|1.6\text{NH}_3@\text{MgO}|\text{Mg}$ . g) Symmetric cell for  $\text{Mg}|1.6\text{NH}_3@\text{MgO}|\text{Mg}$  system. Reproduced with permission.<sup>[76]</sup> Copyright 2020, American Chemical Society. h) Symmetric cycles for  $\text{Mg}/\text{CPS}/\text{Mg}$  cells, inset CPE photo. i) EIS for  $\text{Mg}/\text{CPS}/\text{Mg}$  cells before/after polarizations. Reproduced with permission.<sup>[498]</sup> Copyright 2019, American Chemical Society. j) PVDF-HFP SPEs. k,l) SEM for Mg anodes with PEE (k) and liquid (l). m)  $\text{Mg}/\text{SPEs}/\text{Mg}$  cell cycling. Reproduced with permission.<sup>[501]</sup> Copyright 2021, Elsevier.



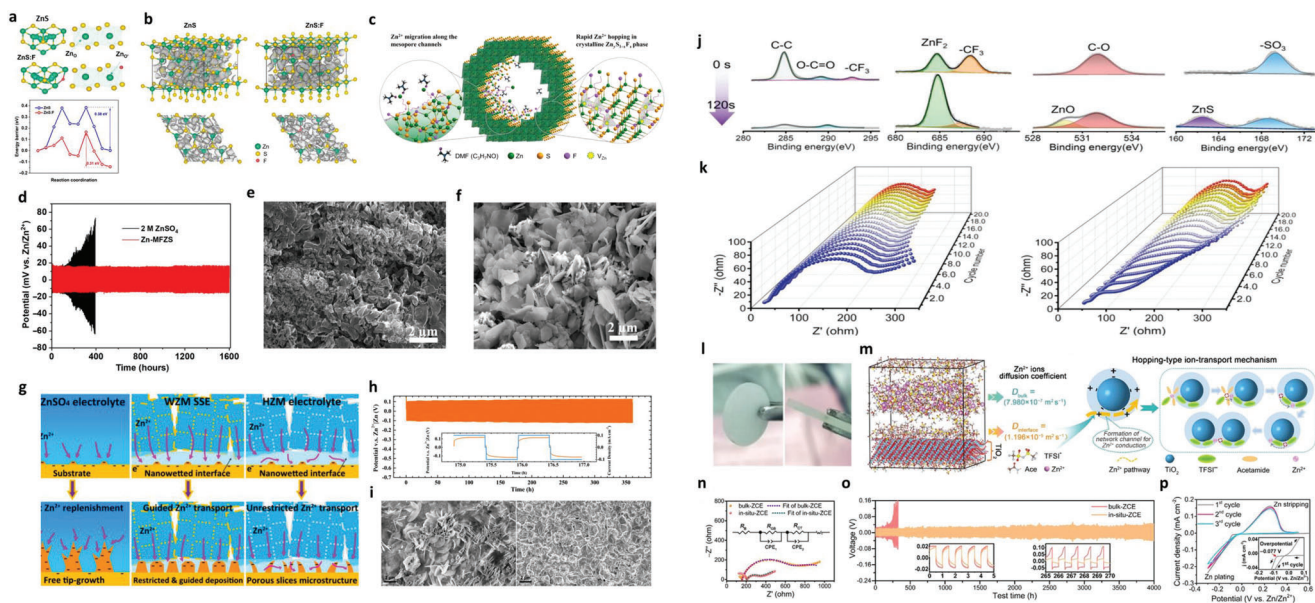


**Figure 26.** a) Diffusion path (top) and energy profiles (bottom) for  $\text{Zn}^{2+}$  in ZnS and ZnS-F for neighboring octahedral Zn sites. b) Probability densities for the diffusion of Zn-ions for ZnS (left) and ZnS-F (right). c) Schematics for  $\text{Zn}^{2+}$  conduction in Zn-MFZS SIEs. d) Zn//Zn plate/stripe cycles. e, f) SEM images for Zn anodes after plate/stripe cycles for Zn-MFZS (e) and 2 m  $\text{ZnSO}_4$  (f). Reproduced with permission under the Creative Commons Attribution Non-Commercial License 4.0 (CC BY-NC).<sup>[518]</sup> Copyright 2023, American Association for the Advancement of Science. g) Zn-deposit kinetics. h) Zn/Zn cells under WZM SSEs. i) SEM images for Zn-anodes after  $\text{ZnSO}_4$  (left) and WZM SSEs (right). Reproduced with permission.<sup>[528]</sup> Copyright 2019, Elsevier. j) XPS spectra for different interphase elements after cycling. k) In situ EIS spectra for Zn//Zn cells for PH/MXene SPE (left) and PH SPE (right). Reproduced with permission.<sup>[533]</sup> Copyright 2022, Wiley VCH. l) Bulk solid membrane. m) MD simulation with  $\text{Zn}^{2+}$  conduction pathways. n) EIS spectra. o) Zn//Zn plate/stripe cycles. p) CVs. Reproduced with permission.<sup>[534]</sup> Copyright 2022, Wiley-VCH.

$\text{S cm}^{-1}$ ) and  $t_{\text{Zn}}^{2+}$ .<sup>[518]</sup> Usually, previous reports comprise the addition of free water or liquid plasticizer (15–70 wt%; PEO, PVDF, poly(vinylidene fluoride-co-hexafluoropropylene); PVHF) blended with ILs or electrolyte-soaked membranes; however, it illustrates hydrogen evolution or corrosion reactions.<sup>[519]</sup> SIEs with high  $\sigma_{\text{Zn}}^{2+}$ , large EWs, and long-life compatibility similar to SIEs for LIBs are highly challenging owing to the multivalent behavior of  $\text{Zn}^{2+}$ .<sup>[520]</sup> SPEs display considerable benefits of ion-conductance over inorganic materials with high flexibility and interface computability with metal anodes.<sup>[521]</sup> Inorganic fillers are critically essential to enhance ion conductance for SPEs. This approach enables the dissociation of Zn salts and ion-transport channels over filler surfaces and functions as plasticizers for decreasing polymer crystallinity and improving segment migration.<sup>[522]</sup> Thus fillers enriched surface chemistries with a high surface area are greatly anticipated for SPEs.

Theoretical calculations explain the doping of  $\text{F}^-$  with  $\text{S}^{2-}$  introduces numerous vacancies of Zn ( $\text{Vac}_{\text{Zn}}$ ) for mesoporous ZnS (MFZS) with reducing  $\text{Zn}^{2+}$  migration barriers for nearby Zn oct-sites for  $\text{Zn}_{0.9}\text{S}_{1-x}\text{F}_x$  crystal phase as super  $\text{Zn}^{2+}$ -ion conductors.<sup>[518]</sup> Zn-MFZS displays EW of  $-0.5$ – $3$  V,  $E_a \approx 0.3$  eV, and  $\sigma_{\text{Zn}}^{2+} \approx 0.66$  mS  $\text{cm}^{-1}$  higher than other solid or hybrid  $\text{Zn}^{2+}$ -conductors. High electronic conductivity for  $\text{Zn}^{2+}$ -SIEs permits the reaction of  $\text{Zn}^{2+}$  with electrons to generate Zn-dendrites in SEs at Zn-plating potential, consistent with the Na- $\beta$ - $\text{Al}_2\text{O}_3$  SIEs.<sup>[523]</sup> The optimal fluorine doping concentration is 5.6 at%, beyond which it reduces ion conductivity due to enlarged surface adoption and decreased substitution of  $\text{F}^-$ . The  $\text{Zn}^{2+}$ -conductors with  $\text{Zn}_2\text{SiO}_4$  (0.028 mS  $\text{cm}^{-1}$ ),  $\text{Bi}_2\text{Zn}_{0.1}\text{V}_{0.9}\text{O}_{5.35}$  (0.034 mS

$\text{cm}^{-1}$ ), and EMI-TFSA@ZIF-8 (0.019 mS  $\text{cm}^{-1}$ ) are also reported with low  $E_a$  and high dielectric constants, which is favorable for  $\text{Zn}^{2+}$ -ions transport.<sup>[524–526]</sup> Alivalent anions substitution in ZnS lattice ensures the generation of anion substitutional defects with cation vacancy. Replacement of monovalent F to divalent S alters the charge distribution inside the ZnS by forming  $\text{Vac}_{\text{Zn}}$  and regulating electron densities for nearby anions and vacancies.<sup>[527]</sup> Smaller ionic radius and strong zincophilicity of F trigger the lattice reduction and phase transitions from ZnS(111) to F-ZnS(100).  $\text{Vac}_{\text{Zn}}$  strengthens the valence band maximum nearby the Fermi level.

Figure 26a–c shows  $\text{Zn}^{2+}$  diffusion kinetics among the oct-sites ( $\text{Zn}_{\text{oct}}$ ) and tet-S-coordinated sites ( $\text{Zn}_{\text{tet}}$ ), in which  $\text{Zn}_{\text{tet}}$  exhibits an energy barrier of 0.27 eV and  $\text{Zn}^{2+}$  diffusion is trailed by  $\text{Zn}_{\text{oct}}$  barrier (0.38 eV).<sup>[518]</sup> F-doping for S-sites obtains a lower energy barrier for  $\text{Zn}_{\text{oct}}$  of 0.31 eV with favorable ZnS lattice illustrating zincophilicity of  $\text{F}_s$  and improved steric effect of  $\text{Vac}_{\text{Zn}}$  with numerous  $\text{Zn}^{2+}$ -transport channels. Zn//Zn-MFZS//Zn cells display stable electrochemical voltage polarizations for 1600 h with a cumulative capacity of 4000 mAh  $\text{cm}^{-2}$  and overpotential of 36 mV (Figure 26d). SEM images for Zn-anode display compact surface with obvious ZnO and dendrites even after 1000 h under Zn-MFZS SIEs, whereas under aqueous electrolyte severe formation of ZnO,  $\text{Zn}(\text{HSO}_4)_2$  and Zn dendrites (Figure 26e,f). Wang et al.<sup>[528]</sup> reported ZnMOF-808  $\text{Zn}^{2+}$ -solid conductor (WZM SSEs) with  $t_{\text{Zn}}^{2+} \approx 0.93$  and  $\sigma_{\text{Zn}}^{2+} \approx 0.21$  mS  $\text{cm}^{-1}$  with  $\text{Zn}^{2+}$ -electrodeposition kinetics. In liquid, rapid refilling of depleted  $\text{Zn}^{2+}$ -ions occurs nearby tips due to faster long-range movability for bulk phases that suppresses Zn-growth of

Cu host with enlarged vertical tip-growth (uneven Zn deposits). But, WZM SEs exhibit sub-nanochannels inside the MOF-hosts with controlled transport of  $\text{Zn}(\text{H}_2\text{O})_6^{2+}$  ions illustrating interfacial wetting and uniform/dense  $\text{Zn}^{2+}$ -depositions (Figure 26g). Zn//WZM//Zn cells display the low overpotential of 0.1–0.12 V with stable dendrite-free Zn deposits/stripping over 350 h demonstrating interfacial compatibility of WZM SEs with Zn-anodes (Figure 26h,i). Chen et al.<sup>[529]</sup> presents the PVHF/MXene-g-PMA SPEs with  $\sigma_{\text{Zn}^{2+}} \approx 0.269 \text{ mS cm}^{-1}$  at RT and dendrite-free stable Zn plate/strip cycle operations for 1200 h with 98.9% CEs. XRD confirms the no obvious ZnO or hydroxides after Zn plating. PVdF-HFP/Zn(Tf)<sub>2</sub> SPEs exhibit the formation of an interfacial layer, including the Zn and SPEs reaction products illustrating the rise of interface resistance and polarization, similar to the Li-SPEs with suppression of dendrites.<sup>[530]</sup> Carboxymethyl cellulose (CMC)/poly(N-isopropylacrylamide) (PNI-PAM) SPEs show large tensile strength and modulus, porous structure, which supports  $\text{Zn}^{2+}$  ions transfer in SPEs with  $t_{\text{Zn}^{2+}} \approx 0.56$ ,  $\sigma_{\text{Zn}^{2+}} \approx 0.168 \text{ mS cm}^{-1}$ , and excellent compatibility of SPEs and Zn-electrodes over 150 h.<sup>[531,532]</sup> Theoretical calculations verify the influence of MXene nanofiller refrain local current density distributions and concentration of Zn ions.<sup>[533]</sup> Local current density is more uniformly distributed with PH/MXene SPEs, causing lower polarization and homogeneous ion transport regulated by MXene. In situ stable organic/inorganic interface realizes the feasible interface transport kinetics and dense Zn deposits. Figure 26j displays interphase compositions, including C-C (284.8 eV), C-O (531.9 eV), and O=C-O (289.2 eV) signals for C 1s, -CF<sub>3</sub> (292.8 eV), -SO<sub>3</sub> (169.2 eV), ZnS (162.3 eV), and ZnF<sub>2</sub> (685.1 eV) for F 1s and S 2p spectra, which illustrates existence of organic (dominant) and inorganic (less) components. Ar<sup>+</sup> etching (120s) weakens the C-C, C-O, and -SO<sub>3</sub> and emerging ZnF<sub>2</sub>, ZnS, and ZnO species due to reductive decomposition of Zn(OTf)<sub>2</sub>/PVdF-HFP complex benefiting the interface stability and ion-transport. In situ EIS under PH/MXene SPE displays an initial decrease of interface resistance and is later stable for more cycles. In contrast, PH SPE shows a gradual increase in resistance, verifying the stable Zn and PH/MXene interfaces Figure 26k.<sup>[533]</sup>

High-entropy eutectic networks or preferred adsorption of TFSI<sup>-</sup> anions deteriorates the association of ions with forming  $\text{Zn}^{2+}$  permeated pathways over the nucleating TiO<sub>2</sub> surfaces ensuring solid crystals with superior  $t_{\text{Zn}^{2+}} \approx 0.57$  and  $\sigma_{\text{Zn}^{2+}} \approx 0.0378 \text{ mS cm}^{-1}$  for ZCE SEs (Figure 26l,m).<sup>[534]</sup> TFSI<sup>-</sup> tethered regions provide the surplus interfacial ion-conduction channels due to Lewis acid-base interactions. Low energy shifting of Zn K-edge after crystallization occurs owing to reduced electron transfer among the Zn and O (TFSI<sup>-</sup>), providing easier transport of  $\text{Zn}^{2+}$  towards the space-charge region.  $\text{Zn}^{2+}$  diffusion kinetics for TiO<sub>2</sub> interface is larger relative to the bulk crystalline phase ( $D_{\text{interface}} = 1.196 \times 10^{-5} \text{ m}^2 \text{ s}^{-1} > D_{\text{bulk}} = 7.980 \times 10^{-7} \text{ m}^2 \text{ s}^{-1}$ ) verifying the fast interface hopping of  $\text{Zn}^{2+}$ . ZCEs tolerate small interface resistance (288 Ω) upon cycling, validating the exceptional solid-solid interface compatibility (Figure 26n). Zn//Zn reversibility under in situ ZCE outperforms 4000 cycles (4000 h) with stable polarization voltage of 30 mV with dense and uniform Zn depositions with unchanged crystal structures (Figure 26o). This confirms the formation of stable SEI (components ZnF<sub>2</sub> and organic S/N) with relieving accompanying strains. CVs vin-

dicate the first voltage hysteresis of -0.077 V for Zn nucleation, implying the minimal energy loss for phase transitions among  $\text{Zn}^{2+}$ -ions and Zn-metal under ZCE (Figure 26p). For feasible interface among the electrolyte/electrodes, construction of several in situ polymer electrolytes (PEO, poly(N-methyl-malonic amide, triethyl phosphate, poly(1,3-dioxolane), PAM, TEP-PC) have been demonstrated using photon- or ultraviolet-assisted printing or methods, however,  $\sigma_{\text{Zn}^{2+}}$  and  $t_{\text{Zn}^{2+}}$ -transfer kinetics is extremely poor.<sup>[535–537]</sup> Extensive efforts have been devoted to the fabrication of SPEs and their interface chemistries with different polymeric hosts (PEO, PPO, PAM, CMCs, PVDF-HFP, PAN, gelatin, PVA, Xanthan gum, PAA, hydroxyethylcellulose, PANa, TEGDA), Zn-salts (Zn(Tf)<sub>2</sub>, Zn(CF<sub>3</sub>SO<sub>2</sub>)<sub>2</sub>, ZnSO<sub>4</sub>, ZnCl<sub>2</sub>, Zn(CH<sub>3</sub>COO)<sub>2</sub>, Zn-TFSI<sub>2</sub>, Zn acrylate, Zn-OTf<sub>2</sub>, Zn(BF<sub>4</sub>)<sub>2</sub>), ILs ([Emim]OTf, EMITf, EMIMTFSI, EMIM]BF<sub>4</sub>), and inorganic fillers (ZnO, Al<sub>2</sub>O<sub>3</sub>, Ti<sub>3</sub>C<sub>2</sub>T<sub>x</sub>, MOF, ZIF, MXene, SiO<sub>2</sub>).<sup>[538–546]</sup>

Figure 27a displays the interfacial reaction kinetics and design processes for patterned Zn-anodes using SF<sub>6</sub> plasma etching with sulfurized or fluorinated surfaces with ZnF<sub>2</sub> and ZnS polar bindings with preferred 101 crystal orientation.<sup>[191]</sup> Patterned Zn anode implied superior mechanical stability under stress-strain and stable polarizations for ≥1000 cycles at current densities of 5–20 mA cm<sup>-2</sup> without dendritic growth under chitosan-biocellulosic SEs (CBCs), which illustrates the greater electrochemical compatibility of patterned Zn-anode (Figure 27b). It shows robust SEI with electrostatic interactions with  $\text{Zn}^{2+}$ -ions and CBCs components. XPS spectra of C, O, Zn, F, and S reveal the presence of inorganic ZnF<sub>2</sub> and ZnS species plays a key role in the stabilization of the Zn-anode with even and compact nucleation process (Figure 27c). CBCs effectively accommodate the volume changes due to their excellent mechanical properties. EIS spectra also confirm the formation of the SEI layer for high/medium frequency region and minor Warburg impedance having ion diffusion kinetics. Theoretical results show the unbalanced charge distributions for interphase regions due to S and F bindings with Zn, which boosts  $\text{Zn}^{2+}$ -diffusion with enhanced mechanical reliance to suppress the corrosion reactions (Figure 27d).

Theoretical calculations reveal the strategies for projecting SEI formation, diffusion behaviors, and dendritic growth suppression using S and F-chemistries (Figure 28a).<sup>[9]</sup> According to the F- and S-loading levels from 5–30%, the Zn anode forms their preferred crystal structures from (002), (100), (101), (102), and (103). Zn(101) confirms the lowest surface diffusion barriers and high surface energies for F and S with minimum compressive strain relative to those of (002), (102), (103), and pristine Zn facilitating impulsive reorientation of Zn crystals and which is epitaxial with Zn surfaces and favorable for SEI (Figure 28b). Further, it shows 3D diffusion kinetics and absorption of  $\text{Zn}^{2+}$ -ions over Zn surfaces with a localized decrease to Zn<sup>0</sup>. Preferential crystal orientations are confirmed in the order of Zn(101) > Zn(100) > Zn(102) > Zn(103) > Zn(002) > Zn<sup>0</sup> owing to the strength of ionic bonds and steric interactions inside the lattices. Zn(101)//Zn(101) cells exhibit the smallest polarization of 52 mV for 5000 cycles for a plating capacity of 5 mAh cm<sup>-2</sup> and 10 mA cm<sup>-2</sup>, 2.5-fold larger than commercial targets. It also demonstrates the commercial-scale plating capacity operations (10 mAh cm<sup>-2</sup> and 10 mA cm<sup>-2</sup>) for >2000 cycles, which illustrates the exceptional electrochemical interface

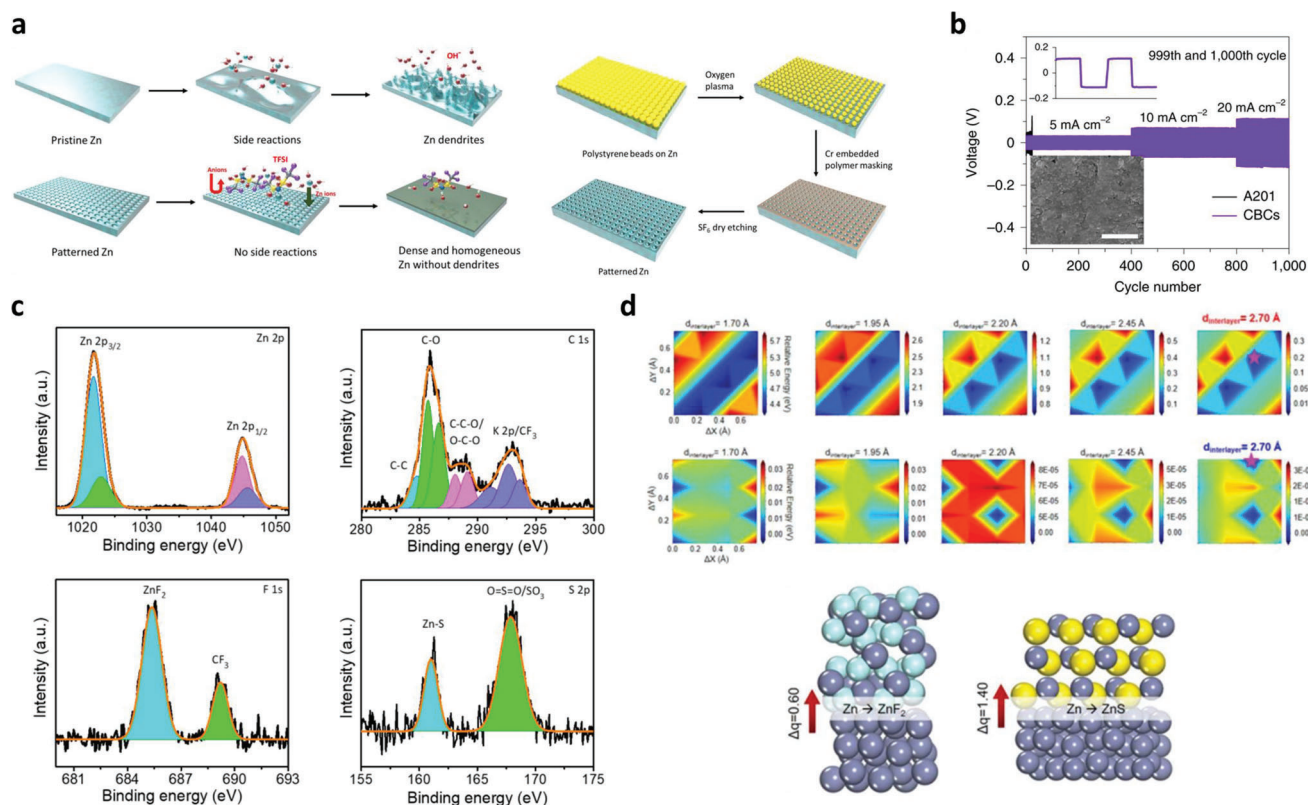


**Figure 27.** a) Schematics for Zn-anode surface structures (left) and synthesis processes of patterned Zn-anodes (right). b) Zn/Zn symmetric cells for different current densities and electrolytes. c) XPS patterns of Zn 2p, C 1s, F 1s, and S 2p elements for SEI layer over patterned Zn anode. d) Theoretical demonstration for interfacial reactions (top) and electron charge transfers (bottom; ZnF<sub>2</sub>@Zn, left and ZnS@Zn, right). Reproduced with permission.<sup>[191]</sup> Copyright 2021, Nature Publishing Group.

stability (Figure 28c). EIS verifies the minimal interfacial resistance and stable operations required for depth of discharge of Zn-based anodes. SEM images display a dense and compact surface for Zn(101). In contrast, the pristine Zn has severe dendritic growth and cracks (Figure 28d). Besides, the thinnest SEI of 10.2 nm was demonstrated for Zn(101) relative to those of other crystal planes, implying good structural stability, as comparable to commercial LIBs kinetics.<sup>[266,547]</sup> TOF-SIMS and XPS validates the ZnF<sub>2</sub>/ZnS-enriched SEI with presence of ≈684.4 (F 1s), ≈161.6 (S 2p), ≈1022.2 (Zn 2p), and ≈1045.2 eV (Zn 2p) peaks. Lower electronic conductance and high ZnF<sub>2</sub>/ZnS-Zn interface energies justify a thin SEI (Figure 28e–h).<sup>[548]</sup> Recently, several approaches for the development of Zn anodes, such as 3D structural design (sponge, MOF) and protection layers for Zn anodes also been reported to minimize the dendrite growth such as CNTs, MXene, carbon-allotropes, graphene, metal alloys such as Hg, Au, Ag, Mg, Si, Sn, Al or metal oxides; however, such artificial buffer layers rigorously degrade the cell capacity and rate performances.<sup>[549,550]</sup>

A comprehensive understanding of Zn-interface chemistry reveals that poor ion-conductance and electrode/SIEs interface are critical for practical applications for all-solid-state-ZIBs. Insertion of ceramic fillers is the most common approach utilized to decrease the crystallinity of SIEs for improving Zn<sup>2+</sup> migration or conductance. Ceramic fillers interact with a polymer matrix to construct the Zn<sup>2+</sup>-conduction pathways, a higher dielec-

tric constant improves the dissociation of Zn-salts and forms numerous free Zn<sup>2+</sup>-ions, and partial amorphous/crystalline structures mainly contribute overall conductivity. Lastly, the recently reported cellulose-based composite SEs and preferentially oriented Zn-anodes Zn(101) with chemical passivation of S, F, or others are the most effective strategies to reach commercial standards, including plating (10 mAh cm<sup>-2</sup>) and cumulative capacity (25 Ah cm<sup>-2</sup>) with standard current density (10 mA cm<sup>-2</sup>) for future Zn-based battery technologies.

### 7.2.3. Aluminum-Ion Batteries (AIBs)

Aluminum metal offers the highest theoretical specific (2980 mAh g<sup>-1</sup>) and volumetric (8046 mAh cm<sup>-3</sup>) capacities, abundant resources, intrinsic safety, and low cost.<sup>[551,552]</sup> The major challenges include Irreversibility, undesirable parasitic reactions, dissolution of cathodes or anodes, and low CEs with inferior cycle life. AIBs research is primarily dedicated to liquid electrolytes. Solid-state AIBs are just under the embryonic stage due to a lack of materials and resources for designing SEs with high Al<sup>3+</sup>-conductivity with compatible anodes or cathodes. Wang et al.<sup>[553]</sup> reported Al<sup>3+</sup>-ion conduction pathways for NASICON-type (Al<sub>0.2</sub>Zr<sub>0.8</sub>)<sub>20/19</sub>Nb(PO<sub>4</sub>)<sub>3</sub> SEs using neutron diffraction and aberration-corrected STEM spectroscopy. (Al<sub>0.2</sub>Zr<sub>0.8</sub>)<sub>20/19</sub>Nb(PO<sub>4</sub>)<sub>3</sub> displays rhombohedral crystal



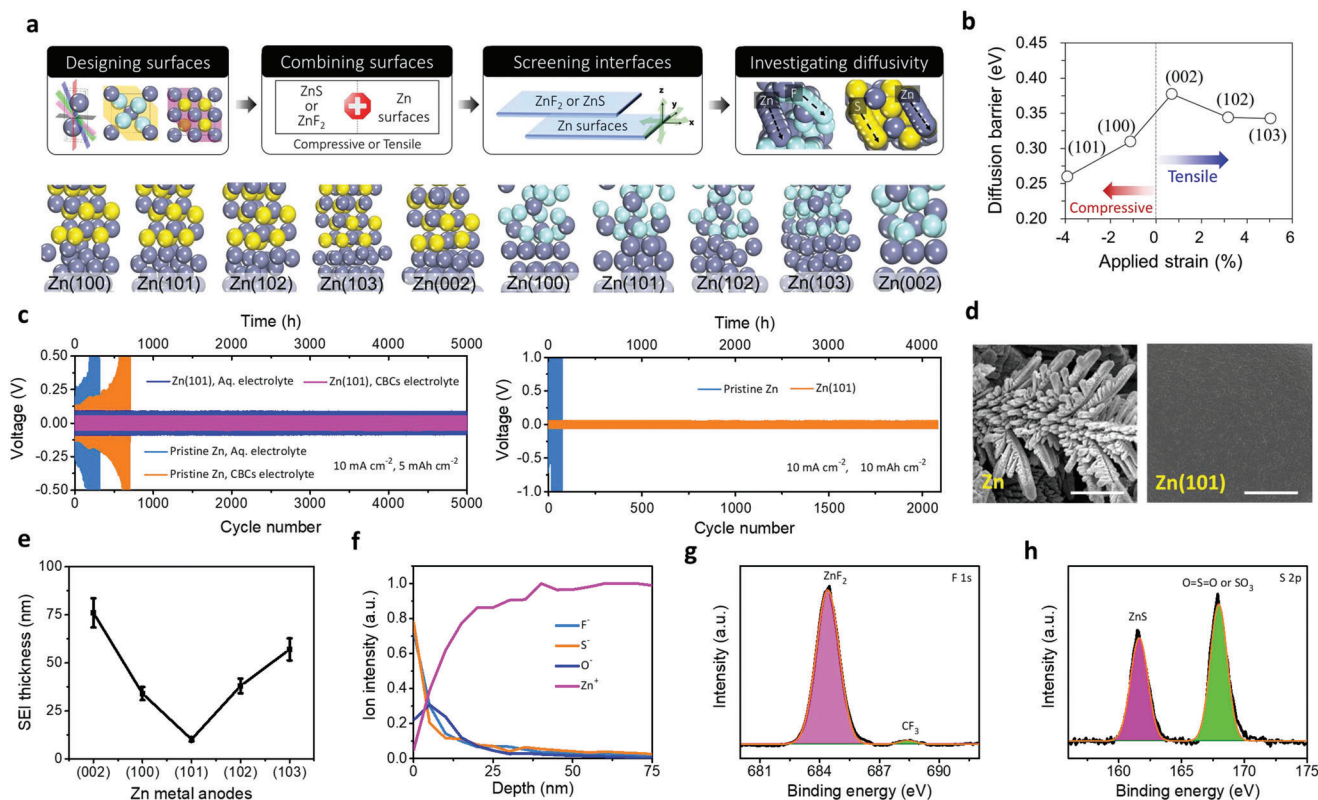


**Figure 28.** a) Theoretical demonstrations for the design of preferred Zn anodes from (100), (101), (102), (103), (002) crystal planes. Yellow and blue balls denote the S and F, respectively. b) Surface diffusion barriers with applied strains. c) Zn/Zn symmetric cells for different areal capacities of 5 mAh cm<sup>-2</sup> (left) and 10 mAh cm<sup>-2</sup> (right). d) SEM images of pristine (left) and Zn(101) (right) after 50 plate/stip cycles. e) SEI thickness versus Zn-anodes. f) TOF-SIMS depth profiles. g, h) XPS spectra of F 1s and S 2p over Zn(101) SEI layer compositions. Reproduced under the terms of a Creative Commons CC BY license.<sup>[9]</sup> Copyright 2023, Wiley VCH.

structures including (Zr,Nb)O<sub>6</sub> for oct-sites sharing corners with (PO<sub>4</sub>) for tet-sites and Al occupies interstitial trigonal anti-prisms revealing larger displacements, which illustrates the random distribution of Al<sup>3+</sup>-ions for c-axis and vacancies promoting Al<sup>3+</sup>-ion transport channels. EIS results confirm the feasibility of SEs with Al anodes with  $\sigma_{Al^{3+}}$  of 10<sup>-4</sup>–10<sup>-6</sup> S cm<sup>-1</sup> for 300–600 °C and  $E_a$  of 3.1 eV. Al<sup>3+</sup>-ion conductance ascribes the weak chemical interactions among the Al and O<sub>2</sub> in the lattices with Al–O<sub>2</sub> distances of 2.64–2.65 Å. The Sn<sub>0.92</sub>Sb<sub>0.08</sub>P<sub>2</sub>O<sub>7</sub> SEs for anhydrous hydroxide-ion conductor ( $\sigma_{hydroxide}$  of 0.01 S cm<sup>-1</sup>) or Al–air batteries has been reported, in which upon discharge Al is oxidized to aluminate species, and it reduced to Al upon charge, verifying the SEs compatibility with Al-metal.<sup>[554]</sup> Poor intercalation barrier of electrolytes and lack of SEI are the major failures kinetics for the AIBs.<sup>[555]</sup> Literature shows the much effort for ILs (50–90 wt%) encapsulated polymer electrolytes such as PVDF, PEO, PAM, PEA, or derived MOFs as GPEs for AIBs; however, poor charge-/mass-transport kinetics for polymers or MOFs, sluggish Al<sup>3+</sup>-ion diffusion, and high interfacial resistance for Al//SEs limits their use for AIBs.<sup>[556–558]</sup> Shen et al.<sup>[559]</sup> reported that soft GPEs provide excess nucleation sites for Al deposits, illustrating the better Al<sup>3+</sup>-plate/stip for soft GPE than rigid GPEs with fractal branched Al-dendrites. PEA-GPE displays  $\sigma_{Al^{3+}} \approx 1.46$  mS cm<sup>-1</sup> and EWs  $\approx 3$  V versus Al/Al<sup>3+</sup> with minimal charge-transfer resistance implying the stable Al//Al

interface polarizations.<sup>[193]</sup> Further, photo-curable PTHF-Epoxy SPEs have been reported with  $\sigma_{Al^{3+}} \approx 0.02$  mS cm<sup>-1</sup>.<sup>[560]</sup>

Besides, to alleviate the passivation effect of native oxide and electrode disintegration that undergoes severe parasitic reactions with continuous depletion of electrolyte even for lower overpotentials, several approaches have been proposed, such as uniform protective Al oxide layer over Al-metal, interface engineering, specifically artificial SEI or buffer layers. However, the formation of ionically insulated native oxides over Al renders unfeasible Al plate/stip, the high bandgap of passivating oxides hinders electrons and ions-transfer across the interface, thick artificial SEI increase the interface resistance and voltage polarizations with extremely poor Al<sup>3+</sup>-plate/stip, CE severely degrades the cell performances. It is highly desirable to fabricate new Al-anodes with high reversibility, new SEs with better interface compatibility, and Al-alloyed anodes. In this context, several modified Al-anodes have been reported, such as Au–Al, Al<sub>82</sub>Cu<sub>18</sub>, ACNI/Al-15, Al<sub>0.265</sub>TiO<sub>2</sub>, MoO<sub>3</sub>, TiO<sub>2</sub>, Al<sub>97</sub>Ce<sub>3</sub>, MXene/E–Al<sub>97</sub>Ce<sub>3</sub>, organic or hybrid materials.<sup>[561–563]</sup> Theoretically AIBs are promising candidates, however, reported practical results are significantly out of scope for large-scale energy applications. Extensive efforts are critically required to develop new compatible cathodes, anodes, and electrolyte materials. The knowledge and in-depth investigation are critically needed for future AIBs in terms of: for SEs, high Al<sup>3+</sup>-ion conductivity with superior de-/intercalation of ions

for both electrodes and broader EWs; for cathodes, tight interactions among the  $\text{Al}^{3+}$ -ions and structures shows sluggish diffusion kinetics, numerous active surfaces, and wide surface area or porosity; for Al anodes, highly reversible without formation of oxide passivation and strong corrosion reactions. Theoretical evaluations of complicated electrochemical reaction kinetics of AIBs regarding structural and electrochemical properties for SEs, Al-anodes, and cathodes are crucial to guide experimental research. We described various mono-/multivalent battery chemistries under SEs for their anode/SEs interface compatibilities.

#### 7.2.4. Calcium-Ion Batteries (CIBs)

CIBs offer significant attention due to their lower redox potential for  $\text{Ca}/\text{Ca}^{2+}$  ( $-2.87$  V vs SHE closer to  $\text{Li}/\text{Li}^+$ ) and smaller charge density and polarization strength with high power and diffusion kinetics compared to those of other multivalent ions and high gravimetric ( $1337$  mAh  $\text{g}^{-1}$ ) and volumetric ( $2073$  mAh  $\text{cm}^{-3}$ ) capacities. However, sluggish ion diffusion-kinetics, the irreversible  $\text{Ca}^{2+}$ -metal plating/stripping, operating at high temperatures only, and undesired parasitic reactions with forming  $\text{CaF}_2$ ,  $\text{CaCl}_2$ ,  $\text{CaCO}_3$ , and  $\text{CaH}_2$  lead to continuous growth of passivated film over Ca-anodes and poor CEs. Limited development for high-performance cathodes, SEs, and anode materials is another challenge for CIBs.<sup>[564–567]</sup> Thus SEs received critical attention for CIBs. Seevers et al.<sup>[568]</sup> developed the  $\text{Ca}^{2+}$ - $\beta''$ - $\text{Al}_2\text{O}_3$  SEs with  $\sigma_{\text{Ca}^{2+}} \approx 36$  mS  $\text{cm}^{-1}$  for  $300$  °C. Katsuhiko et al.<sup>[569]</sup> displays the  $\text{M}^{\text{II}}\text{Zr}_4(\text{PO}_4)_6$  ( $\text{M}^{\text{II}} = \text{Mg}, \text{Ca}, \text{Sr}, \text{Ba}, \text{Mn}, \text{Co}, \text{Ni}, \text{Zn}, \text{Cd}, \text{Pb}$ ) NASICON SEs with  $\sigma_{\text{Ca}^{2+}} \approx 1.4$   $\mu\text{S cm}^{-1}$  and migration barrier of  $146$  kJ  $\text{mol}^{-1}$  for  $800$  °C. The Ni, Co, Mg, and Zn-based materials display order-disorder transitions among  $600$  and  $720$  °C with  $\beta$ - $\text{Fe}_2(\text{SO}_4)_3$ -type structure, whereas Ca, Cd, Ba, Sr, and Pb possess NASICON-type structures without phase transitions among RT and  $1000$  °C. Mn-based SEs display transitions at  $560$  °C. Deyneko et al.<sup>[570]</sup> reports the whitlockite-type  $\text{Ca}_{10.5-x}\text{Pb}_x(\text{VO}_4)_7$  ( $x = 1.9, 3.5, 4.9$ )  $\text{Ca}^{2+}$ -ion conductors with  $\sigma_{\text{Ca}^{2+}} \approx 0.1$  mS  $\text{cm}^{-1}$  for  $800$  K, and  $E_a \approx 1.3$ – $1.5$  eV.  $\text{ACa}_9(\text{VO}_4)_7$  ( $\text{A} = \text{Gd}, \text{Ho}, \text{Lu}, \text{Er}, \text{Eu}, \text{Pr}, \text{Sm}, \text{Bi}, \text{La}, \text{Nd}, \text{Tb}, \text{Yb}, \text{Y}, \text{and Sc}$ ),  $\text{Ca}_7\text{MgPbBi}(\text{VO}_4)_7$ ,  $\text{Ca}_{7.5}\text{ZnPb}_{0.5}\text{Bi}(\text{VO}_4)_7$ ,  $\text{Ca}_{7.5}\text{CdPb}_{0.5}\text{Bi}(\text{VO}_4)_7$ ,  $\text{Ca}_8\text{PbBi}(\text{VO}_4)_7$ ,  $\text{Ca}_3(\text{VO}_4)_2$ ,  $\text{Ca}_{7.5}\text{Pb}_3(\text{VO}_4)_7$ ,  $\text{Ca}_{6.5}\text{Pb}_4(\text{VO}_4)_7$ ,  $\text{Ca}_{6.5}\text{Pb}_{4.5}(\text{VO}_4)_7$   $\text{Ca}^{2+}$ -conductor materials with  $\sigma_{\text{Ca}^{2+}} \approx 10^{-11}$ – $10^{-2}$  S  $\text{cm}^{-1}$  for  $300$ – $1700$  °C have been also reported.  $\sigma_{\text{Ca}^{2+}}$  increased by ten times with insertion of Pb from  $0$ – $4.5$  in  $\text{Ca}_{10.5-x}\text{Pb}_x(\text{VO}_4)_7$  with  $\approx 7\%$  volume expansion of unit cells. The presence of immobile atoms (Bi, Pb, Mg, Zn, or others) in the lattices negatively influences  $\text{Ca}^{2+}$ -conductivity owing to obstacles for  $\text{Ca}^{2+}$ -pathways.<sup>[571,572]</sup> The  $\text{Ca}^{2+}$ -migration pathways are of (I)  $\dots \rightarrow \text{M4} \rightarrow \text{M3} \rightarrow \text{M6} \rightarrow \text{M3} \rightarrow \text{M4} \rightarrow \dots$ , (II)  $\dots \rightarrow \text{M2} \rightarrow \text{M4} \rightarrow \text{M2}'$ , and Pb $^{2+}$  based materials follow the (III)  $\dots \rightarrow \text{M2} \rightarrow \text{M4} \rightarrow \text{M2}'' \rightarrow \text{M1} \rightarrow \text{M6} \rightarrow \text{M1}'' \rightarrow \text{M2}'' \rightarrow \dots$  (Figure 29a–c).<sup>[572]</sup> Chen et al.<sup>[573]</sup> reported the  $\text{Ca}_{1.5}\text{Ba}_{0.5}\text{Si}_5\text{O}_{13}\text{N}_6$  SEs to determine the  $\text{Ca}^{2+}$ -migration kinetics using neutron diffraction and AIMD simulations. The  $\text{Ca}^{2+}$  partially occupies three distinct crystallographic positions with smaller distances among the adjacent Ca sites ( $1.727$ – $2.077$  Å) along the same plane, manifesting determined  $1\text{D}$   $\text{Ca}^{2+}$ -migration (Figure 29d). AIMD verifies the  $\approx 400$  meV  $\text{Ca}^{2+}$ -migration barrier and “vacancy-adjacent” concentrated ion-transport kinetics. Lei et al.<sup>[574]</sup> reports the

$\text{GO}_{[\text{Ca}]}$  SEs with  $\sigma_{\text{Ca}^{2+}} \approx 1.08$  mS  $\text{cm}^{-1}$  and ion diffusion accelerated from  $0.6$  to  $9.8$   $\mu\text{S cm}^{-1}$ . Fluorinated alkoxyaluminates  $\text{Ca}[\text{Al}(\text{HFIP})_4]_2$  electrolytes with high anodic stability ( $>3$ – $5$  V vs  $\text{Ca}/\text{Ca}^{2+}$ ) are also reported.

Theoretic calculations show ternary phase diagrams by constructing A-B-H ( $\text{A} = \text{Li}, \text{Na}, \text{Mg}, \text{Ca}$ ; Figure 29e) to fabricate metal borohydride SEs.  $\text{ABH}_4$  and  $\text{A}_2\text{B}_{12}\text{H}_{12}$  ( $\text{A} = \text{Li}, \text{Na}$ ) are thermodynamically stable, whereas  $\text{B}_{10}\text{H}_{10}^{2-}$  are metastable phases.<sup>[575]</sup> Anions in Li-hydrides are cubic close-packed/fcc, while hcp is for Na-counterparts. Few metastable phases are observed for Ca and Mg.  $\text{BH}_4^-$  and  $\text{B}_{12}\text{H}_{12}^{2-}$  based disordered phases are thermodynamically stable in Ca and Mg.  $\text{B}_{12}\text{H}_{12}^{2-}$  in  $\text{CaB}_{12}\text{H}_{12}$  rotates for  $>1500$  K. At large potentials, Ca and Mg show good stability against electrochemical oxidation  $>5$  V with low diffusion constants (Figure 29f). Koettgen et al.<sup>[576]</sup> also reported  $\text{CaB}_{12}\text{H}_{12}$   $\text{Ca}^{2+}$ -conductor with an activation barrier of  $650$  meV, relatively larger than Li/Mg ( $<400$  meV). Lee et al.<sup>[577]</sup> shows the insertion of  $\text{Ca}^{2+}$ -ions in  $\text{HfNb}(\text{PO}_4)_3$  lattice forms the NASICON-type  $\text{Ca}^{2+}$ -SEs. The high-valence cations ( $\text{Hf}^{4+}$ ,  $\text{Nb}^{5+}$ , and  $\text{P}^{5+}$ ) realize the severe decrease in electrostatic interactions for  $\text{Ca}^{2+}$ -ions inside the structures.  $(\text{Ca}_{0.05}\text{Hf}_{0.95})_{4/3.9}\text{Nb}(\text{PO}_4)_3$  SEs display  $\sigma_{\text{Ca}^{2+}} \approx 10^{-6}$ – $10^{-2}$  S  $\text{cm}^{-1}$  from  $600$ – $1000$  K with smaller  $E_a$ . Figure 29g shows the photo-cross-linked SPEs with polytetrahydrofuran (PTHF) and 3,4-epoxycyclohexylmethyl-3',4'-epoxycyclohexane carboxylate with  $\sigma_{\text{Ca}^{2+}} \approx 0.126$  mS  $\text{cm}^{-1}$  (O:Ca ratio of  $1.9:1$ ) for RT,  $E_a \approx 0.328$  eV, and  $t_{\text{Ca}^{2+}} \approx 0.359$  at  $70$  °C.<sup>[578]</sup> Raman peak of  $1050$   $\text{cm}^{-1}$  manifests the dissociation of nitrate anions owing to increased salt concentration, which illustrates the  $\text{Ca}^{2+}$  complexation to oxygen with appropriate solvation of calcium nitrate in SPEs with compatible  $\text{Ca}^{2+}$ -ion transports.<sup>[579]</sup> Genier et al.<sup>[580]</sup> reports the ethylene oxide to calcium ratios EO/Ca from  $5$  to  $52$  to obtain  $3\text{D}$  cross-linked PEGDA-Ca SPEs. The EO/Ca ratio of  $5$  displays  $\sigma_{\text{Ca}^{2+}} \approx 3$   $\mu\text{S cm}^{-1}$ ,  $E_a \approx 0.25$  for RT and  $0.34$  mS  $\text{cm}^{-1}$  for  $110$  °C.  $T_g$  of PEGDA-Ca increases from  $-13.81$  to  $78.61$  °C for pristine PEGDA to EO/Ca of  $52$ – $5$ . Biria et al.<sup>[581]</sup> displays the PEGDA-1-Ethyl-3-methylimidazolium trifluoromethanesulfonate-GPEs with  $\sigma_{\text{Ca}^{2+}} \approx 10^{-4}$ – $10^{-3}$  S  $\text{cm}^{-1}$  for RT to  $110$  °C, EW of  $\approx 4$  V versus  $\text{Ca}/\text{Ca}^{2+}$ ,  $t_{\text{Ca}^{2+}} \approx 0.17$ , and thermal stability of  $300$  °C with discharge capacity of  $140$  mAh  $\text{g}^{-1}$ . Further, the  $\text{Ca}_x\text{M}_z(\text{ZO}_4)_3$  (where  $\text{M} = \text{Ti}, \text{V}, \text{Cr}, \text{Mn}, \text{Fe}, \text{Co}, \text{or Ni}$  and  $\text{Z} = \text{Si}, \text{P}, \text{or S}$ ) NASICON-based Ca-cathodes also reported.<sup>[582]</sup> Theoretical calculations reveal the  $\text{Ca}_x\text{V}_2(\text{PO}_4)_3$ ,  $\text{Ca}_x\text{Mn}_2(\text{SO}_4)_3$ , and  $\text{Ca}_x\text{Fe}_2(\text{SO}_4)_3$  Ca-NASICONs are favorable Ca-cathodes.

The polyvinyl alcohol (PVA) and  $\text{Ca}(\text{NO}_3)_2$ -based aqueous-gel-electrolytes (AGEs) show stable EWs  $\approx 2.6$  V to fulfill redox couples of S/C-anode and  $\text{Ca}_{0.4}\text{MnO}_2$  cathodes compared to liquid  $1\text{M}$   $\text{Ca}(\text{NO}_3)_2$  electrolyte (Figure 29h).<sup>[583]</sup> With PVA,  $\text{Ca}^{2+}$ - $\text{H}_2\text{O}$  complexes display polymer-like accumulation illustrating numerous  $\text{H}_2\text{O}$  molecules immobilization via PVA chains and highly-concentrated-Ca-salts with suppressing diffusion of polysulfides.<sup>[584]</sup> Amorphous SEI with  $\approx 10$  nm thickness in AGEs is obtained due to participation of PVA-matrix, SEI-S/C anode exhibits Young's modulus of  $\approx 445$  MPa larger than liquid  $165$  MPa, which illustrates the structural integrity against electrode deformations (Figure 29i). DFT and XPS verifies the coordination of three  $\text{NO}_3^-$ -anions with a  $\text{Ca}^{2+}$  solvation sheath and preferential reduction of  $\text{NO}_3^-$ -anions facilitates construction of

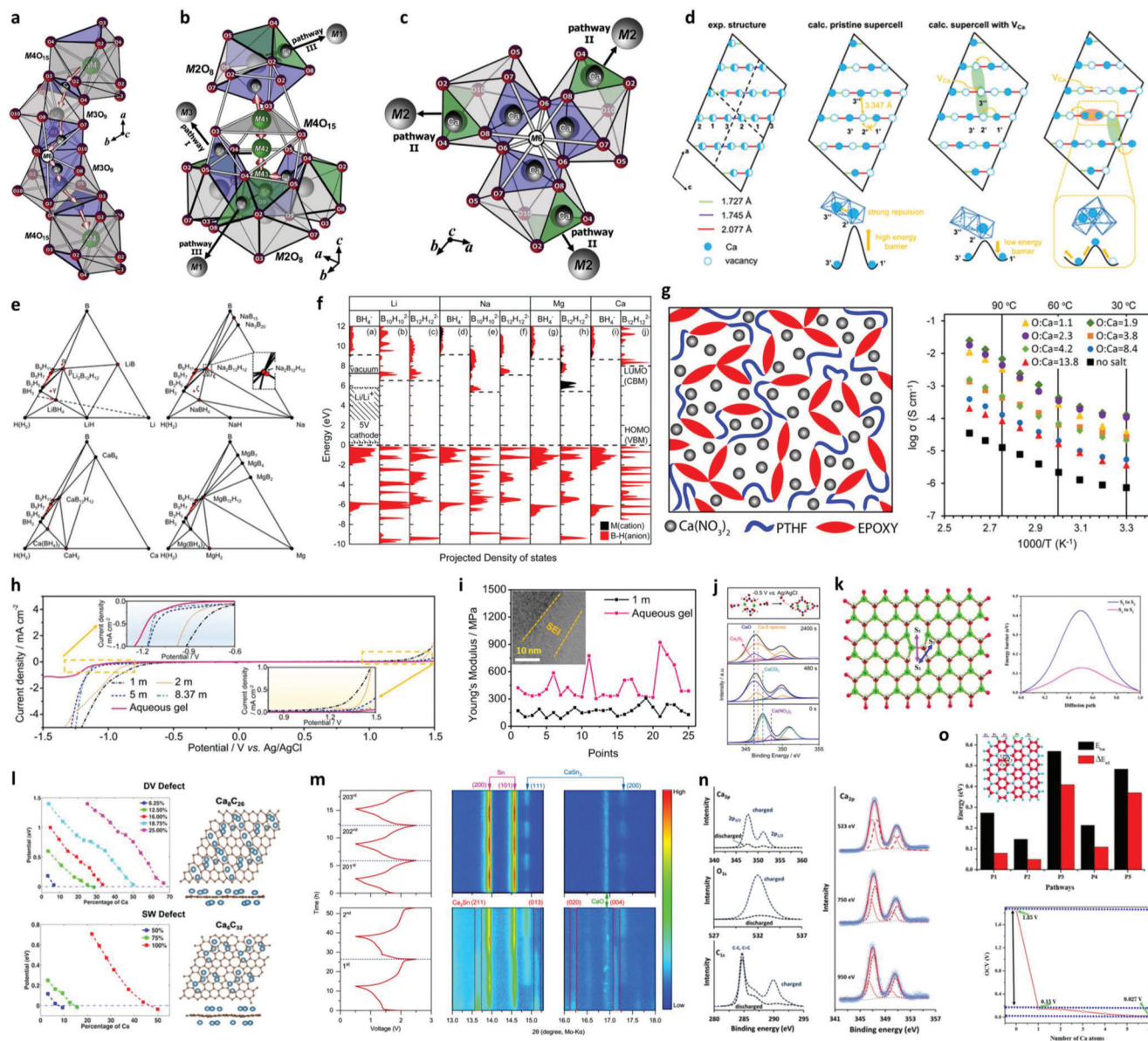


**Figure 29.** a-c)  $\text{Ca}^{2+}$ -migration pathways I (a), II (b), III (c) in  $\beta$ - $\text{Ca}_3(\text{PO}_4)_2$  and  $\text{Ca}_{10.5-x}\text{Pb}_x(\text{VO}_4)_7$ , respectively. Reproduced with permission.<sup>[572]</sup> Copyright 2018, Elsevier. d) Schematics for Ca-ordering and occupied sites in  $\text{Ca}_{1.5}\text{Ba}_{0.5}\text{Si}_3\text{O}_9\text{N}_6$  along (010) orientations. Reproduced with permission.<sup>[573]</sup> Copyright 2022, American Chemical Society. e) Phase diagrams of Li-B-H (top left), Na-B-H (top right), Ca-B-H (bottom left), and Mg-B-H (bottom right) systems. Red squares indicate metastable phases (ground state energy <80 meV/atom above the hull).  $\alpha$  is the  $\text{LiB}_{10}\text{H}_9$ ,  $\beta$  the  $\text{Li}_2\text{B}_{10}\text{H}_{10}$ ,  $\gamma$  the  $\text{LiB}_3\text{H}_8$ ,  $\delta$  the  $\text{Na}_2\text{B}_{10}\text{H}_{10}$ ,  $\epsilon$  the  $\text{Na}_2\text{B}_6\text{H}_6$ , and  $\zeta$  the  $\text{NaB}_3\text{H}_8$ . f) Partial density of states for Li, Na, Mg and Ca with B-H anions relative to stable/metastable phases. Dashed lines are VBMs and CBMs. Reproduced with permission.<sup>[575]</sup> Copyright 2017, American Chemical Society. g) PTHF-Epoxy cross-linked structures (left) and ion conductivity of PTHF-Epoxy SPEs (right). Reproduced with permission.<sup>[578]</sup> Copyright 2019, American Chemical Society. h) EWs of electrolytes. i) Young's modulus of S/C anodes in aqueous gel electrolytes. Inset STEM image showing SEI. j) DFT calculations and in-depth Ca 2p XPS spectra. Reproduced under the terms of a Creative Commons CC BY 4.0 license.<sup>[583]</sup> Copyright 2021, Nature Publishing Group. k) Energy barriers for Ca-diffusion over SW-BN anodes. Reproduced with permission.<sup>[589]</sup> Copyright 2023, Elsevier. l) Calculation potential for adsorbed Ca percentages for DV and SW effects. Reproduced with permission.<sup>[591]</sup> Copyright 2014, American Chemical Society. m) In-situ XRD for Ca-Sn alloy anode phase analysis upon electrochemical process. Reproduced under the terms of a Creative Commons CC BY 4.0 license.<sup>[592]</sup> Copyright 2022, Nature Publishing Group. n) XPS spectra charge-discharged graphite for -2.9 and 0.2 V (left) and synchrotron XPS for various photon energies (right). Reproduced under the terms of a Creative Commons CC BY license.<sup>[593]</sup> Copyright 2019, Wiley VCH. o) Migration pathways (top) and OCVs of  $\text{BC}_3$  with Ca concentrations. Reproduced with permission.<sup>[594]</sup> Copyright 2022, Elsevier.



SEI in AGEs. Ca 2p XPS spectra demonstrates presence of CaO,  $\text{Ca}_3\text{N}_2$ , Ca-S (CaS or  $\text{Ca}(\text{HS})_2$ ),  $\text{CaCO}_3$ , and  $\text{Ca}(\text{NO}_3)_2$  and enhancement of intensity for CaO,  $\text{Ca}_3\text{N}_2$ , and Ca-S species and reduction for  $\text{CaCO}_3$  with etching time manifesting  $\text{CaCO}_3$  is in outer-layer of SEI and CaO,  $\text{Ca}_3\text{N}_2$  are major components of SEI inner-layer (Figure 29j). This inorganic SEI inhibits the polysulfide dissolution and HER.<sup>[585]</sup>

Initially, the electroplating of Ca and Mg failed owing to poor diffusion of divalent cations through passivation layers ( $\text{M-SOCl}_2$ , M = Ca or Mg) with typical formation of  $\text{Ca}^{2+}$ -surface-blocking films restricting the  $\text{Ca}^{2+}$ -deposition.<sup>[586]</sup> Several efforts have been performed to reversible  $\text{Ca}^{2+}$ -plating/stripping from developing Ca-based anodes, electrolytes, and proper solvation chemistries. Tran and Obrovac show metal-alloy anodes for various  $\text{A}_x\text{M}$  batteries (A = Li, Na, K, Mg, Ca, and Al) in terms of volumetric energies and electrode expansion kinetics and revealed the  $\text{Ca}_2\text{Si}$  and  $\text{Ca}_2\text{Sn}$  alloys have larger volumetric energies of 5690 and 4317  $\text{Wh L}^{-1}$  than LIBs anodes, which manifests Ca-Si or Ca-Sn is favorable anodes for CIBs.<sup>[587]</sup> Ponrouch et al.<sup>[588]</sup> reports the electrochemical feasibility for  $\text{Ca}^{2+}$ -decalcification of  $\text{Ca}^{2+}$  for Ca-Si intermetallic alloy with 306% volume expansion by inserting  $\text{Ca}^{2+}$  in the fcc-Si causes structural failure. The Ca-diffusion in Stone-Wales boron nitride (SW-BN) surfaces possess two feasible directions along a- and b-axis (Path-I and II), in which Ca diffuses among the two adjacent more stable hollows ( $\text{S1} \rightarrow \text{S1}$ , Path-I) and another hollow ( $\text{S1} \rightarrow \text{S2}$ , Path-II). Diffusion barriers for path-I and II are 0.11 and 0.49 eV, respectively, which indicates the Ca-transport for SW-BN is superior in path-I (Figure 29k).<sup>[589]</sup> Woodcox and Smeu report the elastic properties DFT calculations for  $\text{Ca}_x\text{Sn}_{1-x}$  alloys anode with four stable ( $x = 0.25, 0.5, 0.625, 0.75$ ) and three metastable ( $x = 0.5$  (two), 0.75 (one)) phases. It shows shear, Young's, and bulk modulus in the range of 21.6–25.3, 56.1–59.1, and 25.7–46.3 GPa, respectively.<sup>[590]</sup> Ca-atoms are mainly positioned closer to O places (i.e., adatom clusters nearby defective zone) for divacancy, and adsorption percentage enhances with a rise in defect density for SW defects (Figure 29l).<sup>[591]</sup> Figure 29m demonstrates the phase evolution of  $\text{Ca}_x\text{Sn}$  anodes under 0.5–2.5 V. For the first cycle, the  $\text{Ca}_2\text{Sn}$  peak decreases upon onset of decalcification and then continuously diminishes intensity with signals of  $\beta$ -Sn upon discharge, whereas,  $\text{CaSn}_3$  peaks newly emerged upon charge. Further, the reversible de-/calcification of  $\text{CaSn}_3$  is verified for repetitive charge-discharge cycles. SEM displays pristine  $\text{Ca}_x\text{Sn}$  aggregates particles of 1–30  $\mu\text{m}$ , while after the 3000<sup>th</sup> cycle's porous and rod-shaped crystalline solids (100–300 nm).<sup>[592]</sup> XPS clarifies the existence of  $\text{Ca}^{2+}$  in the graphite surface by surface adsorption and SEI. Synchrotron XPS displays two Voigt functions of surface  $\text{Ca}^{2+}$  and intercalated Ca- $\text{G}_4$  peaks for 346.6 and 347.5 eV (Figure 29n). By changing photon energy from 523–950 eV, gradual decrease for surface  $\text{Ca}^{2+}$  signals is observed implying the discharged-state Ca-peaks correlates for surface  $\text{Ca}^{2+}$  in XPS. EDS and XPS also justify the higher quantity of Ca in charged graphite compared to discharged graphite and verify the simultaneous increase/decrease for O-contents facilitating reversible de-/intercalation of  $\text{Ca}^{2+}$  with  $\text{G}_4$ .<sup>[593]</sup> Energy barriers and adsorption energies of P1, P2, P3, P4, and P4 are 0.214, 0.147, 0.571, 0.247, 0.458 eV and 0.08, 0.05, 0.41, 0.11, 0.37 eV, respectively for Ca adsorbed boron carbide ( $\text{BC}_3$ ) monolayer. The charge distribution, lattice distortion, electronic, and steric hindrance severely influ-

**Table 4.** State-of-the-art performances for different SSBs chemistries.

Battery systems	Gravimetric energy densities based on active materials mass ( $\text{Wh kg}^{-1}$ )	Cell voltage (V)	Cycle life (number of cycles)	Cycle retention (%)
Li-metal	300–800	3–4.5	100–400	50–60
Lithium-sulfur	1500–1800	2–2.3	100–300	20–40
Na-metal	200–300	3–4	100–250	20–40
K-ion	250–400	3–3.5	100–300	20–40
Mg-ion	50–120	0.8–1.2	50–100	20–30
Zn-metal	300–500	1–1.2	100–250	30–40
Al-ion	100–200	1.7–2.2	50–100	20–30
Ca-ion	<20	0.8–1.2	<20	20–30

ence the migration pathways. P1 (P4) shows small adsorption energy and high migration barrier due to considerable changes in distributed charges and lattice structures. OCV of  $\text{BC}_3$  is 1.85 V and gradually decreases with Ca-concentration from 1.85 to 0.027 for 0 to 6 atoms (Figure 29o).<sup>[594]</sup> Numerous anodes including  $\text{Sn-In}_2\text{O}_3$ ,  $\text{BC}_3$ , tetracarboxylic diimide (PTCDI), Ca-Mg, Ca-Sn, Ca-Si, Ca-Bi, 3,4,9,10-perylenetetracarboxylic dianhydride (PTCDA),  $[\text{Ca}(\text{DMAC})_4]\text{C}_{50}$  ternary graphite-intercalation compounds,  $\text{Ca}_2\text{Zn}$ ,  $\text{CaLi}_2$ ,  $\text{Ti}_3\text{C}_2$ , MCMB, and highly oriented pyrolytic graphite (HOPG) have been investigated, however,  $\text{Ca}^{2+}$ -diffusion, irreversibility for plate/strip, de-/solvation kinetics, and passivated interfaces are major challenges of CIBs anode materials.<sup>[595–600]</sup> In summary, the rational design of SEs allows stable SEI formation on Ca-surface with high-ion conductivity and wide EWs. Comprehensively, CIBs are in an early stage of development due to a lack of electrode/electrolyte materials that can operate at RT. The attractive ways for Ca-anodes are alloying or intercalating carbon-based materials with lower stable potentials. Ca-Sn alloy suggests promising anodes compared to Mg-/Na-ions. To obtain high-energy CIBs, compatible alloy anodes must be coupled with high redox-voltage/capacity cathodes. Close-packed structures typically deliver high energies, up to now reported materials inhibit the reversibility of  $\text{Ca}^{2+}$ -ions upon de-/calcification owing to thermodynamic instabilities of  $\text{Ca}^{2+}$ -ions in the lattice structures. Performance metrics for these battery chemistries and spectroscopic techniques for interfaces are outlined in Tables 4 and 5.

## 8. Comparison of Anode Chemistries in Liquid Counterparts

Unlike conventional graphite or Si, Li-metal anodes are highly reactive with organic liquid electrolytes. Therefore, the salts and solvents from electrolytes promptly reduce with Li-metal contact by forming an SEI layer over the surface of Li-metal. Typically, the SEI layer comprises primarily inorganic species ( $\text{Li}_2\text{CO}_3$ ,  $\text{Li}_2\text{O}$ , and  $\text{LiF}$ ) for the inner layer, whereas organic species ( $\text{ROLi}$ ,  $\text{ROCO}_2\text{Li}$ , and  $\text{RCOO}_2\text{Li}$ ) are in the outer layer, which significantly depends on the electrolyte compositions.<sup>[601]</sup> Ideally, SEI features ion-conduction and electronic-insulation behavior that prevents straight interaction among the Li-metal (or others) and electrolytes; however, it permits migration of  $\text{Li}^+$ -ions (or others)

**Table 5.** State-of-the-art spectroscopy techniques for interface analysis of SSBs.

Spectroscopy techniques	Capability	Sample requirements	Limitations
Time of flight secondary ion mass spectroscopy (ToF-SIMS)	Elemental and molecular ion quantification	Size- 1–1.2 cm <sup>2</sup> , Thickness- <10 cm, Insulator or conductor	Lower quantitative sensitivity
Ar <sup>+</sup> -X-ray photoelectron spectroscopy (XPS)	Element quantification, chemical states	Thickness- <1 mm	Weak lateral resolution ≈3 μm
Synchrotron XPS	Chemical core-states and elemental quantification	Special cell design	Inert for Li
X-ray absorption spectroscopy (XAS)	Element quantification, Chemical and structural kinetics	Special cell design	Inert for Li
X-ray reflectivity (XRR)	Thickness, interface layers, density	Smooth surface	No element detection
Neutron-depth profiling (NDP)	Quantification of interlayer formation, Active finding for Li-ions	Thickness- 4.5 μm Roughness- <10 nm Proper stoichiometric	Depth of detection limits for <150 μm
Rutherford backscattering spectroscopy (RBS)	Film density, impurity profiles, the interaction of inter-diffusion	Smooth surface, good for heavy elements, insulator or conductor	Expensive, Inter-element interface, depth of detection < 1 mm
Auger electron spectroscopy (AES)	Elements or ions, chemical and atomic structure quantification	Thickness- <12 cm, Size- 1–3 cm <sup>2</sup> , only conductors,	Atomic detection limit – 1%, Inert for chemical valence
Nuclear reactions analysis (NRA)	Elements, isotope, and concentrations quantification	Good for light elements in heavy matrix, Insulator or conductors	Expensive, detection limit <150 μm
Glow discharge optical emission spectrometry (GD-OES)	Elemental quantification, Faster sputtering rates, Lower cost	Diameter- >4 mm No size limit, Thermal and mechanical stability, Both insulator or conductors	Poor lateral resolution ≈1 mm, Inter-elements interferences
Laser ablation inductively coupled plasma mass spectrometry (LA-ICP-MS)	Elemental quantification, Faster sputtering rates	Diameter- <40 mm Thickness- <20 mm, Insulator or conductors	Poor lateral resolution ≈10 mm, Inter-elements interferences
Nuclear magnetic resonance (NMR) with magnetic resonance imaging (MRI)	Quantify structures of SEI, chemical shifts, Microstructure of dendrites or deposits	Thermal and mechanical stability, Both insulator or conductors	Limited for a few elements

without decomposition of electrolyte and offers uniform Li<sup>+</sup>-ions (or others) distribution with homogeneous metal-depositions. In practice, the SEI layer is brittle, uneven, and their components did not accommodate the volume expansion of M<sup>+</sup>-metals upon M<sup>+</sup>-plate/stripping. Hence, the SEI layer is certainly ruined upon volume changes triggering severe cracks for SEI. Li<sup>+</sup>-ions display preferential plating, and current density localizes over the cracks due to lower interfacial resistance of newly open Li-surfaces at cracks than Li-surfaces shielded with intact SEI. Thus, Li-metal protrusions rise inhomogeneously from crack regions implying heterogeneous Li<sup>+</sup>-plating. Besides, freshly plated Li-metal is highly reactive with electrolyte depletion, forming additional SEI over new Li<sup>+</sup>-depositions. This repetitive demolition and restructuring for SEI initiated from uneven Li-plate/stripping causes constant depletion of Li-metals and electrolytes, manifesting poor CEs and larger interfacial resistances.<sup>[602–604]</sup>

Han et al.<sup>[605]</sup> reports the electroplating for lithium bis-trifluoromethanesulfonylimide (LiTFSI)–1,3-dioxolane/1,2-dimethoxyethane (DOLDME) electrolytes (1.0 m LiTFSI with 1:1 v/v DOL/DME and 1% LiNO<sub>3</sub>), which displays the generation of Li<sub>metal</sub> spherical particles with Li<sub>bcc</sub> single-crystals along (131) and Li<sub>2</sub>O (111) diffractions. TEM images show dark exoskeleton and light-contrast Li<sub>metal</sub> with a 20 nm transition zone from SEI exoskeleton to inner crystalline Li<sub>bcc</sub> and amorphous Li-matrix (Li<sub>amorphous</sub>) consisting of nanocrystalline Li<sub>2</sub>O,

LiF, or other amorphous phases. Inorganic Li<sub>2</sub>O and Li<sub>2</sub>CO<sub>3</sub> phases are in the SEI exoskeleton inside the organic polymer matrices (**Figure 30a–f**). The F, O, N, and C participate from electrolytes parasitic reactions with half-cell reactions (e<sup>−</sup>(metal) + Li<sup>+</sup>(SEI) = Li-atoms in Li<sub>metal</sub>), illustrating amorphous Li<sub>metal</sub> nearby SEI exoskeletons. Polymeric elements for SEI show partial decomposition for LiC<sub>x</sub> and Li<sub>2</sub>O and C, N, F, O for LiF and Li<sub>2</sub>O. Li, C, N, O, and F K-edge spectra feature mixed valence states for SEI (LiC<sub>x</sub>, Li<sub>2</sub>O, LiF, Li-polymer, π\*(C=C) and σ\*(C-N, C-O, C-C), **Figure 30g–i**).<sup>[606,607]</sup> Theoretical calculations report ≈10 nm SEI consists of densely ordered inorganic layer (≈2.5 nm enriched with C and F) closer to Li-metal anodes and porous organic layers (≈7.5 nm enriched with O and F) closer to electrolytes in [bis(trifluoromethyl-sulfonyl) imide][1-butyl-3-methylimidazolium] ([TFSI][BMIM]) ionic liquid electrolytes (**Figure 30j**).<sup>[608]</sup>

**Figure 30k–r** displays the corrosion depths of Li-metal with/without GaSnIn additives in conventional LiPF<sub>6</sub>-EC/DMC electrolytes.<sup>[609]</sup> Upon first cycle, the corrosion layer thickness is similar in both electrolytes. In contrast, the 10 h cycle's thickness in conventional electrolytes is slightly larger and much higher after 100 and 250 h (582 μm) cycling, which causes cell failure. Massy dendrites, porous, and loosely bound structures with increased contact areas are clearly seen for LiPF<sub>6</sub>-EC/DMC after 50 cycles, implying exacerbated side-reactions with electrolyte

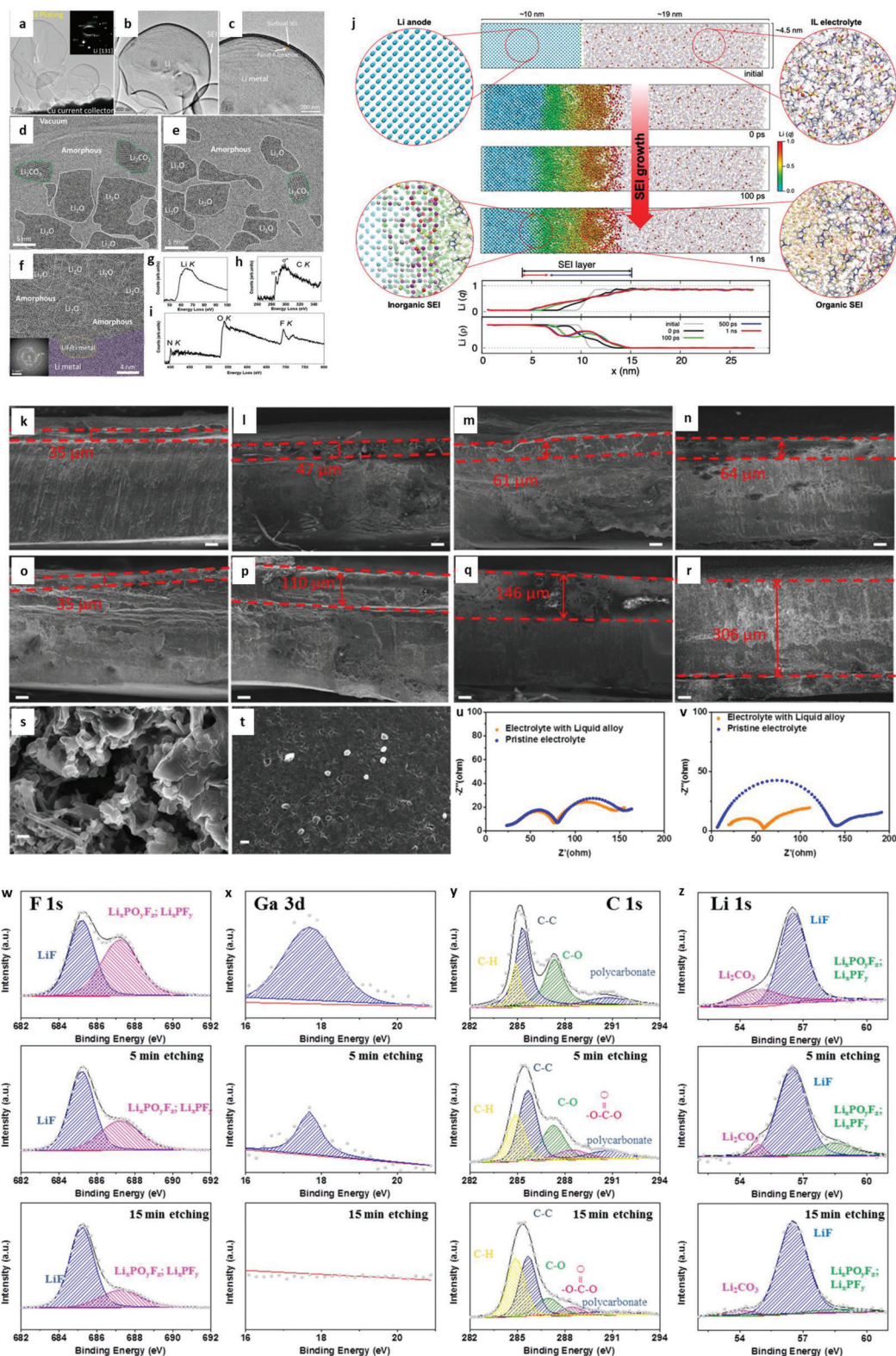


**Figure 30.** a-f) TEM images and g-i) Li, (g) C (h), N, O, and F (i) K-edges from SEI. Reproduced with permission.<sup>[605]</sup> Copyright 2022, Wiley VCH. j) SEI formation by MD simulations in [TFSI][BMIM] IL electrolyte at 300 K. Reproduced with permission.<sup>[608]</sup> Copyright 2023, Wiley VCH. k-r) SEM images with (k-n) and without (o-r) GaSnIn additives in convectional electrolyte. s,t) SEM images of Li-plate in pristine (s) and GaSnIn additives (t) electrolytes. u,v) EIS spectra before/after cycles. w-z) XPS depth profiles of F 1s (w), Ga 3d (x), C 1s (y) and Li 1s (z). Reproduced with permission.<sup>[609]</sup> Copyright 2021, Elsevier.



depletion (Figure 30s). Whereas, the compact and smooth morphology without dendrites are observed for GaSnIn-based liquid electrolytes, manifesting suppression of Li dendritic-growth (Figure 30t). EIS displays stable interfacial impedance (charge-transfer and Li-ion diffusion resistances) for GaSnIn-based electrolyte after long-operations (Figure 30u,v).<sup>[610]</sup> XPS spectra reveal C-H, C-C, C-O,  $\text{CO}_3^{2-}$ , and polycarbonate groups, implying the presence of organic and inorganic species. SEI displays surface layer is enriched with  $\text{Li}_x\text{PF}_y$ ,  $\text{Li}_2\text{CO}_3$ , and the inner layer with LiF, illustrating the importance of the depletion of  $\text{LiPF}_6$  (Figure 30w-z). XPS confirms the formation of gradient SEI layers with GaSnIn additive with flexible polycarbonate surface-rich and inorganic LiF-rich cores with lower  $\text{Li}^+$ -partial molar volume. The weaker binding for LiF-rich inner SEI to Li effectively facilitates lateral diffusion of Li with the prevention of Li-dendrites from cracking SEI layers, whereas the outer polycarbonate-rich flexible layer controls the integrity of other ionic-conductive SEI elements and adhesion for bulk Li-anodes.

Xie et al.<sup>[611]</sup> reports design strategies for fluorinated molecules with fluoroalkyl ( $-\text{CF}_2\text{CF}_2-$ ) as F-resource. The C-F bond defluorination is improved by leaving species on  $\beta$ -sites, illustrating the faster kinetics of LiF-forming reactions (Figure 31a). The 2,2,3,3-tetrafluorobutane-1,4-diol dinitrate (AFA), 1,4-butanediol dinitrate (BDN), and 2,2,3,3-tetrafluoro-1,4-dimethoxybutane (DFA) activated fluoroalkyls are proposed. The active ending group of  $-\text{NO}_3$  is considered due to the robust parting affinity of  $-\text{NO}_3$  in nucleophilic environments and electrochemical reductions; larger reduction potentials provide key degradation on anodes for SEI generation; 3) corrosion products for AFA degradations,  $\text{NO}_x^-$  offers compatible additives.<sup>[612,613]</sup> 30.2% mass ratio for F with faster kinetics for release of fluoride awarded by  $-\text{NO}_3$  are united to concentrate robust fluorinated SEI. Fluorinated SEI generation with AFA in Li-S batteries is examined in Figure 31b-h. F content in SEI with AFA electrolytes is 15% for the surface and 36, 32, 29, and 27 % in-depth areas for etching time of 40, 80, 120, and 160 s, respectively, whereas with  $\text{LiNO}_3$  or DFA electrolytes is <10% (Figure 31b-d). Such significant F content in SEI for AFA illustrates the role of active ending species in endorsing the release of F with effective building fluorinated SEI. XPS displays fluorocarbon anions obtained from the partial degradation of AFA-dS after C-S bond cleavage ( $-\text{CF}_2-$  peak in F 1s) and minor for LiTFSI; however, it is absent in  $\text{LiNO}_3$  electrolytes. C and F signals of fluorocarbon anions reduce SEI inner layer, illustrating C-F bond breaking and formation of LiF with multistep kinetics as (detachment of active  $-\text{S}-$  from AFA-dS for constructing  $\text{R}-\text{CF}_2\text{CH}_2-$  residues, and then C-F elimination for generating LiF as SEI inner layer, Figure 31e-g). Uniform and denser SEI (25–30 nm thickness) for AFS on Li-anodes with crystalline LiF, whereas inhomogeneous 40–50 nm SEI with  $\text{LiNO}_3$ , which manifests the uniform Li plate/stripping and superior Li-ion mobility.<sup>[614]</sup>

As we know, the electron affinity of EC > DMC; thus, EC is favorably reduced in EC:DMC over the Na-metal surface.<sup>[615]</sup> Initially,  $\text{Na}^+$ -ions are solvated by EC molecules with reduction of EC ( $1e^-$ ) ensuing sodium ethylene decarbonate  $\text{NaO}_2\text{CO}-\text{C}_2\text{H}_4-\text{OCO}_2\text{Na}$  (NEDC) that collects and changes in amorphous organic/polymer layer (Figure 32a-c).<sup>[616]</sup> Poor hydrolytic stability of NEDC further generates  $\text{Na}_2\text{CO}_3$ , ethylene, and  $\text{CO}_2$  in

the presence of traces of acid or water in electrolytes by SEI destabilization.<sup>[617]</sup> Upon cycling,  $\text{Na}_2\text{CO}_3$  of SEI decomposes to  $\text{CO}_2$  gas, terminating intact SEI. Lucht et al.<sup>[617]</sup> present reactions among the  $\text{LiPF}_6$ -salt and various lithium carbonates that yields  $\text{Li}_x\text{PF}_y\text{O}_z$  and  $\text{F}_2\text{PO}_2\text{Li}$ . The  $\text{Na}_3\text{PO}_4$  formation also follows similar reactions among the  $\text{NaPF}_6$  and sodium carbonates in the electrolytes. NEDC decomposes larger  $\text{CO}_2$ , and the formed  $\text{Na}_3\text{PO}_4$  undergoes disruptions and follows random distributions in the SEI. Na-dendrites are isolated from hosts owing to inhomogeneous dissolution rates at various regions during stripping, which manifests thicker SEI and Na-depletion with confined Na metal, needle-shaped  $\text{Na}_3\text{PO}_4$ , larger pieces of  $\text{Na}_2\text{CO}_3$ , and mosaic of NEDC polymers (Figure 32b,c). FEC-EC:DMC forms thinner SEI due to the reaction among the FEC and Na-metal, forming a uniform film of NaF over the  $\text{Na}_3\text{PO}_4$  surface for the initial stage of SEI.<sup>[618]</sup> The  $\text{Na}_3\text{PO}_4$  and NaF phases impede electrolyte reduction with severe NEDC and  $\text{CO}_2$  formation decrease. The NEDC and  $\text{Na}_2\text{CO}_3$  are not protected by covering layers and rapidly decompose; thus, the resultant SEI comprises dense inorganic  $\text{Na}_3\text{PO}_4$  and NaF/amorphous composite bilayer structures (Figure 32d-f). Amorphous organic/polymer phases for SEI function significantly due to the protection of SEI by intense volume changes upon cycling, which is intensely associated with battery cycle-life failure. Na//Na cells with FEC-EC:DMC displays stable operations for 500–800 h for all current densities; however, FEC-free EC:DMC deteriorated after 50 cycles for  $0.5 \text{ mA cm}^{-2}$  smaller current density with catastrophic cell failures for higher currents (Figure 32g-i). Further, FEC-EC:DMC displays reliable impedance and stable SEI for 1<sup>st</sup> cycle, whereas FEC-free EC:DMC induces dynamic changes in SEI, resulting in higher impedance (Figure 32j,k). Ji et al.<sup>[619]</sup> reports FEC additive displays a uniform and thinner SEI for SnSb-carbon anodes in Na-ion cells. Besides, Fondard et al.<sup>[620]</sup> proposes the FEC insertion displays reduction of  $\text{Na}_2\text{CO}_3$  formation and decrease in SEI thickness with increasing NaF phase. Many researchers determined complete NaF generation pathways by reduction of FEC for Na-metals by Monte Carlo/molecular dynamics to predict NaF formation over the SEI top surfaces and limitations of solubility issues for amorphous NEDC.<sup>[618,621,622]</sup>

Ding et al.<sup>[623]</sup> report the strategies for stabilization of K-metal interfaces using metal electrode skin (MES) by mimicking human skins. MES consists of GO that can improve in situ SEI generation. GO is fluorinated with partial replacement of oxygen-functional groups to form F-GO MES and then extracted over Cu and K-foils. Wrinkled microstructures with poor flatness and larger undulations for Cu (or K) surfaces are observed, whereas with MES flat and uniform materials coverage in both kinds of electrolytes (3 M KFSI in DME and 0.8 M  $\text{KPF}_6$  in EC/DMC, EC/ DMC = 1:1), implying superior wettability of electrolytes. Cu@MES//K maintains a stable voltage of  $\approx 4 \text{ V}$  with zero current, which implies MES well protects the Cu and the electrolyte did not penetrate F-GO, whereas bare Cu failed to retain 4 V, which suggests strong corrosion for bare Cu. K@MES displays minimal interface impedance and faster  $\text{K}^+$ -ions kinetics, resulting in stable K-deposition and SEI without dendrites upon cycling under symmetric cells, whereas K@GO or bare K possesses large unstable impedance, larger overpotentials, and fluctuations. The irregular K plate/stripping shows unstable SEI initially. Upon several cycles, interfaces become more inferior, ex-

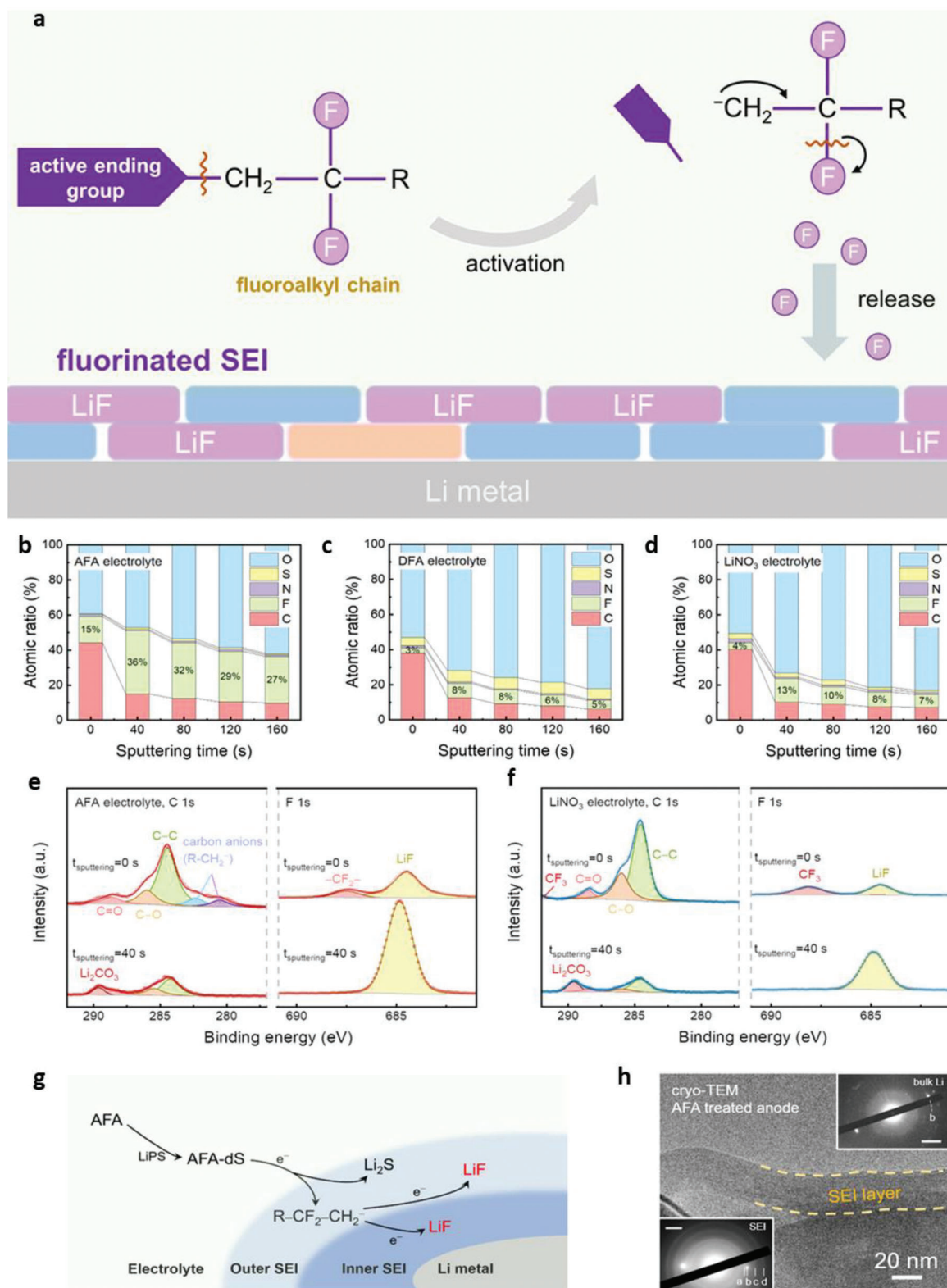


**Figure 31.** a) Fluorinated molecule synthesis scheme. Atomic concentrations of F, O, C, N, and S in formed SEI layer with b) AFA, c) DFA, and d) LiNO<sub>3</sub> electrolytes for various puttering times. C 1s and F 1s XPS spectra for SEI with e) AFA and f) LiNO<sub>3</sub> electrolytes. g) Reaction mechanism. h) Cryo-TEM image for SEI and Li-anodes in AFA electrolytes. Insets are SAED images of SEI and bulk Li. Reproduced with permission.<sup>[611]</sup> Copyright 2022, Wiley VCH.

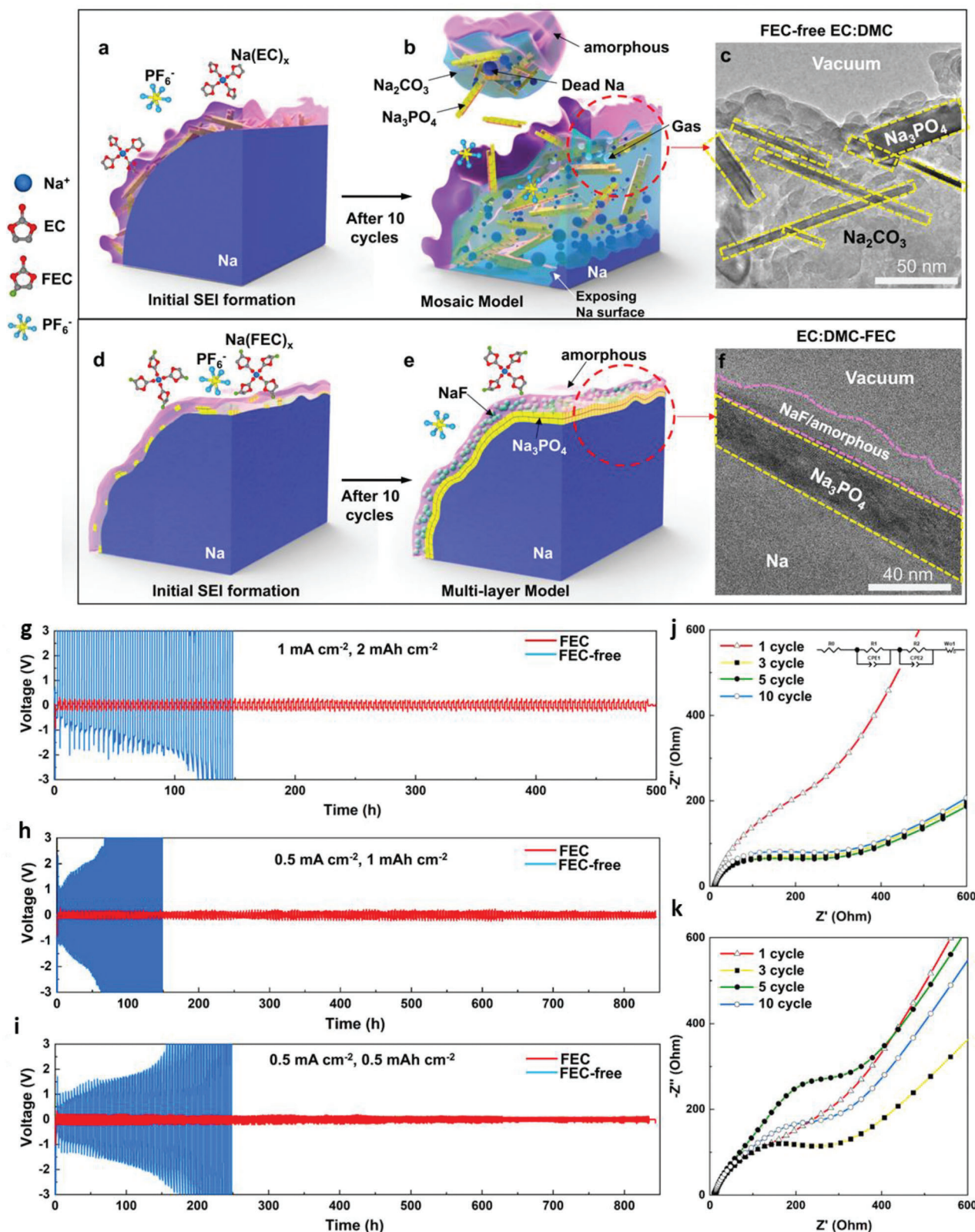


**Figure 32.** a-c) SEI nucleation at 1<sup>st</sup> cycle (a) and final structures after 10 cycle (b) and cryo-TEM image for FEC-free EC:DMC electrolytes after 10 cycles (c). d-f) SEI nucleation at 1<sup>st</sup> cycle (d) and final structures after 10<sup>th</sup> cycle (e) and cryo-TEM image for FEC-EC:DMC electrolytes after 10<sup>th</sup> cycles (f). g-i) Na//Na cell performance and j,k) EIS plots for FEC-EC:DMC (j) and FEC-free EC:DMC (k). Reproduced under the terms of a Creative Commons CC BY license.<sup>[616]</sup> Copyright 2021, Nature Publishing Group.



acerbating the dendritic growth (i of **Figure 33a**). GO-protection for K-metals temporarily alleviates the stress changes due to volume expansions; however, not able to work for more extended operations, and SEI will not protect interface effectively (ii of **Figure 33a**). F-GO interface alternations enhance the surface smoothness of K-anodes by realizing ion concentrations and uniform electric fields. F-GO alleviates volume expansion and promotes C-F bonds, and releases larger F for the construction of F-rich SEI (interface stability for battery operation life and dendrite-free plate/strip; iii of **Figure 33a**). MES for K-metal deposition evolves smoother surfaces without loose and porous materials compared to GO and bare K. In situ optical images display that a large amount of mossy K and dendrites emerged even for 300–600 s for K@GO and bare K, whereas K@MES remains dendrite-free (**Figure 33b,c**). Further, Cu@MES shows denser dendrite-free flat surface loading, while Cu@GO and bare Cu surfaces provide larger volume expansions with severe dendrites for K-metal deposits (**Figure 33d**). K@MES displays 2300 h (3 m KFSI in DME) plate/stripping lifetime, while K@GO fails for 670 h. Similarly, Cu@MES//K achieves 1600 cycles; however, Cu@GO//K and Cu//K give 300 and 60 cycles only (**Figure 33e,f**).

Chinnadurai et al.<sup>[624]</sup> reports the utilization of a series of Mg halides ( $\text{MgX}_2$ , X = Cl, I, F, and Br; **Figure 34**) as additives for conventional magnesium bis(hexamethyldisilazide) ( $\text{Mg}(\text{HMDS})_2$ ; 0.1 M) in 1,2-dimethoxyethane (DME) with a small amount of tetrabutylammonium borohydride ( $\text{TBABH}_4$ ; 30 mM). The  $\text{MgBr}_2$  has nucleation overpotential ( $\Delta n$ ) of 0.39 V lower than those of  $\text{MgCl}_2$  (0.71 V),  $\text{MgI}_2$  (0.70 V), and  $\text{MgF}_2$  (0.54 V), vindicating decreased energy barriers of Mg nucleation with  $\text{MgBr}_2$  additives ( $\sigma_{\text{Mg}}^{2+} \approx 0.462 \text{ mS cm}^{-1}$ ). However,  $\text{MgF}_2$  displays the lowest  $E_a$  suffers with poor Mg plating/stripping reversibility. Mg//Mg cells show longer Mg plate/stripping for 460 cycles with  $\text{MgBr}_2$ ; however, for  $\text{MgI}_2$  (few tens),  $\text{MgF}_2$  (310), and  $\text{MgCl}_2$  (415). XPS for Mg anode-electrolyte interface exhibits C–C (284.4 eV), O–C–O (285.5 eV), C=O (286.52 eV), O–C=O (287.09 eV),  $\text{C}_2\text{O}_4/\text{CO}_3^{2-}$  (289.68 eV), and Si–C (283.25 eV) in C 1s,<sup>[625]</sup> Mg metal (49.8 eV),  $\text{MgO}/\text{MgBr}_2/\text{MgF}_2$  (51.0 eV),  $\text{MgCl}_2$  (51.8 eV),  $\text{MgI}_2$  (52.5 eV), and Mg dangling bonds (48.4 eV) in Mg 2p,<sup>[624,626,627]</sup>  $\text{MgCl}_2$  (199.1 eV),  $\text{MgI}_2$  (618.5 eV),  $\text{MgF}_2$  (685.7 eV),  $\text{MgBr}_2$  (68.75 eV),  $\text{Si}^0$  (99.2–99.5 eV) in halide spectra,<sup>[624,628–630]</sup> Si–C (101–104 eV) in Si 2p, and Mg– $\text{BH}_4$  (188.7 eV) and B-oxides (192 eV) in B 1s spectra.<sup>[624,631]</sup> TOF-SIMS images display Mg-anodes possessing organic-rich SEI with native Mg oxides ( $\text{MgO}$ ,  $\text{Mg}(\text{OH})_2$ ) under  $\text{MgBr}_2$  electrolytes. Below organic-rich SEI, the inorganic SEI with  $\text{MgBr}_2$ ,  $\text{Mg}(\text{BH}_4)_2$ , Mg oxides, and Si components were also observed.  $\text{MgCl}_2$  and  $\text{MgF}_2$  display lower reliability for dispersal organic-rich SEI, while  $\text{MgI}_2$  shows uneven dispersal of organic species with large agglomeration.  $\text{MgBr}_2$  shows uniform deposition of Mg with crystalline nature due to lower nucleation overpotential. Typically,  $\text{Mg}(\text{HMDS})_2$ -based electrolyte suffers anode passivation due to the moisture contents of electrolytes and interactions with anodes. Halide additives possess a minimal amount of  $\text{BH}_4^-$ -ions as moisture scavengers and in situ SEI, which implies reversible Mg-ion transfers. Zhang et al.<sup>[632]</sup> reports  $\text{Mg}(\text{CF}_3\text{SO}_3)_2$ -based electrolyte, in which cycled Mg-anode surface mainly consists of  $\text{MgF}_2$ ,  $\text{MgCl}_2$ ,  $\text{MgS}$ ,  $\text{MgO}$ . According to the structures, the interphase layers with lower dif-

fusion energy barriers contain  $\text{MgS}$ -rich and hybridized polymer frameworks with an effective increase in  $\text{Mg}^{2+}$ -migrations with obtaining robust interfaces.<sup>[633]</sup>

Xiong et al. report controlling strategies for interfacial chemistry using hybrid electrolytes of water and a polar aprotic N,N-dimethylformamide for altering  $\text{Zn}^{2+}$ -solvated structures and formation of in situ  $\text{Zn}^{2+}$ -conducting  $\text{Zn}_5(\text{CO}_3)_2(\text{OH})_6$  SEI over the Zn surface.<sup>[634]</sup> In conventional  $\text{ZnSO}_4$  electrolytes, the formation of hydrated Zn-ions of  $[\text{Zn}(\text{H}_2\text{O})_6]^{2+}$  occurs due to reactions of free water molecules with  $\text{Zn}^{2+}$ -ions. Series of 2 M  $\text{ZnSO}_4\text{--H}_2\text{O--DMF}$  electrolytes in volume ratios of water to DMF (6:0, 5:1, 4:2, 3:3, 2:4, 1:5, and 0:6) has been reported, in which homogeneous solutions are observed for 5:1 and 4:2 ratios of  $\text{H}_2\text{O}/\text{DMF}$  and recrystallization of  $\text{ZnSO}_4$  occurs for  $\text{H}_2\text{O}/\text{DMF}$  ratio up to 3:3, which suggests DMF alterations for  $\text{Zn}^{2+}$ -solvation structures that can be destroyed for excess DMF. Theoretical calculations report the pronounced ion-solvation clusters for  $\text{Zn}^{2+}$  matched with  $\text{SO}_4^{2-}$ ,  $\text{H}_2\text{O}$ , and DMF. Radial distribution functions of  $\text{ZnSO}_4\text{--H}_2\text{O}$  show primary solvation shell of  $\text{Zn}^{2+}$  is of 2.5 Å distance, whereas a distinct Zn–O (DMF) at  $\approx 1.88$  Å with DMF insertion implies DMF critically integrates  $\text{Zn}^{2+}$ -solvated structures.  $\text{Zn}^{2+}$ -BEs has relations as  $\text{Zn}^{2+}\text{--SO}_4^{2-} > \text{Zn}^{2+}\text{--DMF} > \text{Zn}^{2+}\text{--H}_2\text{O}$ , manifests the preferential  $\text{Zn}^{2+}$  coordinations with DMF instead of  $\text{H}_2\text{O}$ . Thus lowered coordinating  $\text{H}_2\text{O}$  and free  $\text{H}_2\text{O}$  illustrate minimal probability for parasitic reactions during Zn-plate/strip. Zn//Zn cells display plate/strip process for 1780 and 2500 h under  $\text{ZnSO}_4\text{--H}_2\text{O--DMF}$  ( $\text{H}_2\text{O}:\text{DMF} = 5:1$  and 4:2) electrolytes, whereas,  $\text{ZnSO}_4\text{--H}_2\text{O}$  fails in 92 h with cell-failure with dendrites.  $\text{ZnSO}_4\text{--H}_2\text{O}$  has a lower overpotential than  $\text{ZnSO}_4\text{--H}_2\text{O--DMF}$  due to poor ion conductance and strong solvation effects.<sup>[635]</sup> XRD displays  $\text{Zn}_4\text{SO}_4(\text{OH})_6\cdot 3\text{H}_2\text{O}$  corrosion byproduct under  $\text{ZnSO}_4\text{--H}_2\text{O}$ , whereas pure Zn-phase for  $\text{ZnSO}_4\text{--H}_2\text{O--DMF}$ . In situ SEI and improved wettability for Zn-anodes show benefits for  $R_{ct}$  and Gibb's free energy reduction for nucleation upon reversible  $\text{Zn}^{2+}$ -plate/strip.<sup>[636]</sup> Zn surface exhibits numerous protrusions and scattered flakes with a  $48.4^\circ$  contact angle under  $\text{ZnSO}_4\text{--H}_2\text{O}$ , whereas smooth dendrite-free surface (contact angle  $\approx 0^\circ$ ) for  $\text{ZnSO}_4\text{--H}_2\text{O--DMF}$  electrolyte. **Figure 35a** displays 60–70 nm thick SEI for Zn-surface under  $\text{ZnSO}_4\text{--H}_2\text{O--DMF}$ . EELS ( $E_{p,\text{SEI}} = 19.2 \text{ eV}/\text{Zn}$  ( $E_{p,\text{Zn}} = 13.5 \text{ eV}$ ) heterostructures) and EDS maps reveal weaker Zn signal than pristine Zn, and stronger O reflections suggest less dense SEI and Zn phases (**Figure 35b,c**). TEM demonstrates  $\text{Zn}_5(\text{OH})_6(\text{CO}_3)_2$ -based composite SEI with d-spacing of 0.338 nm corresponds to (400) crystal-reflection of  $\text{Zn}_5(\text{OH})_6(\text{CO}_3)_2$  phase, whereas Zn-anode displays crystal plane of (002). Zn-anodes under  $\text{ZnSO}_4\text{--H}_2\text{O}$  electrolytes possess  $\text{Zn}_4\text{SO}_4(\text{OH})_6\cdot 4\text{H}_2\text{O}$  byproduct without SEI (**Figure 35e–g**). TOF-SIMS and XPS display  $\text{OH}^-$  ( $m/e = 17$ ),  $\text{CO}_3^{2-}$  ( $m/e = 60$ ), and  $\text{C}^-$  ( $m/e = 12$ , originated from the decomposed  $\text{CO}_3^{2-}$ ) signals for various depths of etching, indicating the formation of  $\text{Zn}_5(\text{OH})_6(\text{CO}_3)_2$  for SEI. Dissolved  $\text{CO}_2$  and  $\text{H}_2\text{O}$  in  $\text{ZnSO}_4\text{--H}_2\text{O--DMF}$  system obtains equilibrium for step-i, then DMF hydrolysis occurs for stage-ii due to acidic environments with the formation of dimethylamine ( $(\text{CH}_3)_2\text{NH}$ ) and formic acid ( $\text{HCOOH}$ ), later  $(\text{CH}_3)_2\text{NH}$  responds with  $\text{HCO}_3^-$  with creation of  $\text{CO}_3^{2-}$  species by bicarbonate deprotonation, and then  $\text{CO}_3^{2-}$  reacts with  $\text{Zn}^{2+}$  and

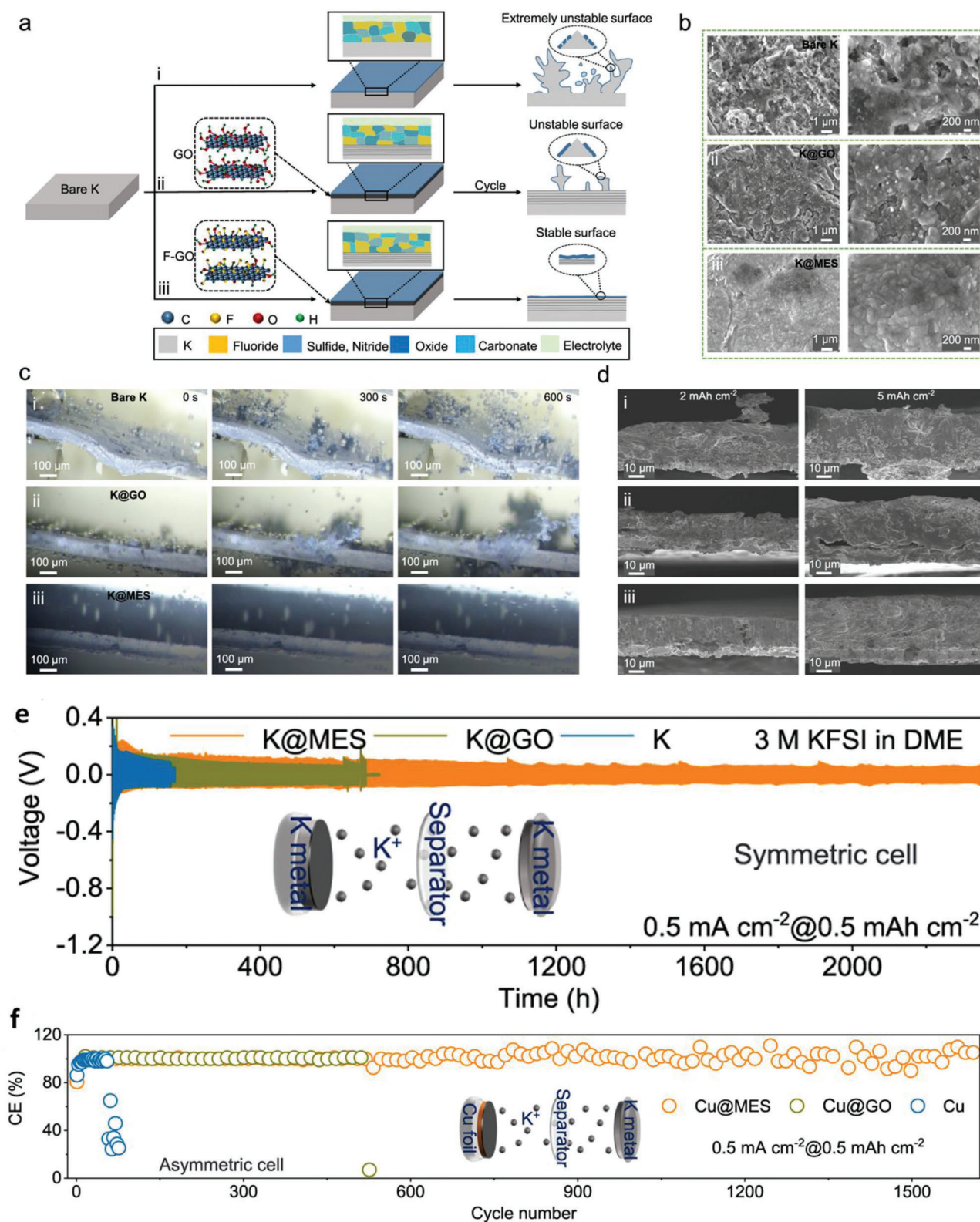


**Figure 33.** a) Scheme for interface evaluation. b) SEM images for various K-metal surfaces after cycling. c) In situ optical images for K-metal depositions. d) Cross-SEM images of K-metal deposited for various CCs, (i) bare K, (ii) K@GO, and (iii) K@MES. e) K-plate/stripping for KFSI electrolyte. f) CEs for Cu//K asymmetric cells. Reproduced under the terms of a Creative Commons CC BY license.<sup>[623]</sup> Copyright 2023, Nature Publishing Group.

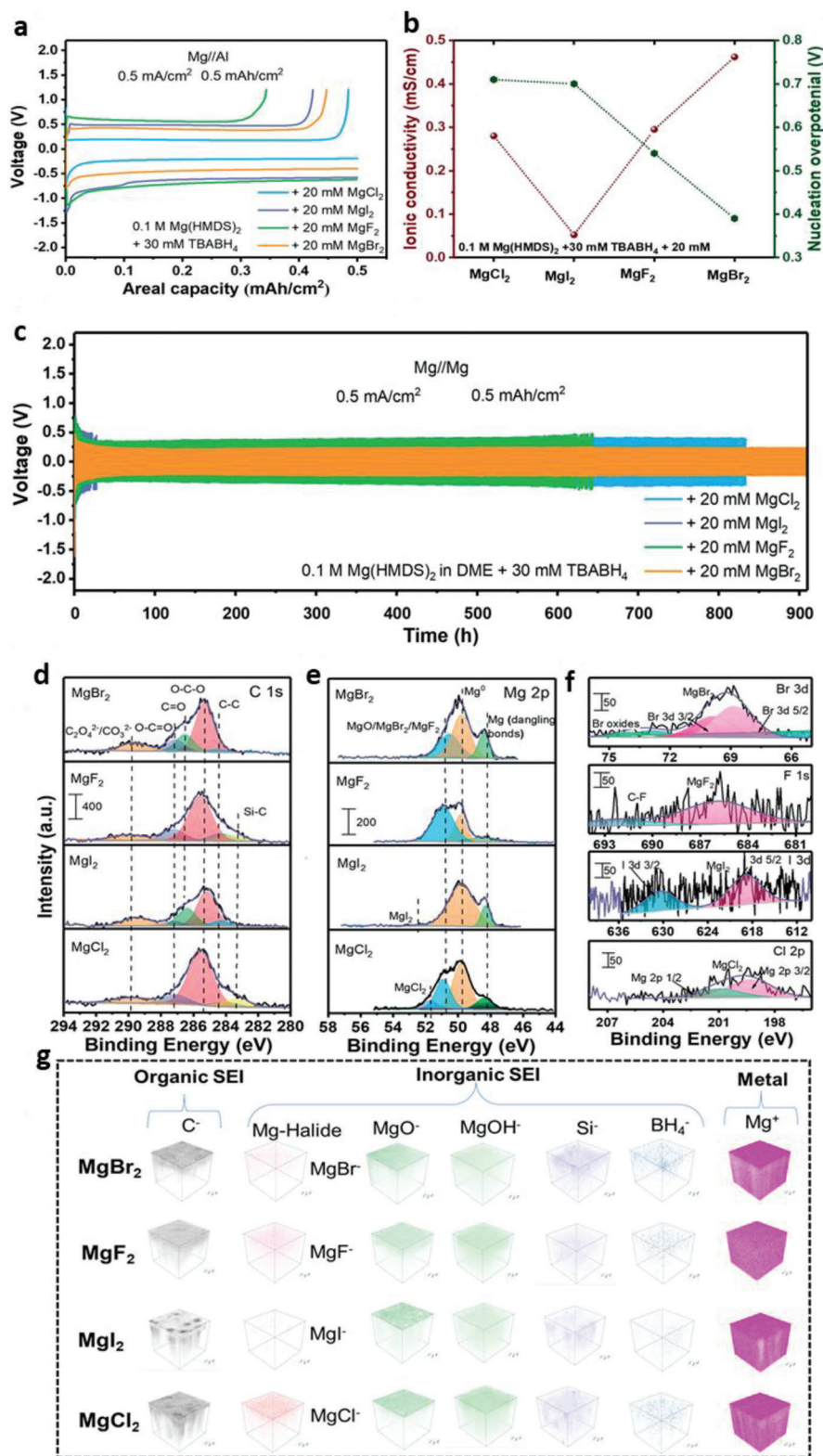


**Figure 34.** a) Mg plate/strip voltage profiles. b) ion conductivity and nucleation potential. c) Mg//Mg symmetric cells. d-f) XPS spectra for C 1s, Mg 2p, and halides. g) TOF-SIMS 3D images after 20 Mg//Mg cycles for Mg anodes. Reproduced with permission.<sup>[624]</sup> Copyright 2023, American Chemical Society.



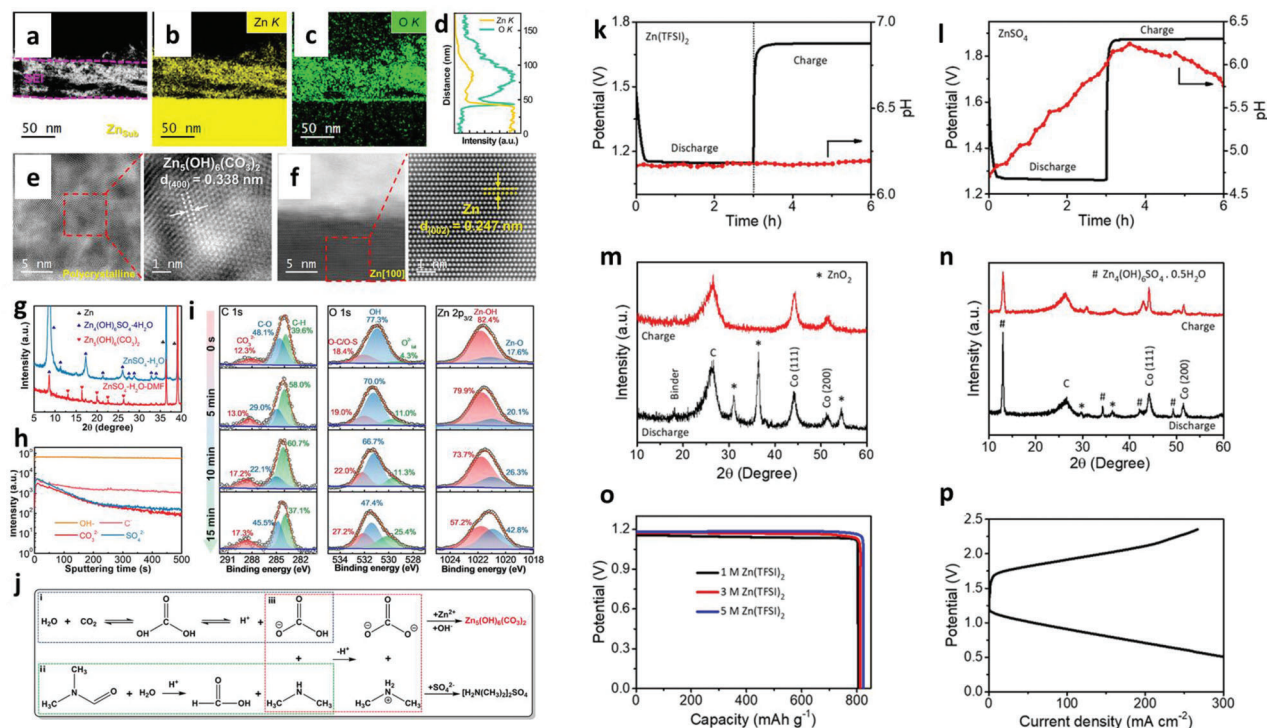


**Figure 35.** a) TEM image of Zn-anode under  $\text{ZnSO}_4\text{-H}_2\text{O-DMF}$ . b,c) EDS maps. d) EELS spectra across interfaces. e,f) ABF-TEM images for polycrystalline SEI and single-crystalline Zn-anode, respectively. g) XRD patterns for Zn under  $\text{ZnSO}_4\text{-H}_2\text{O}$  and  $\text{ZnSO}_4\text{-H}_2\text{O-DMF}$ . h) TOF-SIMS, and i) XPS in-depth spectra in  $\text{ZnSO}_4\text{-H}_2\text{O-DMF}$ . j) Formation mechanism for  $\text{Zn}_5(\text{OH})_6(\text{CO}_3)_2$ -contained SEI. Reproduced with permission.<sup>[634]</sup> Copyright 2023, American Chemical Society. k,l) Charge-discharge plots for  $\text{Zn}(\text{TFSI})_2$  (k) and  $\text{ZnSO}_4$  (l). m,n) XRD patterns. o) Specific capacity. p) C-D profiles for  $\text{Zn}(\text{OTf})_2$  electrolyte. Reproduced with permission.<sup>[204]</sup> Copyright 2023, American Chemical Society.

$\text{OH}^-$  with forming solidified  $\text{Zn}_5(\text{OH})_6(\text{CO}_3)_2$  (Figure 35h–j). Overall reactions are  $2\text{HCON}(\text{CH}_3)_2 + 2\text{CO}_2 + 2\text{H}_2\text{O} + \text{ZnSO}_4 + 4\text{Zn}(\text{OH})_2 \rightarrow \text{Zn}_5(\text{OH})_6(\text{CO}_3)_2\downarrow + [\text{H}_2\text{N}(\text{CH}_3)_2]_2\text{SO}_4 + 2\text{HCOOH}$ . DFT calculations predict a reaction energy of  $-7.78\text{ eV}/\text{Zn}_5(\text{OH})_6(\text{CO}_3)_2$ .<sup>[637–639]</sup>

Cell operating under  $\text{Zn}(\text{TFSI})_2$  retains stable pH during charge-discharge, whereas  $\text{ZnSO}_4$  shows an increase in pH (upon discharge) and decrease upon charge, suggesting  $\text{OH}^-$  formation/consumption for discharge/charge, respectively (Figure 35k,l).<sup>[204]</sup> Zn-anode displays insulating zinc sulfate hydroxide  $[\text{Zn}_4(\text{OH})_6\text{SO}_4 \cdot 0.5\text{H}_2\text{O}]$  (ZHS) formation under  $\text{ZnSO}_4$ , confirming poor reversibility (Figure 35m,n). Gradual increase of ZHS upon long operations leads volume expansions with electrolyte depletion, illustrating challenges for cell operations. Faraday's and ideal gas laws determine the number of transferred electrons towards  $\text{O}_2$  through ORR/OER by analyzing  $\text{O}_2$  consumption/evolution and charge transfers.  $\text{Zn}(\text{TFSI})_2$  displayed the reversible changes under pressure relative to original values. Multiple C-D processes correspond to  $\text{ZnO}_2$  formation with inferior decomposition of  $\text{H}_2\text{O}$  by  $4e^-$  oxygen path-

ways, whereas  $\text{ZnSO}_4$  has irreversible features.  $\text{Zn}(\text{TFSI})_2$  and  $\text{Zn}(\text{CF}_3\text{SO}_3)_2$  electrochemical properties correspond for bulky  $\text{TFSI}^-$  and  $\text{CF}_3\text{SO}_3^-$  anions (versus  $\text{SO}_4^{2-}$  with double charges, Figure 35o,p), which diminishes the number of water molecules surrounded by  $\text{Zn}^{2+}$  cations. Typically,  $\text{Zn}(\text{TFSI})_2$  or  $\text{Zn}(\text{OTf})_2$  has an anhydrous form, but  $\text{ZnSO}_4$  is always hydrated. The molecular polarity index of  $\text{TFSI}^-$  (3.8 eV) and  $\text{OTf}^-$  (4.68 eV) is lower relative to  $\text{SO}_4^{2-}$  (10.47 eV), implying superior hydrophobicity. The lower electrostatic potential of  $\text{SO}_4^{2-}$  than that of  $\text{TFSI}^-$  and  $\text{OTf}^-$  displays the favorable hydrogen bonding by water. Sun et al.<sup>[640]</sup> reports generation of  $\text{Zn}^{2+}$ -rich and  $\text{H}_2\text{O}$ -poor environments with  $\text{Zn}(\text{OTf})_2$  or  $\text{Zn}(\text{TFSI})_2$ -based electrolytes, whereas  $\text{H}_2\text{O}$ -rich environments by  $\text{ZnSO}_4$  for inner Helmholtz layers, clarifying faster kinetics for Zn ions. Reactions among the  $\text{ZnSO}_4$  and  $\text{OH}^-$  form the ZHS intermediates limiting the availability of  $\text{H}_2\text{O}$  or  $\text{ZnSO}_4$  for electrolytes, whereas  $\text{Zn}(\text{TFSI})_2$  did not show consumption of electrolytes, which suggests reversible  $\text{ZnO}_2$  phase formations (Figure 35m,n) well consistent to non-aqueous  $\text{Li-O}_2$  cells. Overall reaction kinetics for  $\text{Zn}(\text{TFSI})_2$ .<sup>[640–642]</sup>

Anode :  $\text{Zn}(\text{s}) \leftrightarrow \text{Zn}^{2+}(\text{aq}) + 2e^-$

[Discharge :  $\text{Zn}(\text{s}) \rightarrow \text{Zn}^{2+}(\text{aq}) + 2e^-$  and Charge :  $\text{Zn}^{2+}(\text{aq}) + 2e^- \rightarrow \text{Zn}(\text{s})$ ]

Cathode :  $\text{O}_2 + 2e^- \leftrightarrow \text{O}_2^{2-}$

Overall :  $\text{Zn} + \text{O}_2 \leftrightarrow \text{ZnO}_2$

(19)

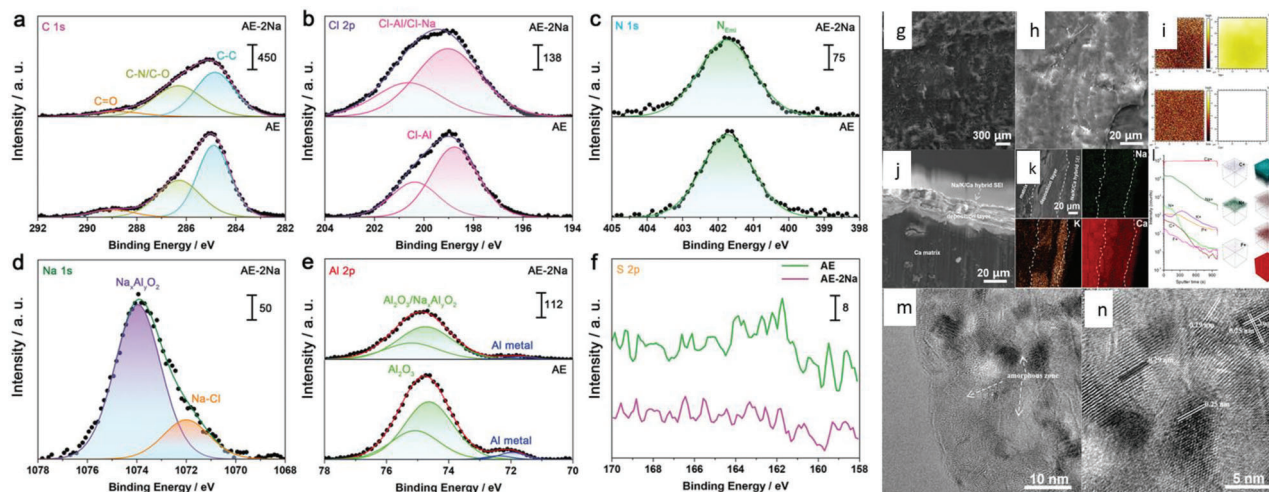
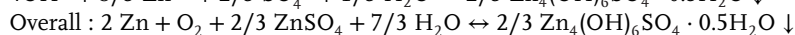
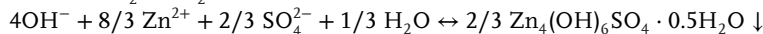
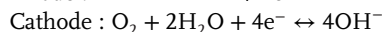
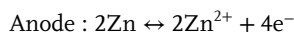


**Figure 36.** a) XPS spectra for Al electrodes from Al-S batteries a) C 1s, b) Cl 2p, c) N 1s, d) Na 1s, e) Al 2p, and f) S 2p. Reproduced with permission under the Creative Commons CC BY 4.0 license.<sup>[643]</sup> Copyright 2023, Wiley-VCH. g-n) Microstructures and compositions for AHSEL-Ca anodes. g,h) SEM, i) TOF-SIMS 2D maps, j,k) SEM and EDS maps. l) TOF-SIMS 3D maps. m,n) TEM images of SEI. Reproduced with permission.<sup>[650]</sup> Copyright 2023, Wiley-VCH.

Overall reaction kinetics for  $\text{ZnSO}_4$ :



(20)

XPS spectra of Al-metal anode displays C-C, C-N/C-O, and C=O in C 1s, Al-Cl and/or Na-Cl in Cl 2p and  $\text{Na}_x\text{Al}_y\text{O}_z$  species in Al-anode and Al-anode-2Na electrolytes (Figure 36a–f).<sup>[643]</sup> Al 2p shows Al-O bindings of  $\text{Al}_2\text{O}_3$  and/or  $\text{Na}_x\text{Al}_y\text{O}_z$  (74.7 eV for Al  $2p_{3/2}$ ), whereas metallic Al with small intensity (71.6 eV for Al  $2p_{3/2}$ ).<sup>[644,645]</sup> Metallic Al has a higher reflection for Al-anode than Al-anode-2Na, implying thicker SEI. Further, smaller intensity for  $\text{Al}_2\text{O}_3$  and/or  $\text{Na}_x\text{Al}_y\text{O}_z$  for Al-anode-2Na is due to NaCl additives. S 2p shows stronger polysulfides for Al-anodes due to larger peaks than Al-anode-2Na. Ran et al.<sup>[562]</sup> reports MXene/ $\text{E-Al}_{97}\text{Ce}_3$  hybrid anodes stable Al plate/stripping >1000 h with a slightly increased overpotential of 49–54 mV outperforms the pure  $\text{E-Al}_{97}\text{Ce}_3$  alloy (280 mV in 210 h) and monometallic Al (1400 mV in 64 h) under aqueous 2 M  $\text{Al}(\text{OTf})_3$  electrolyte. Grafted MXene layer efficiently enables  $\text{Al}^{3+}$  transport by mitigating native oxide passivation influence for Al plate/strip for  $\text{E-Al}_{97}\text{Ce}_3$ , boosting localized galvanic intermetallic pairs for  $\text{Al}_{11}\text{Ce}_3$  and  $\alpha$ -Al nanolamellas corresponding to the monometallic Al.<sup>[646]</sup> Guo et al.<sup>[647]</sup> reports 1-hexadecyl-3-methylimidazolium hexafluorophosphate (HMIH) ILs as anti-corrosive additives, in which EIS displays adsorption intermediates with  $\text{Al}(\text{OH})_{x,\text{ads}}$  for Al/electrolyte interface under HMIM additives, while  $\text{H}_2$ ,  $\text{OH}^-$ , and  $\text{Al}(\text{OH})_{x,\text{ads}}$  for conventional Al-surfaces. XPS spectra clarify the  $\alpha$ - $\text{AlF}_3$ , Al-O, P-O, C=O, C-C, C-O, and C=N bindings with stronger lower BEs shifting after HMIH addition, while pristine Al has  $\alpha$ - $\text{Al}_2\text{O}_3$ ,  $\text{Al}(\text{OH})_3$ ,  $\gamma$ - $\text{Al}_2\text{O}_3$ .<sup>[648,649]</sup>

Artificial hybrid solid electrolyte layer (AHSEL, Figure 36g–n) with Na/Ca carbonate and calcium hydride nitride NPs (<10 nm) compressed by C and N moieties is reported for  $\text{Ca}^{2+}$  with  $\sigma_{\text{Ca}^{2+}} \approx 0.01 \text{ mS cm}^{-1}$  and thickness of 20  $\mu\text{m}$ .<sup>[650]</sup> AHSEL transforms to Na/K/Ca hybrid SEIs consisting of monodispersed NPs of  $\text{Ca}_2\text{NH}$  and smaller amorphous regions with KPF<sub>6</sub> electrolyte, implying a reduction of fluoridation for Ca-depositions. Ca plate/strip over bare Ca under 1 M  $\text{Ca}(\text{PF}_6)_2$  or  $\text{Ca}(\text{BF}_4)_2$  EC/DEC (1:1, v/v) electrolytes displays poor stabilities (<12 h) owing to anion polarizations and corruptions. Further, deposition voltage drops for  $-5.0 \text{ V}$  owing to larger intrinsic resistances by thicker  $\text{CaF}_2$  insulating mass formation.<sup>[651]</sup> Whereas, under KPF<sub>6</sub> EC/DMC/EMC (1:1:1, v/v/v) electrolyte  $\text{Ca}^{2+}$ -plate/strip for 800 and 250 h comparable to Ca with NaPF<sub>6</sub> due to parallel K/Ca-based SEIs consists of  $\text{KCa}(\text{PO}_3)_3$  (JCPDS:39-1408),  $\text{Ca}(\text{H}_2\text{PO}_4)_2$  (JCPDS:70-1381), and  $\text{CaF}_2$  (JCPDS:77-2093) NPs (<20 nm) over  $\text{Ca}^{2+}$ -loadings. However, Ca//Ca cell fails after 258 h, implying K/Ca-based SEIs are still not satisfying due to the lack of organic carbon layers for complete protection of Ca. AHSEL-Ca rapidly suppresses corrosion and polarizations for 1400 h  $\text{Ca}^{2+}$ -plate/strip with uniform  $\text{Ca}^{2+}$ -depositions and Na/K/Ca-based hybrid SEIs that cover K/Ca mixture followed Ca matrix below. SEI consists of the major crystalline phase of  $\text{Ca}_2\text{NH}$  (AHSEL–electrolytes interface) and minor phases of hexagonal  $\text{KCa}(\text{PO}_3)_3$ , orthorhombic  $\text{Na}_3(\text{PO}_3)_3 \cdot \text{H}_2\text{O}$  (JSPDS:15-0740), and cubic  $\text{KCaF}_3$  (JCPDS:03-0567). TOF-SIMS and EDS display uniform N, Ca, K, Na distribution in SEI. The 0.25

and 0.29 nm d-spacing confirms  $\text{Ca}_2\text{NH}$  (222) and (400) reflections. TOF-SIMS depth profiles and 3D maps display  $\text{Ca}_2\text{NH}$ -rich organic-inorganic Na/K/Ca hybrid SEIs with N-/C-rich elements distributions, unlike AHSEL N-rich  $\text{Ca}_2\text{NH}$  and K/Ca SEIs with minor organic materials.<sup>[652]</sup> Theoretical calculations verify  $\text{Ca}^{2+}$ -ions in propylene carbonate have weaker solvation structures with  $\text{H}_2\text{O}$  hybridization, implying  $\text{Ca}^{2+}$ -transports under electrolyte and desolvation kinetics for CEI.<sup>[653]</sup> Li et al.<sup>[654]</sup> verifies the enolization redox processes ( $\text{O}=\text{C}\leftrightarrow\text{C}-\text{O}^-$ ) of perylene tetra-carboxylic diimide with 1D  $\text{Ca}^{2+}$ -diffusion kinetics and lack of covalent-bond cleavages or reformations are the keys for higher  $\text{Ca}^{2+}$ -reversibility and rate-capabilities. Ca-Se with  $\text{Ca}(\text{B}(\text{hfp})_4)_2\text{-DME}$  and  $\text{Ca}_{0.25}\text{V}_2\text{O}_5\cdot n\text{H}_2\text{O}$  with  $\text{Ca}(\text{ClO}_4)_2\text{-acetonitrile-H}_2\text{O}$  electrolytes displays reversible CIBs with 180 and 158.2 mAh  $\text{g}^{-1}$  capacities.<sup>[655,656]</sup>

## 9. Conclusions and Future Perspectives

In general, all types of batteries involve positive cathodes, solid/liquid electrolytes, and negative anodes; these components should be synchronized for operating chemistries. Failure of batteries occurs due to the interactions among these constituents. SSBs demonstrate promising outlooks regarding reliability, safety operations, operating temperature windows, and energy densities relative to commercial liquid-based batteries. However, the ionic conductivity of SEs, volume expansion for electrodes, interfacial resistances, poor cycle life, and flexibility issues are critical challenges for SSBs. Extensive efforts have been considered to overcome these challenges, but the poor interfaces among the electrodes and SEs, EWs, and ion diffusion kinetics impedes the development of SSBs. For well-functioning SSBs, remarkable electrochemical stability, mechanical integrity, and interfaces with minimal resistance are essential.

Physical or chemical contacts, lattice-mismatch, space-charge layers, interdiffusion of elements, chemical reactivity of SEI, and metal dendrites are the key interface issues that severely degrade the cell performances in terms of cell capacity, internal resistances, and cell failures. Multivalent batteries offer substantial attention; however, it critically undergoes challenges for mechanistic understandings of metals (Li, Na, K, Mg, Zn, Al, Ca) nucleation/growth and strategy of interphases and electrodes. There are no standard benchmarks for using electrolytes or electrodes and their design strategies. The overestimated performances based on the gravimetric capacities of particular active or consumed materials did not fully translate under realistic platforms; therefore, careful evaluation for electrode optimization and cell design is essential. Rational design for robust and functional SEI for multivalent metals is also discussed critically.

The employment of high-energy metals as anode materials realizes that SEs can promise future battery technologies. Ion conductance for monovalent metal-ions transport is prolonged for application inception; however, multivalent metal-ion SEs are in the early stages. High conductance and modulus of SIEs compared to SPEs; however, their inferior interfaces towards cathode/anodes limit the required targets of batteries under high current density, rate/areal capacity, and utilizations. Insertion of polymers, gels, or liquids among the electrodes and SIEs can be suitable for developing conformal interface layers to en-

dure great volume changes. The composition of electrolytes describes the metal plate/strip behavior, EWs, and kinetics for M-intercalations. For SPEs, the focus should be on RT ion conductivity, SEs/anode and SEs/cathodes compatibility and structures, crystallinity, tg, and ion-pair dissociation. Crosslinking of segments and electron-removing species for backbones promises electrode-interface stability. Besides, higher storage modulus and partial amorphous structuring confirm the stable metal deposits for metal anodes. For commercial-scale SEs, the compatibility of SEs and anode/cathodes is essential because numerous electrons, ions, heat, and pressure are severely reallocated with different features. The fabrication of SEs with abundant resources can be rewarding for the environment and cost.

For the anode, stable metals such as Li, Na, K, Mg, Zn, Al, and Ca can be employed; however, lower utilization, inert oxide passivation, self-diffusion coefficients, and irreversibility shows a significant loss for energy density. Loading 2D or 3D porous frameworks can enhance mass/charge-transfer kinetics. Depth of discharge or state of charge outbreaks the metal dendrites, poor plate/strip efficiency, decomposition of SEs with parasitic reactions, surface passivation, or gaseous formation. Measuring protocols, including current densities, temperatures, plate/strip capability, and cell configurations critically modify the metal anode's overall performances and have been considered for evaluation, which are the standard benchmarks for practical mono-/multivalent-batteries. A comprehensive understanding of formation kinetics and regulation of flexible SEI layer during cycle operations enable the practical metal batteries. Information on the dynamic structure of SEI needs to investigate on priority, which is the primary approach for SEI modeling. Several elements from SEI will be dissolved for high voltages, and some elements will be reorganized after initial SEI formation deprived of Faraday processes. We proposed several strategies for addressing the present issues of metal-anodes-kinetics regardless of battery chemistries (**Figure 37**): 1) metal surface coating with glasses or composites that exert pressure in contrast to the surfaces and blocks the open spaces, 2) loading of carbon, graphene, or carbon allotropes that restrict depletion of electrolytes and enhances the charge-discharge capability, 3) uniform metal-ion flux that can prevent local population of metal-ions, for instance, better wetting materials coating over separator or additives, 4)  $\text{Cs}^+$ -ions loading for electrolytes that remain positive in charge and repels arriving Li or metal ions from tips causing spherical surface topography, 5) Insertion of 3D patterns, frameworks or metal in powder forms that can improve active surface area by dissipating electron densities for respective current densities, 6) preferred crystal orientation of metals (formation of single crystalline or dominating crystal planes) that decreases nucleation density and improves the diffusion kinetics from 2D to 3D with excess ion-transport channels, 7) chemical pretreatment with preferred crystal orientations that improves the SEI layer stability and localized current density distribution with lowering diffusion energy barriers, 8) metal-alloying with heavy metals or oxides, and 9) artificial buffer layer such as S, F, I, or Se anion species that can generate numerous metal vacancies to increase mobile metal ions. For practical approach post-LIBs, the interface kinetics and electrochemical stability of both electrodes upon charge-discharge with developing innovative materials is the scope for future research.



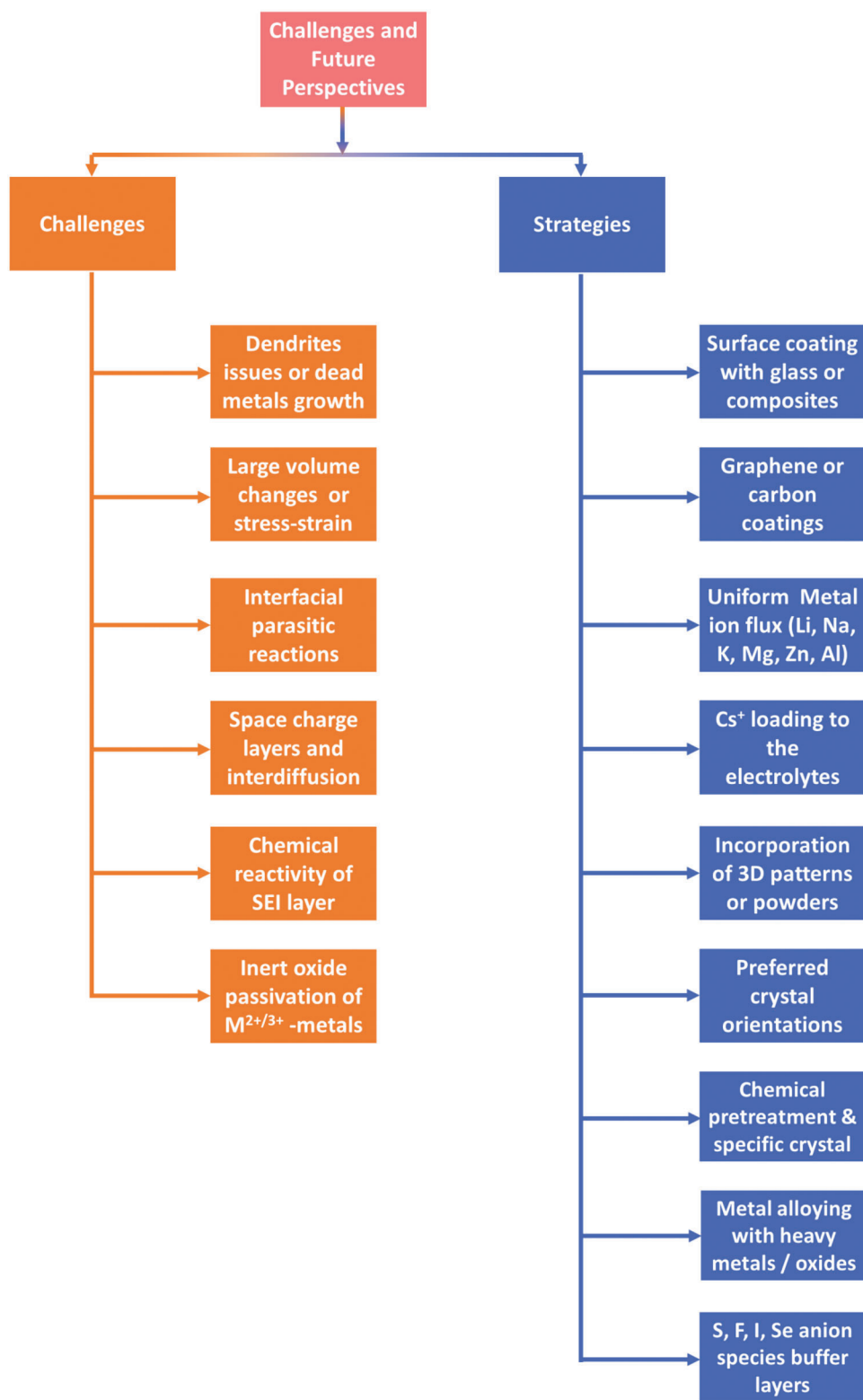


**Figure 37.** Failure mechanisms and perspectives for the anode interface chemistries.

## Acknowledgements

This work was supported by the Creative Materials Discovery Program (2018M3D1A1057844) through the National Research Foundation of Korea (NRF) funded by the Ministry of Science and ICT and the Basic Science Research Program of the NRF (NRF-2023R1A2C3003788).

## Conflict of Interest

The authors declare no conflict of interest.

## Keywords

future perspectives, insights for nucleation deposits, interface issues, ion-transport mechanisms, Li, Na, K, Mg, Zn, Al, and Ca anode interface chemistry, plate/strip for reversible anodes, state-of-the-art SEs, thermodynamics and chemical kinetics

Received: June 25, 2023

Revised: July 30, 2023

Published online: September 24, 2023

- [1] J. Tarascon, M. Armand, *Nature* **2001**, 414, 359.
- [2] S. Chu, A. Majumdar, *Nature* **2012**, 488, 294.
- [3] B. Dunn, H. Kamath, J. Tarascon, *Science* **2011**, 334, 928.
- [4] J. Goodenough, K. Park, *J. Am. Chem. Soc.* **2013**, 135, 1167.
- [5] J. Liu, Z. Bao, Y. Cui, E. Dufek, J. Goodenough, P. Khalifah, Q. Li, B. Liaw, P. Liu, A. Manthiram, Y. Meng, V. Subramanian, M. Toney, V. Viswanathan, M. Whittingham, J. Xiao, W. Xu, J. Yang, X. Yang, J. Zhang, *Nat. Energy* **2019**, 4, 180.
- [6] Y. Lee, S. Fujiki, C. Jung, N. Suzuki, N. Yashiro, R. Omoda, D. Ko, T. Shiratsuchi, T. Sugimoto, S. Ryu, J. Ku, T. Watanabe, Y. Park, Y. Aihara, D. Im, I. Han, *Nat. Energy* **2020**, 5, 299.
- [7] P. Notten, F. Roozeboom, R. Niessen, L. Baggetto, *Adv. Mater.* **2007**, 19, 4564.
- [8] C. Monroe, J. Newman, *J. Electrochem. Soc.* **2005**, 152, A396.
- [9] S. Shinde, N. Wagh, C. Lee, D. Kim, S. Kim, H. Um, S. Lee, J. Lee, *Adv. Mater.* **2023**, <https://doi.org/10.1002/adma.202303509>.
- [10] N. Kamaya, K. Homma, Y. Yamakawa, M. Hirayama, R. Kanno, M. Yonemura, T. Kamiyama, Y. Kato, S. Hama, K. Kawamoto, A. Mitsui, *Nat. Mater.* **2011**, 10, 682.
- [11] Y. Kato, S. Hori, T. Saito, K. Suzuki, M. Hirayama, A. Mitsui, M. Yonemura, H. Iba, R. Kanno, *Nat. Energy* **2016**, 1, 16030.
- [12] F. Mizuno, A. Hayashi, K. Tadanaga, M. Tatsumisago, *Adv. Mater.* **2005**, 17, 918.
- [13] M. Wood, C. Fang, E. Dufek, S. Nagpure, S. Sazhin, B. Liaw, Y. Meng, *Adv. Energy Mater.* **2018**, 8, 1801427.
- [14] X. Cheng, R. Zhang, C. Zhao, F. Wei, J. Zhang, Q. Zhang, *Adv. Sci.* **2016**, 3, 1500213.
- [15] E. Peled, S. Menkin, *J. Electrochem. Soc.* **2017**, 164, A1703.
- [16] W. Liu, P. Li, W. Wang, D. Zhu, Y. Chen, S. Pen, E. Paek, D. Mitlin, *ACS Nano* **2018**, 12, 12255.
- [17] A. Dey, *J. Electrochem. Soc.* **1970**, 117, 222.
- [18] W. Liu, P. Liu, D. Mitlin, *Adv. Energy Mater.* **2020**, 10, 2002297.
- [19] D. Tewari, P. Mukherjee, *J. Mater. Chem. A* **2019**, 7, 4668.
- [20] F. Soto, A. Marzouk, F. El-Mellouhi, P. Balbuena, *Chem. Mater.* **2018**, 30, 3315.
- [21] P. Erhart, K. Albe, *Phys. Rev. B* **2006**, 73, 115207.
- [22] Y. Chu, L. Ren, Z. Hu, C. Huang, J. Luo, *Green Energy & Environ.* **2023**, 8, 1006.
- [23] X. Zeng, J. Mao, J. Hao, J. Liu, S. Liu, Z. Wang, Y. Wang, S. Zhang, T. Zheng, J. Liu, P. Rao, Z. Guo, *Adv. Mater.* **2021**, 33, 2007416.
- [24] H. Yildirim, A. Kinaci, M. Chan, J. Greeley, *ACS Appl. Mater. Interfaces* **2015**, 7, 18985.
- [25] R. Mogensen, D. Brandell, R. Younesi, *ACS Energy Lett.* **2016**, 1, 1173.
- [26] Z. Seh, J. Sun, Y. Sun, Y. Cui, *ACS Cent. Sci.* **2015**, 1, 449.
- [27] J. Ma, F. Meng, Y. Yu, D. Liu, J. Yan, Y. Zhang, X. Zhang, Q. Jiang, *Nat. Chem.* **2019**, 11, 64.
- [28] L. Kuo, A. Moradabadi, H. Huang, B. Hwang, P. Kaghazchi, *J. Power Sources* **2017**, 341, 107.
- [29] H. Wang, D. Zhai, F. Kang, *Energy Environ. Sci.* **2020**, 13, 4583.
- [30] R. Davidson, A. Verma, D. Santos, F. Hao, C. Fincher, S. Xiang, J. Van Buskirk, K. Xie, M. Pharr, P. Mukherjee, S. Banerjee, *ACS Energy Lett.* **2019**, 4, 375.
- [31] J. Forero-Saboya, C. Davoisne, R. Dedryvere, I. Yousef, P. Canepa, A. Ponrouch, *Energy Environ. Sci.* **2020**, 13, 3423.
- [32] Q. Zhao, M. Zachman, W. Al Sadat, J. Zheng, L. Kourkoutis, L. Archer, *Sci. Adv.* **2018**, 4, eaau8131.
- [33] J. Hao, B. Li, X. Li, X. Zeng, S. Zhang, F. Yang, S. Liu, D. Li, C. Wu, Z. Guo, *Adv. Mater.* **2020**, 32, 2003021.
- [34] D. Xie, Y. Sang, D. Wang, W. Diaof, F. Tao, C. Liu, J. Wang, H. Sun, J. Zhang, X. Wu, *Angew. Chem. Int. Ed.* **2023**, 62, e2022169.
- [35] J. Zheng, Q. Zhao, T. Tang, J. Yin, C. Quilty, G. Renderos, X. Liu, Y. Deng, L. Wang, D. Bock, C. Jaye, D. Zhnag, E. Takeuchi, K. Takeuchi, A. Marchilok, L. Archer, *Science* **2019**, 366, 645.
- [36] J. Goodenough, Y. Kim, *Chem. Mater.* **2010**, 22, 587.
- [37] L. Xu, S. Tang, Y. Cheng, K. Wang, J. Liang, C. Liu, Y. Cao, F. Wei, L. Mai, *Joule* **2018**, 2, 1991.
- [38] A. Banerjee, X. Wang, C. Fang, E. Wu, Y. Meng, *Chem. Rev.* **2020**, 120, 6878.
- [39] L. Fan, H. He, C. Nan, *Nat. Rev. Mater.* **2021**, 6, 1003.
- [40] S. An, J. Li, C. Daniel, D. Mohanty, S. Nagpure, D. Wood, *Carbon* **2016**, 105, 52.
- [41] Z. Jian, W. Luo, X. Ji, *J. Am. Chem. Soc.* **2015**, 137, 11566.
- [42] L. Madec, V. Gabaudan, G. Gachot, L. Stievano, L. Monconduit, H. Martinez, *ACS Appl. Mater. Interfaces* **2018**, 10, 34116.
- [43] W. Chang, J. Wu, K. Chen, H. Tuan, *Adv. Sci.* **2019**, 6, 1801354.
- [44] Y. Hu, *Nat. Energy* **2016**, 1, 16042.
- [45] X. Chen, H. R. Li, X. Shen, Q. Zhang, *Angew. Chem., Int. Ed.* **2018**, 57, 16643.
- [46] K. Yoshida, M. Nakamura, Y. Kazue, N. Tachikawa, S. Tsuzuki, S. Seki, K. Dokko, M. Watanabe, *J. Am. Chem. Soc.* **2011**, 133, 13121.
- [47] S. Trasatti, *Pure Appl. Chem.* **1986**, 58, 955.
- [48] P. Peljo, H. Girault, *Energy Environ. Sci.* **2018**, 11, 2306.
- [49] B. Horstmann, et al., *Energy Environ. Sci.* **2021**, 14, 5289.
- [50] Z. Yu, D. Mackanic, W. Michaels, M. Lee, A. Pei, D. Feng, Q. Zhang, Y. Tsao, C. Amannchukwu, X. Yan, H. Wang, S. Chen, K. Liu, J. Kang, J. Qin, Y. Cui, Z. Bao, *Joule* **2019**, 3, 2761.
- [51] K. Nie, Y. Hong, J. Qiu, Q. Li, X. Yu, H. Li, L. Chen, *Front. Chem.* **2018**, 6, 616.
- [52] M. Park, X. Zhang, M. Chung, G. Less, A. Sastry, *J. Power Sources* **2010**, 195, 7904.
- [53] H. Mehrer, *Diffusion in Solids: Fundamentals, Methods, Materials, Diffusion-Controlled Processes*, Springer, New York **2007**.
- [54] P. Kumar, S. Yashonath, *J. Chem. Sci.* **2006**, 118, 135.
- [55] J. Perram, *The Physics of Superionic Conductors and Electrode Materials*, Springer, New York **1983**.
- [56] A. Bard, L. Faulkner, *Electrochemical Methods: Fundamentals and Applications*, 2nd ed, Wiley, Hoboken, NJ **2001**.
- [57] J. Corish, *Handbook of Materials Modeling* (Ed.: S. Yip), Springer, New York **2005**, pp. 1889–1899.
- [58] P. Knauth, H. Tuller, *J. Am. Ceram. Soc.* **2002**, 85, 1654.
- [59] A. Nitzan, M. Ratner, *J. Phys. Chem.* **1994**, 98, 1765.
- [60] O. Borodin, G. Smith, *Macromolecules* **2006**, 39, 1620.
- [61] J. Souquet, *Annu. Rev. Mater. Sci.* **1981**, 11, 211.

- [62] X. He, Y. Zhu, Y. Mo, *Nat. Commun.* **2017**, *8*, 15893.
- [63] C. Chen, J. Maier, *Nat. Energy* **2018**, *3*, 102.
- [64] M. Swift, Y. Qi, *Phys. Rev. Lett.* **2019**, *122*, 167701.
- [65] J. Haruyama, K. Sodeyama, L. Han, K. Takada, Y. Tateyama, *Chem. Mater.* **2014**, *26*, 4248.
- [66] M. Wang, E. Carmona, A. Gupta, P. Albertus, J. Sakamoto, *Nat. Commun.* **2020**, *11*, 5201.
- [67] Q. Tu, L. Barroso-Luque, T. Shi, G. Ceder, *Cell Rep. Phys. Sci.* **2020**, *1*, 100106.
- [68] T. Krauskopf, R. Dippel, H. Hartmann, K. Peppler, B. Mogwitz, F. Richter, W. Zeier, J. Janek, *Joule* **2019**, *3*, 2030.
- [69] M. Motoyama, M. Ejiri, Y. Iriyama, *J. Electrochem. Soc.* **2015**, *162*, A7067.
- [70] A. Pei, G. Zheng, F. Shi, Y. Li, Y. Cui, *Nano Lett.* **2017**, *17*, 1132.
- [71] D. Ely, R. Garcia, *J. Electrochem. Soc.* **2013**, *160*, A662.
- [72] Y. Lu, L. Li, Q. Zhang, Y. Cai, Y. Ni, J. Chen, *Chem. Sci.* **2022**, *13*, 3416.
- [73] C. Bao, B. Wang, P. Liu, H. Wu, Y. Zhou, D. Wang, H. Liu, S. Dou, *Adv. Funct. Mater.* **2020**, *30*, 2004891.
- [74] D. Landmann, G. Graeber, M. Heinz, S. Haussener, C. Battagli, *Mater. Today Energy* **2020**, *18*, 100515.
- [75] J. Zheng, L. Archer, *Sci. Adv.* **2021**, *7*, eabe0219.
- [76] Y. Yan, J. Grinderslev, M. Jorgensen, L. Skov, J. Skibsted, T. Jensen, *ACS Appl. Energy Mater.* **2020**, *3*, 9264.
- [77] A. Mohammad, T. Köhler, S. Biswas, H. Stöcker, D. Meyer, *ACS Appl. Energy Mater.* **2023**, *6*, 2914.
- [78] P. Biswal, S. Stalín, A. Kludze, S. Choudhury, L. Archer, *Nano Lett.* **2019**, *19*, 8191.
- [79] L. Selis, J. Seminario, *RSC Adv.* **2018**, *8*, 5255.
- [80] P. Barai, K. Higa, V. Srinivasan, *Phys. Chem. Chem. Phys.* **2017**, *19*, 20493.
- [81] Z. Ahmad, V. Viswanathan, *Phys. Rev. Lett.* **2017**, *119*, 056003.
- [82] L. Angheluta, E. Jettestuen, J. Mathiesen, F. Renard, B. Jamtveit, *Phys. Rev. Lett.* **2008**, *100*, 096105.
- [83] L. Angheluta, E. Jettestuen, J. Mathiesen, *Phys. Rev. E* **2009**, *79*, 031601.
- [84] M. Zhu, S. Li, B. Li, Y. Gong, Z. Du, S. Yang, *Sci. Adv.* **2019**, *5*, eaau6264.
- [85] Y. Liu, Y. Shi, C. Gao, Z. Shi, H. Ding, Y. Feng, Y. He, J. Sha, J. Zhou, B. Lu, *Angew. Chem. Int. Ed.* **2023**, *62*, e202300016.
- [86] J. Liu, J. Zhang, Z. Zhang, A. Du, S. Dong, Z. Zhou, X. Guo, Q. Wang, Z. Li, G. Li, G. Cui, *ACS Nano* **2022**, *16*, 9894.
- [87] X. Hu, Z. Shen, J. Wan, Y. Song, B. Liu, H. Yan, R. Wen, L. Wan, *Nano Energy* **2020**, *78*, 105338.
- [88] S. McClary, D. long, A. Matias, P. Kotula, D. Prendergast, K. Jungjohann, K. Zavadil, *ACS Energy Lett.* **2022**, *7*, 2792.
- [89] H. Sand, *London, Edinburgh, Dublin Philos. Mag. J. Sci.* **1901**, *1*, 45.
- [90] K. Liu, Y. Liu, D. Lin, A. Pei, Y. Cui, *Sci. Adv.* **2018**, *4*, eaas9820.
- [91] J. Zheng, T. Tang, Q. Zhao, X. Liu, Y. Deng, L. Archer, *ACS Energy Lett.* **2019**, *4*, 1349.
- [92] C. Fang, J. Li, M. Zhang, Y. Zhang, F. Yang, J. Lee, M. Lee, J. Alvarado, M. Schroeder, Y. Yang, B. Lu, N. Williams, M. Ceja, L. Yang, M. Cai, J. Gu, K. Xu, X. Wang, Y. Meng, *Nature* **2019**, *572*, 511.
- [93] L. Kolzenberg, A. Latz, B. Horstmann, *ChemSusChem* **2020**, *13*, 3901.
- [94] M. Jackle, A. Groß, *J. Chem. Phys.* **2014**, *141*, 174710.
- [95] W. Zhou, Y. Li, S. Xin, J. Goodenough, *ACS Cent. Sci.* **2017**, *3*, 52.
- [96] O. Dahunsi, S. Gao, J. Kaelin, B. Li, I. B. A. Razak, B. An, Y. Cheng, *Nanoscale* **2023**, *15*, 3255.
- [97] M. Xu, Y. Li, M. Haq, N. Mubarak, Z. Liu, J. Wu, Z. Luo, J. Kim, *Energy Storage Mater.* **2022**, *44*, 477.
- [98] C. Wei, L. Tan, Y. Zhang, B. Xi, S. Xiong, J. Feng, Y. Qian, *Energy Storage Mater.* **2022**, *48*, 447.
- [99] X. Xiao, W. Liu, K. Wang, C. Li, X. Sun, X. Zhang, W. Liu, Y. Ma, *Nanoscale Adv.* **2020**, *2*, 296.
- [100] H. Liu, Y. Zhang, C. Wang, J. Glazer, Z. Shan, N. Liu, *ACS Appl. Mater. Interfaces* **2021**, *13*, 32930.
- [101] H. Tian, G. Feng, Q. Wang, Z. Li, W. Zhang, M. Lucero, Z. Feng, Z. Wang, Y. Zhang, C. Zhen, M. Gu, X. Shan, Y. Yang, *Nat. Commun.* **2022**, *13*, 7922.
- [102] M. Guo, C. Yuan, T. Zhang, X. Yu, *Small* **2022**, *18*, 2106981.
- [103] S. Wang, Y. Liu, J. Zhang, Y. Wang, L. Hou, C. Yuan, *Energy Technol.* **2021**, *9*, 2000820.
- [104] Y. Liu, S. Wang, X. Sun, J. Zhang, F. Zaman, L. Hou, C. Yuan, *Energy Environ. Mater.* **2023**, *6*, e12263.
- [105] J. Qin, H. Shi, K. Huang, P. Lu, P. Wen, F. Xing, B. Yang, M. Ye, Y. Yu, Z. Wu, *Nat. Commun.* **2021**, *12*, 5786.
- [106] A. Cohn, N. Muralidharan, R. Carter, K. Share, C. Pint, *Nano Lett.* **2017**, *17*, 1296.
- [107] N. Xiao, W. McCulloch, Y. Wu, *J. Am. Chem. Soc.* **2017**, *139*, 9475.
- [108] T. Chen, G. Gautam, P. Canepa, *Chem. Mater.* **2019**, *31*, 8087.
- [109] J. Bae, H. Park, X. Guo, X. Zhang, J. Warnera, G. Yu, *Energy Environ. Sci.* **2021**, *14*, 4391.
- [110] I. Dueramae, M. Okhawilal, P. Kasemsiri, H. Uyama, *Sci. Rep.* **2021**, *11*, 13268.
- [111] K. Wood, E. Kazyak, A. Chadwick, K. Chen, J. Zhang, K. Thornton, N. Dasgupta, *ACS Cent. Sci.* **2016**, *2*, 790.
- [112] L. Hagman, P. Kierkega, *Acta Chem. Scand.* **1968**, *22*, 1822.
- [113] V. Thangadurai, W. Weppner, *Ionics* **2006**, *12*, 81.
- [114] X. Xu, Z. Wen, X. Wu, X. Yang, Z. Gu, *J. Am. Ceram. Soc.* **2007**, *90*, 2802.
- [115] H. Aono, E. Sugimoto, Y. Sadaoka, N. Imanaka, G. Adachi, *Solid State Ionics* **1990**, *40–41*, 38.
- [116] Y. Lu, J. Alonso, Q. Yi, L. Lu, Z. Wang, C. Sun, *Adv. Energy Mater.* **2019**, *9*, 1901205.
- [117] X. Zhao, J. Yan, H. Hong, Y. Zhao, Q. Li, Y. Tang, J. He, Z. Wei, S. He, X. Hou, C. Zhi, H. Li, *Adv. Energy Mater.* **2022**, *12*, 2202478.
- [118] K. Nomura, S. Ikeda, K. Ito, H. Einaga, *J. Electroanal. Chem.* **1992**, *326*, 351.
- [119] J. Goodenough, H. Hong, P. Kafalas, *Mater. Res. Bull.* **1976**, *11*, 203.
- [120] F. Sudreau, D. Petit, J. Boilot, *J. Solid State Chem.* **1989**, *83*, 78.
- [121] Y. Nikodimos, C. Huang, B. Taklu, W. Su, B. Hwang, *Energy Environ. Sci.* **2022**, *15*, 991.
- [122] K. Park, Q. Bai, D. Kim, D. Oh, Y. Zhu, Y. Mo, Y. Jung, *Adv. Energy Mater.* **2018**, *8*, 1800035.
- [123] Y. Yin, J. Yang, J. Luo, G. Lu, Z. Huang, J. Wang, P. Li, F. Li, Y. Wu, T. Tian, Y. Meng, H. Mo, Y. Song, J. Yang, L. Feng, T. Ma, W. Wen, K. Gong, L. Wang, H. Ju, Y. Xiao, Z. Li, X. Tao, H. Yao, *Nature* **2023**, *616*, 77.
- [124] R. Kanno, M. Murayama, *J. Electrochem. Soc.* **2001**, *148*, A742.
- [125] H. Deiseroth, S. Kong, H. Eckert, J. Vannahme, C. Reiner, T. Zaiss, M. Schlosser, *Angew. Chem.* **2008**, *47*, 755.
- [126] Y. Seino, T. Ota, K. Takada, A. Hayashi, M. Tatsumisago, *Energy Environ. Sci.* **2014**, *7*, 627.
- [127] R. Iwasaki, S. Hori, R. Kanno, T. Yajima, D. Hirai, Y. Kato, Z. Hiroi, *Chem. Mater.* **2019**, *31*, 3694.
- [128] P. Adeli, J. D. Bazak, K. H. Park, I. Kochetkov, A. Huq, G. R. Goward, L. F. Nazar, *Angew. Chem.* **2019**, *58*, 8681.
- [129] S. Patel, S. Banerjee, H. Liu, P. Wang, P. Chien, X. Feng, J. Liu, S. P. Ong, Y. Hu, *Chem. Mater.* **2021**, *33*, 1435.
- [130] J. Liang, N. Chen, X. Li, X. Li, K. Adair, J. Li, C. Wang, C. Yu, M. Banis, L. Zhang, S. Zhao, S. Lu, H. Huang, R. Li, Y. Huang, X. Sun, *Chem. Mater.* **2020**, *32*, 2664.
- [131] O. Kwon, M. Hirayama, K. Suzuki, Y. Kato, T. Saito, M. Yonemura, T. Kamiyama, R. Kanno, *J. Mater. Chem. A* **2015**, *3*, 438.
- [132] Y. Lee, J. Jeong, H. Lee, M. Kim, D. Han, H. Kim, J. Yuk, K. Nam, K. Chung, H. Jung, S. Yu, *ACS Energy Lett.* **2022**, *7*, 171.
- [133] L. Zhou, A. Assoud, Q. Zhang, X. Wu, L. Nazar, *J. Am. Chem. Soc.* **2019**, *141*, 19002.



- [134] D. Zeng, J. Yao, L. Zhang, R. Xu, S. Wang, X. Yan, C. Yu, L. Wang, *Nat. Commun.* **2022**, 13, 1909.
- [135] R. Song, J. Yao, R. Xu, Z. Li, X. Yan, C. Yu, Z. Huang, L. Zhang, *Adv. Energy Mater.* **2023**, 13, 2203631.
- [136] C. Liu, B. Chen, T. Zhang, J. Zhang, R. Wang, J. Zheng, Q. Mao, X. Liu, *Angew. Chem. Int. Ed.* **2023**, 62, e2023026.
- [137] O. Sheng, C. Jin, Z. Ju, J. Zheng, T. Liu, Y. Liu, Y. Wang, J. Luo, X. Tao, J. Nai, *Nano Lett.* **2022**, 22, 8346.
- [138] J. Heo, A. Banerjee, K. Park, Y. Jung, S. Hong, *Adv. Energy Mater.* **2018**, 11, 1702716.
- [139] S. Jang, Y. Tateyama, R. Jalem, *Adv. Funct. Mater.* **2022**, 32, 2206036.
- [140] S. Kundu, N. Solomatin, Y. Kauffmann, A. Kraysberg, Y. Eli, *Appl. Mater. Today* **2021**, 23, 100998.
- [141] L. Wang, Z. Karger, F. Klein, J. Chable, T. Braun, A. Schur, C. Wang, Y. Guo, M. Fichtner, *ChemSusChem* **2019**, 12, 2286.
- [142] L. Zhang, D. Zhang, K. Yang, X. Yan, L. Wang, J. Mi, B. Xu, Y. Li, *Adv. Sci.* **2016**, 3, 1600089.
- [143] P. Canepa, S. H. Bo, G. Sai Gautam, B. Key, W. D. Richards, T. Shi, Y. Tian, Y. Wang, J. Li, G. Ceder, *Nat. Commun.* **2017**, 8, 1759.
- [144] Z. Yu, S. Shang, J. Seo, D. Wang, X. Luo, Q. Huang, S. Chen, J. Lu, X. Li, Z. Liu, D. Wang, *Adv. Mater.* **2017**, 29, 1605561.
- [145] H. Wang, Y. Chen, Z. Hood, G. Sahu, A. Pandian, J. Keum, K. An, C. Liang, *Angew. Chem. Int. Ed.* **2016**, 55, 8551.
- [146] A. Martinolich, C. Lee, I. Lu, S. Bevilacqua, M. Preefer, M. Bernardi, A. Schleife, K. See, *Chem. Mater.* **2019**, 31, 3652.
- [147] J. Zhi, S. Zhao, M. Zhou, R. Wang, F. Huang, *Sci. Adv.* **2023**, 9, eade221.
- [148] S. Ikeda, M. Takahashi, J. Ishikawa, K. Ito, *Solid State Ionics* **1987**, 23, 125.
- [149] S. Higashi, K. Miwa, M. Aoki, K. Takechi, *Chem. Commun.* **2014**, 50, 1320.
- [150] M. Matsuo, A. Remhof, P. Martelli, R. Caputo, M. Ernst, Y. Miura, T. Sato, H. Oguchi, H. Maekawa, H. Takamura, A. Borgschulte, A. Züttel, S. Orimo, *J. Am. Chem. Soc.* **2009**, 131, 16389.
- [151] T. Zhang, Y. Wang, T. Song, H. Miyaoka, K. Shinzato, H. Miyaoka, T. Ichikawa, S. Shi, X. Zhang, S. Isobe, N. Hashimoto, Y. Kojima, *Joule* **2018**, 2, 1522.
- [152] K. Kisu, S. Kim, M. Inukai, H. Oguchi, S. Takagi, S. Orimo, *ACS Appl. Energy Mater.* **2020**, 3, 3174.
- [153] R. Mohtadi, M. Matsui, T. Arthur, S. Hwang, *Angew. Chem., Int. Ed.* **2012**, 51, 9780.
- [154] R. Zettl, K. Hogrefe, B. Gadermaier, I. Hanzu, P. Ngene, P. Jongh, H. Martin, R. Wilkening, *J. Phys. Chem. C* **2021**, 125, 15052.
- [155] A. Sakuda, A. Yamauchi, S. Yubuchi, N. Kitamura, Y. Idemoto, A. Hayashi, M. Tatsumisago, *ACS Omega* **2018**, 3, 5453.
- [156] J. Park, J. Son, W. Ko, J. Kim, Y. Choi, H. Kim, H. Kwak, D. Seo, J. Kim, Y. Jung, *ACS Energy Lett.* **2022**, 7, 3293.
- [157] S. Yu, K. Kim, B. Wood, H. Jung, K. Chung, *J. Mater. Chem. A* **2022**, 10, 24301.
- [158] H. Kwak, J. Kim, D. Han, J. Kim, J. Park, G. Kwon, S. Bak, U. Heo, C. Park, H. Lee, K. Nam, D. Seo, Y. Jung, *Nat. Commun.* **2023**, 14, 2459.
- [159] H. Kwak, S. Wang, J. Park, Y. Liu, K. Kim, Y. Choi, Y. Mo, Y. Jung, *ACS Energy Lett.* **2022**, 7, 1776.
- [160] H. Kasper, *Inorg. Chem.* **1969**, 8, 1000.
- [161] C. Devianapoorani, L. Dhivya, S. Ramakumar, R. Murugan, *J. Power Sources* **2013**, 240, 18.
- [162] S. Kim, J. Kim, L. Miara, Y. Wang, S. Jung, S. Park, Z. Song, H. Kim, M. Badding, J. Chang, V. Roey, G. Yoon, R. Kim, J. Kim, K. Yoon, D. Im, K. Kang, *Nat. Commun.* **2022**, 13, 1883.
- [163] M. Nakayama, T. Horie, R. Natsume, S. Hashimura, N. Tanibata, H. Takeda, H. Maeda, M. Kotobuki, *J. Phys. Chem. C* **2023**, 127, 7595.
- [164] J. Allen, J. Wolfenstine, E. Rangasamy, J. Sakamoto, *J. Power Sources* **2012**, 206, 315.
- [165] V. Thangadurai, H. Kaack, W. Weppner, *J. Am. Ceram. Soc.* **2003**, 86, 437.
- [166] T. Deng, X. Ji, Y. Zhao, L. Cao, S. Li, S. Hwang, C. Luo, P. Wang, H. Jia, X. Fan, X. Lu, D. Su, X. Sun, C. Wang, J. Zhang, *Adv. Mater.* **2020**, 32, 2000030.
- [167] R. Eremin, N. Kabanova, Y. Morkhova, A. Golov, V. Blatov, *Solid State Ionics* **2018**, 326, 188.
- [168] H. Yuan, H. Li, T. Zhang, G. Li, T. He, F. Du, S. Feng, *J. Mater. Chem. A* **2018**, 6, 8413.
- [169] A. Omote, S. Yotsuhashi, Y. Zenitani, Y. Yamada, D. Edwards, *J. Am. Ceram. Soc.* **2011**, 94, 2285.
- [170] J. Su, T. Tsuruoka, T. Tsujita, Y. Nishitani, K. Nakura, K. Terabe, *Chem. Mater.* **2019**, 31, 5566.
- [171] B. Liang, V. Keshishian, S. Liu, E. Yi, D. Jia, Y. Zhou, J. Kieffer, B. Ye, R. Laine, *Electrochim. Acta* **2018**, 272, 144.
- [172] M. Aubrey, R. Ameloot, B. Wiers, J. Long, *Energy Environ. Sci.* **2014**, 7, 667.
- [173] G. Feuille, P. Perche, *J. Appl. Electrochem.* **1975**, 5, 63.
- [174] G. Appetecchi, F. Croce, L. Persi, F. Ronci, B. Scrosati, *Electrochim. Acta* **2000**, 45, 1481.
- [175] M. Borghini, M. Mastragostino, S. Passerini, B. Scrosati, *J. Electrochem. Soc.* **1995**, 142, 2118.
- [176] W. Krawiec, L. Scanlon, J. Fellner, R. Vaia, S. Vasudevan, E. Giannelis, *J. Power Sources* **1995**, 54, 310.
- [177] A. Luntz, J. Voss, K. Reuter, *J. Phys. Chem. Lett.* **2015**, 6, 4599.
- [178] Y. Zhu, X. He, Y. Mo, J. Mater. Chem. A **2016**, 4, 3253.
- [179] S. Gao, Y. Pan, B. Li, M. Rahman, M. Tian, H. Yang, P. Cao, *Adv. Funct. Mater.* **2023**, 33, 2210543.
- [180] S. Gao, Z. Li, Z. Zhang, B. Li, X. Chen, G. Yang, T. Saito, M. Tian, H. Yang, P. Cao, *Energy Storage Mater.* **2023**, 55, 214.
- [181] F. Sagane, T. Abe, Y. Iriyama, Z. Ogumi, *J. Power Sources* **2005**, 146, 749.
- [182] M. Okoshi, Y. Yamada, A. Yamada, H. Nakai, *J. Electrochem. Soc.* **2013**, 160, A2160.
- [183] L. Yang, R. Huq, G. Farrington, G. Chiodelli, *Solid State Ionics* **1986**, 18–19, 291.
- [184] Y. Shao, N. Rajput, J. Hu, M. Hu, T. Liu, Z. Wei, M. Gu, X. Deng, S. Xu, K. Han, J. Wang, Z. Nie, G. Li, K. Zavadil, J. Xiao, C. Wang, W. Henderson, J. Zhang, Y. Wang, K. Mueller, K. Persson, J. Liu, *Nano Energy* **2015**, 12, 750.
- [185] A. Aziz, Y. Tominaga, *Ionics* **2018**, 24, 3475.
- [186] K. Tang, A. Du, S. Dong, Z. Cui, X. Liu, C. Lu, J. Zhao, X. Zhou, G. Cui, *Adv. Mater.* **2020**, 32, 1904987.
- [187] L. Ma, X. Li, G. Zhang, Z. Huang, C. Han, H. Li, Z. Tang, C. Zhi, *Energy Storage Mater.* **2020**, 31, 451.
- [188] B. Lee, S. Cui, X. Xing, H. Liu, X. Yue, V. Petrova, H. Lim, R. Chen, P. Liu, *ACS Appl. Mater. Interfaces* **2018**, 10, 38928.
- [189] B. Tang, L. Shan, S. Liang, J. Zhou, *Energy Environ. Sci.* **2019**, 12, 3288.
- [190] J. Fu, J. Zhang, X. Song, H. Zarrin, X. Tian, J. Qiao, L. Rasen, K. Li, Z. Chen, *Energy Environ. Sci.* **2016**, 9, 663.
- [191] S. Shinde, J. Jung, N. Wagh, C. Lee, D. Kim, S. Kim, S. Lee, J. Lee, *Nat. Energy* **2021**, 6, 592.
- [192] F. Mo, G. Liang, Q. Meng, Z. Liu, H. Li, J. Fan, C. Zhi, *Energy Environ. Sci.* **2019**, 12, 706.
- [193] S. Zhang, Z. Liu, R. Liu, L. Du, L. Zheng, Z. Liu, K. Li, M. Lin, Y. Bian, M. Cai, H. Du, *J. Power Sources* **2023**, 575, 233110.
- [194] Z. Yu, S. Jiao, S. Li, X. Chen, W. Song, T. Teng, J. Tu, H. Chen, G. Zhang, D. Fang, *Adv. Funct. Mater.* **2019**, 29, 1806799.
- [195] M. Hamada, R. Tatara, K. Kubota, S. Kumakura, S. Komaba, *ACS Energy Lett.* **2022**, 7, 2244.
- [196] T. Sreekanth, M. Reddy, U. Rao, *J. Power Sources* **2001**, 93, 268.
- [197] X. Zhou, Z. Li, W. Li, X. Li, J. Fu, L. Wei, H. Yang, X. Guo, *Adv. Funct. Mater.* **2023**, 33, 2212866.

- [198] X. Li, L. Liang, M. Su, L. Wang, Y. Zhang, J. Sun, Y. Liu, L. Hou, C. Yuan, *Adv. Energy Mater.* **2023**, 13, 2203701.
- [199] L. Hou, Y. Li, Z. Li, Q. Zhang, B. Li, C. Bi, Z. Chen, L. Su, J. Huang, R. Wen, X. Zhang, Q. Zhang, *Angew. Chem. Int. Ed.* **2023**, 62, e202305466.
- [200] Y. Wang, Q. Li, H. Hong, S. Yang, R. Zhang, X. Wang, X. Jin, B. Xiong, S. Bai, C. Zhi, *Nat. Commun.* **2023**, 14, 3890.
- [201] S. Shinde, C. Lee, J. Jung, N. Wagh, S. Kim, D. Kim, C. Lin, S. Lee, J. Lee, *Energy Environ. Sci.* **2019**, 12, 727.
- [202] S. Shinde, C. Lee, J. Yu, D. Kim, S. Lee, J. Lee, *ACS Nano* **2018**, 12, 596.
- [203] N. Wagh, S. Shinde, C. Lee, J. Jung, D. Kim, S. Kim, C. Lin, S. Lee, J. Lee, *Appl. Catal. B: Environ.* **2020**, 268, 118746.
- [204] N. Wagh, D. Kim, S. Kim, S. Shinde, J. Lee, *ACS Nano* **2021**, 15, 14683.
- [205] S. Shinde, C. Lee, A. Sami, D. Kim, S. Lee, J. Lee, *ACS Nano* **2017**, 11, 347.
- [206] N. Wagh, S. Shinde, C. Lee, S. Kim, D. Kim, H. Um, S. Lee, J. Lee, *Nano-Micro Lett.* **2022**, 14, 190.
- [207] S. Shinde, J. Yu, J. Song, Y. Nam, D. Kim, J. Lee, *Nanoscale Horiz.* **2017**, 2, 333.
- [208] N. Wagh, D. Kim, C. Lee, S. Kim, H. Um, J. Kwon, S. Shinde, S. Lee, J. Lee, *Nanoscale Horiz.* **2023**, 8, 921.
- [209] J. Bates, N. Dudney, G. Gruzalski, R. Zuh, A. Choudhury, C. Luck, J. Robertson, *J. Power Sources* **1993**, 43, 103.
- [210] J. Bates, N. Dudney, B. Neudecker, F. Hart, H. Jun, S. Hackney, *J. Electrochem. Soc.* **2000**, 147, 59.
- [211] J. Bates, N. Dudney, B. Neudecker, A. Ueda, C. Evans, *Solid State Ionics* **2000**, 135, 33.
- [212] Q. Xia, F. Zan, Q. Zhang, W. Liu, Q. Li, Y. He, J. Hua, J. Liu, J. Xu, J. Wang, C. Wu, H. Xia, *Adv. Mater.* **2022**, 35, 2200538.
- [213] J. Xu, Y. Li, P. Lu, W. Yan, M. Yang, H. Li, L. Chen, F. Wu, *Adv. Energy Mater.* **2021**, 12, 21022348.
- [214] V. Lacivita, A. Westover, A. Kercher, N. Phillip, G. Yang, G. Veith, G. Ceder, N. Dudney, *J. Am. Chem. Soc.* **2018**, 140, 11029.
- [215] X. Lu, J. Howard, A. Chen, J. Zhu, S. Li, G. Wu, P. Dowden, H. Xu, Y. Zhao, Q. Jia, *Adv. Sci.* **2016**, 3, 1500359.
- [216] C. Lupo, F. Michel, F. Kuhl, Y. Su, M. Becker, A. Polity, D. Schlottwein, *Phys. Status Solidi B* **2021**, 258, 2100032.
- [217] Y. Su, J. Falgenhauer, A. Polity, T. Leichtweiß, A. Kronenberger, J. Obel, S. Zhou, D. Schlottwein, J. Janek, B. Meyer, *Solid State Ionics* **2015**, 282, 63.
- [218] Y. Su, J. Falgenhauer, T. Leichtweiß, M. Geiß, C. Lupó, A. Polity, S. Zhou, J. Obel, D. Schlottwein, J. Janek, B. Meyer, *Phys. Status Solidi B* **2017**, 254, 1600088.
- [219] F. Michel, F. Kuhl, M. Becker, J. Janek, A. Polity, *Phys. Status Solidi B* **2019**, 256, 1900047.
- [220] P. Mani, S. Saraf, V. Singh, M. Real-Robert, A. Vijayakumar, S. Durand, S. Seal, K. Coffey, *Solid State Ionics* **2016**, 287, 48.
- [221] P. Knauth, *Solid State Ionics* **2009**, 180, 911.
- [222] Z. Zheng, S. Song, Y. Wang, *Solid State Ionics* **2016**, 287, 60.
- [223] X. Song, W. Yu, S. Zhou, L. Zhao, A. Li, A. Wu, L. Li, H. Huang, *Mater. Today Phys.* **2023**, 33, 101037.
- [224] S. Martha, J. Nanda, Y. Kim, R. Unocic, S. Pannala, N. Dudney, *J. Mater. Chem. A* **2013**, 1, 5587.
- [225] A. López-Grande, G. Mather, F. Muñoz, *J. Mater. Chem. A* **2023**, 11, 12282.
- [226] R. Nuwayhid, A. Jarry, G. Rubloff, K. Gregorczyk, *ACS Appl. Mater. Interfaces* **2020**, 12, 21641.
- [227] D. Fontecha, R. Nuwayhid, A. Kozen, D. Stewart, G. Rubloff, K. Gregorczyk, *J. Vac. Sci. Technol. A* **2022**, 40, 032403.
- [228] P. López-Aranguren, M. Reynaud, P. Głuchowski, A. Bustinza, M. Galceran, J. Amo, M. Armand, M. Casas-Cabanas, *ACS Energy Lett.* **2021**, 6, 445.
- [229] J. Su, T. Tsuruoka, T. Tsujita, Y. Inatomi, K. Terabe, *Angew. Chem. Int. Ed.* **2023**, 62, e2022172.
- [230] T. Tsuruoka, T. Tsujita, J. Su, Y. Nishitani, T. Hamamura, Y. Inatomi, K. Nakura, K. Terabe, *Jpn. J. Appl. Phys.* **2020**, 59, S11G08.
- [231] K. Suzuya, D. Price, C. Loong, S. Martin, *J. Non-Cryst. Solids* **1998**, 232–234, 650.
- [232] U. Hoppe, *J. Non-Cryst. Solids* **1996**, 195, 138.
- [233] K. Santosh, R. Longo, K. Xiong, K. Cho, *J. Electrochem. Soc.* **2014**, 161, F3104.
- [234] B. Wu, S. Wang, J. Lochala, D. Desrochers, B. Liu, W. Zhang, J. Yang, J. Xiao, *Energy Environ. Sci.* **2018**, 11, 1803.
- [235] H. Xu, Y. Li, A. Zhou, N. Wu, S. Xin, Z. Li, J. Goodenough, *Nano Lett.* **2018**, 18, 7414.
- [236] K. Yoshima, Y. Harada, N. Takami, *J. Power Sources* **2016**, 302, 283.
- [237] H. Xie, C. Yang, K. Fu, Y. Yao, F. Jiang, E. Hitz, B. Liu, S. Wang, L. Hu, *Adv. Energy Mater.* **2018**, 8, 1703474.
- [238] J. Doux, H. Nguyen, D. Tan, A. Banerjee, X. Wang, E. Wu, C. Jo, H. Yang, Y. Meng, *Adv. Energy Mater.* **2020**, 10, 1903253.
- [239] R. Koerver, W. Zhang, L. Biasi, S. Schweidler, A. Kondrakov, S. Kolling, T. Brezesinski, P. Hartmann, W. Zeier, J. Janek, *Energy Environ. Sci.* **2018**, 11, 2142.
- [240] K. Liao, S. Wu, X. Mu, Q. Lu, M. Han, P. He, Z. Shao, H. Zhou, *Adv. Mater.* **2018**, 30, 1705711.
- [241] S. Visco, V. Nimon, A. Petrov, K. Pridatko, N. Goncharenko, E. Nimon, L. De Jonghe, Y. Volkovich, D. Bogachev, *J. Solid State Electrochem.* **2014**, 18, 1443.
- [242] M. Du, K. Liao, Q. Lua, Z. Shao, *Energy Environ. Sci.* **2019**, 12, 1780.
- [243] K. Okada, N. Machida, M. Naito, T. Shigematsu, S. Ito, S. Fujiki, M. Nakano, Y. Aihara, *Solid State Ionics* **2014**, 255, 120.
- [244] N. Ohta, K. Takada, L. Zhang, R. Ma, M. Osada, T. Sasaki, *Adv. Mater.* **2006**, 18, 2226.
- [245] S. Wang, H. Xu, W. Li, A. Dolocan, A. Manthiram, *J. Am. Chem. Soc.* **2018**, 140, 250.
- [246] K. Takada, N. Ohta, L. Zhang, X. Xu, B. Hang, T. Ohnishi, M. Osada, T. Sasaki, *Solid State Ionics* **2012**, 225, 594.
- [247] N. de Klerk, M. Wagemaker, *ACS Appl. Mater. Interfaces* **2018**, 1, 5609.
- [248] M. Fingerle, R. Buchheit, S. Siculo, K. Albe, R. Hausbrand, *Chem. Mater.* **2017**, 29, 7675.
- [249] A. Schwobel, W. Jaegermann, R. Hausbrand, *Solid State Ionics* **2016**, 288, 224.
- [250] G. Cherkashinin, M. Motzko, N. Schulz, T. Spath, W. Jaegermann, *Chem. Mater.* **2015**, 27, 2875.
- [251] L. Le Van-Jodin, F. Ducroquet, F. Sabary, I. Chevalier, *Solid State Ionics* **2013**, 253, 151.
- [252] L. Wang, R. Xie, B. Chen, X. Yu, J. Ma, C. Li, Z. Hu, X. Sun, C. Xu, S. Dong, T. Chan, J. Luo, G. Cui, L. Chen, *Nat. Commun.* **2020**, 11, 5889.
- [253] Z. Gu, J. Ma, F. Zhu, T. Liu, K. Wang, C. Nan, Z. Li, C. Ma, *Nat. Commun.* **2023**, 14, 1632.
- [254] Z. Cheng, M. Liu, S. Ganapathy, C. Li, Z. Li, X. Zhang, P. He, H. Zhou, M. Wagemaker, *Joule* **2020**, 4, 1311.
- [255] R. Usiskin, J. Maier, *Adv. Energy Mater.* **2020**, 11, 2001455.
- [256] L. Miara, A. Windmüller, C. Tsai, W. Richards, Q. Ma, S. Uhlenbruck, O. Guillon, G. Ceder, *ACS Appl. Mater. Interfaces* **2016**, 8, 26842.
- [257] P. Xu, W. Rheinheimer, S. Shuvo, Z. Qi, O. Levit, H. Wang, Y. Eli, L. Stanciu, *ChemElectroChem* **2019**, 6, 4576.
- [258] R. Zhang, F. Strauss, L. Jiang, L. Casalena, L. Li, J. Janek, A. Kondrakov, T. Brezesinski, *Chem. Commun.* **2023**, 59, 4600.
- [259] J. Kim, J. Park, M. Lee, S. Kang, D. Shin, J. Oh, J. Kim, K. Kim, Y. Lee, Y. Lee, *ACS Energy Lett.* **2020**, 5, 2995.
- [260] C. Chen, J. Oudenhoven, D. Danilov, E. Vezhlev, L. Gao, N. Li, F. Mulder, R. Eichel, P. Notten, *Adv. Energy Mater.* **2018**, 8, 201801430.
- [261] H. Kwak, Y. Park, *Sci. Rep.* **2019**, 9, 8099.

- [262] H. Fu, Y. Wang, G. Fan, S. Guo, X. Xie, X. Cao, B. Lu, M. Long, J. Zhou, S. Liang, *Chem. Sci.* **2022**, *13*, 726.
- [263] E. Gabriele, D. Hou, E. Lee, H. Xiong, *Energy Sci. Eng.* **2022**, *10*, 1672.
- [264] L. Yang, Y. Yuan, Q. Li, J. Wu, T. Chen, J. Wang, X. Zuo, A. Tang, L. Zhang, N. Moelans, F. Pan, *Calphad* **2023**, *80*, 102524.
- [265] T. Xiong, Y. Wang, B. Yin, W. Shi, W. Lee, J. Xue, *Nano-Micro Lett.* **2020**, *12*, 8.
- [266] Z. Liu, Y. Qi, Y. Lin, L. Chen, P. Lu, L. Chen, *J. Electrochem. Soc.* **2016**, *163*, A592.
- [267] S. Yan, C. Yim, V. Pankov, M. Bauer, E. Baranova, A. Weck, A. Merati, Y. Lebdeh, *Batteries* **2021**, *7*, 75.
- [268] W. Zhao, J. Yi, P. He, H. Zhou, *Electrochem. Energy Rev.* **2019**, *2*, 574.
- [269] C. Brissot, M. Rosso, J. Chazalviel, S. Lascaud, *J. Power Sources* **1999**, *81–82*, 925.
- [270] C. Monroe, J. Newman, *J. Electrochem. Soc.* **2003**, *150*, A1377.
- [271] M. Dolle, L. Sannier, B. Beaudoin, M. Trentin, J. Tarascon, *Electrochem. Solid-State Lett.* **2002**, *5*, A286.
- [272] K. Harry, D. Hallinan, D. Parkinson, A. MacDowell, N. Balsara, *Nat. Mater.* **2013**, *13*, 69.
- [273] W. Zhou, S. Wang, Y. Li, S. Xin, A. Manthiram, J. Goodenough, *J. Am. Chem. Soc.* **2016**, *138*, 9385.
- [274] E. Cheng, A. Sharafi, J. Sakamoto, *Electrochim. Acta* **2017**, *223*, 85.
- [275] S. Yu, D. Siegel, *Chem. Mater.* **2017**, *29*, 9639.
- [276] J. Sastre, M. Futscher, L. Pompizi, A. Aribia, A. Priebe, J. Overbeck, M. Stiefel, A. Tiwari, Y. Romanyuk, *Commun. Mater.* **2021**, *2*, 76.
- [277] Y. You, F. Zheng, D. Zhang, C. Zhao, C. Hu, X. Cao, Z. Zhu, S. Wu, *ACS Appl. Energy Mater.* **2022**, *5*, 15078.
- [278] Mingjie Dua, Kaiming Liao, Q. Lu, Z. Shao, *Energy Environ. Sci.* **2019**, *12*, 1780.
- [279] M. Lei, S. Fan, Y. Yu, J. Hu, K. Chen, Y. Gu, C. Wu, Y. Zhang, C. Li, *Energy Storage Mater.* **2022**, *47*, 551.
- [280] S. Zhang, J. You, Z. He, J. Zhong, P. Zhang, Z. Yin, F. Pan, M. Ling, B. Zhang, Z. Lin, *Adv. Funct. Mater.* **2022**, *32*, 2200967.
- [281] Mengqi Zhu, Bin Li, Songmei Li, Zhiguo Du, Yongji Gong, Shubin Yang, *Adv. Energy Mater.* **2018**, *8*, 1703505.
- [282] M. Yan, J. Liang, T. Zuo, Y. Yin, S. Xin, S. Tan, Y. Guo, L. Wan, *Adv. Funct. Mater.* **2020**, *30*, 1908047.
- [283] X. Han, Y. Gong, K. Fu, X. He, G. Hitz, J. Dai, A. Pearse, B. Liu, H. Wang, G. Rubloff, Y. Mo, V. Thangadurai, E. Wachsman, L. Hu, *Nat. Mater.* **2017**, *16*, 572.
- [284] C. Wang, Y. Gong, B. Liu, K. Fu, Y. Yao, E. Hitz, Y. Li, J. Dai, S. Xu, W. Luo, E. Wachsman, L. Hu, *Nano Lett.* **2017**, *17*, 565.
- [285] K. Fu, Y. Gong, Z. Fu, H. Xie, Y. Yao, B. Liu, M. Carter, E. Wachsman, L. Hu, *Angew. Chem., Int. Ed.* **2017**, *56*, 14942.
- [286] F. Hu, Y. Li, Y. Wei, J. Yang, P. Hu, Z. Rao, X. Chen, L. Yuan, Z. Li, *ACS Appl. Mater. Interfaces* **2020**, *12*, 12793.
- [287] K. Fu, Y. Gong, B. Liu, Y. Zhu, S. Xu, Y. Yao, W. Luo, C. Wang, S. Lacey, J. Dai, Y. Chen, Y. Mo, E. Wachsman, L. Hu, *Sci. Adv.* **2017**, *3*, e1601659.
- [288] H. Liu, C. Yang, M. Han, C. Yu, X. Li, Z. Yu, J. Qu, *Angew. Chem.* **2023**, *135*, e202217.
- [289] P. Hundekar, S. Basu, X. Fan, L. Li, A. Yoshimura, T. Gupta, V. Sarbada, A. Lakhot, R. Jain, S. Narayanan, Y. Shid, C. Wang, N. Koratkar, *PNAS* **2020**, *117*, 5588.
- [290] J. Kwak, Y. Jeoun, S. Oh, S. Yu, J. Lim, Y. Sung, S. Yu, H. Lim, *ACS Energy Lett.* **2022**, *7*, 162.
- [291] Q. Li, H. A. Hjuler, R. W. Berg, N. J. Bjerrum, *J. Electrochem. Soc.* **1990**, *137*, 1184.
- [292] H. Chen, H. Xu, S. Wang, T. Huang, J. Xi, S. Cai, F. Guo, Z. Xu, W. Gao, C. Gao, *Sci. Adv.* **2017**, *3*, eaao7233.
- [293] D. Kim, D. Yoo, M. Otley, A. Prokofjevs, C. Pezzato, M. Owczarek, S. Lee, J. Choi, J. Stoddart, *Nat. Energy* **2019**, *4*, 51.
- [294] S. Wang, Z. Yu, J. Tu, J. Wang, D. Tian, Y. Liu, S. Jiao, *Adv. Energy Mater.* **2016**, *6*, 1600137.
- [295] M. Walter, K. V. Kravchyk, C. Böfer, R. Widmer, M. V. Kovalenko, *Adv. Mater.* **2018**, *30*, 1705644.
- [296] V. Yuft, F. Tariq, D. Eastwood, M. Biton, B. Wu, P. Lee, N. Brandon, *Joule* **2019**, *3*, 485.
- [297] T. Zheng, Y. Hu, S. Yang, *J. Magnes. Alloy* **2017**, *5*, 404.
- [298] F. Liu, G. Cao, J. Ban, H. Lei, Y. Zhang, G. Shao, A. Zhou, L. Fan, J. Hu, *J. Magnes. Alloy* **2022**, *10*, 2699.
- [299] T. Wen, B. Qu, S. Tan, G. Huang, J. Song, Z. Wang, J. Wang, A. Tang, F. Pan, *Energy Storage Mater.* **2023**, *55*, 816.
- [300] M. Peng, K. Shin, L. Jiang, Y. Jin, K. Zeng, X. Zhou, Y. Tang, *Angew. Chem. Int. Ed.* **2022**, *61*, e202206770.
- [301] X. Miao, H. Di, X. Ge, D. Zhao, P. Wang, R. Wang, C. Wang, L. Yin, *Energy Storage Mater.* **2020**, *30*, 170.
- [302] L. Zhang, X. Xia, Y. Zhong, D. Xie, S. Liu, X. Wang, J. Tu, *Adv. Mater.* **2018**, *30*, 1804011.
- [303] C. Wu, K. Xie, K. Ren, S. Yang, Q. Wang, *Dalton Trans.* **2020**, *49*, 17629.
- [304] H. He, H. Qin, J. Wu, X. Chen, R. Huang, F. Shen, Z. Wu, G. Chen, S. Yin, J. Liu, *Energy Storage Mater.* **2021**, *43*, 317.
- [305] Z. Zhao, J. Zhao, Z. Hu, J. Li, J. Li, Y. Zhang, C. Wang, G. Cui, *Energy Environ. Sci.* **2019**, *12*, 1938.
- [306] Z. Cao, X. Zhu, D. Xu, P. Dong, M. Chee, X. Li, K. Zhu, M. Ye, J. Shen, *Energy Storage Mater.* **2021**, *36*, 132.
- [307] Z. Wang, D. Santhanagopalan, W. Zhang, F. Wang, H. Xin, K. He, J. Li, N. Dudney, Y. Meng, *Nano Lett.* **2016**, *16*, 3760.
- [308] Y. Du, N. Holzwarth, *J. Electrochem. Soc.* **2007**, *154*, A999.
- [309] K. Kanamura, W. Hoshikawa, T. Umegaki, *J. Electrochem. Soc.* **2002**, *149*, A339.
- [310] M. Fritsch, G. Standke, C. Heubner, U. Langklotz, A. Michaelis, *J. Energy Storage* **2018**, *16*, 125.
- [311] P. Zhu, D. Gastol, J. Marshall, R. Sommerville, V. Goodship, E. Kendrick, *J. Power Sources* **2021**, *485*, 229321.
- [312] M. Lain, J. Brandon, E. Kendrick, *Batteries* **2019**, *5*, 64.
- [313] S. Yoon, H. Jang, S. Kim, J. Kim, K. Cho, *J. Electroanal. Chem.* **2017**, *797*, 37.
- [314] H. Wu, H. Wu, E. Lee, N. Wu, *Electrochem. Commun.* **2010**, *12*, 488.
- [315] H. Wu, E. Lee, N. Wu, T. Jow, *J. Power Sources* **2012**, *197*, 301.
- [316] H. Nara, D. Mukoyama, R. Shimizu, T. Momma, T. Osada, *J. Power Sources* **2019**, *409*, 139.
- [317] B. Key, R. Bhattacharyya, M. Morcrette, V. Seznec, J. Tarascon, C. Grey, *J. Am. Chem. Soc.* **2009**, *131*, 9239.
- [318] R. Spotnitz, J. Franklin, *J. Power Sources* **2003**, *113*, 81.
- [319] G. Xu, L. Huang, C. Lu, X. Zhou, G. Cui, *Energy Storage Mater.* **2020**, *31*, 72.
- [320] H. Li, H. Wang, Z. Xu, K. Wang, M. Ge, L. Gan, Y. Zhang, Y. Tang, S. Chen, *Small* **2021**, *17*, 2103679.
- [321] C. Un, K. Aydin, *Vehicles* **2021**, *3*, 480.
- [322] G. Wang, D. Kong, P. Ping, J. Wen, X. He, H. Zhao, X. He, R. Peng, Y. Zhang, X. Dai, *eTransportation* **2023**, *16*, 100237.
- [323] Z. Shadike, H. Lee, O. Borodin, X. Cao, X. Fan, X. Wang, R. Lin, S. Bak, S. Ghose, K. Xu, C. Wang, J. Liu, J. Xiao, X. Yang, E. Hu, *Nat. Nanotechnol.* **2021**, *16*, 549.
- [324] Y. Li, Y. Li, A. Pei, K. Yan, Y. Sun, C. Wu, L. Joubert, R. Chin, A. Koh, Y. Yu, J. Perrino, B. Butz, S. Chu, Y. Cui, *Science* **2017**, *358*, 506.
- [325] M. Fertig, K. Skadell, M. Schulz, C. Dirksen, P. Adelhelm, M. Stelter, *Batteries Supercaps* **2022**, *5*, 202100131.
- [326] P. Hartmann, T. Leichtweiss, M. Busche, M. Schneider, M. Reich, J. Sann, P. Adelhelm, J. Janek, *J. Phys. Chem. C* **2013**, *117*, 21064.
- [327] S. Wenzel, S. Randau, T. Leichtweiß, D. Weber, J. Sann, W. Zeier, J. Janek, *Chem. Mater.* **2016**, *28*, 2400.
- [328] T. Schwietert, V. Arszewska, C. Wang, C. Yu, A. Vasileiadis, N. Klerk, J. Hageman, T. Hupfer, I. Kerkamm, Y. Xu, E. Maas, E. Kelder, S. Ganapathy, M. Wagemaker, *Nat. Mater.* **2020**, *19*, 428.



- [329] L. Sang, R. Haasch, A. Gewirth, R. Nuzzo, *Chem. Mater.* **2017**, *29*, 3029.
- [330] L. Riegger, R. Schlem, J. Sann, W. Zeier, J. Janek, *Angew. Chem., Int. Ed.* **2021**, *60*, 6718.
- [331] T. Asano, A. Sakai, S. Ouchi, M. Sakaida, A. Miyazaki, S. Hasegawa, *Adv. Mater.* **2018**, *30*, 1803075.
- [332] C. Zheng, L. Li, K. Wang, C. Wang, J. Zhang, Y. Xia, H. Huang, C. Liang, Y. Gan, X. He, X. Tao, W. Zhang, *Batteries Supercaps* **2021**, *4*, 8.
- [333] Y. Xu, K. Dong, Y. Jie, P. Adelhelm, Y. Chen, L. Xu, P. Yu, J. Kim, Z. Kochovski, Z. Yu, W. Li, J. LeBeau, Y. Horn, R. Cao, S. Jiao, T. Cheng, I. Manke, Y. Lu, *Adv. Mater.* **2022**, *12*, 2200398.
- [334] M. Whittingham, *Science* **1976**, *192*, 1126.
- [335] D. Aurbach, E. Zinigrad, Y. Cohen, H. Teller, *Solid State Ionics* **2002**, *148*, 405.
- [336] W. Xu, J. Wang, F. Ding, X. Chen, E. Nasybulin, Y. Zhang, J. Zhang, *Energy Environ. Sci.* **2014**, *7*, 513.
- [337] D. Aurbach, E. Zinigrad, H. Teller, P. Dan, *J. Electrochem. Soc.* **2000**, *147*, 1274.
- [338] R. Sahore, Z. Du, X. Chen, W. Hawley, A. Westover, N. Dudney, *ACS Energy Lett.* **2021**, *6*, 2240.
- [339] Z. Wang, L. Shen, S. Deng, P. Cui, X. Yao, *Adv. Mater.* **2021**, *33*, 2100353.
- [340] R. Rojaee, S. Cavallo, S. Mogurampelly, B. Wheatle, V. Yurkiv, R. Deivanayagam, T. Foroozan, M. Rasul, S. Asl, A. Phakatkar, M. Cheng, S. Son, Y. Pan, F. Mashayek, V. Ganesan, R. Yassar, *Adv. Funct. Mater.* **2020**, *30*, 1910749.
- [341] H. Li, Y. Du, Q. Zhang, Y. Zhao, F. Lian, *Adv. Energy Mater.* **2022**, *12*, 2103530.
- [342] K. Wen, X. Tan, T. Chen, S. Chen, S. Zhang, *Energy Storage Mater.* **2020**, *32*, 55.
- [343] Fei He, Wenjing Tang, Xinyue Zhang, Lijun Deng, Jiayan Luo, *Adv. Mater.* **2021**, *33*, 2105329.
- [344] X. Lin, C. Chu, Z. Li, T. Zhang, J. Chen, R. Liu, P. Li, Y. Li, J. Zhao, Z. Huang, X. Feng, Y. Xie, Y. Ma, *Nano Energy* **2021**, *89*, 106351.
- [345] H. Li, Y. Du, X. Wu, J. Xie, F. Lian, *Adv. Funct. Mater.* **2021**, *31*, 2103049.
- [346] D. Zhang, Z. Liu, Y. Wu, S. Ji, Z. Yuan, J. Liu, M. Zhu, *Adv. Sci.* **2022**, *9*, 2104277.
- [347] X. Lin, S. Xu, Y. Tong, X. Liu, Z. Liu, P. Li, R. Liu, X. Feng, L. Shi, Y. Ma, *Mater. Horiz.* **2023**, *10*, 859.
- [348] B. Yuan, B. Zhao, Q. Wang, Y. Bai, Z. Cheng, Z. Cong, Y. Lu, F. Ji, F. Shen, P. Wang, X. Han, *Energy Storage Mater.* **2022**, *47*, 288.
- [349] V. Jabbari, V. Yurkiv, M. Rasul, A. Phakatkar, F. Mashayek, R. Yassar, *Energy Storage Mater.* **2023**, *57*, 1.
- [350] Q. Ma, S. Fu, A. Wu, Q. Deng, W. Li, D. Yue, B. Zhang, X. Wu, Z. Wang, Y. Guo, *Adv. Energy Mater.* **2023**, *13*, 2203892.
- [351] Y. Lin, T. Wang, L. Zhang, X. Peng, B. Huang, M. Wu, T. Zhao, *Nano Energy* **2022**, *99*, 107395.
- [352] Q. Liu, D. Zhou, D. Shanmukaraj, P. Li, F. Kang, B. Li, M. Armand, G. Wang, *ACS Energy Lett.* **2020**, *5*, 1456.
- [353] E. Gil-González, L. Ye, Y. Wang, Z. Shadike, Z. Xu, E. Hu, X. Li, *Energy Storage Mater.* **2022**, *45*, 484.
- [354] L. Ye, X. Li, *Nature* **2021**, *593*, 218.
- [355] K. Wang, Q. Ren, Z. Gu, C. Duan, J. Wang, F. Zhu, Y. Fu, J. Hao, J. Zhu, L. He, C. Wang, Y. Lu, J. Ma, C. Ma, *Nat. Commun.* **2021**, *12*, 4410.
- [356] S. Wang, Q. Bai, A. Nolan, Y. Liu, S. Gong, Q. Sun, Y. Mo, *Angew. Chem., Int. Ed.* **2019**, *58*, 8039.
- [357] J. Liang, X. Li, S. Wang, K. Adair, W. Li, Y. Zhao, C. Wang, Y. Hu, L. Zhang, S. Zhao, S. Lu, H. Huang, R. Li, Y. Mo, X. Sun, *J. Am. Chem. Soc.* **2020**, *142*, 7012.
- [358] N. Ahmad, S. Sun, P. Yu, W. Yang, *Adv. Funct. Mater.* **2022**, *32*, 2201528.
- [359] F. Mo, J. Ruan, S. Sun, Z. Lian, S. Yang, X. Yue, Y. Song, Y. Zhou, F. Fang, G. Sun, S. Peng, D. Sun, *Adv. Energy Mater.* **2019**, *9*, 1902123.
- [360] X. Ji, S. Hou, P. Wang, X. He, N. Piao, J. Chen, X. Fan, C. Wang, *Adv. Mater.* **2020**, *32*, 2002741.
- [361] J. Li, Y. Li, J. Cheng, Q. Sun, L. Dai, N. Ci, D. Li, L. Ci, *J. Power Sources* **2022**, *518*, 230739.
- [362] J. Tao, Y. Chen, A. Bhardwaj, L. Wen, J. Li, O. Kolosov, Y. Lin, Z. Hong, Z. Huang, S. Mathur, *PNAS* **2022**, *119*, 2211059119.
- [363] B. Cui, X. Han, W. Hu, *Small Struct.* **2021**, *2*, 2000128.
- [364] S. Luo, X. Liu, X. Zhang, X. Wang, Z. Wang, Y. Zhang, H. Wang, W. Ma, L. Zhu, X. Zhang, *ACS Energy Lett.* **2022**, *7*, 3064.
- [365] X. Song, C. Wang, J. Chen, S. Xin, D. Yuan, Y. Wang, K. Dong, L. Yang, G. Wang, H. Zhang, S. Zhang, *Adv. Funct. Mater.* **2022**, *32*, 2108706.
- [366] M. Ghafari, Z. Sanaee, A. Babaei, S. Mohajerzadeh, *J. Mater. Chem. A* **2023**, *11*, 7605.
- [367] N. Tolganbek, A. Serikkazyeva, S. Kalybekkyzy, M. Sarsembina, K. Kanamura, Z. Bakenov, A. Mentbayeva, *Mater. Adv.* **2022**, *3*, 3055.
- [368] P. Shi, J. Ma, M. Liu, S. Guo, Y. Huang, S. Wang, L. Zhang, L. Chen, K. Yang, X. Liu, Y. Li, X. An, D. Zhang, X. Cheng, Q. Li, W. Lv, G. Zhong, Y. He, F. Kang, *Nat. Nanotechnol.* **2023**, *18*, 602.
- [369] K. Yang, L. Chen, J. Ma, Y. He, F. Kang, *InfoMat.* **2021**, *3*, 1195.
- [370] W. Guo, S. Liu, X. Guan, X. Zhang, X. Liu, J. Luo, *Adv. Mater.* **2019**, *9*, 1900193.
- [371] G. Yang, X. Bai, Y. Zhang, Z. Guo, C. Zhao, L. Fan, N. Zhang, *Adv. Funct. Mater.* **2023**, *33*, 2211387.
- [372] Y. Liu, J. Meng, M. Lei, Y. Yu, C. Lai, C. Li, *Adv. Funct. Mater.* **2023**, *33*, 2208013.
- [373] K. Shi, Z. Wan, L. Yang, Y. Zhang, Y. Huang, S. Su, H. Xia, K. Jiang, L. Shen, Y. Hu, S. Zhang, J. Yu, F. Ren, Y. He, F. Kang, *Angew. Chem., Int. Ed.* **2020**, *59*, 11784.
- [374] T. Hwang, P. Conlin, M. Cho, K. Cho, *J. Phys. Chem. C* **2023**, *127*, 7528.
- [375] J. Kim, Y. Lee, S. Cho, J. Gwon, H. Cho, M. Jang, S. Lee, S. Lee, *Energy Environ. Sci.* **2019**, *12*, 177.
- [376] G. Zhou, E. Paek, G. Hwang, A. Manthiram, *Nat. Commun.* **2015**, *6*, 7760.
- [377] S. Chung, A. Manthiram, *Adv. Mater.* **2014**, *26*, 7352.
- [378] X. Yu, Z. Bi, F. Zhao, A. Manthiram, *Adv. Energy Mater.* **2016**, *6*, 1601392.
- [379] S. Wang, J. Zhou, S. Feng, M. Patel, B. Lu, W. Li, C. Soulen, J. Feng, Y. Meng, P. Liu, *ACS Energy Lett.* **2023**, *8*, 2699.
- [380] B. Wei, S. Huang, Y. Song, X. Wang, M. Liu, H. Jin, G. Cao, *J. Mater. Chem. A* **2023**, *11*, 11426.
- [381] R. Deng, B. Ke, Y. Xie, S. Cheng, C. Zhang, H. Zhang, B. Lu, X. Wang, *Nano-Micro Lett.* **2023**, *15*, 73.
- [382] X. Wang, K. He, S. Li, J. Zhang, Y. Lu, *Nano Research* **2023**, *16*, 3741.
- [383] S. Wang, Y. Ding, G. Zhou, G. Yu, A. Manthiram, *ACS Energy Lett.* **2016**, *1*, 1080.
- [384] J. Liang, Q. Sun, Y. Zhao, Y. Sun, C. Wang, W. Li, M. Li, D. Wang, X. Li, Y. Liu, K. Adair, R. Li, L. Zhang, R. Yang, S. Lu, H. Huang, X. Sun, *J. Mater. Chem. A* **2018**, *6*, 23712.
- [385] Q. Zhang, N. Huang, Z. Huang, L. Cai, J. Wu, X. Yao, *J. Energy Chem.* **2020**, *40*, 151.
- [386] X. Tao, Y. Liu, W. Liu, G. Zhou, J. Zhao, D. Lin, O. Sheng, W. Zhang, H. Lee, Y. Cui, *Nano Lett.* **2017**, *17*, 2967.
- [387] C. Yu, S. Ganapathy, E. Eck, H. Wang, S. Basak, Z. Li, M. Wagemaker, *Nat. Commun.* **2017**, *8*, 1086.
- [388] G. Eshetu, X. Judez, C. Li, M. Martinez-Ibañez, I. Gracia, O. Bondarchuk, J. Carrasco, L. Rodriguez-Martinez, H. Zhang, M. Armand, *J. Am. Chem. Soc.* **2018**, *140*, 9921.
- [389] B. Ding, J. Wang, Z. Fan, S. Chen, Q. Lin, X. Lu, H. Du, A. Najundam, G. Yushin, X. Zhang, Y. Yamauchi, *Mater. Today* **2020**, *40*, 114.
- [390] A. Hayashi, T. Ohtomo, F. Mizuno, K. Tadanaga, M. Tatsumisago, *Electrochem. Commun.* **2003**, *5*, 701.

- [391] H. Qiu, T. Tang, M. Asif, W. Li, T. Zhang, Y. Hou, *Nano Energy* **2019**, 65, 103989.
- [392] H. Zhong, L. Sang, F. Ding, J. Song, Y. Mai, *Electrochim. Acta* **2018**, 277, 268.
- [393] L. Kong, L. Wang, Z. Ni, S. Liu, G. Li, X. Gao, *Adv. Funct. Mater.* **2019**, 29, 1808756.
- [394] C. Duan, Z. Cheng, W. Li, F. Li, H. Liu, J. Yang, G. Hou, P. He, H. Zhou, *Energy Environ. Sci.* **2022**, 15, 3236.
- [395] H. Pan, M. Zhang, Z. Cheng, H. Jiang, J. Yang, P. Wang, P. He, H. Zhou, *Sci. Adv.* **2022**, 8, eabn4372.
- [396] Y. Kato, K. Kawamoto, R. Kanno, M. Hirayama, *Electrochemistry* **2012**, 80, 749.
- [397] L. Loaiza, L. Monconduit, V. Seznec, *Small* **2020**, 16, 1905260.
- [398] G. Li, Y. Gao, X. He, Q. Huang, S. Chen, S. Kim, D. Wang, *Nat. Commun.* **2017**, 8, 850.
- [399] X. Gu, J. Dong, C. Lai, *Engineering Rep.* **2021**, 3, e12339.
- [400] Y. Zhao, Y. Ye, F. Wu, Y. Li, L. Li, R. Chen, *Adv. Mater.* **2019**, 31, 1806532.
- [401] C. Bi, M. Zhao, L. Hou, Z. Chen, X. Zhang, B. Li, H. Yuan, J. Huang, *Adv. Sci.* **2022**, 9, 2103910.
- [402] Y. Hashimoto, *Solid State Ionics* **2004**, 175, 177.
- [403] Y. Gui, Z. Liu, L. Chen, H. Huang, H. Ning, *J. Funct. Mater.* **2019**, 50, 9027.
- [404] Y. Liu, R. Ma, Y. He, M. Gao, H. Pan, *Adv. Funct. Mater.* **2014**, 24, 3944.
- [405] S. Matsuda, Y. Kubo, K. Uosaki, S. Nakanishi, *Carbon* **2017**, 119, 119.
- [406] F. Sun, D. Zhou, X. He, M. Osenberg, K. Dong, L. Chen, S. Mei, A. Hilger, H. Markötter, Y. Lu, S. Dong, S. Marathe, C. Rau, X. Hou, J. Li, M. Stan, M. Winter, R. Dominko, I. Manke, *ACS Energy Lett.* **2020**, 5, 152.
- [407] C. Sun, X. Huang, J. Jin, Y. Lu, Q. Wang, J. Yang, Z. Wen, *J. Power Sources* **2018**, 377, 36.
- [408] Z. Li, K. Zhu, P. Liu, L. Jiao, *Adv. Energy Mater.* **2022**, 12, 2100359.
- [409] Z. Xu, Z. Guo, R. Madhu, F. Xie, R. Chen, J. Wang, M. Tebyetekerwa, Y. Hu, M. Titirici, *Energy Environ. Sci.* **2021**, 14, 6381.
- [410] B. Sun, P. Li, J. Zhang, D. Wang, P. Munroe, C. Wang, P. Notten, G. Wang, *Adv. Mater.* **2018**, 30, 1801334.
- [411] H. Wang, E. Matios, J. Luo, W. Li, *Chem. Soc. Rev.* **2020**, 49, 3783.
- [412] C. Ma, T. Xu, Y. Wang, *Energy Storage Mater.* **2020**, 25, 811.
- [413] Y. Lu, L. Li, Q. Zhang, Z. Niu, J. Chen, *Joule* **2018**, 2, 1747.
- [414] W. Luo, Y. Zhang, S. Xu, J. Dai, E. Hitz, Y. Li, C. Yang, C. Chen, B. Liu, L. Hu, *Nano Lett.* **2017**, 17, 3792.
- [415] S. Chi, X. Qi, Y. Hu, L. Fan, *Adv. Energy Mater.* **2018**, 8, 1702764.
- [416] J. Luo, C. Wang, H. Wang, X. Hu, E. Matios, X. Lu, W. Zhang, X. Tao, W. Li, *Adv. Funct. Mater.* **2019**, 29, 1805946.
- [417] Y. Zhao, C. Wang, Y. Dai, H. Jin, *Nano Energy* **2021**, 88, 106293.
- [418] Z. Zhang, S. Wenzel, Y. Zhu, J. Sann, L. Shen, J. Yang, X. Yao, Y. Hu, C. Wolverton, H. Li, L. Chen, J. Janek, *ACS Appl. Energy Mater.* **2020**, 3, 7427.
- [419] C. Wang, H. Jin, Y. Zhao, *Small* **2021**, 17, 2100974.
- [420] Y. Zhu, X. He, Y. Mo, *ACS Appl. Mater. Interfaces* **2015**, 7, 23685.
- [421] S. Wenzel, S. Sedlmaier, C. Dietrich, W. Zeier, J. Janek, *Solid State Ionics* **2018**, 318, 102.
- [422] Z. Sun, Y. Zhao, Q. Ni, Y. Liu, C. Sun, J. Li, H. Jin, *Small* **2022**, 18, 2200716.
- [423] S. Liu, Y. Zhao, X. Li, J. Yu, J. Yan, B. Ding, *Adv. Mater.* **2021**, 33, 2008084.
- [424] Y. Wang, Z. Wang, F. Zheng, J. Sun, J. Oh, T. Wu, G. Chen, Q. Huang, M. Kotobuki, K. Zeng, L. Lu, *Adv. Sci.* **2022**, 33, 2105849.
- [425] M. Baptista, H. Khalifa, A. Araújo, B. Maia, M. Souto, M. Braga, *Adv. Funct. Mater.* **2023**, 33, 2212344.
- [426] Y. Li, M. Li, Z. Sun, Q. Ni, H. Jin, Y. Zhao, *Energy Storage Mater.* **2023**, 56, 582.
- [427] X. Chi, F. Hao, J. Zhang, X. Wu, Y. Zhang, S. Gheyhani, Z. Wen, Y. Yao, *Nano Energy* **2019**, 62, 718.
- [428] C. Wang, H. Xie, L. Zhang, Y. Gong, G. Pastel, J. Dai, B. Liu, E. Wachsman, L. Hu, *Adv. Energy Mater.* **2018**, 8, 1701963.
- [429] W. Zhou, Y. Li, S. Xin, J. Goodenough, *ACS Cent. Sci.* **2017**, 3, 52.
- [430] L. Porz, T. Swamy, B. Sheldon, D. Rettenwander, T. Frömling, H. Thaman, S. Berendts, R. Uecker, W. Carter, Y. Chiang, *Adv. Energy Mater.* **2017**, 7, 1701003.
- [431] H. Tang, Z. Deng, Z. Lin, Z. Wang, I. Chu, C. Chen, Z. Zhu, C. Zheng, S. Ong, *Chem. Mater.* **2018**, 30, 163.
- [432] X. Chi, Y. Zhang, F. Hao, S. Kmiec, H. Dong, R. Xu, K. Zhao, Q. Ai, T. Terlier, L. Wang, L. Zhao, L. Guo, J. Lou, H. Xin, S. Martin, Y. Yao, *Nat. Commun.* **2022**, 13, 2854.
- [433] M. Lazar, S. Kmiec, A. Joyce, S. Martin, *ACS Appl. Energy Mater.* **2020**, 3, 11559.
- [434] Y. Tian, T. Shi, W. Richards, J. Li, J. Kim, S. Hang, G. Ceder, *Energy Environ. Sci.* **2017**, 10, 1150.
- [435] E. Wu, C. Kompella, Z. Zhu, J. Lee, S. Lee, I. Chu, H. Nguyen, S. Ong, A. Banerjee, Y. Meng, *ACS Appl. Mater. Interfaces* **2018**, 10, 10076.
- [436] W. Weng, G. Liu, Y. Li, L. Shen, X. Yao, *Appl. Mater. Today* **2022**, 27, 101448.
- [437] A. Nasu, T. Inaoka, F. Tsuji, K. Motohashi, A. Sakuda, M. Tatsumisago, A. Hayashi, *ACS Appl. Mater. Interfaces* **2022**, 14, 24480.
- [438] L. Jhang, D. Wang, A. Silver, X. Li, D. Reed, D. Wang, *Nano Energy* **2023**, 105, 107995.
- [439] X. Wang, C. Zhang, M. Sawczyk, J. Sun, Q. Yuan, F. Chen, T. Mendes, P. Howlett, C. Fu, Y. Wang, X. Tan, D. Searles, P. Král, C. Hawker, A. Whittaker, M. Forsyth, *Nat. Mater.* **2022**, 21, 1057.
- [440] Y. Tian, Y. Sun, D. Hannah, Y. Xiao, H. Liu, K. Chapman, S. Bo, G. Ceder, *Joule* **2019**, 3, 1037.
- [441] Y. Xiang, G. Zheng, Z. Liang, Y. Jin, X. Liu, S. Chen, K. Zhou, J. Zhu, M. Lin, H. He, J. a Wan, S. Yu, G. Zhong, R. Fu, Y. Li, Y. Yang, *Nat. Nanotechnol.* **2020**, 15, 883.
- [442] S. Wei, S. Choudhury, J. Xu, P. Nath, Z. Tu, L. Archer, *Adv. Mater.* **2017**, 29, 1605512.
- [443] M. Yang, F. Feng, Z. Shi, J. Guo, R. Wang, Z. Xu, Z. Liu, T. Cai, Z. Wang, C. Wang, S. Chen, Z. Ma, T. Liu, *Energy Storage Mater.* **2023**, 56, 611.
- [444] R. Fang, Y. Li, N. Wu, B. Xu, Y. Liu, A. Manthiram, J. Goodenough, *Adv. Funct. Mater.* **2023**, 33, 2211229.
- [445] M. Bay, M. Wang, R. Grissa, M. Heinz, J. Sakamoto, C. Battaglia, *Adv. Energy Mater.* **2019**, 10, 1902899.
- [446] Y. Zheng, Q. Pan, M. Clites, B. Byles, E. Pomerantseva, C. Li, *Adv. Energy Mater.* **2018**, 8, 1801885.
- [447] R. Tatara, H. Suzuki, M. Hamada, K. Kubota, S. Kumakura, S. Komaba, *J. Phys. Chem. C* **2022**, 126, 20226.
- [448] K. Holguin, M. Mohammadiroudbari, K. Qin, C. Luo, *J. Mater. Chem. A* **2021**, 9, 19083.
- [449] S. Gandhi, V. Vaddadi, S. Panda, N. Goona, S. Parne, M. Lakavat, A. Bhaumik, *J. Power Sources* **2022**, 521, 230930.
- [450] J. Wu, W. Zhou, Z. Wang, W. Wang, X. Lan, H. Yan, T. Shi, R. Hu, X. Cui, C. Xu, X. He, B. Mao, T. Zhang, J. Liu, *Adv. Mater.* **2023**, 35, 2209833.
- [451] Y. Tian, G. Zeng, A. Rutt, T. Shi, H. Kim, J. Wang, J. Koettgen, Y. Sun, B. Ouyang, T. Chen, Z. Lun, Z. Rong, K. Persson, G. Ceder, *Chem. Rev.* **2021**, 121, 1623.
- [452] K. Cao, X. Zhao, J. Chen, B. Xu, M. Shahzad, W. Sun, H. Pan, M. Yan, Y. Jiang, *Adv. Energy Mater.* **2021**, 11, 2101299.
- [453] P. Shi, L. P. Hou, C. B. Jin, Y. Xiao, Y. X. Yao, J. Xie, B. Q. Li, X. Q. Zhang, Q. Zhang, *J. Am. Chem. Soc.* **2022**, 144, 212.
- [454] C. Chen, L. Fu, J. Maier, *Nature* **2016**, 53, 159.
- [455] V. Schott, M. Föhnle, P. Madden, *J. Phys. Condens. Matter* **2000**, 12, 1171.

- [456] H. Yan, K. Tantratian, K. Ellwood, E. Harrison, M. Nichols, X. Cui, L. Chen, *Adv. Energy Mater.* **2011**, *11*, 2102283.
- [457] R. Tataru, K. Ishihara, T. Hosaka, K. Aoki, Y. Takei, T. Matsui, T. Takayama, S. Komaba, *Electrochim. Acta* **2023**, *439*, 141561.
- [458] Y. Zhang, P. Qiu, J. Zheng, X. Chen, X. Chen, S. Li, C. Ji, Y. Wu, X. Chen, *ACS Appl. Mater. Interfaces* **2022**, *14*, 17378.
- [459] S. Li, P. Qiu, J. Kang, Y. Ma, Y. Zhang, Y. Yan, T. Jensen, Y. Guo, J. Zhang, X. Chen, *ACS Appl. Mater. Interfaces* **2021**, *13*, 17554.
- [460] J. Zheng, H. Fang, L. Fan, Y. Ren, P. Jena, Y. Wu, *J. Phys. Chem. Lett.* **2021**, *12*, 7120.
- [461] Y. Tian, G. Zeng, A. Rutt, T. Shi, H. Kim, J. Wang, J. Koettgen, Y. Sun, B. Ouyang, T. Chen, *Chem. Rev.* **2021**, *121*, 1623.
- [462] J. Doux, L. Leguay, A. Salle, O. Joubert, E. Quarez, *Solid State Ionics* **2018**, *324*, 260.
- [463] Y. Xu, T. Ding, D. Sun, X. Ji, X. Zhou, *Adv. Funct. Mater.* **2022**, *33*, 2211290.
- [464] T. Masese, K. Yoshii, Y. Yamaguchi, T. Okumura, Z. Huang, M. Kato, K. Kubota, J. Furutani, Y. Orikasa, H. Senoh, H. Sakaebe, M. Shikano, *Nat. Commun.* **2018**, *9*, 3823.
- [465] J. Wang, G. Lei, T. He, H. Cao, P. Chen, *J. Energy Chem.* **2022**, *69*, 555.
- [466] T. Hosaka, S. Muratsubaki, K. Kubota, H. Onuma, S. Komaba, *J. Phys. Chem. Lett.* **2019**, *10*, 3296.
- [467] H. Fei, Y. Liu, Y. An, X. Xu, J. Zhang, B. Xi, S. Xiong, J. Feng, *J. Power Sources* **2019**, *433*, 226697.
- [468] R. Tataru, S. Nishimura, Y. Okamoto, K. Ueno, M. Watanabe, K. Dokko, *J. Phys. Chem. C* **2020**, *124*, 15800.
- [469] H. Fei, Y. Liu, Y. An, X. Xu, G. Zeng, Y. Tian, L. Ci, B. Xi, S. Xiong, J. Feng, *J. Power Sources* **2018**, *399*, 294.
- [470] M. Elmanzalawy, E. Ahijón, O. Kisacik, J. González, E. Martínez, *ACS Appl. Energy Mater.* **2022**, *5*, 9009.
- [471] M. Rayung, M. Aung, A. Ahmad, M. Su'ait, L. Abdullah, S. Jamil, *Mater. Chem. Phys.* **2019**, *222*, 110.
- [472] Y. Zhang, A. Bahi, F. Ko, J. Liu, *Small* **2022**, *18*, 2107186.
- [473] E. Manarin, F. Corsini, S. Trano, L. Fagiolari, J. Amici, C. Francia, S. Bodoardo, S. Turri, F. Bella, G. Griffini, *ACS Appl. Polym. Mater.* **2022**, *4*, 3855.
- [474] J. Muldoon, C. Bucur, T. Gregory, *Chem. Rev.* **2014**, *114*, 11683.
- [475] F. Liu, T. Wang, X. Liu, L. Fan, *Adv. Energy Mater.* **2020**, *10*, 2000787.
- [476] Y. Liang, H. Dong, D. Aurbach, Y. Yao, *Nat. Energy* **2020**, *5*, 646.
- [477] R. Gummow, G. Vamvounis, M. Kannan, Y. He, *Adv. Mater.* **2018**, *30*, 1801702.
- [478] H. Yoo, I. Shterenberg, Y. Gofer, G. Gershtinsky, N. Pour, D. Aurbach, *Energy Environ. Sci.* **2013**, *6*, 2265.
- [479] Z. Karger, R. Liu, W. Dai, Z. Li, T. Diemant, B. Vinayan, C. Minella, X. Yu, A. Manthiram, R. Behm, *ACS Energy Lett.* **2018**, *3*, 2005.
- [480] J. Muldoon, C. Bucur, A. Oliver, J. Zajicek, G. Allred, W. Boggess, *Energy Environ. Sci.* **2013**, *6*, 482.
- [481] X. Hu, Y. Shi, S. Lang, X. Zhang, L. Gu, Y. Guo, R. Wen, L. Wan, *Nano Energy* **2018**, *49*, 453.
- [482] Z. Zhang, Y. Shao, B. Lotsch, Y. Hu, H. Li, J. Janek, C. Nan, L. Nazar, J. Maier, M. Armand, L. Chen, *Energy Environ. Sci.* **2018**, *11*, 1945.
- [483] R. Shannon, *Acta Crystallogr. Sect. A* **1976**, *32*, 751.
- [484] M. Patrie, J. Flahaut, L. Domage, *C. R. Hebd. Acad. Sci.* **1964**, *258*, 2585.
- [485] K. Mitchell, J. Ibers, *Chem. Rev.* **2002**, *102*, 1929.
- [486] J. Bachman, S. Muy, A. Grimaud, H. Chang, N. Pour, S. Lux, O. Paschos, F. Maglia, S. Lupart, P. Lamp, L. Giordano, Y. Horn, *Chem. Rev.* **2016**, *116*, 140.
- [487] J. Koettgen, C. Bartel, G. Ceder, *Chem. Commun.* **2020**, *56*, 1952.
- [488] A. Navrotsky, C. Ma, K. Lilova, N. Birkner, *Science* **2010**, *330*, 199.
- [489] N. Imanaka, Y. Okazaki, G. Adachi, *J. Mater. Chem.* **2000**, *10*, 1431.
- [490] L. Skov, J. Grinderslev, A. Rosenkranz, Y. Lee, T. Jensen, *Batteries & Supercaps* **2022**, *5*, e202200163.
- [491] Y. Yan, J. Grinderslev, T. Burankova, S. Wei, J. Embs, J. Skibsted, T. Jensen, *J. Phys. Chem. Lett.* **2022**, *13*, 2211.
- [492] T. Ikeshoji, E. Tsuchida, S. Takagi, M. Matsuo, S. Orimo, *RSC Adv.* **2014**, *4*, 1366.
- [493] E. Roedern, R. Kühnel, A. Remhof, C. Battaglia, *Sci. Rep.* **2017**, *7*, 46189.
- [494] I. Golub, M. Heere, V. Gounaris, X. Li, T. Steenhaut, J. Wang, K. Robeyns, H. Li, I. Dovgaliuk, K. Ikeda, G. Hautier, Y. Filinchuk, *Dalton Trans.* **2023**, *52*, 2404.
- [495] N. Anuar, S. Adnan, N. Mohamed, *Ceramics International* **2014**, *40*, 13719.
- [496] J. Torres, D. Gamboa, L. Tovar, L. González, S. Arciniega, E. Juárez, I. Gómez, E. Sánchez, *J. Electronic Mater.* **2023**, *52*, 1250.
- [497] Y. Zheng, J. Guo, D. Ning, Y. Huang, W. Lei, J. Li, J. Li, G. Schuck, J. Shen, Y. Guo, Q. Zhang, H. Tian, H. Ian, H. Shao, *J. Mater. Sci. Technol.* **2023**, *144*, 15.
- [498] R. Deivanayagam, M. Cheng, M. Wang, V. Vasudevan, T. Foroozan, N. Medhekar, R. Yassar, *ACS Appl. Energy Mater.* **2019**, *2*, 7980.
- [499] F. Croce, G. Appetecchi, L. Persi, B. Scrosati, *Nature* **1998**, *394*, 456.
- [500] M. Cheng, Y. Jiang, W. Yao, Y. Yuan, R. Deivanayagam, T. Foroozan, Z. Huang, B. Song, R. Rojaee, T. Shokuhfar, Y. Pan, J. Lu, R. Shahbazian-Yassar, *Adv. Mater.* **2018**, *30*, 1800615.
- [501] T. Wang, X. Zhao, F. Liu, L. Fan, *J. Energy Chem.* **2021**, *59*, 608.
- [502] G. Kumar, N. Munichandraiah, *Electrochim. Acta* **2002**, *47*, 1013.
- [503] M. Morita, N. Yoshimoto, S. Yakushiji, M. Ishikawa, *Electrochem. Solid-State Lett.* **2001**, *4*, A177.
- [504] J. Oh, J. Ko, D. Kim, *Electrochim. Acta* **2004**, *50*, 903.
- [505] A. Polu, R. Kumar, H. Rhee, *Ionics* **2015**, *21*, 125.
- [506] O. Chusid, Y. Gofer, H. Gizbar, Y. Vestfrid, E. Levi, D. Aurbach, I. Riech, *Adv. Mater.* **2003**, *15*, 627.
- [507] Y. Pang, Y. Zhu, F. Fang, D. Sun, S. Zheng, *J. Mater. Sci. Technol.* **2023**, *161*, 136.
- [508] L. Wang, S. Welborn, H. Kumar, M. Li, Z. Wang, V. Shenoy, E. Detsi, *Adv. Energy Mater.* **2019**, *9*, 1902086.
- [509] M. Matsui, H. Kuwata, D. Mori, N. Imanishi, M. Mizuhata, *Front. Chem.* **2019**, *7*, 7.
- [510] R. Shah, V. Mittal, E. Matsil, A. Rosenkranz, *Adv. Mechanical Eng.* **2021**, *13*, 1.
- [511] R. Lv, X. Guan, J. Zhang, Y. Xia, J. Luo, *National Sci. Rev.* **2020**, *7*, 333.
- [512] D. Kundu, B. Adams, V. Duffort, S. Vajargah, L. Nazar, *Nat. Energy* **2016**, *1*, 16119.
- [513] J. Luo, W. Cui, P. He, Y. Xia, *Nat. Chem.* **2010**, *2*, 760.
- [514] F. Wang, O. Borodin, T. Gao, X. Fan, W. Sun, F. Han, A. Faraone, J. Dura, K. Xu, C. Wang, *Nat. Mater.* **2018**, *17*, 543.
- [515] P. Yu, Y. Zeng, H. Zhang, M. Yu, Y. Tong, X. Lu, *Small* **2019**, *15*, 1804760.
- [516] G. Fang, J. Zhou, A. Pan, S. Liang, *ACS Energy Lett.* **2018**, *3*, 2480.
- [517] L. Ma, S. Chen, H. Li, Z. Ruan, Z. Tang, Z. Liu, Z. Wang, Y. Huang, Z. Pei, J. A. Zapien, C. Zhi, *Energy Environ. Sci.* **2018**, *11*, 2521.
- [518] J. Zhi, S. Zhao, M. Zhou, R. Wang, F. Huang, *Sci. Adv.* **2023**, *9*, eade2217.
- [519] L. Ma, S. Chen, N. Li, Z. Liu, Z. Tang, J. Zapien, S. Chen, J. Fan, C. Zhi, *Adv. Mater.* **2020**, *32*, 1908121.
- [520] H. Qiu, X. Du, J. Zhao, Y. Wang, J. Ju, Z. Chen, Z. Hu, D. Yan, X. Zhou, G. Cui, *Nat. Commun.* **2019**, *10*, 1.
- [521] H. Xu, H. Zhang, J. Ma, G. Xu, T. Dong, J. Chen, G. Cui, *ACS Energy Lett.* **2019**, *4*, 2871.
- [522] H. Zhai, P. Xu, M. Ning, Q. Cheng, J. Mandal, Y. Yang, *Nano Lett.* **2017**, *17*, 3182.
- [523] L. De Jonghe, *J. Electrochem. Soc.* **1982**, *129*, 752.
- [524] D. Bharti, M. Gupta, A. Srivastava, *Nano-Structures & Nano-Objects* **2019**, *17*, 123.
- [525] P. Kurek, M. Breiter, *Solid State Ionics* **1996**, *86–88*, 131.



- [526] K. Fujie, K. Otsubo, R. Ikeda, T. Yamada, H. Kitagawa, *Chem. Sci.* **2015**, 6, 4306.
- [527] J. Chen, C. Lin, D. Zhao, M. Luo, G. Peng, B. Li, S. Yang, Y. Sun, N. Ye, *Angew. Chem. Int. Ed.* **2020**, 59, 23549.
- [528] Z. Wang, J. Hu, L. Han, Z. Wang, H. Wang, Q. Zhao, J. Liu, F. Pan, *Nano Energy* **2019**, 56, 92.
- [529] Z. Chen, X. Li, D. Wang, Q. Yang, L. Ma, Z. Huang, G. Liang, A. Chen, Y. Guo, B. Dong, X. Huang, C. Yang, C. Zhi, *Energy Environ. Sci.* **2021**, 14, 3492.
- [530] J. Liu, Z. Khanam, R. Muchakayala, S. Song, *J. Mater. Sci. Mater. Electron.* **2020**, 31, 6160.
- [531] I. Dueramae, M. Okhawilai, P. Kasemsiri, H. Uyama, R. Kita, *Sci. Rep.* **2020**, 10, 12587.
- [532] D. Wang, X. Guo, Z. Chen, Y. Zhao, Q. Li, C. Zhi, *ACS Appl. Mater. Interfaces* **2022**, 14, 27287.
- [533] J. Feng, D. Ma, K. Ouyang, M. Yang, Y. Wang, J. Qiu, T. Chen, J. Zhao, B. Yong, Y. Xie, H. Mi, L. Sun, C. He, P. Zhang, *Adv. Funct. Mater.* **2022**, 32, 2207909.
- [534] H. Qiu, R. Hu, X. Du, Z. Chen, J. Zhao, G. Lu, M. Jiang, Q. Kong, Y. Yan, J. Du, X. Zhou, G. Cui, *Angew. Chem. Int. Ed.* **2022**, 61, e202113086.
- [535] F. Bu, Y. Gao, Q. Wang, Y. Wang, C. Li, J. Yang, X. Liu, C. Guan, *Small* **2023**, <https://doi.org/10.1002/sml.202303108>.
- [536] G. Ni, M. Sun, Z. Hao, G. Zou, F. Cao, L. Qin, W. Chen, C. Zhou, *Mater. Today Energy* **2023**, 31, 101204.
- [537] L. Ma, S. Chen, X. Li, A. Chen, B. Dong, C. Zhi, *Angew. Chem.* **2020**, 132, 24044.
- [538] D. Liu, Z. Tang, L. Luo, W. Yang, Y. Liu, Z. Shen, X. Fan, *ACS Appl. Mater. Interfaces* **2021**, 13, 36320.
- [539] J. Liu, S. Ahmed, Z. Khanam, T. Wang, S. Song, *Polymers* **2020**, 12, 1755.
- [540] J. Lu, P. Jaumaux, T. Wang, C. Wang, G. Wang, *J. Mater. Chem. A* **2021**, 9, 24175.
- [541] Q. Han, X. Chi, Y. Liu, L. Wang, Y. Du, Y. Ren, Y. Liu, *J. Mater. Chem. A* **2019**, 7, 22287.
- [542] Y. Lv, Y. Xiao, L. Ma, C. Zhi, S. Chen, *Adv. Mater.* **2022**, 34, 2106409.
- [543] W. Qiu, Y. Tian, Z. Lin, S. Lin, Z. Geng, K. Huang, A. Lei, F. Huang, H. Feng, F. Ding, Y. Li, X. Lu, *J. Energy Chem.* **2022**, 70, 283.
- [544] J. Li, J. Ren, C. Li, P. Li, T. Wu, S. Liu, L. Wang, *Nano Res.* **2022**, 15, 7190.
- [545] J. Zhao, H. Ren, Q. Liang, D. Yuan, S. Xi, C. Wu, W. Manalastas, J. Ma, W. Fang, Y. Zheng, C. Du, M. Srinivasan, Q. Yan, *Nano Energy* **2019**, 62, 94.
- [546] H. Li, C. Han, Y. Huang, Y. Huang, M. Zhu, Z. Pei, Q. Xue, Z. Wang, Z. Liu, Z. Tang, Y. Wang, F. Kang, B. Li, C. Zhi, *Energy Environ. Sci.* **2018**, 11, 941.
- [547] M. Nie, D. Abraham, D. Seo, Y. Chen, A. Bose, B. Lucht, *J. Phys. Chem. C* **2013**, 117, 25381.
- [548] J. Crawford Jr., F. Williams, *J. Chem. Phys.* **1950**, 18, 775.
- [549] X. Zheng, T. Ahmad, W. Chen, *Energy Storage Mater.* **2021**, 39, 365.
- [550] H. Jia, Z. Wang, B. Tawiah, Y. Wang, C. Chan, B. Fei, F. Pan, *Nano Energy* **2020**, 70, 104523.
- [551] Y. Ai, S. Wu, K. Wang, T. Yang, M. Liu, H. Liao, J. Sun, J. Chen, S. Tang, D. Wu, T. Su, Y. Wang, H. Chen, S. Zhang, W. Liu, Y. Chen, L. Lee, H. He, Z. Wang, Y. Chueh, *ACS Nano* **2020**, 14, 8539.
- [552] R. Li, R. Deng, Z. Wang, Y. Wang, G. Huang, J. Wang, F. Pan, *J. Solid State Electrochem.* **2023**, 27, 1291.
- [553] J. Wang, C. Sun, Y. Gong, H. Zhang, J. Alonso, M. Díaz, Z. Wang, J. Goodenough, *Chinese Phys. B* **2018**, 27, 128201.
- [554] T. Hibino, K. Kobayashi, M. Nagao, *J. Mater. Chem. A* **2013**, 1, 14844.
- [555] M. Agiorgousis, Y. Sun, S. Zhang, *ACS Energy Lett.* **2017**, 2, 689.
- [556] Z. Yu, S. Jiao, J. Tu, W. Song, H. Lei, H. Jiao, H. Chen, D. Fang, *J. Mater. Chem. A* **2019**, 7, 20348.
- [557] D. Ma, D. Yuan, C. León, Z. Jiang, X. Xia, J. Pan, *Energy Environ. Mater.* **2023**, 6, e12301.
- [558] I. Kim, S. Jang, K. Lee, Y. Tak, G. Lee, *Energy Storage Mater.* **2021**, 40, 229.
- [559] X. Shen, T. Sun, Z. Wu, L. Tan, *J. Mater. Chem. A* **2022**, 10, 8178.
- [560] T. Yao, F. Genier, S. Biria, I. Hosein, *Results Phys.* **2018**, 10, 529.
- [561] S. Nayem, A. Ahmad, S. Shah, A. Alzahrani, A. Ahammad, M. Aziz, *Chem. Rec.* **2022**, 22, e202200181.
- [562] Q. Ran, S. Zeng, M. Zhu, W. Wan, H. Meng, H. Shi, Z. Wen, X. Lang, Q. Jiang, *Adv. Funct. Mater.* **2023**, 33, 2211271.
- [563] P. Meng, J. Huang, Z. Yang, F. Wang, T. Lv, J. Zhang, C. Fu, W. Xiao, *Adv. Mater.* **2022**, 34, 2106511.
- [564] D. Aurbach, R. Skaletsky, Y. Gofer, *J. Electrochem. Soc.* **2019**, 138, 3536.
- [565] A. Ponrouch, C. Frontera, F. Bardé, M. Palacín, *Nat. Mater.* **2016**, 15, 169.
- [566] B. Ji, H. He, W. Yao, Y. Tang, *Adv. Mater.* **2021**, 33, 2005501.
- [567] C. Han, H. Li, Y. Li, J. Zhu, C. Zhi, *Nat. Commun.* **2021**, 12, 2400.
- [568] R. Seever, J. DeNuzzio, G. Farrington, B. Dunn, *J. Solid State Chem.* **1983**, 50, 146.
- [569] N. Katsuhiko, I. Shoichiro, I. Kaname, E. Hisahiko, *Bull. Chem. Soc. Jpn.* **1992**, 65, 3221.
- [570] D. Deyneko, D. Petrova, S. Aksenov, S. Stefanovich, O. Baryshnikova, S. Fedotov, P. Burns, M. Kosmyna, A. Shekhovtsov, B. Lazoryak, *CrystEngComm* **2019**, 21, 1309.
- [571] J. Evans, J. Huang, A. Sleight, *J. Solid State Chem.* **2001**, 157, 255.
- [572] S. Stefanovich, D. Petrova, V. Morozov, E. Fortalnova, D. Belov, D. Deyneko, O. Barishnikova, A. Belik, B. Lazoryak, *J. Alloys Compd.* **2018**, 735, 1826.
- [573] Y. Chen, C. Bartel, M. Avdeev, Y. Zhang, J. Liu, P. Zhong, G. Zeng, Z. Cai, H. Kim, H. Ji, G. Ceder, *Chem. Mater.* **2022**, 34, 128.
- [574] D. Lei, Q. Zhang, N. Liu, Z. Liu, T. Su, L. Wang, Z. Ren, P. Jia, W. Lu, Y. Gao, *Cell Rep. Phys. Sci.* **2022**, 3, 101050.
- [575] Z. Lu, F. Ciucci, *Chem. Mater.* **2017**, 29, 9308.
- [576] J. Koettgen, C. Bartel, J. Shen, K. Persson, G. Ceder, *Phys. Chem. Chem. Phys.* **2020**, 22, 27600.
- [577] W. Lee, S. Tamura, N. Imanaka, *Chem. Lett.* **2017**, 46, 1486.
- [578] J. Wang, F. Genier, H. Li, S. Biria, I. Hosein, *ACS Appl. Polym. Mater.* **2019**, 1, 1837.
- [579] D. Irish, G. Walrafen, *J. Chem. Phys.* **1967**, 46, 378.
- [580] F. Genier, C. Burdin, S. Biria, I. Hosein, *J. Power Sources* **2019**, 414, 302.
- [581] S. Biria, S. Pathreker, F. Genier, I. Hosein, *ACS Appl. Polym. Mater.* **2020**, 2, 2111.
- [582] D. Tekliye, A. Kumar, X. Weihang, T. Mercy, P. Canepa, G. Gautam, *Chem. Mater.* **2022**, 34, 10133.
- [583] X. Tang, D. Zhou, B. Zhang, S. Wang, P. Li, H. Liu, X. Guo, P. Jaumaux, X. Gao, Y. Fu, C. Wang, C. Wang, G. Wang, *Nat. Commun.* **2021**, 12, 2857.
- [584] J. Xie, Z. Liang, Y. Lu, *Nat. Mater.* **2020**, 19, 1006.
- [585] L. Suo, O. Borodin, T. Gao, M. Olguin, J. Ho, X. Fan, C. Luo, C. Wang, K. Xu, *Science* **2015**, 350, 938.
- [586] R. Staniewicz, *J. Electrochem. Soc.* **1980**, 127, 782.
- [587] T. Tran, M. Obrovac, *J. Electrochem. Soc.* **2011**, 158, A1411.
- [588] A. Ponrouch, D. Tchitchekova, C. Frontera, F. Barde, M. Dompablo, M. Palacin, *Electrochem. Commun.* **2016**, 66, 75.
- [589] M. Hadi, M. Kadhim, I. Al-Azawi, S. Abdullaha, A. Majdi, S. Hachim, A. Rheima, *Comput. Theor. Chem.* **2023**, 1219, 113940.
- [590] M. Woodcox, M. Smeu, *J. Electrochem. En. Conv. Stor.* **2021**, 18, 040903.
- [591] D. Datta, J. Li, V. Shenoy, *ACS Appl. Mater. Interfaces* **2014**, 6, 1788.
- [592] Z. Karger, Y. Xiu, Z. Li, A. Reupert, T. Smok, M. Fichtner, *Nat. Commun.* **2022**, 13, 3849.

- [593] S. Prabakar, A. Ikhe, W. Park, K. Chung, H. Park, K. Kim, D. Ahn, J. Kwak, K. Sohn, M. Pyo, *Adv. Sci.* **2019**, *6*, 1902129.
- [594] Y. Cao, K. Sharma, A. Rajhi, S. Alamri, A. Anqi, A. Shafay, A. Aly, B. Felemban, S. Rashidi, M. Derakhshandeh, *J. Electroanal. Chem.* **2022**, *910*, 115929.
- [595] P. Wang, H. Wang, Z. Chen, J. Wu, J. Luo, Y. Huang, *Nano Res.* **2022**, *15*, 701.
- [596] R. Li, J. Yu, F. Chen, Y. Su, K. Chan, Z. Xu, *Adv. Funct. Mater.* **2023**, *2214304*.
- [597] M. Wang, C. Jiang, S. Zhang, X. Song, Y. Tang, H. Cheng, *Nat. Chem.* **2018**, *10*, 667.
- [598] J. Li, C. Han, X. Ou, Y. Tang, *Angew. Chem. Int. Ed.* **2022**, *61*, e202116668.
- [599] J. Park, Z. Xu, G. Yoon, S. Park, J. Wang, H. Hyun, H. Park, J. Lim, Y. Ko, Y. Yun, K. Kang, *Adv. Mater.* **2020**, *32*, 1904411.
- [600] H. Tinker, C. Howard, M. Zhou, Y. Xu, *Mater. Adv.* **2023**, *4*, 2028.
- [601] D. Aurbach, A. Zaban, A. Schechter, Y. Ein-Eli, E. Zinigrad, B. Markovsky, *J. Electrochem. Soc.* **1995**, *142*, 2873.
- [602] B. Wu, J. Lochala, T. Taverne, J. Xiao, *Nano Energy* **2017**, *40*, 34.
- [603] M. He, R. Guo, G. Hobold, H. Gao, B. Gallant, *Proc. Natl. Acad. Sci.* **2020**, *117*, 73.
- [604] J. Xiao, Q. Li, Y. Bi, M. Cai, B. Dunn, T. Glossmann, J. Liu, T. Osaka, R. Sugiura, B. Wu, J. Yang, J. Zhang, M. Whittingham, *Nat. Energy* **2020**, *5*, 561.
- [605] B. Han, X. Li, Q. Wang, Y. Zou, G. Xu, Y. Cheng, Z. Zhang, Y. Zhao, Y. Deng, J. Li, M. Gu, *Adv. Mater.* **2022**, *34*, 2108252.
- [606] F. Langenhorst, V. Solozhenko, *Phys. Chem. Chem. Phys.* **2002**, *4*, 5183.
- [607] Y. Jin, N. Kneusels, L. Marbella, E. Castillo-Martínez, P. Magusin, R. Weatherup, E. Jónsson, T. Liu, S. Paul, C. Grey, *J. Am. Chem. Soc.* **2018**, *140*, 9854.
- [608] M. Yang, S. Zybín, T. Das, B. Merinov, W. Goddard, E. Mok, H. Hah, H. Han, Y. Choi, S. Kim, *Adv. Energy Mater.* **2023**, *13*, 2202949.
- [609] W. Xu, X. Liao, W. Xu, C. Sun, K. Zhao, Y. Zhao, C. Hu, *Nano Energy* **2021**, *88*, 106237.
- [610] W. Xu, C. Sun, N. Wang, X. Liao, K. Zhao, G. Yao, Q. Sun, H. Cheng, Y. Wang, X. Lu, *Nano Energy* **2021**, *81*, 105584.
- [611] J. Xie, S. Sun, X. Chen, L. Hou, B. Li, H. Peng, J. Huang, X. Zhang, Q. Zhang, *Angew. Chem. Int. Ed.* **2022**, *61*, e202204776.
- [612] A. Manthiram, S. Chung, C. Zu, *Adv. Mater.* **2015**, *27*, 1980.
- [613] T. Li, X. Bai, U. Gulzar, Y. Bai, C. Capiglia, W. Deng, X. Zhou, Z. Liu, Z. Feng, R. Proietti Zaccaria, *Adv. Funct. Mater.* **2019**, *29*, 1901730.
- [614] M. Smeu, K. Leung, *Phys. Chem. Chem. Phys.* **2021**, *23*, 3214.
- [615] K. Tasaki, *J. Phys. Chem. B* **2005**, *109*, 2920.
- [616] B. Han, Y. Zou, Z. Zhang, X. Yang, X. Shi, H. Meng, H. Wang, K. Xu, Y. Deng, M. Gu, *Nat. Commun.* **2021**, *12*, 3066.
- [617] S. Heiskanen, J. Kim, B. Lucht, *Joule* **2019**, *3*, 2322.
- [618] A. Bouibes, N. Takenaka, T. Fujie, K. Kubota, S. Komaba, M. Nagaoka, *ACS Appl. Mater. Interfaces* **2018**, *10*, 28525.
- [619] L. Ji, M. Gu, Y. Shao, X. Li, M. Engelhard, B. Arey, W. Wang, Z. Nie, J. Xiao, C. Wang, J. Zhang, J. Liu, *Adv. Mater.* **2014**, *26*, 2901.
- [620] J. Fondard, E. Irisarri, C. Courrèges, M. Palacin, A. Ponrouch, R. Dedryvère, *J. Electrochem. Soc.* **2020**, *167*, 070526.
- [621] M. Dahbi, N. Yabuuchi, K. Kubota, K. Tokiwa, S. Komaba, *Phys. Chem. Chem. Phys.* **2014**, *16*, 15007.
- [622] U. Purushotham, N. Takenaka, M. Nagaoka, *RSC Adv.* **2016**, *6*, 65232.
- [623] H. Ding, J. Wang, J. Zhou, C. Wang, B. Lu, *Nat. Commun.* **2023**, *14*, 2305.
- [624] D. Chinnadurai, W. Lieu, S. Kumar, G. Yang, Y. Li, Z. Seh, *Nano Lett.* **2023**, *23*, 1564.
- [625] H. Fan, X. Zhang, J. Xiao, Y. Lin, S. Ren, Y. Zhao, H. Yuan, L. Pan, Q. Lin, H. Liu, Y. Su, Y. Su, Y. Liu, Y. Zhang, *Energy Storage Mater.* **2022**, *51*, 873.
- [626] Y. Li, P. Zuo, R. Li, H. Huo, Y. Ma, C. Du, Y. Gao, G. Yin, R. Weatherup, *ACS Appl. Mater. Interfaces* **2021**, *13*, 24565.
- [627] P. Wang, K. Küster, U. Starke, C. Liang, R. Niewa, M. Buchmeiser, *J. Power Sources* **2021**, *515*, 230604.
- [628] D. Huang, S. Tan, M. Li, D. Wang, C. Han, Q. An, L. Mai, *ACS Appl. Mater. Interfaces* **2020**, *12*, 17474.
- [629] X. Li, T. Gao, F. Han, Z. Ma, X. Fan, S. Hou, N. Eidson, W. Li, C. Wang, *Adv. Energy Mater.* **2018**, *8*, 1701728.
- [630] H. Dou, X. Zhao, Y. Zhang, W. Zhao, Y. Yan, Z. Ma, X. Wang, X. Yang, *Nano Energy* **2021**, *86*, 106087.
- [631] C. Wagner, A. Naumkin, A. Kraut-Vass, J. Allison, C. Powell, J. Rumble, *Nist Standard Reference Database 20, Version 3.4 (Web Version)*, National Institute of Standards and Technology, Gaithersburg, MD **2003**, p. 20899.
- [632] G. Agarwal, J. Howard, V. Prabhakaran, G. Johnson, V. Murugesan, K. Mueller, L. Curtiss, R. Assary, *ACS Appl. Mater. Interfaces* **2021**, *13*, 38816.
- [633] D. Zhang, S. Duan, X. Liu, Y. Yang, Y. Zhang, W. Ren, S. Zhang, M. Cheng, W. Yang, J. Wang, Y. NuLi, *Nano Energy* **2023**, *109*, 108257.
- [634] P. Xiong, Y. Kang, N. Yao, X. Chen, H. Mao, W. Jang, D. Halat, Z. Fu, M. Jung, H. Jeong, Y. Kim, J. Reimer, Q. Zhang, H. Park, *ACS Energy Lett.* **2023**, *8*, 1613.
- [635] S. Wang, Z. Wang, Y. Yin, T. Li, N. Chang, F. Fan, H. Zhang, X. Li, *Energy Environ. Sci.* **2021**, *14*, 4077.
- [636] J. Hao, J. Long, B. Li, X. Li, S. Zhang, F. Yang, X. Zeng, Z. Yang, W. Pang, Z. Guo, *Adv. Funct. Mater.* **2019**, *29*, 1903605.
- [637] C. Li, A. Shyamsunder, A. Hoane, D. Long, C. Kwok, P. Kotula, K. Zavadil, A. Gewirth, L. Nazar, *Joule* **2022**, *6*, 1103.
- [638] F. Chowdhury, H. Yamada, T. Higashii, K. Goto, M. Onoda, *Ind. Eng. Chem. Res.* **2013**, *52*, 8323.
- [639] T. Loerting, J. Bernard, *ChemPhysChem* **2010**, *11*, 2305.
- [640] W. Sun, F. Wang, B. Zhang, M. Zhang, V. Küpers, X. Ji, C. Theile, P. Bieker, K. Xu, C. Wang, M. Winter, *Science* **2021**, *371*, 46.
- [641] H. Pan, Y. Shao, P. Yan, Y. Cheng, K. Han, Z. Nie, C. Wang, J. Yang, X. Li, P. Bhattacharya, K. Mueller, J. Liu, *Nat. Energy* **2016**, *1*, 16039.
- [642] J. Huang, Z. Wang, M. Hou, X. Dong, Y. Liu, Y. Wang, Y. Xia, *Nat. Commun.* **2018**, *9*, 2906.
- [643] C. Xu, T. Diemant, X. Liu, S. Passerini, *Adv. Funct. Mater.* **2023**, *33*, 2214405.
- [644] P. Bolt, E. Grotenhuis, J. Geus, F. Habraken, *Surf. Sci.* **1995**, *329*, 227.
- [645] R. Ibáñez, F. Martín, J. Ramos-Barrado, D. Leinen, *Surf. Coatings Technol.* **2006**, *200*, 6368.
- [646] S. Zhang, Z. Wang, X. Chang, W. Hou, J. Wang, *Corr. Sci.* **2011**, *53*, 3007.
- [647] L. Guo, Q. Zhang, Y. Huang, S. Kaya, X. Zheng, R. Zhang, W. Shi, I. Obot, *J. Electroanal. Chem.* **2023**, *941*, 117535.
- [648] T. Pham, W. Lee, J. Kim, *J. Mol. Liq.* **2022**, *347*, 118269.
- [649] T. Wang, H. Cheng, Z. Tian, Z. Li, Z. Lin, Z. You, Y. Lu, Y. Zhu, W. Li, Y. Yang, Q. Zhong, Y. Lai, *Energy Storage Mater.* **2022**, *53*, 371.
- [650] H. Song, C. Wang, *Energy Environ. Mater.* **2023**, *6*, e12325.
- [651] H. Song, J. Su, C. Wang, *Adv. Mater.* **2021**, *33*, 2006141.
- [652] H. Song, L. Shen, J. Wang, C. Wang, *Nano Energy* **2017**, *34*, 47.
- [653] F. Zeng, S. Li, S. Hu, M. Qiu, G. Zhang, M. Li, C. Chang, H. Wang, M. Xu, L. Zheng, Y. Tang, C. Han, H. Cheng, *Adv. Funct. Mater.* **2023**, *2302397*.
- [654] R. Li, J. Yu, F. Chen, Y. Su, K. Chan, Z. Xu, *Adv. Funct. Mater.* **2023**, *33*, 2214304.
- [655] S. Kim, N. Hahn, T. Fister, N. Leon, X. Lin, H. Park, P. Zapol, S. Lapidus, C. Liao, J. Vaughey, *Chem. Mater.* **2023**, *35*, 2363.
- [656] X. Qin, X. Zhao, G. Zhang, Z. Wei, L. Li, X. Wang, C. Zhi, H. Li, C. Han, B. Li, *ACS Nano* **2023**, *17*, 12040.



**Sambhaji S. Shinde** is a research professor of materials science and chemical engineering at Hanyang University, Republic of Korea. His research interests focus on advanced electrode materials for zinc/lithium/aluminum-based batteries, all-solid-state batteries, and new materials design for energy storage and reaction mechanisms.



**Nayantara K. Wagh** received her Ph.D. in materials science and chemical engineering from Hanyang University in 2022. She is currently a postdoctoral researcher at Hanyang University, Republic of Korea. Her research interests are the rational design of cathode materials for solid and liquid metal-air batteries.



**Sung-Hae Kim** is a graduate student in materials science and chemical engineering at Hanyang University under the supervision of Prof. Jung-Ho Lee. He received his M.S. in 2019. His research interest focuses on synthesizing and characterizing solid electrolytes and metal anodes for metal-air batteries.



**Jung-Ho Lee** is a materials science and chemical engineering professor at Hanyang University, Korea. He obtained his Ph.D. in materials science and engineering at the Korea Advanced Institute of Science & Technology (KAIST) in 1995. His research interests focus on high-energy next-generation all-solid-state batteries for EV, UAM, aircraft, wearable, and military applications. In 2022, he founded Flexolyte, Inc with Dr. Shinde as a start-up to commercialize all-solid-state zinc-air batteries.